

Resistive Switching in MgO and Si/Ag Metal-Insulator-Metal structures

Catarina Dias

Doutoramento em Física
Departamento de Física e Astronomia
2019

Orientador

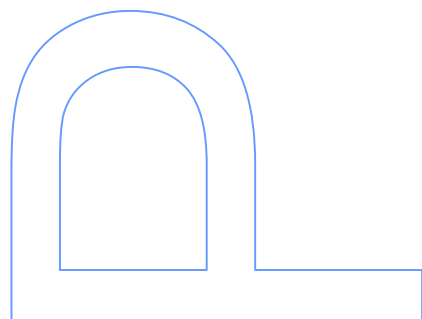
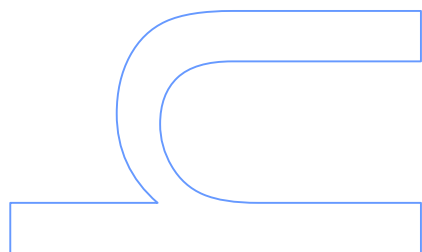
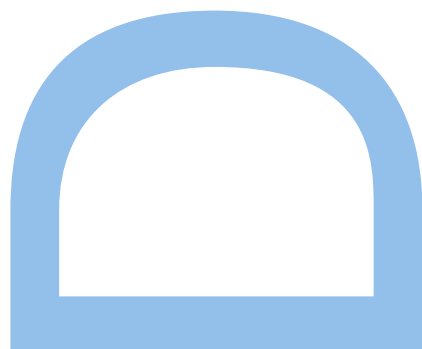
Dr. João Ventura, IFIMUP e Faculdade de Ciências, Universidade do Porto

Coorientador

Dra. Susana Cardoso, INESC-MN e Instituto Superior Técnico

Coorientador

Dr. Paulo Aguiar, INEB e i3S, Universidade do Porto



Catarina Dias

Resistive Switching in MgO and Si/Ag Metal-Insulator-Metal structures



Supervisor: Dr. João Ventura

Co-supervisor: Dr. Susana Cardoso

Co-supervisor: Dr. Paulo Aguiar

*Thesis submitted to the Faculty of Sciences of the University of Porto
in partial fulfilment of the requirements for the degree of Doctor in Physics*

IFIMUP-IN

Department of Physics and Astronomy
Faculty of Sciences of the University of Porto

2019

Institutions (where the work was carried out):



Universitat
de les Illes Balears

Funding:

This PhD work was supported by the Fundação para a Ciência e a Tecnologia (Portuguese Agency for Research) fellowships SFRH/B1/52521/2014 and SFRH/BD/101661/2014, and STSM grant COST-STSM-IC1401-36548 within the MemoCIS COST Action IC1401.



"Apart from memory, learning was the greatest of our brain's gifts."

— MIGUEL NICOLELIS,

Beyond Boundaries: The New Neuroscience of Connecting Brains with Machines – and how it will change our lives

Acknowledgments

First and foremost, I would like to express my sincere gratitude to my supervisor Dr. João Ventura for his infinite patience (I surely tested it!) and trust in me. This work was only possible with his optimism balancing my inherent pessimism. Likewise, many thanks for his always intensive and fast review of all the manuscripts.

I am also thankful to my co-supervisors. To Dr. Susana Cardoso for always being available to receive me with countless runsheets and for actively dealing with fabrication problems. To Dr. Paulo Aguiar for his professionalism and scientific integrity.

I am especially thankful to the extremely competent technicians that always helped me: Eng. Francisco Carpinteiro from IFIMUP, and Eng. Fernando Silva, Eng. Virginia Soares and Eng. Zé Bernardo from INESC-MN.

Many thanks to Dr. Armanda Sá, Isabel Alves and Natércia Correia for all the bureaucratic support with my travels to Lisbon and conferences.

I am thankful to Rodrigo Picos and the MemoCIS COST Action IC1401 for allowing me to work one month at the *Universitat de les Illes Balears*.

To Dr. Ana Botelho do Rego and Dr. Ana Ferraria from CQFM for the guidance in XPS. Thanks to Arlete Apolinário for the AFM measurements, and Prof. Paulo Freitas and Dr. Leonard Francis for the TEM analysis.

I want to acknowledge Pedro Cruz for all his time and patience in solving computer (oh, the irony..) and measuring issues.

Thanks to Luís Guerra, for beginning this journey with me and truly understanding all the difficulties involved! Also, thanks for the careful thesis reading.

I want to acknowledge Diana Leitão for all the support and persistence with new challenges, and Ana Silva for all the assistance and patience.

Thanks to Lv and Tomás for the help with the cleanroom processes and DWL scheduling. To the remaining INESC-MN group for adopting me each single week that I was there and for giving me priority in the equipments.

Shukraan Moner for the support during my staying at Palma, for the model and for keeping me company in many international conferences.

I would like to offer my special thanks to Bernardo Bordalo for the measuring software and code critics, and Gonçalo Oliveira for all the help with Latex. I would like to acknowledge André

Guerra for always clarifying me regarding the doctoral procedures. Thanks to Rui M. Costa for the time spent in debugging code with me.

I am grateful for the IFIMUP group and my colleagues who put up with me most of the days: Ana Pires, Ana Silva, Arlete Apolinário, Bogdan Postolnyi, Cátia Rodrigues, Gonçalo Oliveira, Inês Figueiredo, João Horta, Leandro Martins, Mónica Cerquido, Ricardo Teixeira, Rui Costa, Rui M. Costa, Paula Quitério, Pedro Rodrigues, Suellen Moraes and Vivian Andrade. A special thanks to all of you that made our basketball and volleyball games possible, for the relaxing moments. To the new students, Ludgero Peixoto, Margarida Maia and Simão Sá, I hope that my scientific frustration has not discouraged you.

I thank *Fundação para a Ciência e a Tecnologia* (FCT) for the funding essential to this work, both through the PhD personal grant and the group projects. I also thank MAP-fis doctoral program for the first year funding and traveling financial support.

A huge acknowledgment to Alexandra Elbakyan, creator and responsible for Sci-hub. Without your courage to share knowledge and make it free, scientific research would lose meaning and it would be even harder! I truly admire you.

I am deeply grateful to my family. Thanks for all the care, love and food. Sorry for not having the patience to explain you my work. My greatest regret is all the time that I lost from your last years and cannot take back from your age.

Thanks to Rui Miguel for having the patience to continuously try to keep me with healthy schedules and a social life, and, above all, for always being there to support and criticize me. From now on I will focus on learning from you how not to get stressed.

Yours sincerely,
Catarina Dias

Resumo

Os computadores modernos, baseados na arquitectura determinística de von Neumann, onde a memória e o processamento estão fisicamente separados, não conseguem aprender e adaptar-se a novos ambientes de maneira eficiente e prática. Assim, é necessária uma nova abordagem e dispositivos capazes de simultaneamente armazenarem e processarem informação são blocos essenciais de construção. O memresistor é uma memória não volátil de dois terminais baseada em estruturas metal-isolador-metal que estabelece uma relação não-linear entre o historial de corrente e tensão através de comutação resistiva. Satisfaz os dois critérios de memória e computação, sendo um candidato promissor para esta nova era de informação.

Neste trabalho, estudámos a comutação resistiva de dois tipos de estruturas metal-isolador-metal, utilizando óxido de magnésio como camada isoladora e a dinâmica do sistema silício/prata. Começámos por estudar a estrutura Pt/MgO/Ta/Ru e observámos comportamento unipolar em múltiplos modos, ditados pelas polaridades de tensão. Usando a análise de XPS, observámos a existência de uma camada de TaO_x na interface MgO/Ta, que actua como um reservatório de oxigénio e é responsável por este comportamento. Testámos ainda estruturas de Pt/MgO/Pt e obtivemos tensões mais altas, quando comparando com o eléctrodo de Ta. Além disso, dispositivos sem um passo de quebra de vácuo na interface superior de MgO/Pt mostram um passo inicial de *forming*. Para metais reactivos como eléctrodos de cima, observámos a transição para comutação resistiva bipolar no caso de Ag. Neste caso, os filamentos metálicos responsáveis pelas mudanças de resistência são compostos por iões de prata. Foram usadas duas técnicas de deposição diferentes foram usadas para depositar a camada de MgO, nomeadamente, pulverização com magnetrão e deposição por feixe de iões. Para a mesma espessura de óxido, a primeira origina estruturas com a necessidade de um passo de *forming*, ao contrário da última. Camadas duplas de óxido Al₂O₃/MgO foram ainda fabricadas e observou-se que as tensões de operação aumentam com a espessura. O modelo *Random Circuit Breaker* foi implementado e a dependência das tensões de *forming*, *Set* e *Reset* na espessura do óxido foi comparada com dados experimentais. Para ambos os casos, apenas a tensão de *forming* aumenta com a espessura, mostrando que, após o primeiro passo, a formação e ruptura do filamento conductor ocorre apenas numa espessura menor. Uma maior percentagem de defeitos conductivos iniciais na camada isoladora também promove o processo de *forming*.

A estrutura metal-isolador-metal Pt/Si/Ag/TiW foi fabricada e caracterizada. O comportamento de comutação resistiva bipolar observado é consistente com a formação e ruptura de filamentos metálicos de prata. A mesma estrutura foi depositada em cima de substratos rígidos de Si e substratos flexíveis de PET e de celulose (comercial e bacteriana), tendo sido obtida comutação

resistiva em ambos os casos. Usando um eléctrodo de baixo de ITO, em vez de Pt, em cima de PET as tensões de *Set* e *Reset* diminuem. O espaço corrente–tensão foi modelado com sucesso através do cálculo de pontos de transição e descrição dos diferentes estados no espaço de carga–fluxo. Caracterizámos a probabilidade de transição no espaço tempo–tensão, como resultado da estocasticidade do fenómeno.

Também implementámos memresistores como sinapses e neurónios, usando simulações numéricas. Uma memória associativa Willshaw foi estudada em *Spice* com memresistores binários como junções sinápticas e testada a capacidade e robustez da rede na presença de ruído. Concluimos que os defeitos dos memresistores e a variabilidade não implicam (até certo ponto) a falha catastrófica de operação da rede e podem de facto ser superados usando uma estratégia de operação bem informada. Dois memresistores em “anti-fase” foram usados para definir cada peso de um Perceptrão de uma camada. O algoritmo em *Python* foi utilizado para classificar os dados gerados de índice de massa corporal e as bases de dados de sonar e cancro da mama. Por fim, o circuito de Hodgkin-Huxley com memresistors imitando canais iónicos foi implementado em *Spice* e um potencial de membrana preliminar foi observado.

Palavras-chave: Cumutação Resistiva, Memresistors, Memórias, Redes Neurais Artificiais, Metal-Isolador-Metal, Óxido de Magnésio, Silício.

Abstract

Modern-day computers, based on the deterministic von Neumann architecture, where memory and processing are physically separated, cannot learn and adapt to new environments in an efficient and practical way. A novel approach is thus necessary and devices capable of simultaneously storing memory and processing information are essential building blocks. The memristor is a non-volatile two-terminal nanoscale memory device based on metal-insulator-metal structures that establishes a nonlinear relationship between the histories of current and voltage, through resistive switching. It comprises both criteria of memory and computing, being a promising candidate for this new data era.

In this work, we studied the resistive switching of two types of metal-insulator-metal structures, namely using magnesium oxide as the insulator layer and silicon/silver system dynamics. We started to study the Pt/MgO/Ta/Ru stack and observed unipolar multi mode operation, dictated by the voltage polarities. Using XPS analysis we observed the existence of a TaO_x layer at the MgO/Ta interface, acting as an oxygen reservoir and being responsible for this behavior. We further tested Pt/MgO/Pt structures and obtained higher operating voltages, comparatively to the Ta electrode. Furthermore, devices without a vacuum break step at the top MgO/Pt interface show an initial forming step. For reactive metals as top electrodes, we observed the transition to bipolar resistive switching in the case of Ag. In this case, the metallic filaments responsible for the resistance changes are composed of silver ions. Two different deposition techniques were used to deposit the MgO layer, namely magnetron sputtering and Ion Beam Deposition. For the same oxide thickness, the former results in structures with the need of a forming step, unlike the latter. Double Al₂O₃/MgO oxide layers were further fabricated and it was observed that the operating voltages increase with the thickness. The Random Circuit Breaker model was implemented and the dependence of the forming, Set and Reset voltages on the oxide thickness was compared with experimental data. For both cases, only the forming voltage increases with the thickness, showing that, after the first step, the conductive filament formation and rupture happens only at a thinner thickness. A higher percentage of initial conductive defects in the oxide layer also promote the forming step.

The Pt/Si/Ag/TiW metal-insulator-metal structure was fabricated and characterized. The observed bipolar resistive switching behavior is consistent with formation and rupture of metallic Ag filaments. The same stack was deposited and resistive switching behavior was obtained on top of Si rigid substrates, and cellulose (commercial and bacterial) and PET flexible substrates. Using an ITO bottom electrode on top of PET, instead of Pt, decreases Set and Reset voltages. The current–voltage space was successfully modeled through the calculation of transition points and

different states description in the charge–flux space. We characterized the switching probability in the time–voltage, as a result of the phenomenon stochasticity.

We further implemented memristors as synapses and neurons using numerical simulations. A *Spice* Willshaw associative memory was studied with binary memristors as synaptic junctions and the capacity and robustness to noise of the network was tested. We concluded that memristor defects and variability do not imply (to some extent) the catastrophic failure of a network operation and can in fact be overcome by using a well informed operation strategy. Two memristors in “anti-phase” were used to define each weight of a single layer Perceptron. The *Python* algorithm was used to classify generated body mass index data, and sonar and breast cancer databases. Finally, the Hodgkin-Huxley circuit with memristors mimicking ionic channels was implemented in *Spice* and a preliminary action potential signature was observed.

Keywords: Resistive Switching, Memristors, Memories, Artificial Neural Networks, Metal-Insulator-Metal, Magnesium Oxide, Silicon.

Contents

1	Introduction	1
1.1	Memristors and Memristive Systems	2
1.1.1	Theory	3
1.2	Resistive Switching	4
1.2.1	Metal-Insulator-Metal Memristors	4
1.2.2	Operation	5
1.2.3	Resistive Switching Mechanisms	6
1.3	Resistive Random Access Memory	11
1.4	Device structure and material choices	11
1.4.1	Crossbar	11
1.4.2	Materials	12
1.5	Performance	13
1.5.1	Defects	13
1.5.2	Stability	14
1.5.3	Variability	14
1.5.4	Scaling	15
1.6	Neuromorphic Properties of Memristors	16
1.6.1	Spike Timing Dependent Plasticity	16
1.6.2	Short and Long Term Memory	17
1.7	Artificial Neural Networks	18
1.7.1	Perceptron	19
1.7.2	Associative Memories	21
1.8	Summary	24
1.9	Thesis Outline	24
2	Experimental Methods	27
2.1	Deposition Systems	27
2.1.1	Magnetron Sputtering Deposition	27
2.1.2	Ion Beam Deposition	29
2.2	Microfabrication Techniques	31
2.2.1	Mask Definition	31
2.2.2	Etching (Ion Milling)	32
2.2.3	Lift-off	33

2.3	Microfabrication Processes	33
2.3.1	Single-step	33
2.3.2	Two-steps	34
2.4	Characterization Methods	34
2.4.1	X-Ray Photoelectron Spectroscopy	34
2.4.2	Electrical Characterization	35
2.5	Simulations	36
2.5.1	Random Circuit Breaker	36
2.5.2	Willshaw Network	36
2.5.3	Perceptron	36
3	Resistive Switching in MgO structures	37
3.1	Multi Mode Resistive Switching	37
3.1.1	Structural Characterization	38
3.1.2	Resistive Switching	38
3.1.3	Resistive Switching in Smaller Areas	47
3.2	Influence of Vacuum Break on Resistive Switching	48
3.2.1	Structural Characterization	48
3.2.2	Morphological Characterization	49
3.2.3	Resistive Switching	50
3.2.4	Discussion	52
3.3	Influence of Top Electrodes on Resistive Switching	53
3.3.1	Discussion	55
3.4	Resistive Switching in $\text{Al}_2\text{O}_3/\text{MgO}$ Double Layer	56
3.4.1	Structural Characterization	56
3.4.2	Resistive Switching	57
3.4.3	Discussion	65
3.5	Influence of MgO Thickness on Resistive Switching	66
3.5.1	Random Circuit Breaker Model	66
3.6	Conclusions	71
4	Resistive Switching in Si/Ag structures	75
4.1	Resistive Switching	75
4.2	Charge-Flux Model	80
4.3	Stochastic Resistive Switching	83
4.3.1	Time-Voltage Stochasticity	84
4.4	Flexible Substrates	86
4.4.1	Cellulose	87
4.4.2	Polyethylene Terephthalate	91
4.4.3	Discussion	92
4.5	Conclusions	94

5	Artificial Neural Networks Simulations	95
5.1	Willshaw Network	95
5.1.1	Principle of Operation	96
5.1.2	Results	98
5.1.3	Discussion	102
5.2	Perceptron	102
5.2.1	Principle of Operation	103
5.2.2	Results	104
5.3	Hodgkin-Huxley Model	108
5.3.1	Results	109
5.4	Conclusions	110
6	Conclusions and Outlook	111
	References	112
A	Runsheets	143
A.1	Shadow Mask	143
A.2	Single Junction	145
A.3	Crossbar Network	148
B	Quantitative analysis of XPS data	153
C	Random Circuit Breaker	155
D	Perceptron	169

List of Figures

1.1	(a) The four fundamental circuit variables (q , φ , I , V). (b) Equivalent circuit and symbol of the memristor. (c) I–V hysteresis collapses with a ten fold increase in sweep frequency.	3
1.2	The two most common operation modes of ReRAMs. I–V sweep operation and pulse modes for both (a) bipolar and (b) unipolar resistive switching.	5
1.3	Geometrical location (vertical and lateral) of the switching in a MIM structure. . . .	7
1.4	Memory cell structure schematics and I–V characteristics for (a) ECM, (b) VCM and (c) TCM.	8
1.5	Sketch of the steps of the (a)–(d) Set and (e) Reset operations of ECM.	9
1.6	Sketch of the steps of the (a)–(b) Set and (c) Reset operations of VCM.	10
1.7	Schematics of (a) a RRAM crossbar array and (b) of the leakage paths in the array. .	13
1.8	Summary of the materials used in ReRAMs.	14
1.9	Schematic illustration of the natural (biological) and ReRAM-based artificial synapses. .	17
1.10	(a) Memristor synaptic weight as a function of the relative timing of the neuron spikes. (b) Measured and calculated I–V characteristics. (c) Pavlov’s dog implementation with two memristive synapses, two input and one output neurons.	18
1.11	(a) Graph and (b) crossbar network architectures.	20
1.12	(a) Single layer perceptron and (b) illustration of the hyperplane for a two-dimensional (2D) classification problem.	21
1.13	Schematic of an associative neural network.	22
2.1	Schematic of a Magnetron Sputtering system.	28
2.2	Schematic of an Ion Beam Deposition system.	30
2.3	Schematic of the physical shadow mask process.	32
2.4	Schematic of the physical single-step process.	33
2.5	Schematic of the physical two-steps process.	34
2.6	(a) Electrical measurement setup showing the tungsten microprobes on the sample, support microscope and lamp. (b) LabView control program panel.	35
2.7	Schematic of the the applied (a) voltage swept and (b) voltage pulses over time. . .	36
3.1	XPS spectrum and fitting of the Ta 4d region for a Pt / MgO / Ta (2) / Ru (1) (nm) sample.	38

3.2	I–V characteristics (a) of a pristine device showing the forming process and the switchings between the two resistance states and (b) showing resistive switching with different combinations of voltage polarity.	39
3.3	Retention time for the OFF and ON resistance states up to 14 h for the (+,+) mode, measured with 10 mV every 2 s.	40
3.4	I-V curves for the four voltage polarity combinations: (a) (+,+), (b) (+,-), (c) (-,+) and (d) (-,-).	41
3.5	Reset cycles of the (+,-) mode showing an initial abrupt transition followed by a smooth variation.	41
3.6	Cumulative probability of the absolute (a) Set and (b) Reset voltages for all voltage polarity combinations.	42
3.7	Reset voltage and current for two different devices with all switchings in the order (a) (+,+) → (+,-) → (-,+) → (-,-) and (b) (-,-) → (-,+) → (+,-) → (+,+).	42
3.8	Cumulative probability of the ON and OFF resistance states for (a) each voltage polarity combination and (b) all measurements combined.	43
3.9	Cumulative probability of the Set and Reset voltages for the (a) (+,-) and (b) (-,-) modes with forming at positive and negative voltages.	44
3.10	Cumulative probability of the Set and Reset voltages for the (a) (+,+) and (-,-), and (b) (+,-) and (-,+) modes at positive and negative forming voltages.	44
3.11	First Set (a) 10 cycles for (-,+) after (+,-) and (b) 6 for (+,-) after (-,+).	45
3.12	Reset power for two different devices with switchings in the order (+,+) → (+,-) → (-,+) → (-,-) and (-,-) → (-,+) → (+,-) → (+,+).	46
3.13	Schematic filament formation and rupture for the four different operation modes.	46
3.14	Sample obtained using a two step lithography process, showing individual device areas of 2×2, 3×3, 5×5 and 10×10 μm^2 and 9×9 crossbar networks of 10×10 μm^2 devices.	47
3.15	I–V characteristics (a) of a virgin device with an area of 10×10 μm^2 showing the forming process and the following Resets and Set, and (b) 100 consecutive cycles.	47
3.16	XPS spectra and corresponding fitting of the (a) Mg 1s, (b) O 1s, (c) Mg 2s and (d) Pt 4f regions for two Pt/MgO/Pt (3 nm) samples: with (A) and without (C) top vacuum break.	49
3.17	AFM map for a Pt/MgO/Pt structure (a) without (B) and (b) with (C) vacuum break before the top electrode deposition.	50
3.18	Pt/MgO/Pt structure A. I–V characteristics (a) of a pristine device showing the first Set and the following switchings between the two resistance states, and (b) showing 10 seeping cycles for the (+,-) and (+,+) switching modes. (c) I–V characteristics for the (-,+) mode.	51
3.19	Pt/MgO/Pt structure B. I–V characteristics (a) of a pristine device showing the first Set and the following switchings between the two resistance states in the (+,-) operation mode, and (b) two consecutive cycles in the (-,+) operation mode.	51

3.20 Pt/MgO/Pt structure C. I–V characteristics of a pristine device showing the forming process, the respective Reset and the following switchings between the two resistance states in the (+,-).	52
3.21 I–V characteristics of a Pt/MgO/Al/Ru device showing the first Set and Reset steps.	53
3.22 I–V characteristics for the four voltage polarity combinations with Al electrodes, each over 10 cycles: (a) (+,-), (b) (-,+), (c) (-,+) and (d) (-,-).	54
3.23 (a) I–V characteristics of a Pt/MgO/Cu/Ru pristine device showing the first Set and Reset steps for two different devices. (b) I–V characteristics for the (+,-) mode.	55
3.24 (a) I–V characteristics of a Pt/MgO/Ag/Ru pristine device showing the first Set and Reset steps. (b) Retention time for the OFF and ON resistance states up to 10^4 s.	55
3.25 (a) HAADF and (b) STEM EDX images of the double layer structures with 0.5 nm Al_2O_3 thickness, and (c) and (d) with 1 nm.	57
3.26 (a) I–V characteristics of a Pt/MgO/Ta pristine device showing forming and first Set and Reset steps. (c) I–V characteristics for the (+,-) mode over 100 cycles.	58
3.27 Initial resistance for the double layer structures as a function of Al_2O_3 thickness.	59
3.28 I–V characteristics for 0.5 nm of Al_2O_3 . (a) In the pristine state and (b) for the four polarity modes. (c) I–V characteristics for the (+,-) mode over 100 voltage sweep cycles. (d) Evolution of the resistance under incremental voltage pulses.	59
3.29 (a) Initial I–V characteristics and for the four voltage polarity combinations over 10 cycles: (b) (+,+), (c) (+,-), (d) (-,+) and (e) (-,-) for 1 nm of Al_2O_3	60
3.30 I–V characteristics for 2 nm of Al_2O_3 pristine state showing the forming process and the switchings between the two resistance states in the (+,+) operation mode.	61
3.31 I–V characteristics for 2 nm of Al_2O_3 over 100 cycles for the four voltage polarity combinations: (a) (+,+), (b) (+,-), (c) (-,+) and (d) (-,-).	61
3.32 I–V characteristics for 5 nm of Al_2O_3 (a) in the pristine state and unipolar behavior. (b) I–V showing complete (+,-) and (-,-) modes, incomplete (+,+) mode and final negative Reset. (c) Retention time for the OFF and ON resistance states up to 10^4 s and (d) resistance states separation under pulsed operation mode.	62
3.33 I–V characteristics for 5 nm of Al_2O_3 for the two voltage polarity combinations over 100 cycles: (a) (+,-) and (b) (-,-).	63
3.34 (a) I–V for 5 nm of Al_2O_3 showing gradual Reset. (b) Incremental Reset cycle amplitude. (c) Resistance dependence on the maximum negative voltage averaged over 50 repetitions.	63
3.35 I–V characteristics for 10 nm of Al_2O_3 (a) in the pristine state and following cycles. (b) I–V for 10 repetitions.	64
3.36 I–V characteristics for only 10 nm of Al_2O_3 (a) in the pristine state and following cycles. (b) I–V for 20 repetitions.	64
3.37 (a) Set and Reset voltages for the double layer structures as a function of Al_2O_3 thickness. (b) Resistance ratio for the double layer structures as a function of the current compliance.	65

3.38 (a) Forming, Set and Reset voltages as a function of MgO thickness. (b) Simplified schematic of filament complete growth and partial rupture in a MIM structure.	67
3.39 (a) Schematic of a network model composed of circuit breakers (resistors) in between two parallel electrodes. Transitions between (b) R_H to R_L and (c) R_L to R_H resistance states for each circuit breaker in the network when subjected to a critical (switching) ΔV	67
3.40 (a) Dendritic evolution of the conductive filament in the forming operation. (b) One-iteration Reset process with partial filament rupture and (c) two-iterations Set process. (d) Corresponding I–V data for the processes occurring in (a)-(c).	69
3.41 Forming, Set and Reset voltages in a 2D simulation as a function of thickness, for fixed width, an initial probability of defects of 0.5% and averaged over 100 simulations.	70
3.42 Voltage needed for switching in a 2D device as a function of initial defects percentage, averaged over 100 repetitions.	71
4.1 I–V characteristics of the Pt/Si/Ag/TiW device.	76
4.2 I–V characteristics for 100 consecutive switching cycles.	77
4.3 Cumulative probability for (a) Set and Reset voltages and (b) ON and OFF resistances over the 100 cycles shown in Fig. 4.2.	77
4.4 Evolution of both ON and OFF resistance states over 10 h with a reading voltage of 1 mV.	78
4.5 (a) Applied voltage over time in the pulsed mode and (b) resistance states over pulse number for the pulsed switching mode.	78
4.6 Dependence of (a) the ON resistance, (b) resistance ratios and (c) σ/μ on the current compliance used during Set.	79
4.7 (a) Resistance evolution over time for constant applied voltage. (b) Dependence of the switching time on the amplitude of the constant applied voltage.	80
4.8 Set and Reset transitions in (a) $q-\varphi$ and (b) I–V spaces.	82
4.9 Statistical distribution of the (a) voltage and (b) flux for 100 cycles.	82
4.10 Dependence of the (a) Reset voltage and (b) square root of the flux on the time needed for the Reset.	83
4.11 (a) ON/OFF resistance states after each Set/Reset pulse for fixed 1 V and 100 ns, 100 μ s and 100 ms of duration. (b) ON/OFF resistance states after each Set/Reset pulse for fixed -2 V and 1 μ s, 50 μ s and 50 ms of duration. (c) Switching probability distribution over pulse amplitude and duration for both Set and Reset transitions.	85
4.12 (a) Schematic of the Pt/Si/Ag/TiW stack on a flexible substrate. (b) Radius of curvature (r) between two edges of the substrate.	87
4.13 (a) SEM image of the Pt/Si/Ag/TiW stack on a paper flexible substrate. (b) First electrical response of a measured device.	88
4.14 (a) Consecutive I–V cycles in the flat configuration. (b) Retention time for the OFF and ON resistance states up to 10^4 s, measured with 1 mV every 1 s. (c) Resistance states separation under pulsed operation mode.	88

4.15	I–V electrical response when the substrate is flat, bent in a curvature radius of 3.5 mm and again flat.	89
4.16	(a) SEM image of the Pt/Si/Ag/TiW stack on a cellulose flexible substrate. (b) First electrical response of a measured device.	90
4.17	(a) I–V cycles for Pt/Si/Ag/TiW on a cellulose flexible substrate over 100 voltage sweep cycles in the flat configuration. (b) Retention time for the OFF and ON resistance states up to 10^4 s. (c) Resistance states separation under pulsed operation mode.	90
4.18	(a) I–V characteristic averaged from 10 consecutive measurements when the substrate is flat or bent (tension) under a curvature radius of 3.5 mm. (b) Distribution of Set and Reset voltages for 100 consecutive cycles in flat and 10 in bent modes.	92
4.19	Si/Ag/TiW stack (a) on a PET flexible substrate and first electrical response for (b) ITO, (c) Pt and (d) ITO/Pt bottom electrodes.	93
4.20	Repetition over 50 voltage consecutive cycles for ITO bottom electrode.	93
5.1	(a) 4×4 Willshaw network arranged in a crossbar configuration. (b) Average number of incorrect units in the retrieved patterns for 50 random repetitions.	96
5.2	Average error counts in the 128×128 network for different reading thresholds, as a function of defects percentage: a) percentage of <i>stuck-at-0</i> and b) of <i>stuck-at-1</i> defects.	99
5.3	Response of a 128×128 network to noise in the cue: a) control (<i>defect-free</i>), b) 5% probability of <i>stuck-at-0</i> defects and c) 5% probability of <i>stuck-at-1</i> defects.	100
5.4	Robustness to (a) threshold voltage and (b) ON/OFF resistances distributions of a 128×128 network.	101
5.5	Single-layer memristive perceptron schematics for 2 inputs, 1 bias and 1 output, with 4 memristors as weights.	103
5.6	Experimental conductance change as a function of initial conductance, when applying -1.7 V pulses for Set transitions and 2.6 V for Reset.	105
5.7	(a) Training and test dataset, and resulting classification (hyperplane). (b) Error sum over the training process.	106
5.8	(a) Individual weights variation over each iteration and (b) asynchronous voltage pulse application for each memristor.	107
5.9	(a) Hodgkin-Huxley model circuit and (b) schematic of the action potential of the squid giant axon.	108
5.10	(a) Memristor-based Hodgkin-Huxley circuit implemented in <i>LTSpice</i> and (b) memristors I–V and respective model parameters.	109
5.11	Dynamics evolution of the circuit with the parameter described in Fig. 5.10: (a) K^+ and (b) Na^+ memristors I–V response; (c) K^+ and Na^+ memristors resistance and (d) voltages across K^+ and Na^+ memristors and leak resistor over time; (e) input current stimulus and output action potential.	110

A2.1 Memristive-perceptron classification of the (a) AND, (b) OR, (c) NAND and (d) NOR logical operations.	172
--	-----

List of Tables

1.1	Characteristics of different storage devices, including competing ReRAM and Phase-Change Memory (PCM) technologies, and more standard Spin-Transfer Torque (STT), DRAM, Flash and Hard Disk (HD).	12
3.1	Mean values of the resistive switching parameters of Pt/MgO/Ta/Ru for all four measurement modes.	43
3.2	Labels of structures with vacuum breaks at different interfaces.	48
3.3	Resistive switching parameters resume for the three structures with vacuum breaks at different interfaces.	52
3.4	Resistive switching parameters resume for the three structures with different top electrodes.	56
3.5	Resistive switching parameters resume as a function of Al_2O_3 thickness.	65
3.6	RCB model simulations parameters.	69
3.7	Resume of resistive switching parameters for all MgO structures discussed in this chapter.	72
4.1	Main resistive switching parameters for the Si/Ag/TiW stack on different substrates.	94
5.1	Capacity of a 128×128 network for control (<i>defect-free</i>) and different probabilities of both <i>stuck-at-0</i> and <i>stuck-at-1</i> defects.	99
B.1	XPS ratios expected vs. experimental.	153
A2.1	AND, OR, NAND and NOR logical operations.	172

Nomenclature

Acronyms/Abbreviations

2D	Two-Dimensional
3D	Three-Dimensional
AFM	Atomic Force Microscopy
ANN	Associative Neural Network
BE	Bottom Electrode
c. p. s.	Counts per Second
CAFM	Conductive Atomic Force Microscopy
CF	Conductive Filament
CMOS	Complementary Metal-Oxide-Semiconductor
CPU	Central Processing Unit
DC	Direct Current
DWL	Direct Write Laser
ECM	Electrochemical Metallization Mechanism
HAADF	High-Angle Annular Dark-Field Imaging
HP	Hewlett-Packard Company
HRS	High Resistance State
IBD	Ion Beam Deposition
IBM	International Business Machines Corporation
IoT	Internet of Things
LRS	Low Resistance State
MIM	Metal-Insulator-Metal
MNIST	Modified National Institute of Standards and Technology
MRAM	Magnetic Random Access Memory
PVD	Physical Vapor Deposition

ReRAM	Redox-based Resistive Random Access Memory
RF	Radio Frequency
RNG	Random Number Generator
RRAM	Resistive Random Access Memory
RS	Resistive Switching
SCLC	Space-Charge Limited Current
STEM	Scanning Transmission Electron Microscopy
TCM	Thermochemical Mechanism
TE	Top Electrode
TEM	Transmission Electron Microscopy
VCM	Valence Change Mechanism
VLSI	Very Large Scale Integration
XPS	X-ray Photoelectron Spectroscopy

Materials

Ag	Silver
Al	Aluminum
Al ₂ O ₃	Aluminum Oxide
C	Carbon
Cu	Copper
IPA	Isopropilic Alcohol
ITO	Indium Tin Oxide
Mg	Magnesium
MgO	Magnesium Oxide
O	Oxygen
PET	Polyethylene Terephthalate
Pt	Platinum

Ru	Ruthenium
Si	Silicon
Ta	Tantalum
TaO	Tantalum Oxide
Ti	Titanium
TiW	Titanium Tungsten

M	Memristance
q	Electric charge
R	Resistance
V	Voltage

Units

μA	microampere
μm	micrometer
Ω	ohm
\AA	angstrom
A	ampere
eV	electronvolt
$\text{k}\Omega$	kiloohm
mA	milliampere
mC	millicoulomb
ms	millisecond
mV	millivolt
mW	milliwatt
nm	nanometer
ns	nanosecond
rpm	rotations per minute
S	siemens
V	volt
W	watt
Wb	weber

Variables

φ	Magnetic flux
C	Capacitance
G	Conductance
I	Current

CHAPTER 1

Introduction

The extraordinary rise in processing power, speed and storage capacity of present day computers is coming to a stall due to physical scaling and energy efficiency limits [1, 2]. Furthermore, with the huge increase of digital data and the emerging era of the Internet of Things (IoT), there is the need for fast and scalable technologies for memory and computation [3]. Furthermore, personal computers cannot cope with the amount of information inherent to complex, real world environments or with the intricacy of making real-time decisions based on that information [4]. Such gap is intrinsic to the underlying (von Neumann) architecture in which instructions and data flow over a limited capacity bus. It becomes increasingly less efficient when large amounts of data have to be moved around and processed quickly [5, 6]. There is thus an enormous opportunity to completely rethink the foundations of the present information age and open new paths into alternative forms of computation. This new era of creativity is further encouraged by the near end of Moore's law [7, 8, 9].

Memory. The search for novel memory approaches has gained new momentum due to growing demands for high-density digital information storage and the approach to integration limit in Flash memories. Flash memories represent the state-of-the-art nonvolatile memory technology, because of their high density and low fabrication costs. However, they suffer from low endurance, low write speed, high writing voltages and complicated data management. Furthermore, the continuing increase in Flash density (scaling) is already running into physical limits [10, 11]. Dynamic Random Access Memories (DRAMs) also have high density and low fabrication costs. However, they use a capacitor as the storage element and are consequently volatile. Moreover, they are also reaching the physical limits of further downscaling of the capacitor footprint [12]. Resistive Random Access Memory (RRAM) based operation relies on the ability of the device to reversely change its resistance from a high value state to a low value upon an electrical stimulation [13, 14]. Due to its high speed, high density (nanoscale two-terminal structure) and low fabrication cost [3], it offers the potential for a cheap, simple memory capable of replacing current market-leading memory technologies [15, 16, 12].

Neuromorphic computation. Computational architectures departing from the present von Neumann paradigm, which relies on a deterministic approach in which learning and adaptation to

new environments cannot be captured, are being intensively sought after. In particular, biological systems relying on an indeterministic approach with massive parallelism of simple processing units (neurons), have *memory* and *adaptation* as the essential building blocks for learning and decision-making [1, 2, 17]. In the brain, virtually every element (neuron) of the neural network simultaneously stores information (as synaptic strength) and uses it to compute in a massively parallel architecture [5, 6]. This results in huge power efficiency, adaptation, and resilience to unit failure [1, 2]. In fact, when compared to artificial systems, biological networks are six to nine orders of magnitude more effective in real world scenarios. As an example, just to simulate a part of the complexity of a cat's brain (at an 83 times slower pace) IBM's Blue Gene supercomputer requires clusters of 147 456 microprocessors and 144 TB of memory, which translates into a staggering power consumption of 1.4 MW. On the contrary, even the human brain, with all its complexity, dissipates a mere 10 W [2, 18]. Furthermore, the brain is adaptive and defect tolerant, constantly changing connectivities, and still being able to perform at the same time [19].

Artificial systems in which processing and memory functions are located in the same level have for long been a scientific dream, since they promise large improvements in performance along with the opportunity to design and build brain-like systems. The advent of nanotechnology and the recent experimental realization of memristor nanodevices is paving the way for the fabrication of new memories and brain-inspired artificial intelligence systems within our epoch. Memristors are two terminal electronic structures whose nonvolatile dynamic resistance can be controlled by an external current or voltage, and whose function strongly resembles the dynamical properties of biological synapses. The stored resistance without external power and the reduced dimension favor their implementation in low-power intelligent machines [20].

1.1 Memristors and Memristive Systems

In 1971, L. Chua theoretically introduced the concept of the memristor (abbreviation of memory-resistor) as the fourth basic circuit element alongside the resistor, the capacitor, and the inductor [22]. Chua postulated that there are four fundamental circuit variables (voltage V , current I , charge q and magnetic flux φ) which can be combined two at a time in six possible ways, corresponding to Eqs. (1.1)-(1.6) [see Fig. 1.1(a)]:

$$\text{Definition of current : } dq = Idt \quad (1.1)$$

$$\text{Faraday's law : } d\varphi = Vdt \quad (1.2)$$

$$\text{Resistor : } dV = RdI \quad (1.3)$$

$$\text{Capacitor : } dq = CdV \quad (1.4)$$

$$\text{Inductor : } d\varphi = LdI \quad (1.5)$$

$$\text{Memristor : } d\varphi = M(q)dq, \quad (1.6)$$

where R , C , L , M and t are resistance, capacitance, inductance, memristance and time respectively. In short, the resistor relates voltage and current, and the memristor relates flux and charge [Eq. (1.6)]. In 1976, Kang and Chua [23] further extended the previous analysis to *memristive systems* and showed that diverse systems such as thermistors, Josephson junctions, neon bulbs and even the ionic transport in neurons are special cases of memristive systems [23, 24, 25].

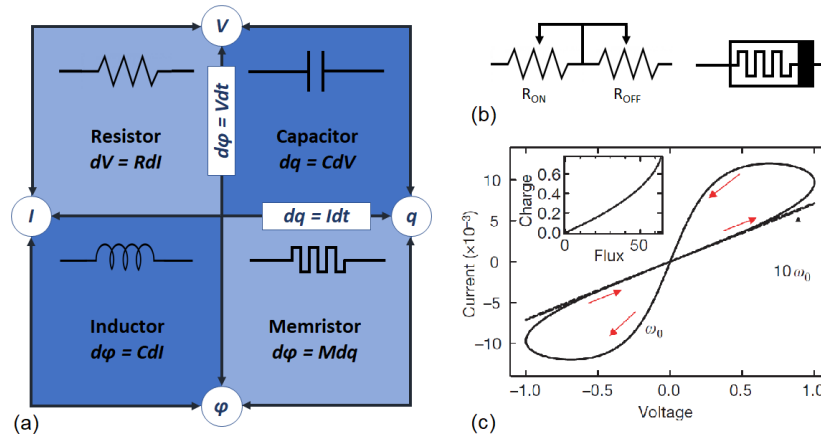


Figure 1.1 – (a) The four fundamental circuit variables (q , ϕ , I , V) can be combined in six possible ways: two of them correspond to fundamental relationships, and four correspond to the canonical two-terminal passive circuit elements (Adapted from Ref. [21]). (b) Equivalent circuit (left; R_{ON} and R_{OFF} are the minimum and the maximum memristance, respectively) and symbol of the memristor (right; polarity indicated by a black bar – the memristance is decreased/increased when current flows from the left/right to the right/left). (c) I – V hysteresis collapses with a ten fold increase in sweep frequency. The inset shows the representation in the charge–flux space (Reprinted by permission from Springer Nature [21], Copyright © 2008).

Although Chua’s formulation and the observation of pinched hysteresis loops in the I – V characteristics of different solid state materials took place around the same time [26, 27, 28, 29, 30, 31, 32], the memristor was only experimentally identified in 2008, with the pioneering work of Strukov *et al.* [21]. They showed that a sinusoidal voltage produces a pinched-hysteretic I – V characteristic in Pt/TiO₂/Pt nanostructures due to the motion of charged dopants. Since its experimental realization, the memristor has become one of the most promising candidates for the post-complementary metal oxide semiconductor (CMOS) era.

1.1.1 Theory

An ideal current-controlled *memristor* [equivalent circuit and symbol shown in Fig. 1.1(b)] is defined as:

$$V(t) = M(q(t))I(t) = M\left[\int_{-\infty}^t dt' I(t')\right]I(t), \quad (1.7)$$

where the proportionality function, $M(q(t))$, has the dimensions of a resistance (memristance) and $q(t)$ is the charge that flows in the system. If $M(q(t))$ is independent of time, Eq. (1.7) reduces to the Ohmic form. An ideal voltage-controlled memristor is defined by the relation [25]:

$$V(t) = M\left[\int_{-\infty}^t dt' V(t')\right]I(t). \quad (1.8)$$

The memristor belongs to a more complex class of dynamical systems [25, 33], where the state variable that determines the state of the system at a given time could be other than the charge in which case a *memristive system* is defined instead. So, let one define x as the set of n possible

state variables (related with a particular device) with the time evolution:

$$\frac{dx}{dt} = f(x, I, t), \quad (1.9)$$

where $f(x, I, t)$ is a continuous n -dimensional vector function. As the state variable of a memristor is not a bias but an integration of the total current, it can also work as a multi-state memory [34]. The functions defining a current-controlled and a voltage-controlled *memristive system* are then:

$$V(t) = M(x, I, t) I(t), \quad (1.10)$$

$$V(t) = M(x, V, t) I(t). \quad (1.11)$$

Hysteretic Loop. The response of a memristive system to a periodic current (or voltage) input is a "pinched hysteretic loop" [Fig. 1.1(c)], which is one of the most important properties of these systems, as hysteresis is a typical signature of memory devices. With respect to the periodic stimulus, for very high frequencies ($10w_0$) a memristive system operates as a typically linear resistor since the state variable is not able to follow the stimulus in each oscillation, while for low frequencies (w_0) it operates as a non-linear resistor, in which the state variable is given enough time to adjust. A variety of I–V characteristics depending on the excitation frequency [24] and voltage time history [33] are then possible.

1.2 Resistive Switching

Resistive switching (RS) stands for the reversible change in resistance in two-terminal devices, upon an electrical stimulus and in a nonvolatile fashion. Nonvolatile means that the resistance remains constant for a (long) retention time after the stimulus has been removed [35].

1.2.1 Metal-Insulator-Metal Memristors

The simplest nanostructure displaying resistive switching and memristive properties is the metal-insulator-metal (MIM) junction. A MIM device is simply an insulator material sandwiched between electrochemically active and/or inert metallic electrodes in a capacitor structure [36, 13, 37, 38]. The recent interest in these structures aims at a new class of memories called resistive random access memories (RRAMs), since their switching is fast, non-volatile and can result in a large resistance variation. Furthermore, MIM structures are the only where both types (bipolar and unipolar; see below) of RS can be observed, depending on the metal/insulator interfacial properties [36].

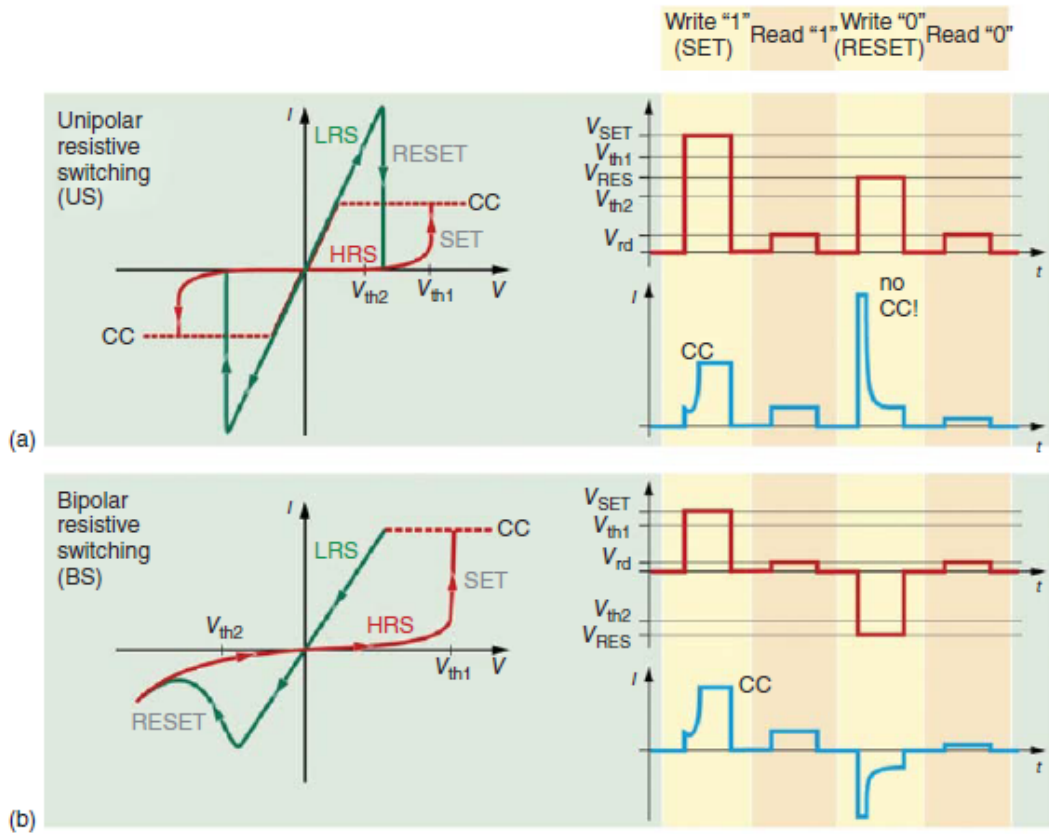


Figure 1.2 – The two most common operation modes of ReRAMs. I–V sweep operation (left) and pulse modes (right) for both (a) unipolar and (b) bipolar resistive switching (Reprinted by permission of John Wiley & Sons, Inc. [35] Copyright © 2016).

1.2.2 Operation

The most appealing property of *memristive systems* (for memory applications) is their RS between a low resistance state (LRS; R_{ON}) and a high resistance state (HRS; R_{OFF}), upon the application of an external voltage or current. The HRS to LRS switching is called Set (or write), while the reverse is called Reset (or erase) [39]. When the switching direction does not depend on the polarity of the applied bias, but just on its amplitude, the switching is called unipolar. Thus, Set and Reset can occur for the same bias polarity [Fig. 1.2(a)]. On the other hand, when it depends on the polarity, it is called bipolar switching and Reset can only occur at the reverse polarity of the Set process [Fig. 1.2(b)] [36]. Figure 1.2 schematically shows the two operation modes: current–voltage (I–V) diagrams under periodic voltage sweeps (left) and voltage pulse excitation with current response (right). Voltage or current sweeps are frequently used for the identification of switching behavior and to determine the approximate threshold voltages for the pulse operation, whereas pulses are useful for the quantitative investigation of switching kinetics. The information can be retrieved by measuring the electrical current when a small read voltage is applied [35, 40].

Unipolar switching allows simple circuits and unipolar diodes as selectors, if operating with only positive polarity. However, it usually has lower uniformity and endurance. In bipolar switching, the higher endurance can be attributed to the re-utilization of the migrating defects during Set and

Reset [3]. The coexistence of unipolar and bipolar RS in the same device has also been reported due to a defective microstructure or the generation of a highly disordered network in the conductive filament region, which is likely to act as a migration channel, during forming (see Section 1.2.3 below for more details). Both unipolar and bipolar operation modes were obtained after forming in TiN/HfO₂/Pt, where a high-quality amorphous HfO₂ layer was prepared by ALD [41]. Coexisting of the two modes were also evidenced in TiO₂ cells [42] as well as in perovskite systems [43].

Forming. For some devices an (electro)forming step is a pre-requisite for RS, before the first Set. Electroforming, or just forming, denotes an electrochemical process during which metal ions or particles are injected into and cause semi-permanent structural modifications inside the otherwise insulating medium [18]. In general, it requires a higher voltage and enables the subsequent Sets at lower voltages [10]. Under electrical stress, defects are generated in the oxide bulk and at the interfaces, being forming triggered when a critical density of defects is reached. From physical analysis, it is observed that the average density of defects required for dielectric breakdown decreases with the oxide thickness, while the statistical variations increase. The defect generation rate increases with the voltage and also depends on the temperature [44]. The most common forming method is applying a voltage/current sweep, resulting in a drastic change in the measured current (resistance decrease). During this process, the current must be limited by a current compliance, since the associated high current overshoot can cause significant local self-heating (reaching several hundred °C) and hard dielectric breakdown effects [40, 45]. In the case of filamentary RS (see Section 1.2.3.1 below), before the forming the conduction is uniformly distributed in area either by tunneling injection or by defect (trap)-assisted mechanisms such as Poole–Frenkel emission or inelastic trap-assisted tunneling, while after forming the electrical conduction is localized in a nanoscale filament, whose size has been estimated to be from 1 to 10 nm [44]. As soon as one conductive filament is formed, the resistance of the structure is dramatically reduced, which results in the drop of both the current and electrical field across the oxide. This typically prevents the formation of further filaments, self-limiting the process ("winner-take-all procedure") [39, 13, 46].

Note that forming differs from hard dielectric breakdown, where there is a permanent resistance degradation and the high resistance cannot be recovered. Dielectric breakdown is an undesired event in CMOS circuits, since it might cause circuit failure. However, in RRAM structures it is intrinsic to the device operation [44].

1.2.3 Resistive Switching Mechanisms

Besides polarity, other criteria have been established to distinguish the different types of resistive switching observed, including: i) location; ii) filamentary or surface area; iii) mobile cations or anions; iv) with or without a tunnel gap; v) using organic or inorganic films for ion transport [47]. Regarding the location, RS can occur at/near the electrode interfaces, at the center or the entire path between the electrodes [35]. Regarding RS type, it can be filamentary, in which switching occurs due to the formation and dissolution of a conducting filament, or area-proportional, where it

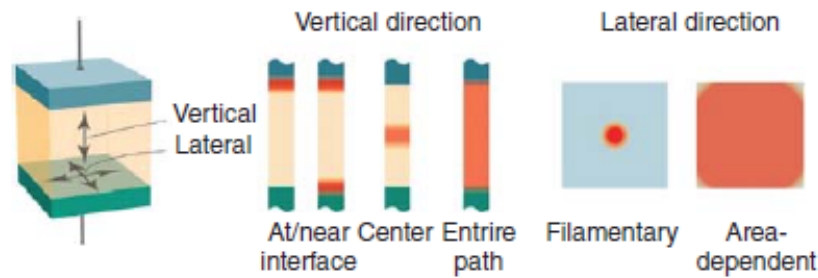


Figure 1.3 – Geometrical location (vertical and lateral) of the switching in a MIM structure (Reprinted by permission of John Wiley & Sons, Inc. [35] Copyright © 2016).

takes part over the entire cross section. The latter is called interface-type, since it typically occurs close to one of the electrodes. Figure 1.3 schematically illustrates these scenarios. In reality, many intermediate cases have been reported, such as single and multiple filament RS or entire and partial area RS [48, 49, 50, 51, 52, 53]. The most frequent resistive switching reported in the literature is filamentary switching and will therefore be detailed here [35].

1.2.3.1 Filamentary Switching

A conducting filament (CF) that acts as a circuit switch between two electrodes is believed to be responsible for most resistive switching phenomena. Such CF formation occurs during the electroforming and Set processes and can be described by nucleation and growth process. Its initial growth is an electric-field-driven phenomenon, that imparts the directionality of the subsequent growth [46]. Most of the filamentary RS phenomena are related with ionic motion [13, 54], involving the transport and electrochemical reactions of cations and/or anions [39, 55]. Ionic motion may occur because of a concentration gradient (diffusion), an electrical potential gradient (drift) or a temperature gradient (thermodiffusion) [56]. Both single and multiple CF may occur, depending on the thickness and microstructure of the insulator and the forming conditions [57]. Usually the resistance of the HRS is lower than the resistance before forming. This can be understood by an incomplete CF dissolution during Reset [Fig. 1.4(a)] [3], with the Set process then recovering the electrical conductivity of the locally ruptured part of the CF [39, 46].

The filamentary RS model is widely accepted and to our knowledge no reasonable alternative has been suggested up to date. The arguments supporting it are the drastic change in the resistance, the possibility to vary the ON resistance (filament size) using the applied current and the fact that the ON resistance does not scale with the electrode diameter [12]. Furthermore, several techniques have been used to reveal this, such as conductive atomic force microscopy (CAFM) [59], thermal (infrared) imaging [60] and in situ transmission electron microscopy (TEM) during switching [61, 62, 63, 64]. Waser *et al.* confirmed the confinement of the current path and showed where the CF touches the anode, while Yang *et al.* reported *in-situ* and *ex-situ* TEM imaging of nanoscale conducting filaments in SiO₂-based resistive memories [65].

The mechanisms involved in the filamentary RS can be subdivided into Electrochemical Met-

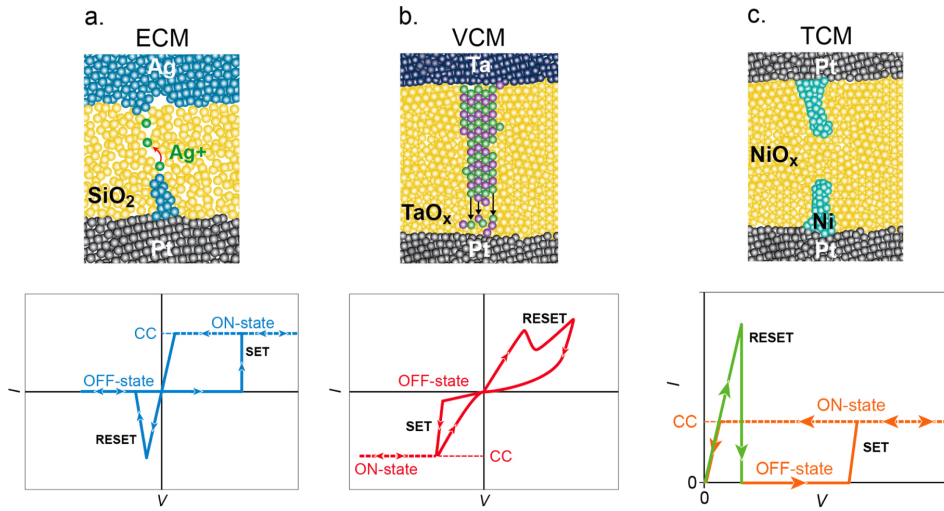


Figure 1.4 – Memory cell structure schematics and I – V characteristics for (a) ECM, (b) VCM and (c) TCM (Reprinted by permission of John Wiley & Sons, Inc. [58] Copyright © 2016).

allization (ECM), Valence Change (VCM) and Thermochemical Mechanisms (TCM). TCMs and VCMs can be placed into one group in which the insulating materials play the dominant role, while in ECMs the metal electrodes are crucial [11]. Figure 1.4 compares the structure and I – V behavior for the three types of mechanisms.

Electrochemical Metallization Mechanism. The electrochemical metallization mechanism/memory (ECM or conductive-bridge) stands for devices based on cation motion [39, 47, 66]. It relies on mobile cations created by the oxidation of an electrochemically active electrode (Ag, Cu or Ni), their drift in the insulating layer due to an applied electric field and reduction at the (inert) counter electrode (Pt, Ir, W or Au), forming a highly conductive filament in the ON state. When reversing the electric field polarity, an electrochemical dissolution of the filament takes place, resetting the system into the OFF state [10, 11].

In the initial high resistance state, no electrodeposit of the metal M from the active electrode is present on the inert electrode [Fig. 1.5(a)]. The Set occurs if a sufficiently high positive bias voltage is applied to the active electrode, involving the following steps:

- (i) anodic dissolution of the active metal (M) [Fig. 1.5(b)]:



where M^{z+} represents the metal cations in the insulator;

- (ii) migration (drift) of the M^{z+} cations across the insulator under the applied electrical field;
- (iii) reduction of M (nucleation and growth of metallic electrodeposits) on the surface of the inert electrode [Fig. 1.5(c)]:



The reduction process is electric field-enhanced and leads to the formation of a metallic filament

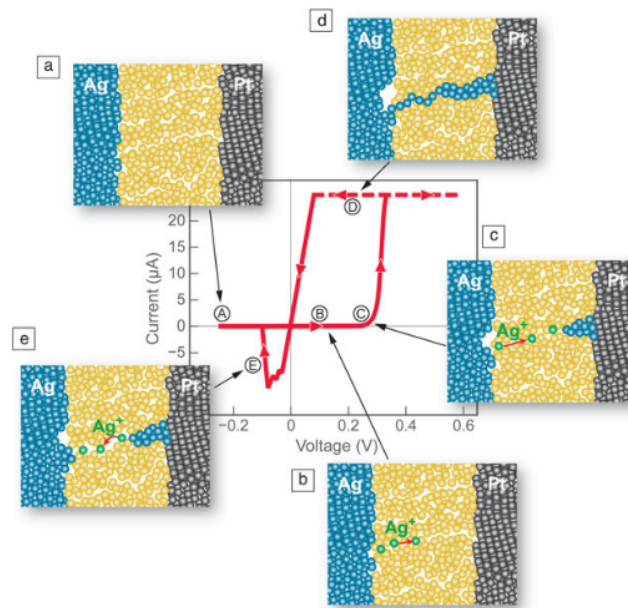


Figure 1.5 – Sketch of the steps of the (a)–(d) Set and (e) Reset operations of ECM (© IOP Publishing. Reproduced with permission. All rights reserved [12]).

growing preferentially in the direction of the active electrode. The ON state [Fig. 1.5(d)] is kept unless a sufficient voltage of opposite polarity is applied and an electrochemical dissolution of the CF takes place [Fig. 1.5(e)], resetting the system into the OFF state. During the initial Reset stage there is both an electronic current through the CF and an electrochemical current (Faradaic current) which dissolves the metallic filament [13, 39, 55, 11]. Figure 1.5 sketches the principle of operation of an ECM memory cell and its typical I–V switching cycle under a triangular voltage signal [12]. The theoretical description of the cation mobility inside the dielectric can be found in detail in Ref. [11].

An extraordinary variety of insulating or semiconducting materials can be utilized in ECM, such as chalcogenides, e.g. GeS_x , GeSe_x , GeTe , GeSbTe , CuS , and oxides, e.g. SiO_2 , WO_3 , Al_2O_3 , TiO_2 . Regarding the active electrode material that acts as the source of ions to form the filament, Ag and Cu are the most widely used. For counter electrodes Pt, W, TiN, Au, TiW and Ru for example have been used [12, 67].

The distinguishing feature of ECM devices is that the active electrode is a metal that can be easily electrochemically dissolved into, and conducted through the insulator, whereas the counter electrode cannot [12]. ECM cells can be tuned to switch at currents below 1 nA (albeit with low retention), by reducing the device size or optimizing the switching materials [68].

Valence Change Mechanism. The valence change mechanism/memory (VCM or OxRAM) stands for devices based on anion motion (Fig. 1.6(a)) [47, 66]. It results from a valence change in cations, triggered by the drift of anions, such as oxygen (or their vacancies), due to the internal electric field, towards the anode (or cathode), as shown in Fig. 1.6(b). A subsequent change of

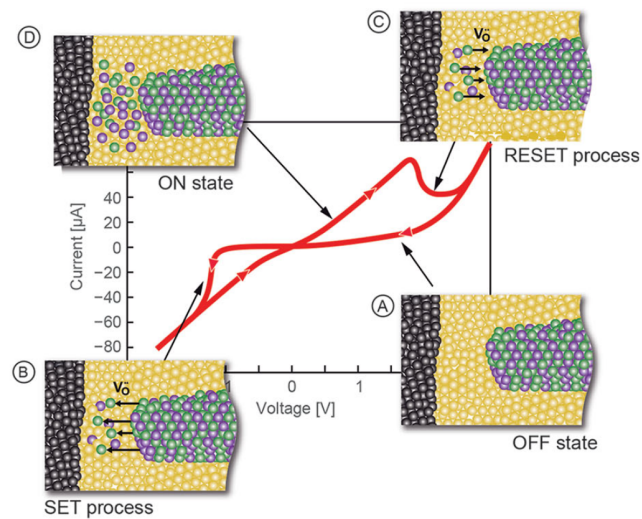


Figure 1.6 – Sketch of the steps of the (a)–(b) Set and (c) Reset operations of VCM (Reprinted by permission of John Wiley & Sons, Inc. [69] Copyright © 2015).

the stoichiometry leads to a redox reaction expressed by a valence change of the cation sublattice and a change in the electronic conductivity [Fig. 1.6(d)] [39, 70, 11]. During Reset, oxygen ions migrate back to the bulk either to recombine with the oxygen vacancies or to oxidize the metal precipitates [Fig. 1.6(c)] [36, 46].

VCM cells consist of an insulating layer (metal oxide) stacked between a top and a bottom electrode [3] and differ from the ECM structure mainly by the type of material used for active electrode (Ta, Hf and Ti) and insulators (Ta_2O_5 , HfO_2 , TiO_2 , SrTiO_3 , SrRuO_3 , ZrO_2 , etc). Different combinations have been reported in the literature. In particular, HfO_x , AlO_x , NiO_x , TiO_x , MgO_x and TaO_x have drawn the most attention [36, 39, 71, 72, 16]. The counter electrode material is Pt or other high work function, chemically inert material that ensures a sufficiently high Schottky barrier [47]. VCM materials are most likely to be quite insulating in their pristine state, with the exception to already leaky materials (semiconducting) [70].

Initially, it has been suggested that only oxygen ions (vacancies) are mobile. However, it has been recently found that also cations in many metal oxides have comparable mobility and participate in the formation of filaments [47, 73, 74, 75].

Thermochemical Mechanism. The thermochemical mechanism/memory (TCM) stands for devices based on both cation and anion motion [47, 66], since the switching is dominated by thermally controlled diffusion and redox reactions. On these devices a change of the stoichiometry occurs due to a voltage induced increase of temperature [11]. As the change in voltage polarity is not required, TCM cells are inherently unipolar and involve currents in the mA range [35].

1.3 Resistive Random Access Memory

In resistive random access memory (RRAM) the resistance serves as a state variable, between only two external terminals, instead of the three terminals in conventional CMOS-based DRAM or Flash [3]. It is operated by changing the device resistance using an external electrical bias [76], and information is stored on different resistance states, with the OFF state as Boolean 0 and the ON state as Boolean 1 [47].

RRAM is a general name that includes ReRAM (redox-based RRAM), PCM (phase change memories), MRAM (magnetoresistance RAM), among others. From the above mechanisms, the resistive switching in MIM structures belongs to the ReRAM class. ReRAMs are fast (sub-nano seconds regime) nanoionic systems, since they rely on redox reactions and ionic motion [47], can work at very low temperatures (e.g. 4 K) [77], are resistant to high energy particles (cosmic rays, neutrons etc.) and electromagnetic noise, making them ideal for space and medical applications [78]. Other advantages of ReRAMs include their high scalability (atomic level), low operation voltages (from some hundred mV up to few volts), and thus low power consumption, high OFF/ON resistance ratio, multi-level resistance states (analog memory), over 10 years retention time and over 10^{12} cycles endurance. ReRAMs can also be used as selector devices or as building units of beyond von Neumann architectures (neuromorphic computing) [34, 79, 80, 81], and are compatible with 3D stacking, nanobatteries, neuroelectronics and Boolean logic operations [76]. Moreover, they can be fabricated in the back end of line at relatively low temperatures, allowing easy integration with existing CMOS devices [3]. For these reasons, ReRAM are considered the most favorable alternative to conventional memories in the future nanoelectronics [47]. In addition, they can also fill the gap between DRAM (high performance, low density) and Flash (high density, slow operation) [3]. The ReRAM endurance required depends on the technological application: 10^{15} cycles for DRAM replacement and as few as 10^3 cycles for Flash memory replacement [12]. Table 1.1 presents the status of the technology for different memory storage devices [82].

1.4 Device structure and material choices

1.4.1 Crossbar

Passive crossbar memory arrays are simple matrices consisting only of bit and word connecting lines and a resistive switch at each junction [MIM structure; Fig. 1.7(a)] [40, 83]. Therefore, ReRAMs can be densely built in a crossbar array, allowing an extremely small bit area of only $4F^2$, where F is the minimum feature size allowed by the technology (lithography) [3]. Higher memory density can be achieved in crossbar architectures than in typical CMOS architectures and even more is possible with 3D stacking [39]. Crossbar ReRAMs also have the advantage of device individually program operation, while Flash memories require block erasing [3], and vector matrix multiplication can be directly performed using Ohm's and Kirchhoff's laws [84]. In the crossbar architecture each junction should be associated with a nonlinear selector, both to select

Table 1.1 – Characteristics of different storage devices, including competing ReRAM and PCM technologies, and more standard Spin-Transfer Torque (STT), DRAM, Flash and Hard Disk (HD) (Adapted from Ref. [82]).

	ReRAM	PCM	STT-RAM	DRAM	Flash	HD
Chip area per bit (F^2)	4	10	14–64	6–8	4–8	n/a
Energy per bit (pJ)	0.1–3	10^{1-2}	0.1–1	1	10^3	10^4
Read time (ns)	<10	20–70	10–30	10–50	10^{4-5}	10^4
Write time (ns)	20–30	10^{1-2}	10^{1-2}	10	10^5	10^6
Retention (years)	10	10	10^{-1}	10^{-5}	10	10
Cycles endurance	10^{12}	10^{7-8}	10^{15}	10^{17}	10^{5-8}	10^{15}
3D capability	yes	no	no	no	yes	n/a

the addressed memory cell (high current) and to electrically isolate the nonaddressed cells (limited current), in order to avoid programming disturbs [Fig. 1.7(b)] [57].

As an example employing memristive crossbar structures, Hewlett-Packard Labs proposed a revolutionary supercomputer, The Machine, an all-in-one portable device (server, workstation, PC and phone) that uses photonic memories, using light to connect hundreds of memristive racks in a low-latency 3D structure [85]. Moreover, in a crossbar structure, the two-terminal memristor formed at each crosspoint can be seen as a synapse connecting pre- and post-synaptic neurons (see Section 1.7) [18, 40].

1.4.2 Materials

Several materials have been used for the fabrication of ReRAMs, both as storage medium and electrode materials. Figure 1.8 shows some examples of the oxides and metals used in the case of binary oxides.

Interface Dynamics. Interfaces provide rich interaction dynamics, including neutral particle diffusion, chemical dissolution and surface formation of barrier films. All these lead to chemical asymmetry of electrode/storage medium interfaces and chemical potential gradients within the storage medium films [66].

Storage Medium. The choice of storage medium determines the cell stability, RS reproducibility and device performance. At the nanoscale several different effects, such as overlapping space charge layers, small effective diffusion length, high electric fields and extremely high current densities combine [87]. Therefore, even nanoscale insulating (high-k) oxides can conduct ions (and electrons) and their properties are better described as mixed ionic-electronic conductors rather than insulators [88]. Thus, ReRAMs can use oxide thin films from macroscopic insulators to conduct ions [47]. For instance, macroscopic room temperature insulators, also used as high-k

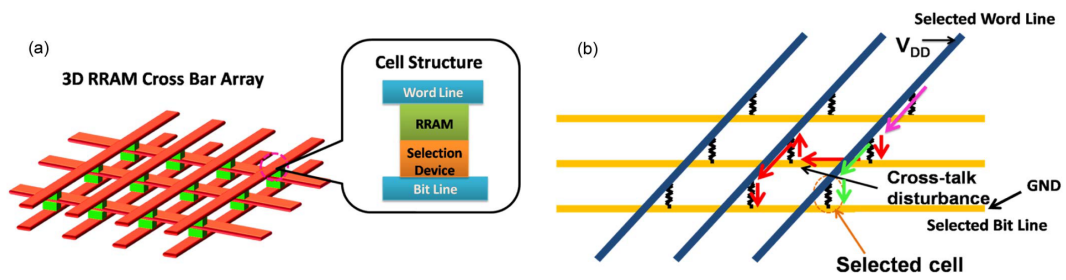


Figure 1.7 – Schematics of (a) a RRAM crossbar array (the inset shows each cross point of bit lines and word lines, composed of a RRAM and a selector device) and (b) of the leakage paths in the array (the current may flow into selected, green, and unselected, red, devices) (Reprinted by permission © 2013 IEEE [86]).

dielectrics (Ta_2O_5 , HfO_2 , Al_2O_3 , etc.), demonstrate a sufficient ability to transport either oxygen ions or cations to ensure resistive switching in times scales below 100 ns [66, 89]. A vast number of combinations of materials exhibit RS, due to nanoscale ionic transport and redox reactions [10]. Various oxide, chalcogenide and halide materials are used to transport ions in ECM [3, 90, 91], VCM [88] and TCM [87] cells. Oxides are typically the choice for both ECM and VCM, since they are chemically stable, allow deviations in stoichiometry without decomposition, can be doped to improve properties and many of them are compatible with CMOS processes [47].


Electrode Material. The choice of the active electrode has to take into account the reversibility of the redox reaction, the interface contact (Schottky or Ohmic) and interactions between the storage medium and the inert electrode. Inert metals are typically preferred as electrodes to avoid any parasitic redox reactions. Nevertheless, the use of different inert electrodes is not thoroughly studied, with Pt being the electrode of choice so far [66, 68].

1.5 Performance


1.5.1 Defects

The small size of ReRAMs (down to <10 nm) combined with applied electric fields in the range of $E \sim 10^8 \text{ Vm}^{-1}$ and current densities of $j \sim 10^9 \text{ Acm}^{-2}$ imply that imperfections of the interfaces will strongly affect the local charge and mass fluxes, leading to statistical deviation in their performance. The main types of imperfections include: 1) surface roughness higher than approximately 10% of the film thickness; 2) formation of hillocks; 3) intermixing of electrode and storage medium during the deposition procedures (e.g. high-energy particles penetrating into the underlying film during sputtering deposition); 4) chemical dissolution of the electrode or formation of barrier layers due to the interaction with the storage medium or the environment (e.g. oxygen or moisture) [66].

The Periodic Table of the Elements



corresponding binary oxide that
exhibits bistable resistance switching



metal that is used for electrode

1 H																	1 H	2 He	
3 Li	4 Be																	9 F	10 Ne
11 Na	12 Mg																	17 Cl	18 Ar
19 K	20 Ca	21 Sc	22 Ti	23 V	24 Cr	25 Mn	26 Fe	27 Co	28 Ni	29 Cu	30 Zn	31 Ga	32 Ge	33 As	34 Se	35 Br	36 Kr		
37 Rb	38 Sr	39 Y	40 Zr	41 Nb	42 Mo	43 Tc	44 Ru	45 Rh	46 Pd	47 Ag	48 Cd	49 In	50 Sn	51 Sb	52 Te	53 I	54 Xe		
55 Cs	56 Ba	57 La	58 Ce	59 Pr	60 Nd	61 Pm	62 Sm	63 Eu	64 Gd	65 Tb	66 Dy	67 Ho	68 Er	69 Tm	70 Yb	71 Lu			
87 Fr	88 Ra	89 Ac	90 Th	91 Pa	92 U	93 Np	94 Pu	95 Am	96 Cm	97 Bk	98 Cf	99 Es	100 Fm	101 Md	102 No	103 Lr			

Figure 1.8 – Summary of the materials used in ReRAMs. Metals of the corresponding oxides are in yellow and metals used for the electrodes are in blue (Reprinted by permission © 2011 IEEE [36]).

1.5.2 Stability

The most important characteristics of ReRAM are the ON and OFF states stability (retention) and the maximum number of Set/Reset cycles attainable (endurance). Both are inherently related to the chemical stability and the mechanical degradation of the system. The chemical stability is influenced by the nature of the active metal and the storage medium, and by environmental factors such as temperature, ultraviolet/visible light exposure and moisture. The mechanical degradation is determined by the ionic dynamics, high local electrical fields, high current densities, high power dissipation (several TWcm^{-3}) and high temperature (above 1000°C) attained during the repeated formation/dissolution of new phases, including volume expansion and void formation [3, 66].

There is also a trade-off between energy consumption and retention. In general, higher resistive filaments (low current operation) tend to show a reduced retention. Moreover, endurance is shorter for unipolar than for bipolar devices, due to the higher temperature required for Reset (electromigration) and the gradual loss of species (metallic ions, oxygen vacancies, etc.), since the same polarity voltage is always applied [57]. Endurance is one of the highest priorities especially for memory applications, where the memory might be frequently accessed by the central processing unit (CPU) for in-memory computing purposes [3, 92].

1.5.3 Variability

As the structure of the device is being constantly modified (CF systematic formation/dissolution), ReRAMs are strongly affected by switching variability. The variability in all read and switching parameters comes from the stochastic nature of the CF at the atomic scale. The wide distributions of the LRS and HRS resistances may shrink the memory window below critical values [3, 35]. In general, the voltage distribution is wider for unipolar than for bipolar RS, which may be attributed to the difficulty in controlling the Reset mechanism, since it is a self-accelerated process. Variability

also increases in the case of multiple-CF [93].

Moisture. Another source of variability was shown to be moisture, absorbed from the local environment or during fabrication [47], since many deposition processes (CVD or ALD) cannot avoid its presence. The water molecules act as a source for a counter electrode reaction [73, 94], provide additional charges in the oxide matrix (oxygen protons), enhance the ion diffusion and act as corrosive agents. However, without moisture no forming (and subsequent RS) appears to be possible in ReRAMs. Water can easily undergo electrode reactions with the formation of oxygen and hydrogen (and/or intermediate ionic products), where in parallel ionic charge carriers are generated. Thus, H_2O molecules can contribute to the increase of the total conductivity (decrease of the OFF state resistance), by providing mobile species (both oxygen and hydrogen ions). Moisture influences not only Set/Reset processes, but also the ON and OFF states [47].

1.5.4 Scaling

Memristive effects are appreciable only at the nanoscale and in order for a proper scaling, the RS mechanisms need to be understood in detail [3, 24, 39, 46]. Filamentary switching cells are considered to be highly scalable devices, since the ON-state current is carried by a very narrow filament or multiple filaments with non-uniform distribution over the area. In this case, the resistance of the LRS is independent on the area, whereas the HRS increases with the inverse of the area (Ohm's law). Thus, the HRS/LRS (memory window) ratio benefits from device scaling [13, 12, 36].

The ultimate size of the CF is of just two atomic defects (oxygen vacancies or M atoms) connecting the top and bottom electrodes. Consequently, the minimum thickness of the switching layer is of two atomic units (2δ), while the width of the active area is of around 10δ to allow for lateral displacement of the two defects from the CF. Thus, the minimum device size that is envisaged for ReRAMS is of around $10\delta = 2.6$ nm [3]. This extreme scaling was already confirmed by the fabrication of devices with an electrode size in the range of 2–3 nm [95]. State-of-the-art ReRAM cells are scalable laterally below 10 nm per side [96] and vertically down to some tens of nanometers. Pi *et al.* fabricated a 2×2 nm² memristor crossbar array using Pt nanofins as electrodes [97]. At these dimensions, the physical and chemical properties will differ from the macroscopic systems and the opportunity of using unconventional systems is enhanced [66].

There are potential reliability concerns regarding such small device sizes, since data retention, noise and variability have a dependence on the CF size. The limitation of the CF size is imposed by the mandatory Set/Reset current reduction (to avoid excessive voltage drop). This trade-off between reliability and low-current operation can be partially solved by adopting ReRAM devices with relatively large resistance windows [3]. The issue regarding the high electrode resistance limiting the performance of devices at the nanoscale, also needs to be addressed [98, 99].

1.6 Neuromorphic Properties of Memristors

Two fundamental units of the human brain, the neuron and the synapse, play essential roles in learning and memory formation. Neurons are electrically excitable cells and are able to respond to stimuli, to conduct impulses, and to communicate with each other. Synapses are specialized junctions between neurons that allow the rapid transmission of electrical and chemical signals so that neurons can communicate with each other [100]. Thus, they are responsible for providing a neuron with a converted input from another neuron that is proportional to the importance of that signal. When an action potential, generated by a neuron, reaches a pre-synaptic terminal, a cascade of events leads to the release of neurotransmitters that give rise to a flow of ionic currents into or out of the post-synaptic neuron.

Learning and memory in human brains are the capabilities to gain new information and store it in a recallable way. It is now generally accepted that information is stored in the synaptic strength (weight), with learning being accomplished by modifying (either increasing or decreasing) this strength [101]. Such synaptic plasticity makes possible to store information and to react to inputs based on past knowledge [102]. As shown in Fig. 1.9, a similarity can be seen between a biological synapse and a metal–insulator–metal structure, if one thinks of adjustable synaptic strength between two neuron terminals as adjustable resistance between two electrodes.

Different examples of biological learning rules where mimicked using memristors, such as hebbian learning, spike timing dependent plasticity and short and long term memory, as will be discussed below.

1.6.1 Spike Timing Dependent Plasticity

According to the hebbian learning, objects once experienced together tend to become associated, so that when any one of them is thought of, the others are likely to be thought of also, in the same order of coexistence as before [101]. Spike timing dependent plasticity (STDP) is an experimentally verified biological phenomenon in which the precise timing of spikes affects the sign and magnitude of changes in synaptic strength. STDP can be divided into long-term potentiation (LTP) and long-term depression (LTD). In the former, synapses increase their efficiency as a pre-neuron is activated momentarily before a post-neuron, while in the latter synapses decrease their efficiency as a post-neuron is activated momentarily before a pre-neuron [104].

To relate memristance to biological STDP, one requires a voltage/flux controlled bipolar memristor with voltage threshold, below which no variation of the resistance is observed and an exponential behavior beyond threshold, to be able to continuously increment and decrement the conductance [105]. Jo *et al.* were the first to demonstrate STDP in nanoscale Si-based memristors in a crossbar structure [Fig. 1.10(a)]. The conductance continuously increases (decreases) during the positive (negative) voltage sweeps, and the I – V slope of each subsequent sweep picks up where the last sweep left off [Fig. 1.10(b)] [18]. It was also found that the strength of STDP learning in memristors

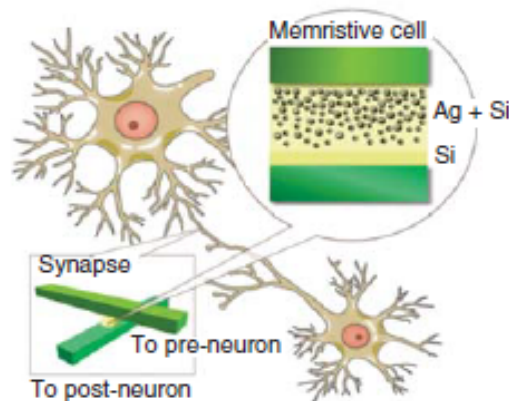


Figure 1.9 – Schematic illustration of the natural (biological) and ReRAM-based artificial synapses (Reprinted with permission from [18]. Copyright 2010 American Chemical Society.).

can be modulated by changing the amplitudes (or shapes) of the electric spikes, which means that the conductivity can be tuned depending on the precise timing between the post- and pre-synaptic spikes and the learning window by changing the shape of the pulses [105, 106]. Choi *et al.* fabricated Pt/Cu₂O/W MIM structures and experimentally demonstrated the successful storing of synaptic weight variations. They also showed the reliability of plasticity by varying the amplitude and pulse-width of the input voltage signal, matching their results with biological plasticity [102]. Pavlov’s experiment was also implemented using memristive synapses in a two-input, one-output system [Fig. 1.10(c)] [37]. The output is initially only triggered by one input but after a “learning step”, in which both inputs fire, the output can be triggered by either input. Furthermore, Zarudnyi *et al.* successfully showed STDP in unipolar SiO_x resistive switching devices through appropriate stimulation pulse programming [106].

1.6.2 Short and Long Term Memory

Memory is believed to occur in the human brain as a result of two types of synaptic plasticity: short-term potentiation (STP) and long-term potentiation (LTP). Here, synaptic plasticity refers to changes that occur in the organization of the brain as a result of experience. STP is achieved through the temporal enhancement of a synaptic connection, which then quickly decays to its initial state. However, repeated stimulation can cause a permanent change in the connection to reach LTP and shorter repetition intervals enable efficient LTP formation from fewer stimuli [34, 101, 107].

Depending on the input voltage pulses, different memorization behaviors were observed in memristive devices: short term memory (STM) for low and long term memory (LTM) for high repetition rates [38] (STP and LTP are terms used in neuroscience, whereas STM and LTM are terms used to describe psychological phenomena [107]). STM can only be sustained by constantly rehearsing the same stimulus, while LTM, despite the presence of natural forgetting, can be maintained for a longer period of time without follow-up stimuli. The transition from STM to LTM also happens through repetitions (rehearsal) but involves a much more intricate process with

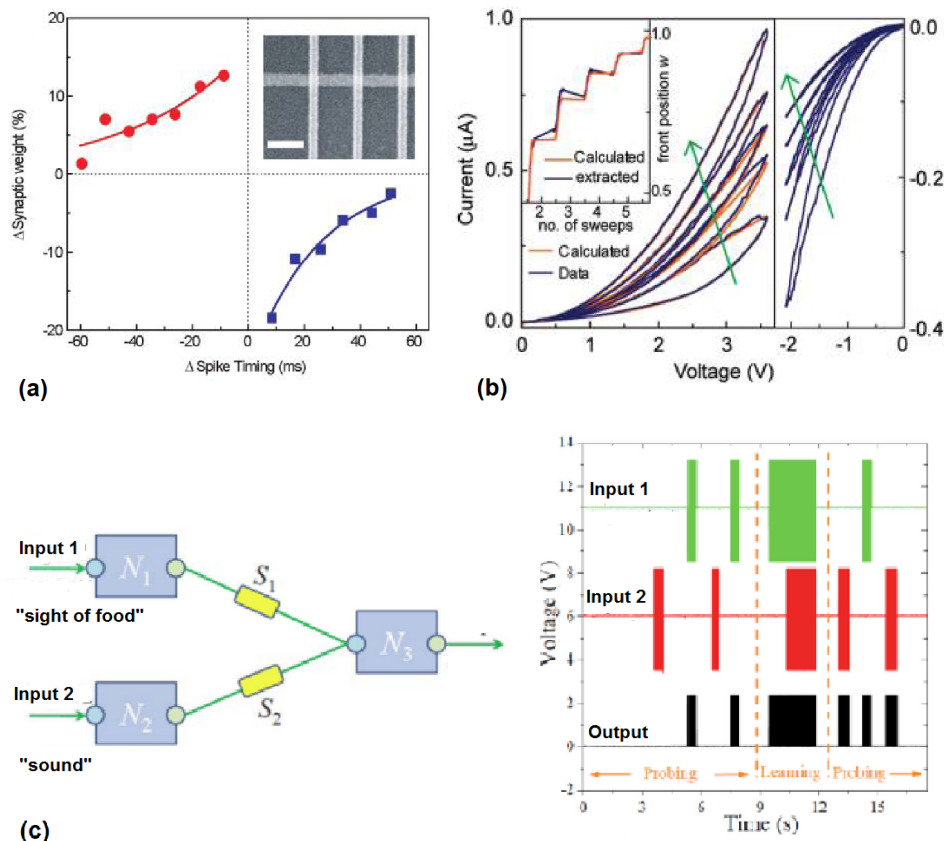


Figure 1.10 – (a) Memristor synaptic weight as a function of the relative timing of the neuron spikes. The inset shows the SEM image of the crossbar array. (b) Measured (blue) and calculated (orange) I–V characteristics (Reprinted with permission from [18]. Copyright 2010 American Chemical Society). (c) Pavlov's dog implementation with two memristive synapses (S_1 and S_2), two input (N_1 and N_2), and one output (N_3) neurons. In the initial probing phase, output only fires when input 1 fires. In the learning phase, S_2 is adjusted such that, in the probing phase, the output fires when either input 1 or input 2 fires (Reprinted from [103] © 2010, with permission from Elsevier).

structural changes (consolidation) [17, 107]. Three memory stages (unmemorized, STM and LTM) were observed in a Ni-rich nickel oxide device by Liu *et al.* and memorization from STM to LTM can also be obtained by repeated forward and backward voltage sweepings [1]. Tsuruoka *et al.* found LTM in an Ag/Ta₂O₅/Pt cell under voltage bias for a high repetition rate of input pulses, which is analogous to the behavior of biological synapses [38] and Wan *et al.* mimicked STM and LTM in nanogranular phosphorus-doped SiO₂ films by tuning the pulse gate voltage amplitude [108].

1.7 Artificial Neural Networks

As seen in the previous section, several attempts are being made to mimic the biological learning rules in artificial synapses. The next natural step is to construct artificial neural networks (ANNs) capable of performing complex functions. A neural network is based on the transmission of events from one source node (neuron) to multiple nodes by edges [synapses; see examples in Fig. 1.11]. In most ANN models, synapses are dynamical two-terminal entities that connect a pre- (source) to a post-synaptic neuron (sink). The source emits a signal that is modified by a synaptic transfer

function and delivered to the sink. To facilitate the communication between neurons, the action potential is propagated as a digital pulse [109]. The output of a neural network node is a function of the sum of all input signals [37]. The sink has a state variable that partially depends upon the history of incoming signals received from synapses that drive it. This variable, along with the source signal, determine the evolution of the synaptic state variable.

A radical approach in the construction of artificial neural networks is to use very large scale integration (VLSI) to implement directly in silicon the required computational model of a neural system. IBM researchers built a complex chip using 5.4 billion transistors to simulate 1 million neurons and 256 million synapses [110]. In neuromorphic implementations, the key challenge is to design circuits with large time constants while keeping the neuronal structure simple, occupying small silicon area and using only one electronic device as an artificial synapse. However, the silicon area occupied by the synaptic circuit can vary significantly, as it depends on the choice of layout design solutions and more conservative solutions use large transistors. Implementing the large connectivity of the brain with transistors on a single chip is a huge challenge, since a large number of transistors is needed [100, 104]. Therefore, the electronic conventional implementation is not practical and a simple and scalable device able to emulate synaptic functions is required [104]. The resistance of such device must be continuously variable, depending on the history of the input signals, mimicking the gradual potentiation (or depression) of biological synapses [102, 104]. The memristor displays such properties, making it the most promising candidate to be used in scalable neural networks. Note that the memristor is a promising candidate to emulate both neurons and synapses. Wang *et al.* successfully implemented a fully memristive neural network for pattern classification using diffusive memristors as artificial neurons, connected with non-volatile memristive synapses [81].

A possible architecture for brain-based nano-electronic computation is the crossbar array, which is a simple matrix consisting only of orthogonal crossing lines linking the nodes (neurons; source and sink) and an edge (synapse) at each junction, as shown in Fig. 1.11(b) [40, 83]. Every neuron in the pre-neuron layer of the crossbar configuration is directly connected to every neuron in the post-neuron layer [18, 40]. The information can be stored changing the value at the edges through an applied voltage between the nodes that they link and can have the meaning of a memory representation (data storage) or of a function representation (computation).

In the following sections we will introduce the most prominent artificial neural networks, namely the classic perceptron and the associative memories.

1.7.1 Perceptron

In 1957, F. Rosenblatt developed a simple neural network for pattern classification problems of linearly separable patterns: the perceptron [111]. It is the simplest kind of neural network capable of learning and parallel processing [112]. It consists of a main neuron that accepts several inputs from sensory neurons, connected by adjustable synaptic weights, and sums all weighted inputs [Fig. 1.12(a)]. Depending on the result this neuron will fire (or not) if the result is positive (or negative),

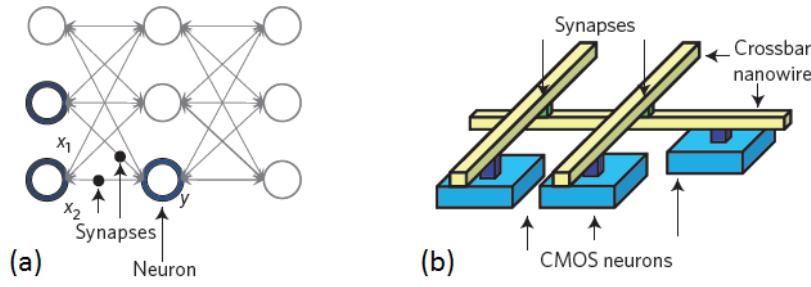


Figure 1.11 – (a) Graph and (b) crossbar network architectures (Reprinted by permission from Springer Nature [79], Copyright © 2013).

based on error-correlation learning [113, 114, 85]. The learning process for pattern classification occupies a finite number of iterations. Rosenblatt also proved that, if the patterns (vectors) used to train the perceptron are drawn from two linearly separable classes, then the perceptron algorithm converges and positions the decision surface in the form of a hyperplane between the two classes [114], a division of space into two halves by a straight line, for 2D classification, where one half is "positive" and the other is "negative" [Fig. 1.12(b)] [85].

The learning algorithm of the perceptron is based on the knowledge that in brains the neuron firing rate defines how "activated" it is. Therefore, based on how much the input neurons fire and how strong the neural connections are, the main neuron will respond accordingly [85].

Mathematically, the perceptron can be modulated as an input vector $x = x_1, x_2, \dots, x_m$ arriving from m neurons, with m stored weights, w_1, w_2, \dots, w_m , at the main neuron that computes a sum, a . Also, it is often convenient to have a non-zero threshold, which is achieved introducing a single scalar bias term into the neuron, so that activation is always increased by some fixed value b . The overall sum a , parameterized by m weights, and a bias value b is given by [85]:

$$a = \left[\sum_{d=1}^m w_d x_d \right] + b, \quad (1.14)$$

which for the two inputs case is the line (decision boundary) separating the data in the (x_1, x_2) plane shown in Fig. 1.12(b):

$$w_1 x_1 + w_2 x_2 + b = 0. \quad (1.15)$$

The weights are easy to interpret: if one input has a zero weight, then the activation is the same regardless of its value and it is ignored. Furthermore, positive (negative) weights are indicative of positive (negative) examples because they cause the activation to increase (decrease).

This is the first learning algorithm in which the abilities of learning and pattern classification were achieved by Artificial Intelligence [113] and one of those algorithms that is incredibly simple and yet works amazingly well for some types of problems [85]. As a classifier, perceptron applications include pattern recognition (fingerprint and iris) [112, 115, 116], classification of medical images [112] (cancer classification for example [117]) or gene array analysis [117], surface classification, object detection, distance measurement [116], and forecast ozone and nitrogen dioxide levels

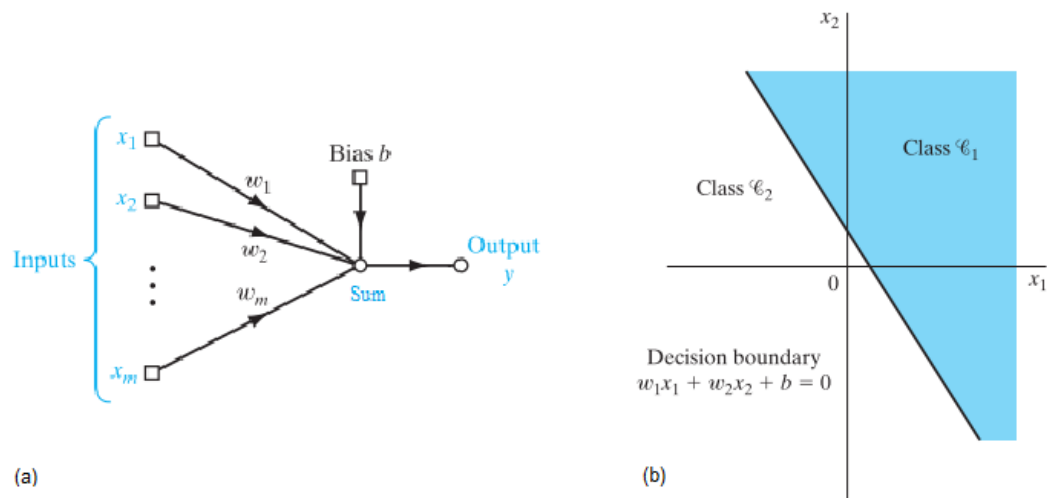


Figure 1.12 – (a) Single layer perceptron and (b) illustration of the hyperplane for a two-dimensional (2D) classification problem (Copyright © 2009 by Pearson Education, Inc., [114]).

measurement in real-time [118]. The perceptron can thus be determinant in many fields such as obstacle detection for autonomous robots or vehicles, identification, surveillance, security systems, medical applications, industrial processes and navigation [112, 116]. As an example, imagine, for the medical case, that you have databases from previous diagnosed patients for different disease indicators, each with a certain influence on the diagnosis. You can then train your perceptron to learn to identify the given disease and even make it more probable to give false positives than false negatives or vice-versa. You can compute the results of several medical exams to help determine if the patient is ill or not.

1.7.2 Associative Memories

The associative memory is the fundamental learning block of the human brain. We learn how to adapt to changing environments and retain/recall events by making associations. In biological systems, this transmission, processing and storage of information occurs in neuronal circuits. The most famous associative memory experiment is that of Pavlov's dog and was already replicated using memristive synapses (see Section 1.6.1) [119].

There are many models describing information storage in neuronal populations that only consider that a neuron can be active or inactive. Although the data storage process usually involves spatio-temporal neuronal patterns of activity, in associative memories only spatial coding is used. Regarding memory storage capacity, if for a population of N neurons a memory is represented by M active neurons, there are $\binom{N}{M}$ possible patterns. This means, for example, that if 5% of a 1000 neurons population are active, there are 1085 different patterns. In the simplest case, the connections are also considered to be binary (weak or strong). To avoid information corruption these models divide operation into two modes: storage and retrieval. The typical model choice for the neuronal activation criteria is the McCulloch-Pitts model [120]: the output neuron is active only

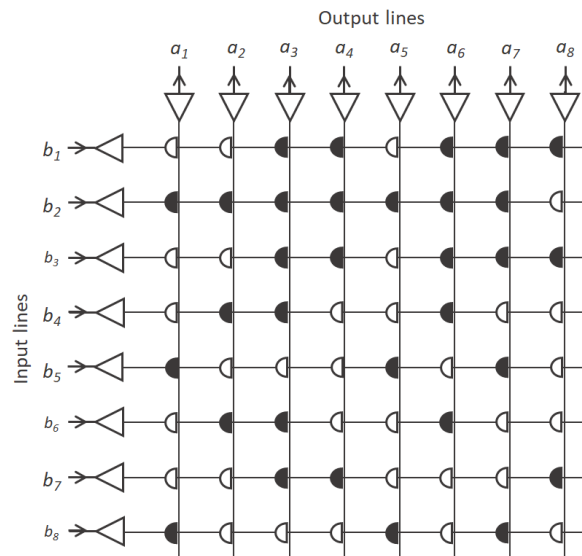


Figure 1.13 – Schematic of an associative neural network.

if the sum of its inputs is equal or above a threshold value, T . As for the choice of the learning rule applied to the synapses, it lies in the Hebb rule.

These memories can be subdivided into auto- and hetero-associative memories. In the first type the information is stored in the recurrent connections of a single population, whereas in the latter information is stored in the feed-forward connections between two populations. Regarding architecture, input and output populations are fully connected, with each neuron in the input population connected to all neurons in the output population (Fig. 1.13). It is thus obvious that the best architecture to implement associative memories is the crossbar array.

Associative memories are a type of content-addressable memory and are a special type of computer memory used in very-high-speed searching applications. As the name implies, the search operation is performed by comparing the input data against a table of stored data, returning the matching data. Unlike random access memory, where the information is stored in and retrieved from explicit locations, and content-addressable memory, that only recognizes an input if it matches a stored vector (memory address), an associative memory is able to retrieve information from incomplete or corrupted inputs. In other words, as the information is encoded in groups of units, the loss of individual storage units does not result in an abrupt memory failure, thus circumventing natural degradation. This shows how this type of memory is robust to noise and incomplete information, abilities of huge importance in the solution of problems such as pattern recognition.

Furthermore, since an associative memory searches its entire memory in a single operation, it is much faster than the standard computer memory in virtually all search applications. The main disadvantage is that each individual memory bit needs its own associated comparison circuit to detect a match between the stored and the input, which increases physical size, manufacturing cost and power dissipation. Therefore, it is appropriate for specialized searching applications only. For instance, it would be well suited for real-time pattern recognition, which could be used in

autonomous robotics.

As discussed above, memristors both present synaptic properties and support crossbar architecture fabrication, being therefore excellent candidates to mimic biological neural networks. They have already been shown to have a good performance in hetero-associative [121, 122] and auto-associative [123, 124, 125, 126] memories. Here we will briefly review the hetero-associative Willshaw and the auto-associative Hopfield memories.

1.7.2.1 Willshaw Network

The Willshaw network is an associative memory that stores associations (data) between the activity patterns of an input population of neurons and the activity patterns of an output population. As it involves two different populations of neurons, it is denominated a hetero-associative memory [127]. It uses a matrix of binary synapses and stores sparse data vectors, as represented on Fig. 1.13. Being known that the neural activity in parts of the brain is sparse (visual and auditory cortices) and that this is beneficial in metabolic efficiency, sparse vector searches in Willshaw network are a good approach to reduce the power consumption of hardware implementations [121]. This network presents high capacity, robustness to noise and auto-completion properties. Its computational implementation using memristors has been considered by Lehtonen *et al.* and by us [121, 122].

1.7.2.2 Hopfield Network

The alternative content-addressable associative memory architecture is the auto-associative network [128], where all the neurons are connected to each other in a single population, i.e. each neuron acts both as input and output. This network has been used to solve, for example, the traveling salesman problem and the location allocation problem [123, 129, 130].

Hopfield networks have already been realized using transistors as synapses [131, 132]. However, and as pointed out above, the chip area and power consumption are too large to scale such system, which makes memristive-based systems the most promising technology to realize hardware based Hopfield networks [123, 124, 125, 126, 133]. To this end, Guo *et al.* realized a Hopfield network with hybrid CMOS/memristor circuits [124] and Hu *et al.* have developed a Hopfield network using HfO₂-based memristors that proved to be capable to retrieve pieces of data [123]. The Hopfield network requires analog synaptic weights and it is a dynamical system, whose neurons need to communicate with each other multiple times during each search to find the output, which increases the complexity of its realization. Also, it has a capacity directly proportional to the size of the input vector. Since the Willshaw network gives the same or higher capacity with a simpler implementation, in our perspective, it seems to be best suited for a memristive implementation [121].

1.8 Summary

Beyond the incapability of continuing to satisfy our technological needs, the performance of present day computers is a limiting factor in the progress of computational research. Many metal–insulator–metal systems show electrically induced resistive switching and have therefore been proposed as the basis for future non-volatile memories [13]. ReRAMs look promising from several perspectives regarding its speed, scalability and operation power. The simple ReRAM concept might resemble that of a switch, which can be settled in two different configurations to allow an electrical current to flow or not. Although simple, the explanation of the physical processes responsible for the switching has not been completely unveiled yet [35]. Moreover, there are still reliability, technology and knowledge limits which must be overcome with the improvement in our understanding of resistive switching mechanisms and the relation between materials properties and device functionalities [3, 47]. There is also still a high complexity involved to achieve a working technology, such as a crossbar nonvolatile memory [35].

Furthermore, it is envisaged that the understanding of biological brains will lead to the construction of future brain-like computer systems, and that the overall architecture and principles of operation of these future computing devices could be closely modeled on those of biological brains. Considering memory an essential building block in learning and decision-making, the demonstration of such functionalities in a nanoscale memristor synapse is crucial to emulate neuromorphic systems and ANNs [17]. As memristors are able to mimic basic neuron and synapse functionality, they are promising to bring us closer to achieving a true intelligent machine and helping to expand our knowledge of neuroscience [134].

Forty years after the first projection regarding the similarity between resistive switching in a metal/insulator interface and the axon coupling in a synaptic junction [23], the development of a solid-state electronic device to replicate the functions of the human brain is finally within our grasp. Ten years after the HP realization of a nanoscale memristor, there are still no revolutionary computer paradigm available in the market [21]. The goal of a human-level intelligence machine will only be possible by the convergence of interdisciplinary knowledge from neuroscientists (observing learning at the single synapse level), psychologists (looking deeply at human behaviors), computational neuroscientists (developing neural models to describe neural mechanisms) and engineers (developing computer hardware).

1.9 Thesis Outline

This Doctoral Thesis focus on the resistive switching phenomenon of two types of structures: MgO and Si/Ag. This work describes the fabrication, characterization and simulation of memristor-based systems and is organized as follows. Chapter 2 describes the different experimental techniques and processes used here to fabricate and characterize our structures. The fabrication steps were all performed at INESC-MN, the electrical characterization at IFIMUP and structural characteriza-

tion at CQFM (XPS), INL (TEM) and CEMUP (AFM). Chapter 3 focus on the characterization of MgO structures. Multi mode resistive switching was observed in Pt/MgO/Ta/Ru structures and attributed to the presence of a thin TaO_x layer at the interface. The influence of vacuum breaks at metal/insulator interfaces was also analyzed, as well as the effect of different electrode materials on the resistive switching behavior. The dependence of the switching parameters on the insulator thickness and defect percentage was inferred from simulation with the random circuit breaker model. A double oxide layer structure (Al₂O₃/MgO) was further characterized for variable Al₂O₃ thickness. In Chapter 4, Si/Ag structures are studied on top of Si rigid substrates, and cellulose and PET flexible substrates. For the latter, measurements were performed both in flat and bent configurations. The inherent stochasticity of resistive switching devices was studied in the switching time–voltage amplitude domain for pulses down to 100 ns. Furthermore, the electrical current–voltage response was modeled in the charge–flux space. Chapter 5 reports the results on numerical simulations for a memristor-based Willshaw network, a Perceptron driven by experimental memristor conductance curves and an Hodgkin-Huxley model circuit using memristors as ion channels. Finally, Chapter 6 states the major conclusions of this work, as well as the open prospects, focusing on the characterization of the resistive switching behavior and the fabrication of crossbar arrays.

CHAPTER 2

Experimental Methods

The microfabrication of metal-insulator-metal (MIM) structures where nanoscale filamentary resistive switching (RS) takes place is one of the most critical steps to obtain successful devices. This process was developed taking advantage of INESC-MN clean room facilities. Furthermore, chemical, structural and electrical techniques are keys to characterize and understand the phenomenon. These were performed using tools at IFIMUP, CQFM, INL and CEMUP. Complementary simulations were performed using the software to simulate electronic circuits *LTspice* and the programming language *Python 2.7*.

2.1 Deposition Systems

Two main physical vapor deposition (PVD) methods were used throughout this work, namely magnetron sputtering and ion beam deposition (IBD). Both are based on the volatilization of the target material by means of the impact of high-energy inert gas particles. The material then condensates on the substrate, maintaining its stoichiometry and with a uniform deposition in large areas. Any material can be deposited using these techniques, since they only imply its volatilization. Below follows the technical details of the used systems, available at INESC-MN. Unless specified otherwise, the MIM structures were always deposited on top of a Si/SiO₂ substrate.

2.1.1 Magnetron Sputtering Deposition

Sputtering is the most used PVD method and is performed in vacuum. A plasma is created between the target and the substrate by introducing an inert gas (Ar or Xe) in the chamber and applying a voltage to the target. The transfer of momentum between the ions of the plasma and the atoms in the target leads to their volatilization and subsequent condensation on the substrate. The cascade of collisions that originates the plasma starts with the presence of a small amount of ions within the mostly electrically neutral gas atoms. The fundamental component of sputtering deposition is the magnetron, which allows the plasma to ignite with a lower concentration of atoms (as the confinement increases the ionization probability), although at the expense of a higher target wear in the region of larger ionization which follows the shape of the magnetic field lines. Figure 2.1 shows the schematic representation of the phenomenon. Magnetron sputtering can be

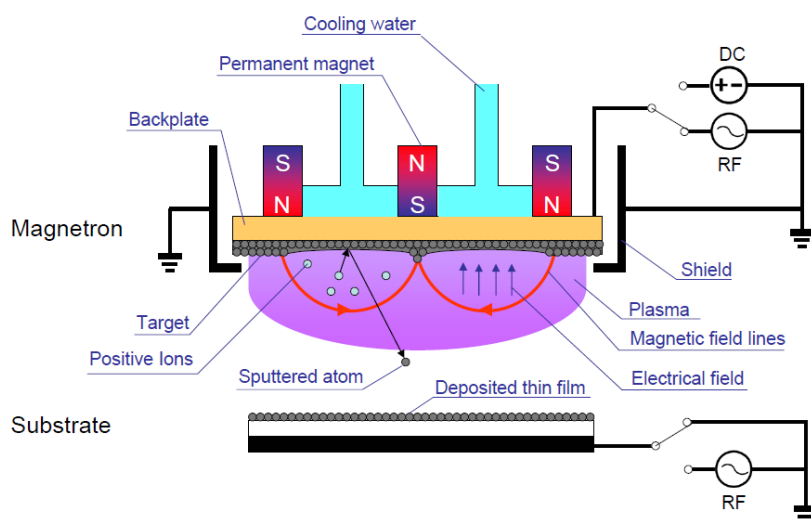


Figure 2.1 – Schematic of a Magnetron Sputtering system (Credits to Ref. [135]).

operated in two modes: DC and RF. In the former, the target is biased with a negative voltage, which accelerates the positively charged ions towards it. If they have enough energy they will ionize more neutral atoms along the way. The trajectory of the resulting electrons is confined by the permanent magnets under the target, and can also favor plasma ignition if carrying enough momentum. Target atoms can also get ionized, contributing with electrons to this process. Finally, if the incoming ions have an energy larger than the binding energy of the atoms in the target, the collision results in emission of these atoms. As they are neutral, they are not affected by the electrical and magnetic fields and travel across the vacuum chamber to the substrate. Relatively low pressures are required in order for the atoms not to loose momentum. This mode is used to deposit metallic materials. For the deposition of insulating materials the target is biased by an RF power supply so that electrical charges are not accumulated at the surface, which would repel incoming ions. With an RF voltage, sputtering takes place in the negative voltage part of the cycle while neutralization of the target with plasma electrons takes place in the positive part of the cycle. The rest of the process is similar to that of DC deposition. In both cases the generated heat is dissipated through a cooling water circuit to prevent any damage to the magnetrons.

2.1.1.1 Nordiko 2000

The Nordiko 2000 tool is an automated magnetron sputtering system with a loadlock connected to the deposition chamber reaching a base pressure of 5×10^{-8} Torr (cryo pump). It allows 6 different targets in the chamber and one sample loaded at a time, with substrate rotation. In this work the Nordiko 2000 tool was used for the deposition of MgO, Ta and Ru thin films using the standard conditions shown in Appendix A. Our 1 inch² substrates are placed directly on the substrate holder for deposition.

2.1.1.2 Alcatel SCM 450

Alcatel SCM 450 is a manual magnetron sputtering tool with a single chamber, no loadlock and connected to a turbo molecular pump (2×10^{-7} Torr). The chamber has three magnetrons in the bottom, four substrate holders on the top and three shutters that can be moved to cover the magnetrons selectively. The substrate table has four possible static positions including the three positions directly aligned over each magnetron. The magnetrons can be supplied with either RF or DC power. In this work, the Alcatel SCM 450 tool was used for the deposition of Si and Ag (Appendixes A.2 and A.3). Our 1 inch² substrates were mounted with kapton onto a 3 inch metallic holder for deposition.

2.1.1.3 Nordiko 7000

The Nordiko 7000 tool is an automated system that consists of a central module connected to a loadlock and four other process modules. Each process module is pumped with cryogenic pumps which provide base pressures of 5×10^{-9} Torr, while the loadlock is pumped with a turbo pump (5×10^{-6} Torr).

Module 2 was here used to perform a soft sputter etching step with ions from an Ar plasma. An RF power source is connected to the substrate and accelerates the ions used to remove the material, with a plasma being maintained by a second RF source. This step is essential to remove the native oxide on top of a pre-existing metal, ensuring good ohmic contact before a new metal is deposited. Module 3 was used for the DC sputtering deposition of TiW from a Ti₁₀W₉₀ target. Standard conditions used in both modules are shown in Appendixes A.2 and A.3. Nordiko 7000 is installed in a class 100 clean room at INESC-MN. Our 1 inch² substrates were mounted with kapton onto a 3 inch metallic holder for deposition.

2.1.2 Ion Beam Deposition

Ion Beam Deposition (IBD) is an appropriate method for the fabrication of metal-insulator-metal structures, with the advantage of operating with any material both for target and substrate. Similarly to sputtering, ion beam deposition is performed by acceleration of the inert gas ions towards the target, removing atoms that are then deposited on the substrate. The ions are generated inside an ion gun and accelerated in a collimated beam to the chamber. Therefore, the sample is not exposed to the plasma, since this is confined to the ion gun. Furthermore, the incoming energy to the substrate is well controlled because all generated ions have the same energy. Thus, more homogeneous and denser films can be produced. Although it is not as fast as magnetron sputtering, this technique allows close monitoring of the process conditions (power, pressure, deposition rate), improving layer thickness control. Also, since the deposition pressure is lower, there is a smaller amount of contaminants.

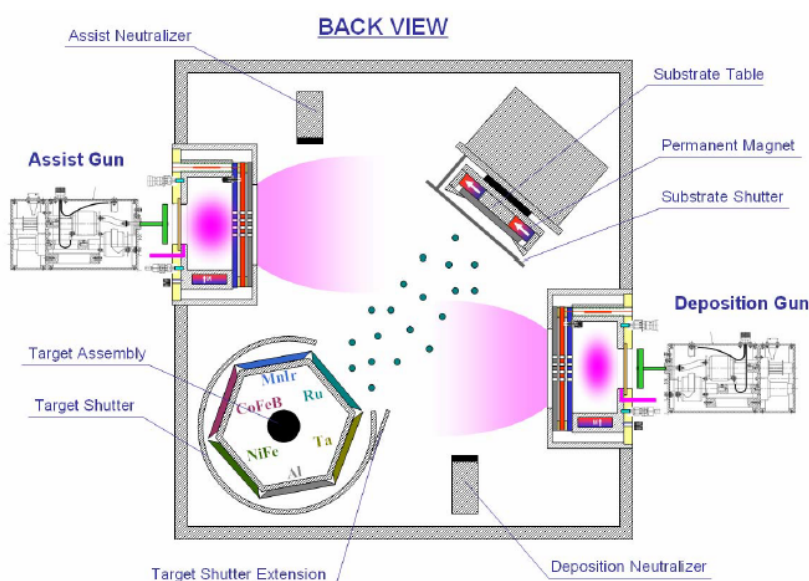


Figure 2.2 – Schematic of an Ion Beam Deposition system (Credits to Ref. [135]).

2.1.2.1 Nordiko 3000

The Nordiko 3000 ion beam system has one deposition module and one loadlock. It incorporates two ion beam guns, a substrate table and a target assembly in a "Z" configuration (Fig. 2.2). Up to 6 targets can rotate around the holder axis in order to align each one with the deposition gun, with a shutter covering all the other to minimize target contamination. Another shutter covers the substrate holder to protect the samples during the guns preparation steps. This holder can rotate up to 30 rpm to improve deposition uniformity. Furthermore, it can also be rotated in the plane defined by the two ion beam guns to change the angle between the substrate and the ion beams: 0° pan angle for horizontal substrate (loading/unloading position) and 90° pan angle for vertical substrate (facing the assist gun). There are two neutralizers at the ion beams exiting from both assist and deposition guns, emitting electrons with the purpose of neutralizing the beams to avoid surface charge accumulation in an insulator target. When pointed at the sample, the assist gun can be used for ion milling (physical etching), reactive deposition, assisted deposition, oxidation processes and ion beam smoothing.

Both the main chamber and the loadlock are pumped with turbo molecular pumps which are backed by rotary mechanical pumps. The chamber is further pumped with a cryogenic pump (3.8×10^{-8} Torr base pressure) which is backed by an oil free mechanical pump. The plasma is created inside the positively charged gun, being the power required to ionize the gas atoms provided through an RF power supply. A set of three voltage biased grids are used to accelerate the plasma ions and focus the beam into the target. The ions inside the gun are attracted towards the negative grid (and also by pressure gradient) and have the chance to escape towards the chamber. The openings of the three grids are aligned in order to collimate the beam. The gun is surrounded by a grounded shield to prevent the leakage of electromagnetic fields to the vacuum chamber. The heat generated by the plasma is evacuated through a water cooling circuit carved

inside the gun body. An array of 20 permanent magnets is placed around the gun, creating a magnetic field that prevents most of the electrons from reaching the wall, increasing the density of electrons in the plasma and promoting secondary ionization, thus lowering the RF power required to maintain the plasma.

This system was used to deposit Ti, Pt, MgO, Ta, Al and Al₂O₃. The standard deposition conditions are shown in the corresponding Runsheets (Appendixes A.2 and A.3). Since the N3600 tool handles 6 inch wafers, our 1 inch² substrates were mounted with kapton onto a 6 inch metallic holder for deposition.

2.2 Microfabrication Techniques

Microfabrication consists in the fabrication of individual devices in the micrometer (μm) range by selectively adding and removing material from a substrate, patterned with a mask, using etching and lift-off steps.

2.2.1 Mask Definition

2.2.1.1 Shadow Mask

A pattern can be defined by a thin physical hard mask (metal sheets for instance; Fig. 2.3). The minimum feature size is decreased to the size of the mechanical drill able to design the pattern in the hard mask, plus the shadow effect from the metal thickness. In this work, this process was used for substrates sensitive to chemical products (Appendix A.1) using 0.12 mm thick brass sheets with 0.4 mm diameter circular holes.

2.2.1.2 Optical Lithography

Optical Lithography is a process widely used to create the masks required for pattern transfer. The sample is coated with a photo sensitive polymer (photo-resist), which breaks or reinforces its molecular connections when exposed to a certain light wavelength. A physical shadow mask can be placed between the sample and light source (mask aligner) or a laser beam can be swept over the coated surface and turned on and off according to a software defined mask layout (direct write laser; DWL). Depending on the type of photo-resist, it can become soluble (positive photo-resist) or insoluble (negative photo-resist) to a proper developer solution by the exposure light.

At INESC-MN, 1.5 μm thick positive resist (PFR7790G27cP, by JSR Electronics) is deposited using a Silicon Valley Group resist automatic coating track. A Heidelberg DWL 2.0 direct write laser system using a 440 nm NeAr laser is used to transfer the mask layout, being the minimum feature size limited by the size of the laser spot (0.8 μm) and the alignment precision by the stage resolution (0.1 μm). The same automatic coating track is used for the development process

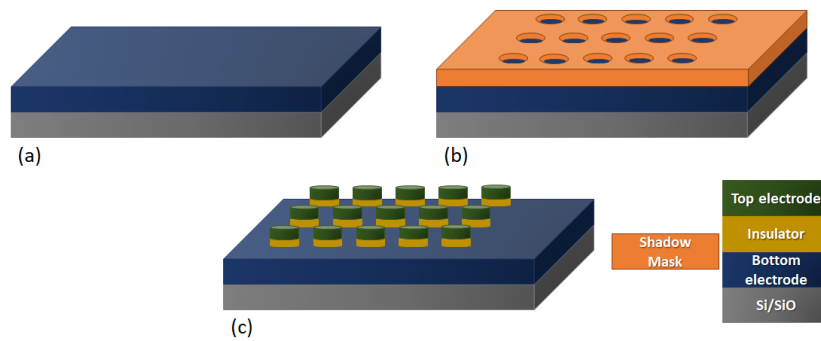


Figure 2.3 – Schematic of the physical shadow mask process. (a) The bottom electrode is deposited on the substrate, (b) covered by a physical shadow mask with circular holes, (c) that leaves the pillars of insulating layer and top electrode when removed.

(Pth70eg or TMA 238WA solutions from JSR). DWL and automatic coating track are installed in a class 100 clean room. Since the coating track handles 6 inch wafers, our 1 inch² substrates were mounted with kapton onto a Si wafer for coating, exposure and developing. For more technical detail on the parameters relating process, time and temperature please see Appendix A.

2.2.2 Etching (Ion Milling)

For the etching process, the substrate with the material already deposited is selectively covered with a mask, made with optical lithography for example, that protects portions of its surface. The protected material is then removed during the ion milling step. Ion milling consists on the physical remotion of a material from a substrate by the collision of inert gas ions (similarly with the target case for sputtering deposition). Other methods can be used such as reactive plasma etch, wet etch, etc. When the mask is removed, the material shaped in the pattern of the mask is left on the substrate. This method allows sharp features, but needs good calibration for the stop timing when removing the material and depends on a physical or chemical process for material removal.

In this work, the remaining photo-resist after the etching process was removed in a resist strip process where the sample is heated up to 60 °C in a Microstrip 2001 solvent in ultra-sounds (Appendix A). Afterwards, the sample is rinsed with IPA (isopropilic alcohol), then with deionized water and finally blow dried with N₂ flow.

2.2.2.1 Nordiko 3600

While this system is very similar to the Nordiko 3000 from a conceptual stand, it is considerably larger, enabling the processing of 8 instead of 6 inch wafers. This system was here used to perform ion milling, using the standard conditions shown in the Appendix A. Again, the angle between the assist gun beam and the substrate holder is varied depending on the type of milling to be performed. A pan angle of 30° (40° between the sample surface and the assist gun beam) is used during the pilar definition and a pan angle of 70° (80° between sample and assist beam) is used whenever material re-deposition is not an issue. In both cases the milling rate with the shown

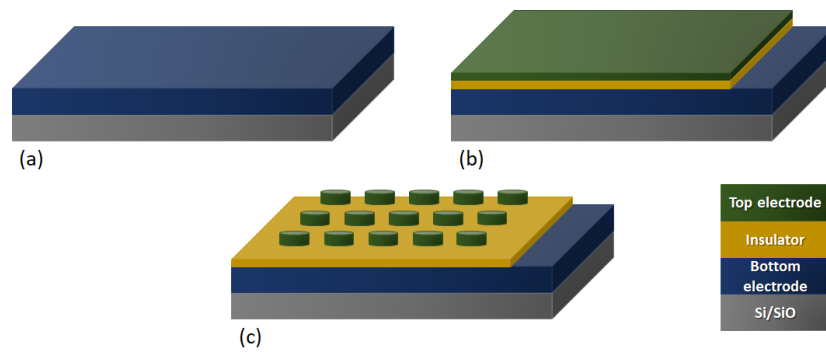


Figure 2.4 – Schematic of the physical single-step process. (a) The bottom electrode is deposited on the substrate, (b) then the insulating layer and top electrode, (c) finally the pillars are defined by a single step of photolithography and physical etching.

conditions is close to 1 Å/s. This system was used for soft etch steps and the deposition of Cu and Ru. Since the N3600 tool handles 8 inch wafers, our 1 inch² substrates were mounted with kapton onto a 8 inch metallic holder for ion milling.

2.2.3 Lift-off

When using the lift-off process, the material to be patterned is deposited on top of a mask selectively covering the substrate. When the mask is removed the material on top is also taken away, letting the deposited material with the pattern of the mask empty spaces. This method is a good option to pattern on top of an existing stack, but does not provide sharp features and can originate "rabbit ears" defects on the sides, not being suitable for multilayer patterning.

In this work, the mask is defined by photo-resist that is removed in a resist strip process where the sample is put in acetone in ultra-sounds (Appendix A) after the top material deposition. Afterwards, the sample is rinsed with IPA (isopropilic alcohol), then with deionized water and finally blow dried with N₂ flow.

2.3 Microfabrication Processes

Using the above techniques, two processes were established and used in this work. The majority of structures in this work were deposited and microfabricated on top of plasma oxidized commercial Si substrates (SiO/Si/SiO) and Ti (25 nm adhesion layer) / Pt (150 nm) layers as bottom electrode.

2.3.1 Single-step

In order to quickly and easily test interfaces, the single-step method allows to measure micrometer junctions in the perpendicular configuration. After the total deposition of the metal-insulator-metal stack, the junctions patterns are defined by a lithography step. Then, using physical etching, the surrounding material is removed, leaving only the junctions defined (Fig. 2.4). In this work, circular

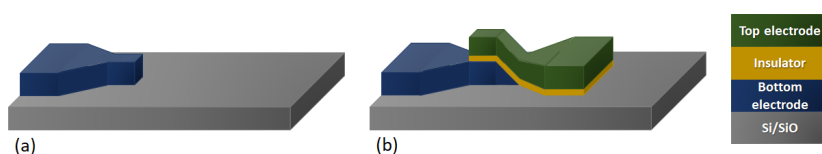


Figure 2.5 – Schematic of the physical two-steps process. (a) The bottom electrode is deposited and defined by a photolithography and physical etching step, (b) then the insulating layer and top electrode are deposited inside the areas defined by a second photolithography step and lift-off.

pillars of 300 μm of diameter were defined. The complete process is described in Appendix A.2.

2.3.2 Two-steps

To defined more complex connecting networks between single devices, a two-steps method was established. In this case, the bottom electrode is firstly defined by optical lithography and then etching at 45° angle to smooth the step between layers [Fig. 2.5(a)]. Then the remaining stack is deposited inside pattern defined again using lithography and revealed by a lift-off step. The final structures can be seen in Fig. 2.5(b). The step by step process is described in Appendix A.3.

2.4 Characterization Methods

2.4.1 X-Ray Photoelectron Spectroscopy

X-ray photoelectron spectroscopy (XPS) allows the quantitative measurement of the elemental composition, chemical and electronic states of the elements within surface resolution (0-10 nm depth). The material is irradiated with a beam of X-rays in vacuum and the kinetic energy and number of the resulting electrons is measured.

In this work, XPS was performed at CQFM to characterize the MgO/Ta and MgO/Pt interfaces in detail. Given the surface specificity of X-ray photoelectron spectroscopy (XPS), thinner samples consisting of MgO (30 nm) / Ta (2 nm) / Ru (1 nm) and MgO (30 nm) / Pt (3 nm) were prepared. Ex-situ XPS was performed to characterize the chemical states using a dual anode non monochromatic XSAM800 spectrometer from KRATOS. The spectrometer was operated in FAT mode, with a pass energy of 20 eV. Samples were irradiated with Al K_{α} radiation ($h = 1486.6$ eV) applying at the source a voltage of 12 kV and a current of 10 mA. Data were acquired for a take-off angle of 0° (relative to the surface normal) and recorded by the software Vision 2 for Windows, Version 2.2.9 from KRATOS. Data treatment was performed as referred in Ref. [136], except for the Ru 3d region that was fitted with asymmetric profiles with TS and TL parameters equal to 0.34 and 116, respectively (TS and TL are peak shape and tail extension asymmetry parameters in XPSPeak 4.1 asymmetric Gaussian-Lorentzian sum function⁵⁴). No charge correction was needed. For quantification purposes, sensitivity factors were 0.278 for C 1s, 0.78 for O 1s, 4.273 for Ru 3d, 2.043 for Ru 3p, 5.158 for Ta 4d, 2.171 for Ta 4p_{3/2}, 2.26 for Mg 1s and 0.252 for Mg 2s.

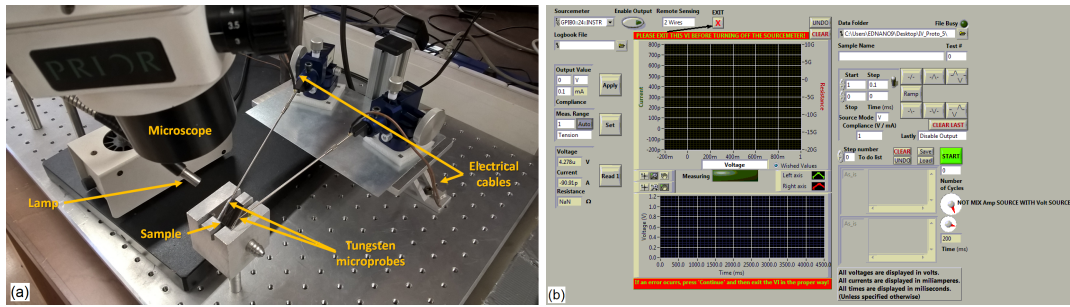


Figure 2.6 – (a) Electrical measurement setup showing the tungsten microprobes on the sample, support microscope and lamp. (b) LabView control program panel.

2.4.2 Electrical Characterization

Direct Current (DC) measurements were performed at room temperature using two tungsten microprobes connected to a Keithley SourceMeter 2400 [Fig. 2.6(a)]. For all measurements, the voltage was applied on the top electrode with the bottom electrode grounded. Positive and negative current compliances were established to avoid damaging the sample when justified. To control the SourceMeter an existing interface developed in LabView was used [Fig. 2.6(b)]. Below are the details of the used operation modes.

Since the minimum voltage pulse duration that can be applied using the Keithley SourceMeter 2400 is ~ 200 ms, the ArC ONE hardware platform from ArC Instruments [137] was used for higher speed and optimized memristive analysis in Section 4.3.

I–V characteristic. The current–voltage (I–V) measurement method is widely used for the characterization of ReRAM devices. The principle of the method is based on a linear variation of the applied potential with the time (voltage ramp). During the measurements, the voltage was swept in the $0 \rightarrow V_{max} \rightarrow 0 \rightarrow V_{min} \rightarrow 0$ sequence (where V_{max} is the maximum positive and V_{min} is the maximum negative applied voltage; allowing asymmetric cycles to be performed), with separately defined voltage steps (δV^+ , δV^-) and delay times (δt^+ , δt^-) for positive and negative ranges [Fig. 2.7(a)]. The delay time is the duration each voltage step is applied.

Pulsed Mode. Pulsed measurements are performed by applying a time defined rectangular voltage (or current) pulse where the current– or the voltage–time transients are recorded, respectively. This switching mode (write, read, erase, and read steps) was also implemented, using a defined number of pulses of V_{Set} , V_{Read} , V_{Reset} , t_{Set} , t_{Read} , t_{Reset} and t_{wait} , with a limiting current (compliance) for each [Fig. 2.7(b)].

Endurance. Retention reliability tests were performed applying a fixed small voltage over time, reading the current at each defined time step. The same mode can be used to apply higher constant voltages over time.

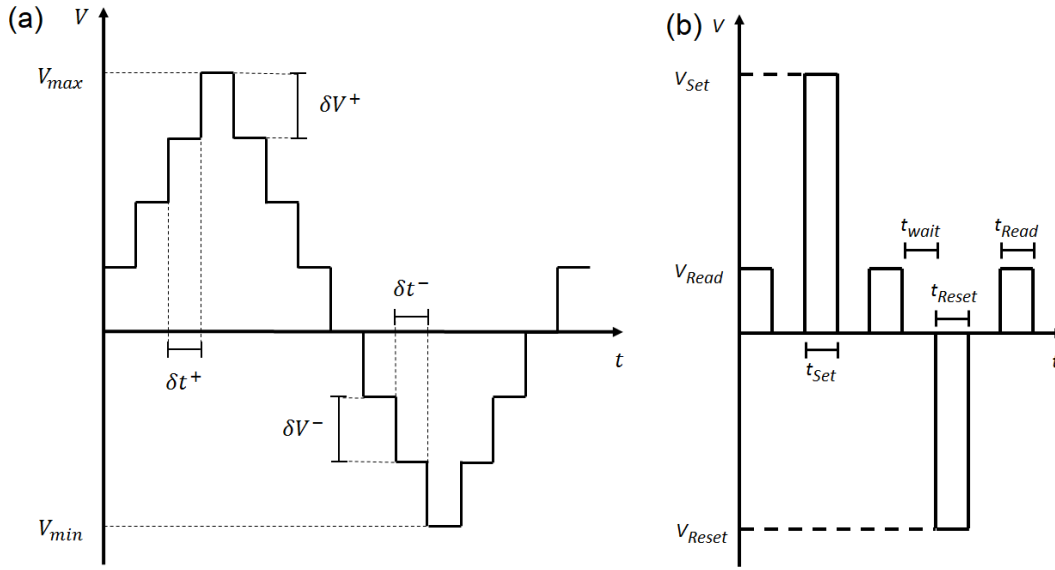


Figure 2.7 – Schematic of the the applied (a) voltage swept and (b) voltage pulses over time.

2.5 Simulations

2.5.1 Random Circuit Breaker

The 2D Random Circuit Breaker network was established on Python 2.7, using ahkab v0.18 package [138], a spice-like electronic circuit simulator, to map the network and the *Python* Imaging Library (PIL) for the graphical representation. The circuit solution uses a modified version of the Newton Rhapsod method. This language is open-source. To look for the source code please go to Appendix C.

2.5.2 Willshaw Network

A 128×128 memristor-based Willshaw Network was implemented using *LTspice* and the memristor model developed by Pino *et al.* [139]. An equivalent *Python* 2.7 algorithm developed by us is made available to the public for particular testing, implementation and further development [140, 141].

2.5.3 Perceptron

A single layer memristor-based Perceptron was implemented using *Python* 2.7. More details can be seen on Appendix D and the algorithm developed by us is made available to the public for particular testing, implementation and further development [140, 141].

CHAPTER 3

Resistive Switching in MgO structures

Many materials have been shown to display resistive switching [93, 37, 142, 143], including binary oxides (e.g., SiO_x [144, 61]) and particularly binary metal oxides (e.g., TiO_x [21, 145], TaO_x [146, 147], Al_2O_3 [148], HfO_2 [149], NiO_x [150], MgO_x [151, 152, 153, 154, 155, 156, 157, 158, 159, 160], ZnO_x [161], CuO_x [162] and WO_x [163]). Among such variety of RS materials, binary oxides show the best switching performance in terms of speed and endurance [16]. Furthermore, they are compatible with conventional complementary metal-oxide-semiconductor (CMOS) processes due to their simple composition and easy fabrication. For example, HfO_x based materials have a high dielectric constant and are usually implemented for bipolar RS; AlO_x shows low reset currents due to the large band gap (8.9 eV); NiO_x shows unipolar RS and is compatible with a large number of electrodes but has a poor switching uniformity; TiO_x is the most studied material for both bipolar and unipolar RS, having a higher reset current for the unipolar mode than for the bipolar one; TaO_x is well known for its large endurance [36]. On the other hand, MgO has been intensively studied in magnetic tunnel junctions [164, 165, 166], acting as the insulating barriers for magnetic random access memories (MRAMs). More recently, it has also been suggested for ReRAMs [157, 156, 167, 168, 151, 169, 170]. Although the origin of RS in MgO structures is still not completely understood, the formation of conductive filaments has been suggested as the responsible mechanism [155]. MgO is a binary oxide with a large bandgap in the 7.3 eV–7.8 eV range, ensuring sufficiently large band offsets with Si, and a high breakdown field (12 MV/cm), improving the reliability [171]. It has an empirical formula of MgO and consists of a lattice of Mg^{2+} ions and O^{2-} ions held together by ionic bonding in a NaCl-type crystal structure [172].

3.1 Multi Mode Resistive Switching

Here, we studied the resistive switching of Si / SiO_2 / Ti (25) / Pt (150) / MgO (30) / Ta (20) / Ru (5) (nm) structures with a yield of 96% of working devices obtained. The influence of the voltage polarity operation mode, regarding Set and Reset voltage polarities [$(V_{\text{Set}}, V_{\text{Reset}})$: (+,+), (+,-), (-,-) and (-,+)], on switching voltages and resistance variabilities were analyzed from the statistical distribution of consecutive voltage sweep cycles.

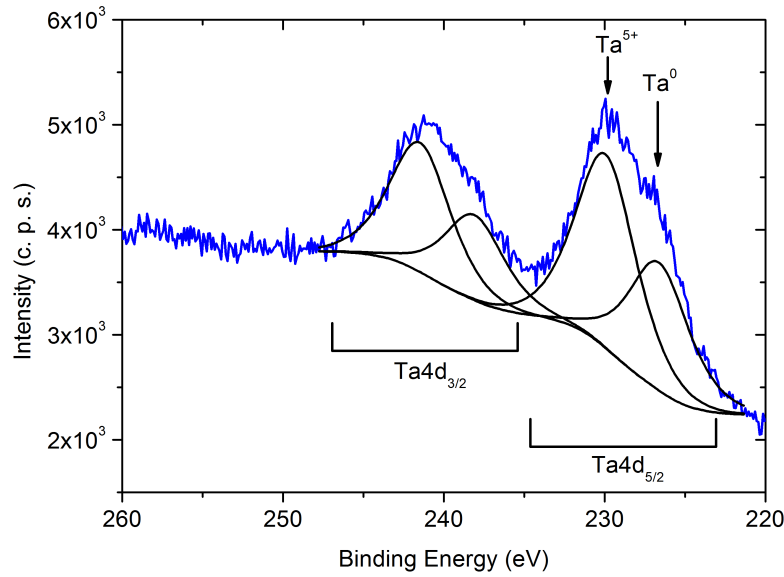


Figure 3.1 – XPS spectrum and fitting of the Ta 4d region for a Pt / MgO / Ta (2) / Ru (1) (nm) sample.

3.1.1 Structural Characterization

Given the surface specificity of X-ray photoelectron spectroscopy (XPS; performed at CQFM), a thinner sample consisting of MgO (30) / Ta (2) / Ru (1) (nm) was prepared, in order to study the MgO/Ta interface. Figure 3.1 shows the XPS region of Ta 4d, revealing that it is composed by 2 doublets with main components (Ta 4d_{5/2}) centered at 226.6 and 229.9 eV and assigned to Ta⁰ and Ta₂O₅, respectively [173]. Given the high affinity of Ta to oxygen, the presence of this TaO_x interfacial layer results from the migration of oxygen from the MgO. The approximate fraction of oxidized tantalum (Ta⁵⁺) is estimated to be 72 % (~ 1.4 nm) neglecting any stratification within the layer (see Appendix B for calculation details). This TaO_x layer then already exists in the as-prepared devices and its influence on the subsequent resistive switching processes must be considered, as will be shown below. Quantitative analysis of XPS data shows that the only striking difference between the experimental XPS ratios and the ones estimated based on the deposited nominal structure was found for the Mg 2s/Mg 1s ratio. That difference may be explained by the existence of intermixing between the layers.

3.1.2 Resistive Switching

All measured devices initially exhibited a high resistance state ($R_0 \sim 1 \times 10^{10} \Omega$). Independently of the polarity, when increasing the voltage from the initial state, the current starts to abruptly increase at a high voltage value of ~ 9 V, indicating the transition to the low resistance state [LRS $\sim 140 \Omega$; step 1 in Fig. 3.2(a)]: forming process. Starting again from 0 V and without limiting the current, the device switches to a HRS of $2 \times 10^5 \Omega$ (lower than the initial state; step 2): Reset process. The LRS and HRS can then be reproducibly obtained by increasing the voltage with (step 3; Set) and without (step 4; Reset) current compliance, respectively, leading to a HRS to LRS ratio of 3

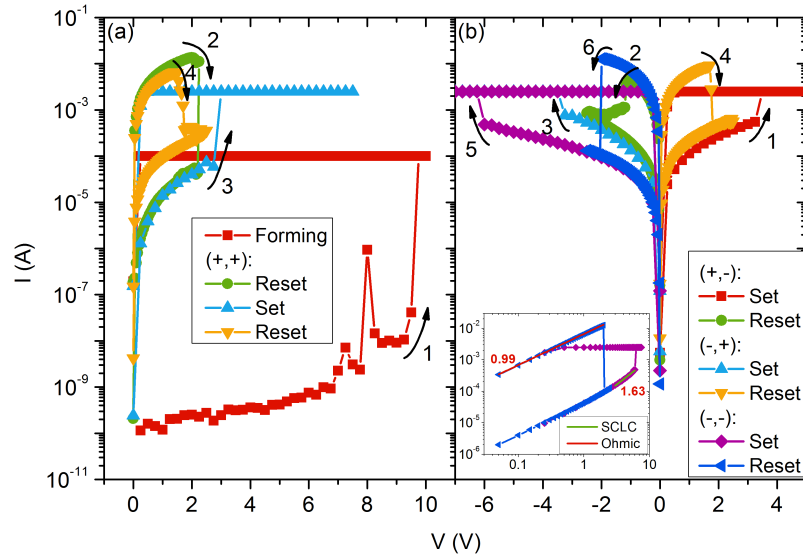


Figure 3.2 – *I–V characteristics (a) of a pristine device showing the forming process (step 1) and the switchings between the two resistance states (steps 2 and 3) in the (+,+) operation mode, and (b) showing resistive switching with different combinations of voltage polarity - (steps 1 and 2: +,-); (steps 3 and 4: -,+) and (steps 5 and 6: -,-). The inset shows the conduction mechanisms involved in the resistance states.*

orders of magnitude. The first Set is a forming process, since it occurred at a much higher voltage (~ 9 V) than the following ones (~ 2 V) and the subsequent HRS were always smaller than R_0 . This shows that structural changes, that cannot be fully reversed, took place in the device during forming. This indicates that a metallic filament was created during forming that is only partially ruptured from then on. Given the presence of the TaO_x layer formed by capturing oxygen from the MgO, we can infer that this metallic-like filament is composed by oxygen vacancies. This is confirmed by the conduction mechanism involved in the ON state being the ohmic (unitary slope in the log-log scale) and space-charge limited current (SCLC) in the OFF state, as shown in the inset of Fig. 3.2(b).

Even though the second Set was performed with a higher current compliance than the first, the final ON resistance is similar to that after forming. This shows that there are typically only two resistance states in our devices. Interestingly, the same low and high resistance states could be obtained by switching the devices with the other voltage polarity combinations: positive Set and negative Reset, (+,-) [steps 1 and 2 in Fig. 3.2(b)]; negative Set and positive Reset, (-,+) (steps 3 and 4); and negative Set and Reset (-,-) (steps 5 and 6). The devices can also be arbitrarily switched between switching modes. Furthermore, retention reliability tests up to 14 h under 10 mV showed that both resistance states are stable, with a resistance ratio of two orders of magnitude on average and no degradation being observed for more than 10⁴ s for the (+,+) mode (Fig. 3.3). This indicates that a 10-year lifetime is expected and further confirms the nonvolatile nature of the fabricated MgO-based resistive switching device.

One of the major problems associated with these type of devices is the still large variability of the switching parameters, such as Set and Reset voltages or ON and OFF resistances on cycling.

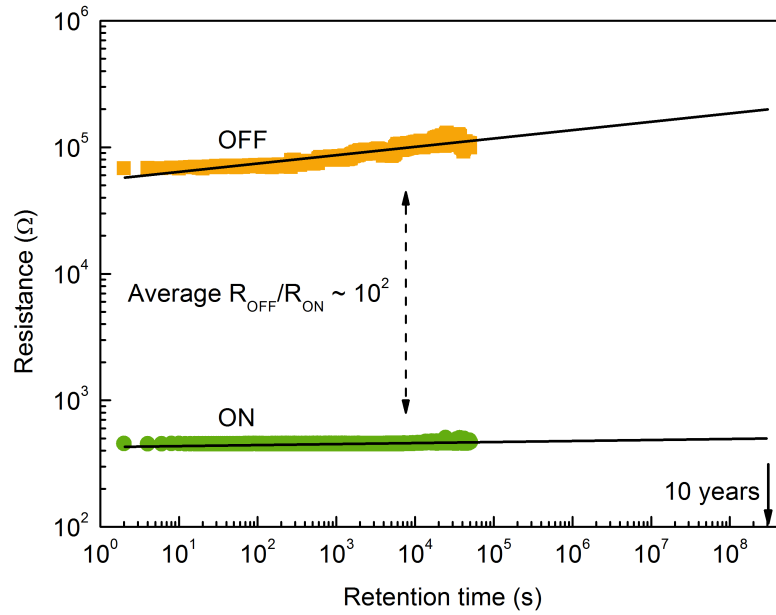


Figure 3.3 – Retention time for the OFF and ON resistance states up to 14 h for the (+,+) mode, measured with 10 mV every 2 s (lines show a linear fit to the data).

This is a critical device characteristic as successful applications require low variability [79, 174]. Such variability is associated with material and fabrication defects typical of nanoscale processes and to the intrinsic stochasticity of the switching process. Several strategies are being studied to diminish this problem, including current compliance control, forming voltage polarity and operation voltages magnitude and polarity [148, 175, 176, 145, 177, 178, 179, 180, 149].

We then performed a thorough study on the voltage and current variability (vertical and horizontal bar plots in Fig. 3.4, respectively) for all voltage modes up to 50 cycles. The same current compliance was used in all cases (2.5 mA) and the voltage sweeps were always performed in the ranges 0 V → 7.5 (-7.5) V → 0 V for Set and 0 V → 2.5 (-2.5) V → 0 V for Reset, with a voltage step of 0.25 and 0.05 V, respectively. The insets of Fig. 3.4 show the evolution of the ON and OFF resistance states when voltage pulses are applied to perform the switching. Note that, as the devices are unipolar, they get easily stuck in the low resistance state by doing a Set in the place of a Reset (higher current), therefore damaging the structure. Both Set and Reset transitions are always abrupt except for the case of the Reset step of the (+,-) mode [Fig. 3.5]. In this mode there is an semi-abrupt initial current decrease (step 1) followed by a smooth decrease (step 2). This smooth decrease may be related with the diffusion of the oxygen vacancies after the major filament ruptures.

The cumulative probabilities of the Reset [Fig. 3.6(a)] and Set [Fig. 3.6(b)] voltages show that the variability is always higher in the Set case than in the Reset one. Nevertheless, lower variability for both Set and Reset voltages was observed when the Set was performed under positive voltages [modes (+,+) and (+,-); Figs. 3.4(a) and 3.4(c)], particularly for the (+,-) mode [Fig. 3.6(a)]. Furthermore, the average values of the Reset voltage and current during cycling are also the

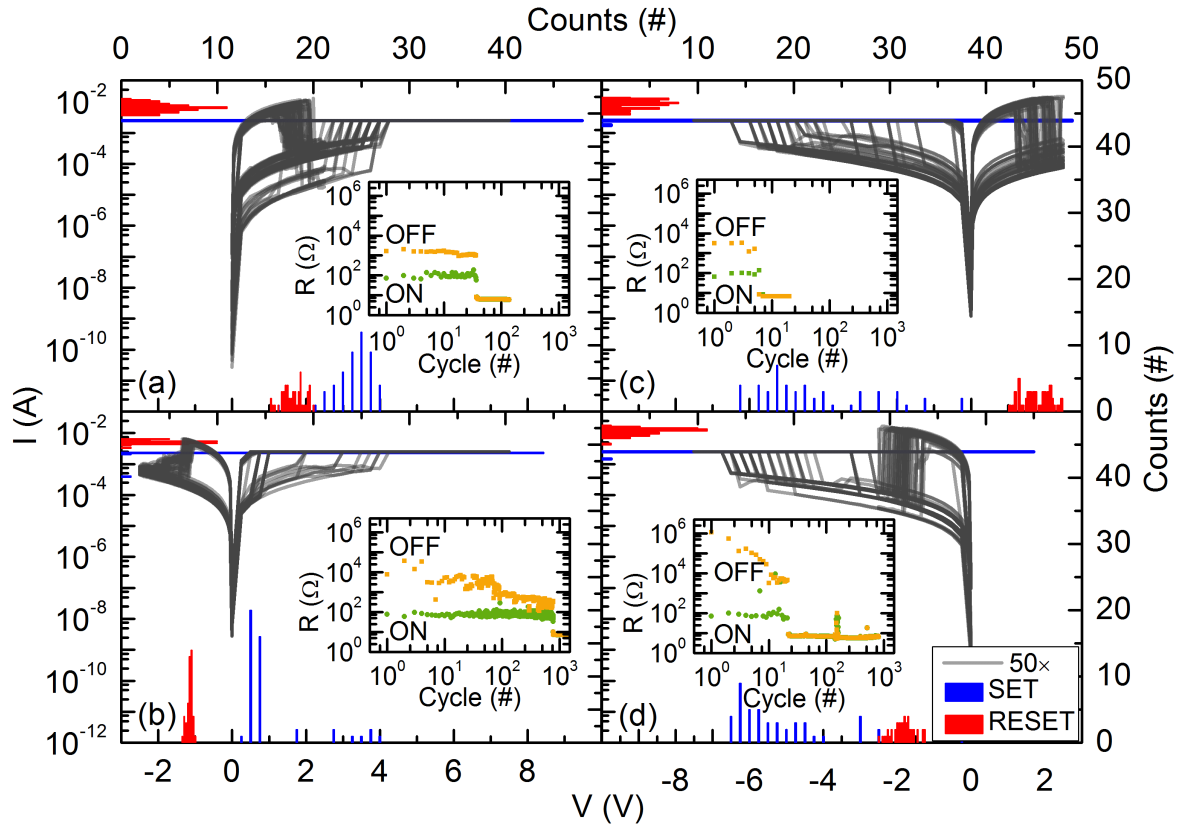


Figure 3.4 – *I-V* curves for the four voltage polarity combinations: (a) (+,+), (b) (+,-), (c) (-,+) and (d) (-,-). The right (top) axis denotes the voltage (current) distribution. The insets show the resistance values for the pulsed operation mode ($|V_{Set}| = 7.5$ V, $I_C = 2.5$ mA, $|V_{Reset}| = 2.5$ V, $\Delta t = 1$ s and $V_{Read} = 1$ mV).

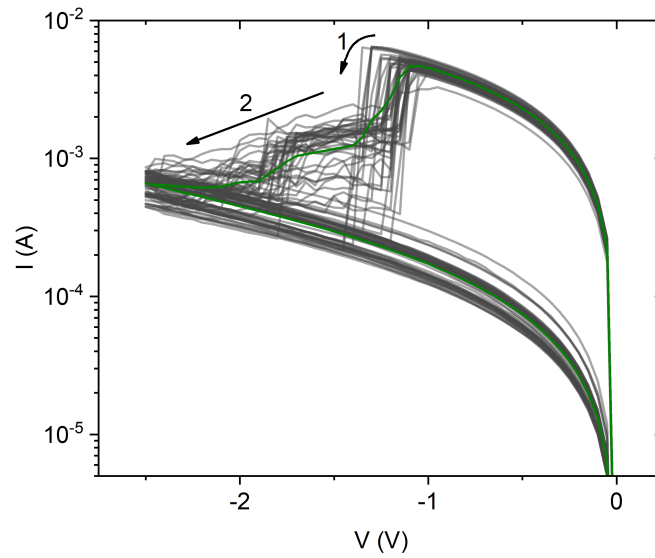


Figure 3.5 – Reset cycles of the (+,-) mode [Fig. 3.4(b)] showing an initial abrupt transition (step 1) followed by a smooth variation (step 2). The green line shows the average of all the cycles point by point.

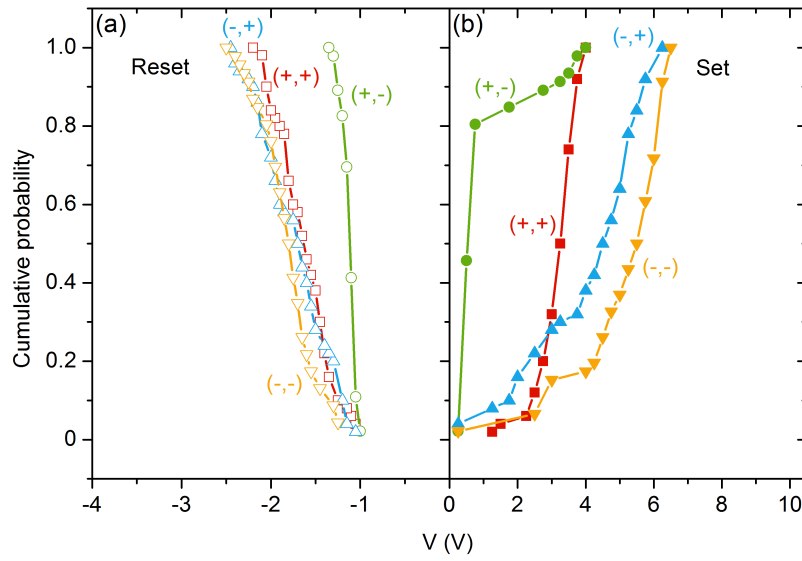


Figure 3.6 – Cumulative probability of the absolute (a) Set and (b) Reset voltages for all voltage polarity combinations.

smallest for the (+,-) case [1 V, 5 mA versus 2 V, 10 mA; Fig. 3.7(a)]. Note that this improvement in the switching distribution was observed irrespectively of the order that the measurement modes were performed [Fig. 3.7(b)].

Considering the resistance variability, values of $10^2 \Omega$ for ON and $10^3 - 10^5 \Omega$ for OFF states were obtained, both considering each voltage polarity separately [Fig. 3.8(a)] or all the measurements together [Fig. 3.8(b)]. The variability is higher for the OFF state as it is common in this type of devices [181] and again a lower variability is obtained for the (+,-) mode, although it is also the one with the smallest resistance ratio.

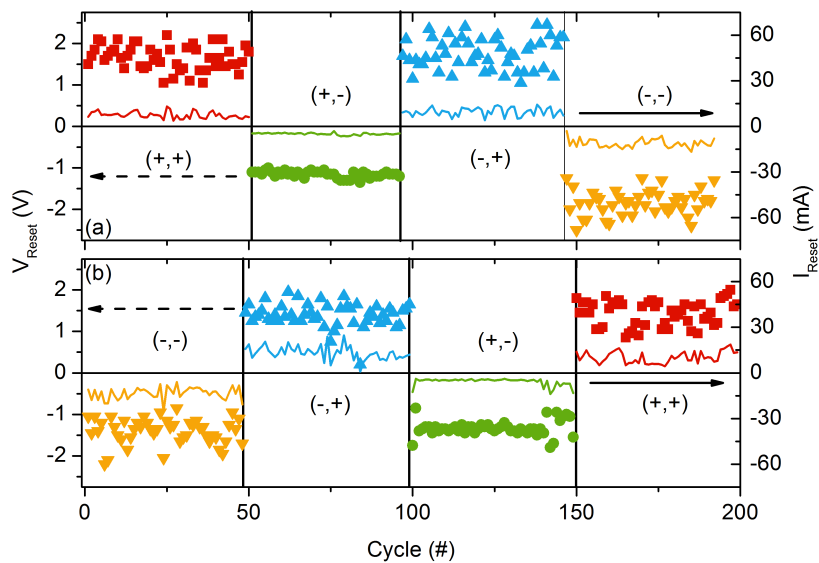


Figure 3.7 – Reset voltage (left axis; symbols) and current (right axis; lines) for two different devices with all switchings in the order (a) (+,+) → (+,-) → (-,+) → (-,-) and (b) (-,-) → (-,+) → (+,-) → (+,+).

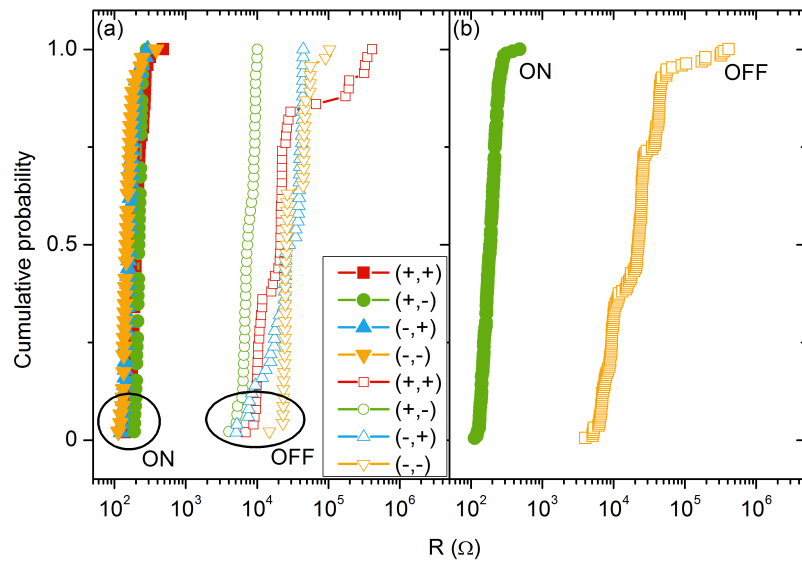


Figure 3.8 – Cumulative probability of the ON (closed symbols) and OFF (open symbols) resistance states for (a) each voltage polarity combination and (b) all measurements combined.

Table 3.1 summarizes average resistance and voltage values for the forming step and all operation modes. The analysis of the forming voltage variability gives an average value of (7.5 ± 1.9) V. Also, the forming voltage polarity was not observed to have a meaningful influence on the RS behavior, implying that the filament grows from the Ta electrode towards the Pt one, independently of the applied voltage polarity, since the TaO_x layer works as an oxygen reservoir (oxygen vacancies created in MgO).

Additional measurements for positive and negative formings were performed in order to confirm that the polarity of the forming has no influence on the resistive switching behavior. Figure 3.9 shows the cumulative probabilities of Set and Reset voltages with formings at both positive and negative voltages for the (+,-) [Fig. 3.9(a)] and (-,-) [Fig. 3.9(b)] modes. A good repeatability was obtained for both cases, showing that there is no influence from the forming polarity on the resistive switching behavior. Figure 3.10 depicts the same study for (+,+) and (-,-) [Fig. 3.10(a)]

Table 3.1 – Mean values of the resistive switching parameters of Pt/MgO/Ta/Ru for all four measurement modes. The statistical data was calculated from 50 cycles.

Operation Mode	R_{OFF} (Ω)	σ/μ (%)	R_{ON} (Ω)	σ/μ (%)	V_{Set} (V)	σ/μ (%)	V_{Reset} (V)	σ/μ (%)
Forming	1.3×10^{10}	-	-	-	7.5	25	-	-
(+,+)	5.5×10^4	179	217	25	3.25	18	1.66	18
(+,-)	7.8×10^3	20	221	9	1.08	97	-1.15	7
(-,+)	2.9×10^4	46	170	21	-4.17	39	1.76	22
(-,-)	3.5×10^4	50	161	28	-5.14	27	-1.84	16

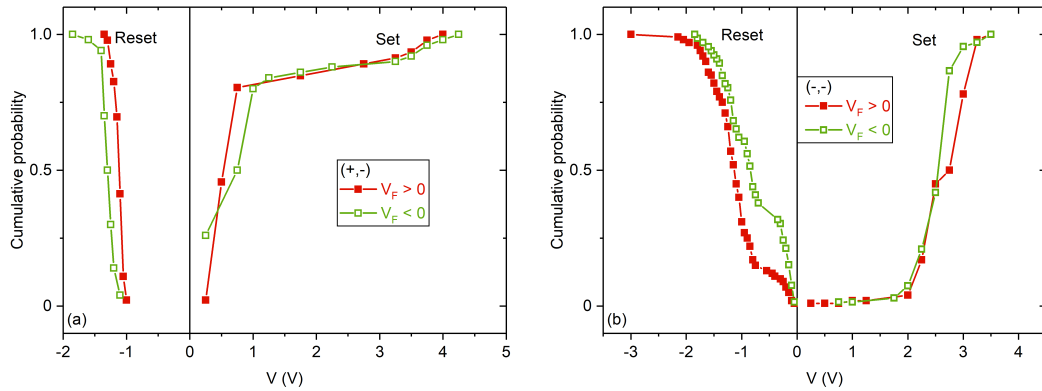


Figure 3.9 – Cumulative probability of the Set and Reset voltages for the (a) (+,-) and (b) (-,-) modes with forming at positive and negative voltages.

and (+,-) with (-,+ [Fig. 3.10(b)]. If the filament growth direction changed with the forming polarity, the results for the modes would just be reversed as: $(+,+) \longleftrightarrow (-,-)$ and $(+,-) \longleftrightarrow (-,+)$. As can be seen, this does not occur, as the modes behave equally between then for different forming polarities and differently from the other modes.

The mixed ionic electronic conduction model can predict this behavior by attempting to solve the coupled ionic and electronic continuity equations. It shows that the positive charges are attracted towards the cathode, to form a conductive region, unless their concentration in the vicinity of the anode is sufficient to initiate the formation of a conductive region there, followed by its propagation towards the cathode [182, 183]. Yalon *et al.* obtained this result from the Gummel plot characteristics of HfO_2 devices with two and only one inert electrodes [178].

It is also observed that the OFF resistance is always lower than the initial resistance (before forming) and that the ON resistance is independent of the operation mode ($\sim 2 \times 10^2 \Omega$; complete filament). Although the resistance ratio is smaller for the (+,-) mode, it has the lowest Set (0.99 V) and Reset (-1.15 V) voltages of all combinations. Such values are comparable to those obtained in bipolar devices. The second mode with smaller average Set (3.25 V) and Reset (1.66 V) voltages

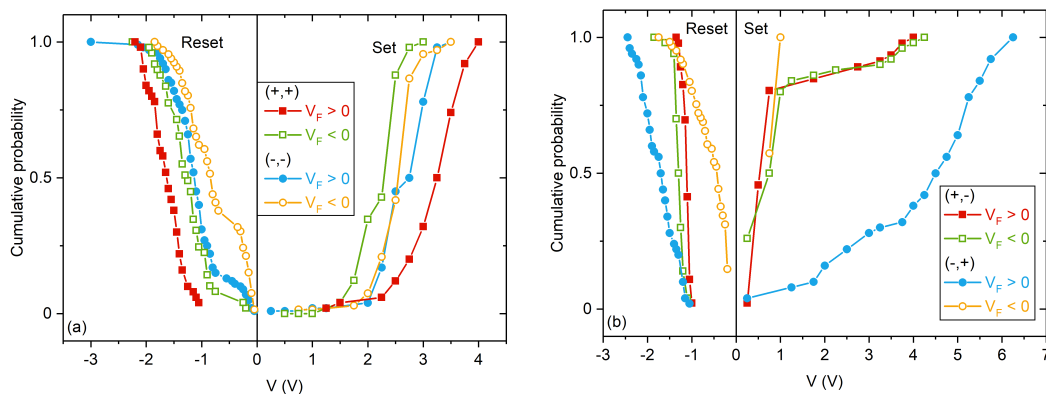


Figure 3.10 – Cumulative probability of the Set and Reset voltages for the (a) (+,+) and (-,-), and (b) (+,-) and (-,+) modes at positive and negative forming voltages.

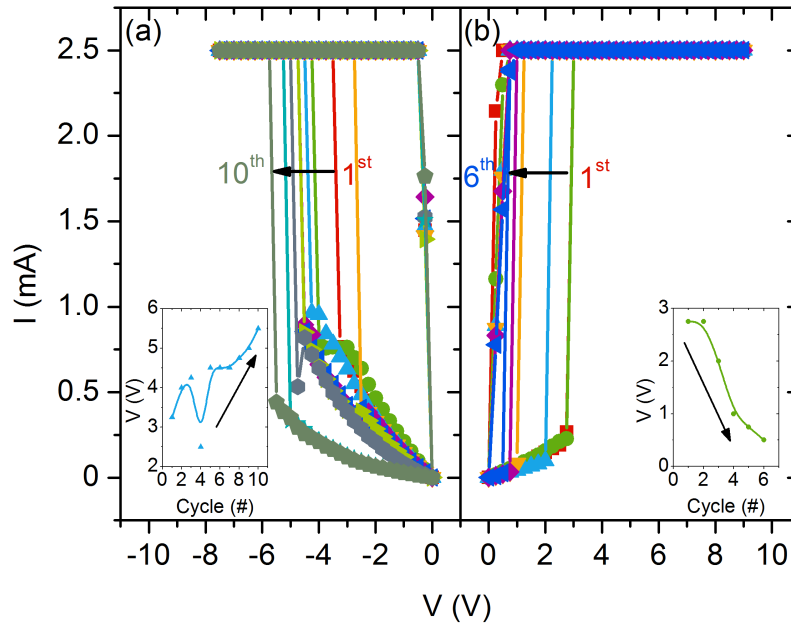


Figure 3.11 – First Set (a) 10 cycles for $(-,+)$ after $(+,-)$ and (b) 6 for $(+,-)$ after $(-,+)$. The insets show the evolution of the Set voltage over cycle number for each case.

is the $(+,+)$ mode, that also shows the highest OFF resistance ($5.5 \times 10^4 \Omega$). This reinforces the influence of a positive Set voltage on the switching behavior of our devices, as it is reported that devices having an oxygen exchange layer (Ta for example) at the anode exhibit superior resistive switching characteristics [178]. These results are further confirmed by the endurance data presented in the insets of Fig. 3.4, with the $(+,-)$ mode showing the highest number of cycles.

In order to determine the mechanism underlying the influence of the Set voltage polarity, we looked closer to the first cycles at the transition between $(+,-)$ and $(-,+)$ modes for the devices depicted in Fig. 3.7. This analysis showed that, at the polarity changes [$(+,-)$ to $(-,+)$, $(-,+)$ to $(+,-)$], there is an overall increase/decrease of the voltage amplitude for the first few cycles, respectively (Fig. 3.11). This suggests a change on the filament morphology, from hourglass to conical [as one changes the switching mode from $(+,-)$ to $(-,+)$] and then from conical to hourglass [$(-,+)$ to $(+,-)$].

Returning to Table 3.1, the mode with the highest Set voltage (-5.14 V) is the $(-,+)$. These results indicate that Set is facilitated when the electric field points from the Ta to the Pt electrode, i.e. with decreasing work function for the electrons (4.25 eV versus 5.65 eV). This may be understood by the growth direction of the filament (Ta \rightarrow Pt). Regarding only the Reset voltage, it can also be observed that the absolute value for the $(+,+)$, $(-,+)$ and $(-,-)$ modes is very similar, which can be explained by the rupture of the filament being aided by Joule heating [184]. Figure 3.12 shows the average value of the Reset power for each mode, highlighting the smaller value for the $(+,-)$ mode and, between the filament shapes, for the hourglass.

The schematic representation of the processes involved in resistive switching is shown in Fig. 3.13. For forming and both Set voltage polarities the filament composed of oxygen vacancies connects the two electrodes, growing from Ta towards Pt. For positive Set voltages [$(+,+)$ and

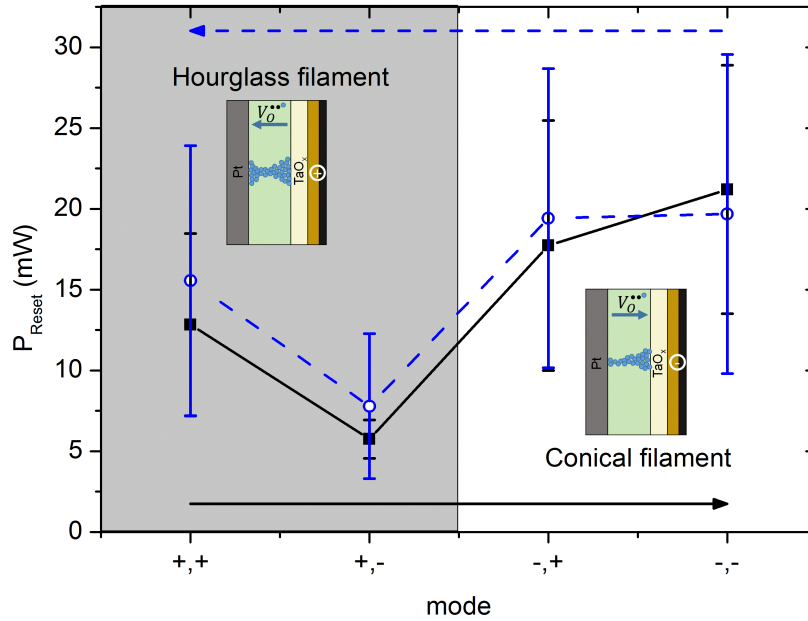


Figure 3.12 – Reset power for two different devices with switchings in the order $(+,+) \rightarrow (+,-) \rightarrow (-,+) \rightarrow (-,-)$ (full line) and $(-,-) \rightarrow (-,+) \rightarrow (+,-) \rightarrow (+,+)$ (dashed line).

$(+,-)$; left panel], the drift direction is the same as that of the filament growth and therefore smaller voltages are needed (1.08 V and 3.25 V, respectively) and the filament has a hourglass shape. Then, for negative Reset $(+,-)$, the direction of the electric field is opposite to the filament growth so that its rupture will be facilitated (small Reset voltage; -1.15 V) in contrast with the case of positive voltage (1.66 V; Joule heating only). However, note that for the first case, the final OFF resistance is the smallest of the modes, showing that a smaller portion of the filament was ruptured. This also explains why, between the two operating modes, $(+,-)$ has the smallest Set voltage (less

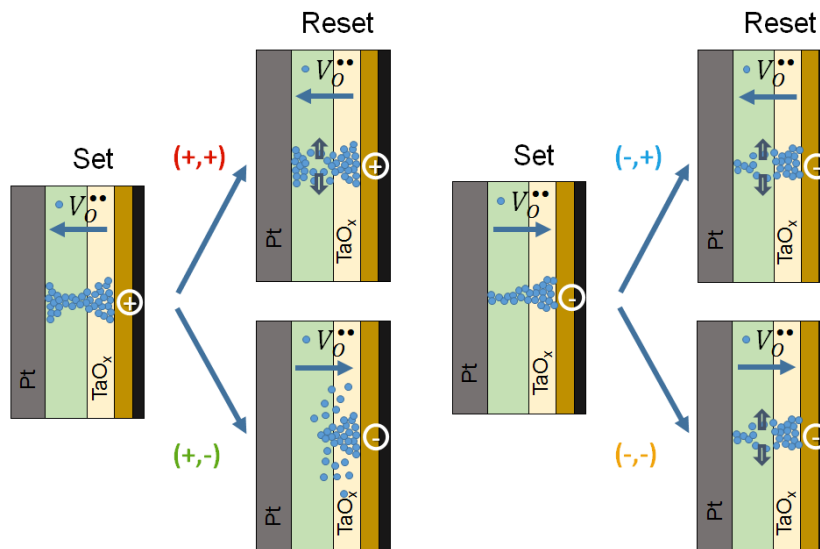


Figure 3.13 – Schematic filament formation and rupture for the four different operation modes (the blue spheres represent the oxygen vacancies with +2 of relative charge, V_o^{**}).

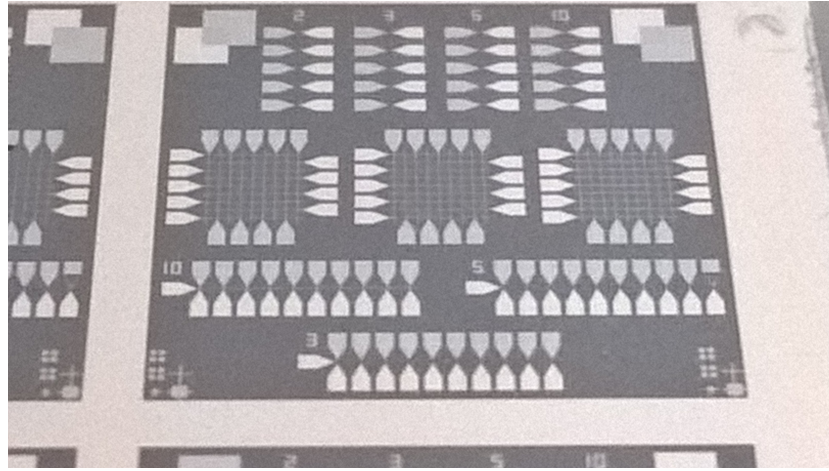


Figure 3.14 – Sample obtained using a two step lithography process, showing individual device areas of 2×2 , 3×3 , 5×5 and $10 \times 10 \mu\text{m}^2$ and 9×9 crossbar networks of $10 \times 10 \mu\text{m}^2$ devices.

filament left to regrow). When applying negative Set voltage [(-,-) and (-,+); right panel], oxygen vacancies are attracted to the anion (Ta) and therefore the growth towards the cathode implies a higher voltage (-5.14 V and -4.17 V, respectively) and the filament has a conical shape. For both Reset polarities a similar amount of voltage is needed, showing that the filament breaks due to Joule heating, even for negative Reset, since the filament is thin.

3.1.3 Resistive Switching in Smaller Areas

Using the Pt/MgO/Ta/Ru stack we defined smaller device areas and crossbar networks using a two step lithography process (Section 2.3.2) as shown in Fig. 3.14. Similarly to the $300 \mu\text{m}$ diameter devices, $10 \times 10 \mu\text{m}^2$ devices start in a high resistance state ($\sim 10^9 \Omega$) and need a forming voltage of 9.6 V to switch to a low resistance state ($\sim 10^2 \Omega$) for the first time [Fig. 3.15(a); step 1]. The device then returns to a high resistance state, lower than the initial ($10^4 \Omega$), at -1.75 V (step

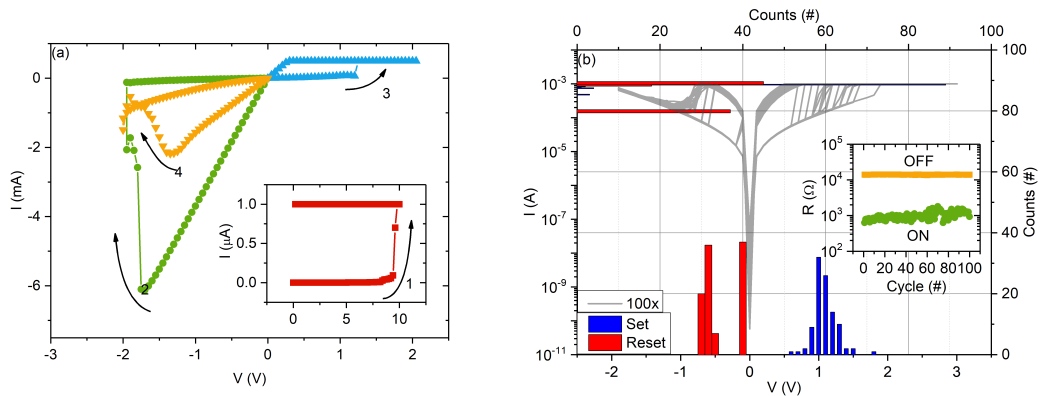


Figure 3.15 – I - V characteristics (a) of a virgin device with an area of $10 \times 10 \mu\text{m}^2$ showing the forming process (inset; step 1) and the following Resets (steps 2 and 4) and Set (step 3), and (b) 100 consecutive cycles. The right (top) axis denotes the voltage (current) distribution. The inset shows the resistance values for ON and OFF states over the cycles.

2) and to the low resistance state at 1.2 V (step 3). A statistical analysis was performed for 100 consecutive voltage sweep cycles, as shown in Fig. 3.15(b). An average resistance ratio of one order of magnitude is achieved ($10^4 \Omega / 10^3 \Omega$), as well as averages of (1.09 ± 0.17) V and (-0.43 ± 0.26) V for Set and Reset voltages, respectively.

Note that all the RS parameters are very similar to the ones of the bigger area. This was expected for the ON resistance, since it does not scale with the area (metallic filament) and comprehensible for the OFF resistance, since the area decrease was not considerable. The same can be assumed for the forming voltage or that the identical value for the two areas meaning an independence of the voltage on the area. Set and Reset voltages are also unchanged between them. We observed resistive switching behavior, however the process needs to be further optimized, to enable measurements of complete crossbar arrays.

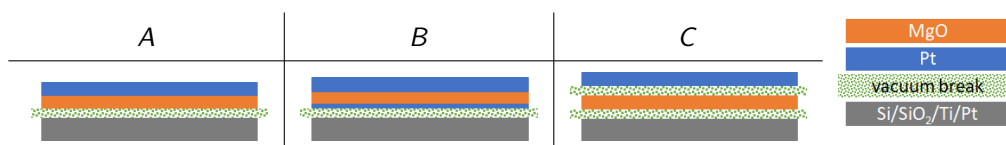
3.2 Influence of Vacuum Break on Resistive Switching

Knowing that the presence of defects influences the resistive switching behavior of metal-insulator-metal structures, we studied three different Pt/MgO interface combinations, using a noble metal (Pt) as both bottom and top electrode. The first combination, *A*, is based on the above discussed structures and consists on the deposition of 30 nm of MgO and 25 nm of Pt on top of pre-deposited Si/SiO₂/Ti/Pt substrates. In the second structure, *B*, there is an intentional vacuum break after the deposition of the MgO layer and right before the Pt top electrode is grown. Finally, we produced a structure, *C*, without interfaces exposed to air, by depositing a 5 nm Pt layer on top of the existing bottom electrode. The remaining stack follows the typical MgO/Pt structure. All these structures were deposited using Ion Beam Deposition (Section 2.1.2.1) and 300 μm circular pillars were defined using a single lithography and physical etch steps (Section 2.3.1). For ease of reading, the structures were labeled according to Table 3.2.

3.2.1 Structural Characterization

As in Section 3.1.1, a XPS analysis was performed (at CQFM) to characterize the influence of the vacuum break on the MgO/Pt interface. Two *A* and *C* thinner samples consisting of MgO (30) / Pt (3) (nm) were prepared. Given the known specificity of XPS to the surface, being able to probe an utmost layer of 10 nm in depth, no Si or Ti from the underneath layers were detected. Figure 3.16 shows the relevant XPS regions of both structures. The XPS spectra show much more Pt for the *A* stack; in other words, the Pt layer is much thicker in the no vacuum break case (~ 22

Table 3.2 – Labels of structures with vacuum breaks at different interfaces.



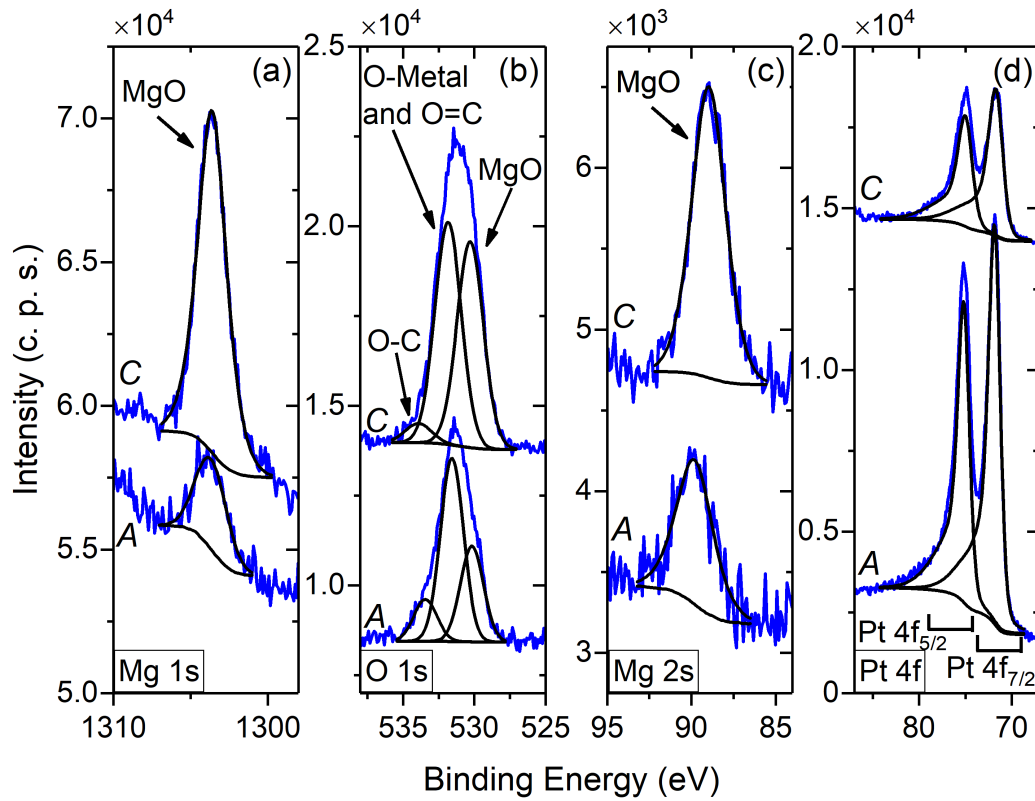


Figure 3.16 – XPS spectra and corresponding fitting of the (a) Mg 1s, (b) O 1s, (c) Mg 2s and (d) Pt 4f regions for two Pt/MgO/Pt (3 nm) samples: without (A) and with (C) top vacuum break. Spectra were vertically offset for clarity purposes.

nm versus ~ 7 nm). Also, an excess of oxygen was detected and quantified (from the O 1s and Mg 2s areas) at the surface, giving an O/Mg atomic ratio of 2.3 for A and 2.0 for C. If the oxygen contribution arose only from the MgO, this value was expected to be equal to 1 (O/Mg atomic ratio). After subtracting the contribution of the carbonaceous contamination (C–O, C=O and/or O–C=O species), the experimental (O–C oxidized)/Mg atomic ratio is 1.6 ± 0.1 for both cases, which is compatible with the existence of OH^- groups replacing O^{2-} at the surface and/or an oxidation of the Pt layer. Furthermore, particularly for C, a model assuming some degree of mixture of the Mg on the Pt layer fits better the experimental results, which indicates the presence of roughness at the interface.

3.2.2 Morphological Characterization

Atomic Force Microscopy (AFM) measurements were performed (at CEMUP) on the Pt/MgO/Pt structures with (C) and without (A) vacuum break before the 30 nm Pt top electrode deposition to infer the possible roughness change due to a vacuum break, as suggested by the XPS analysis. The measurements were performed in the non-contact tapping mode. Figure 3.17 shows the AFM maps of the samples. The roughnesses calculated from the mean square of the pixels height are of 0.66 nm when there is a vacuum break and 0.80 nm when there is no vacuum break. These

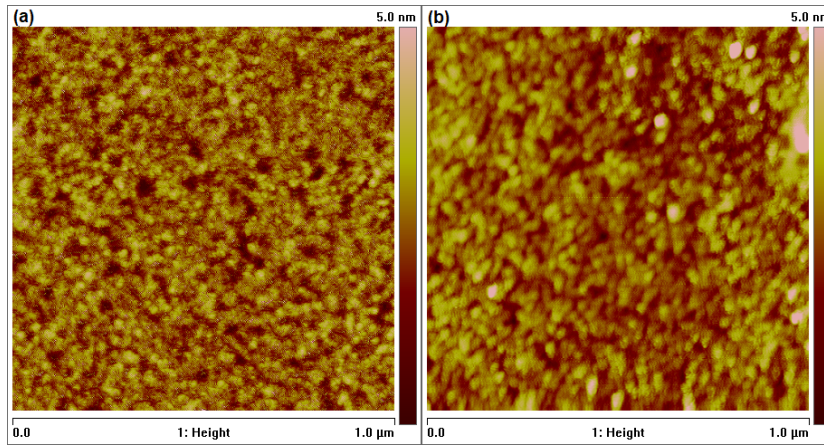


Figure 3.17 – AFM map for a Pt/MgO/Pt structure (a) without (B) and (b) with (C) vacuum break before the top electrode deposition. The height is given by the color bar on the side of the images.

values reveal a very low surface roughness ($< 1\text{ nm}$) in both structures, although no significant difference between the interfaces could be inferred.

3.2.3 Resistive Switching

The devices without a vacuum break before the deposition of the Pt top electrode, A, show unipolar RS without the need of a forming step. They start in a HRS ($\sim 10^5 \Omega$) and switch to a LRS ($\sim 10^1 \Omega$) at around -4.5 V (Set; step 1) [Fig. 3.18(a)]. The HRS ($\sim 10^6 \Omega$) is then recovered at 1.2 V (Reset; step 2). The two following transitions occur around the same voltage values, demonstrating that the first Set did not make any permanent structural changes in the structure and thus, that there was no forming process. Figure 3.18(b) shows 10 consecutive I–V cycles for the (+, -) and (+, +) modes, demonstrating the unipolar behavior of this structure, with no apparent influence of the voltage polarity. The statistical analysis [Fig. 3.18(c)] shows the typical distribution for 93/100 successful cycles, with a good separation between the two resistance states ($10^8 \Omega / 10 \Omega$), and average Set and Reset voltages of $(-5.1 \pm 1.3)\text{ V}$ and $(1.6 \pm 0.6)\text{ V}$ for Set and Reset voltage, respectively.

For the structure without any vacuum break, B, we also observed unipolar RS without a forming step. Starting from an OFF state of around $10^8 \Omega$, the Set transition occurs under a voltage of 6.8 V (step 1) to an ON state of around $10^2 \Omega$, as shown in Fig. 3.19(a). The Reset transition to the OFF state ($10^8 \Omega$) then occurs at -3.8 V (step 2). As the following Set voltages are similar to the first one, we again conclude that there is no forming process in these structures. Figure 3.19(b) shows two consecutive complete cycles in the (-, +) operation mode, revealing the unipolar behavior of this structure and similar voltage amplitudes for each step at opposite polarities. Both operating voltages and resistance values are similar to the ones involved in the resistive switching of structure A.

In the case of the devices with a vacuum break at both interfaces, C, a forming voltage of 14.6 V (step 1) is necessary to switch the device from the initial HRS ($10^{10} \Omega$) to the LRS ($10^2 \Omega$) for

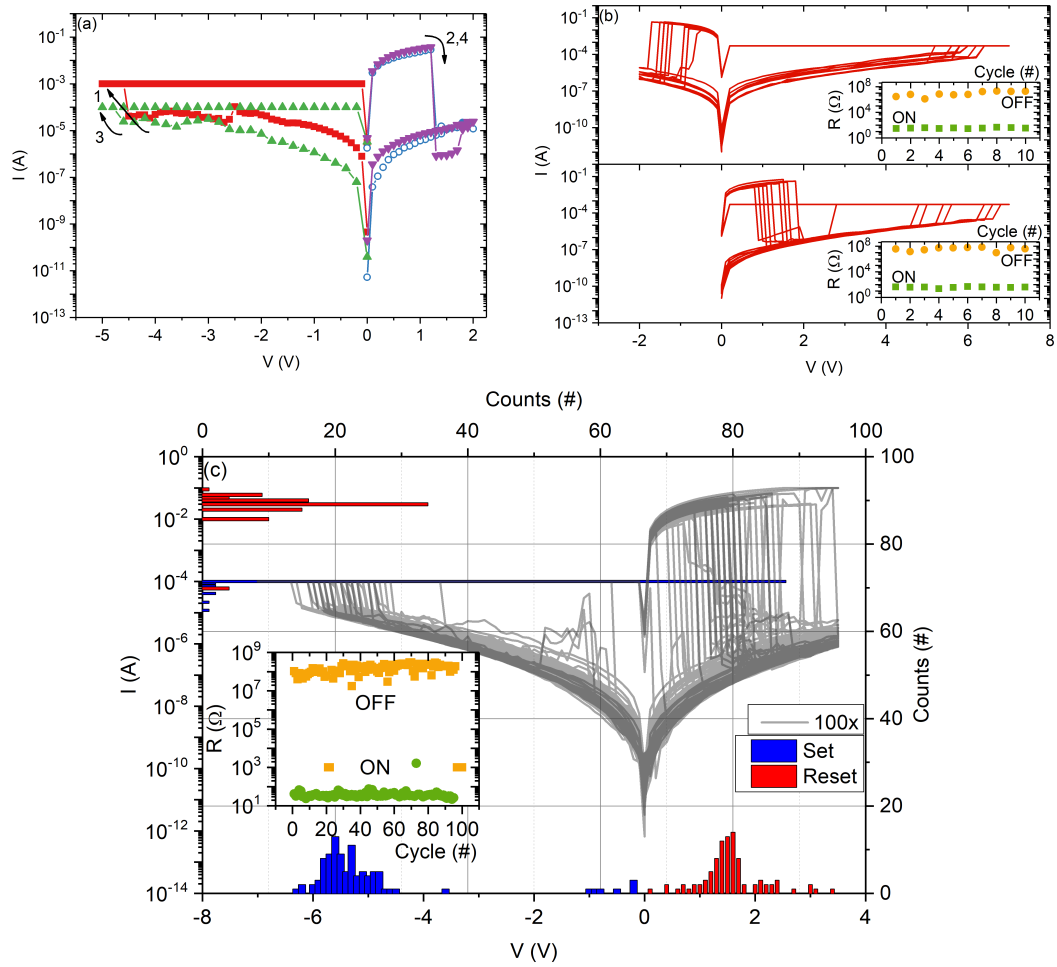


Figure 3.18 – Pt/MgO/Pt structure A. I – V characteristics (a) of a pristine device showing the first Set (step 1) and the following switchings between the two resistance states (steps 2-4) in the (+,-) operation mode, and (b) showing 10 seeping cycles for the (+,-) (top) and (+,+) (bottom) switching modes. (c) I – V characteristics for the (-,+) mode. The right (top) axis denotes the voltage (current) distribution. The inset shows the resistance values over the cycles.

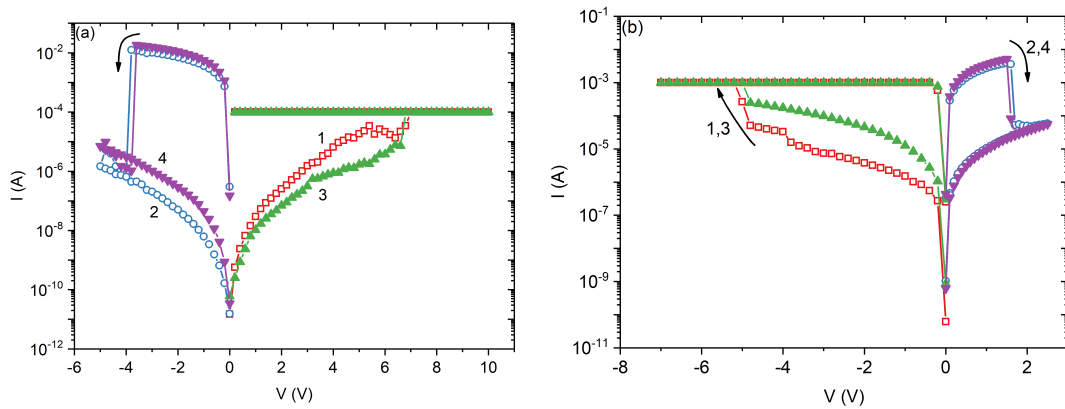


Figure 3.19 – Pt/MgO/Pt structure B. I – V characteristics (a) of a pristine device showing the first Set (step 1) and the following switchings between the two resistance states (steps 2-4) in the (+,-) operation mode, and (b) two consecutive cycles in the (-,+) operation mode.

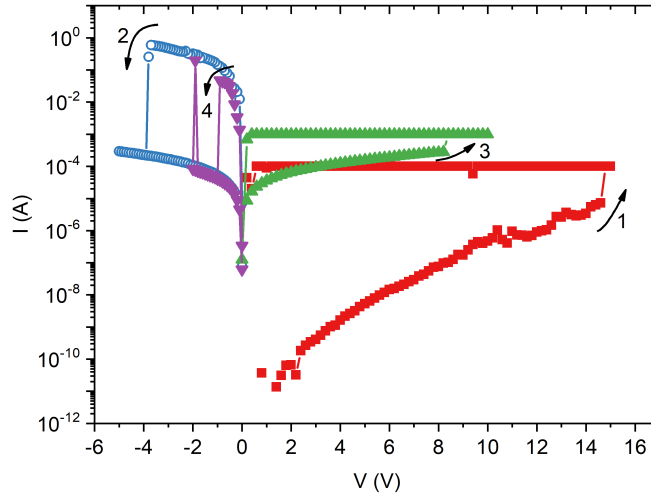


Figure 3.20 – Pt/MgO/Pt structure C. *I–V* characteristics of a pristine device showing the forming process (step 1), the respective Reset (step 2) and the following switchings between the two resistance states in the (+,-) mode, steps 3 and 4, respectively.

the first time [Fig. 3.20]. The Reset then occurs around -3.7 V (step 2), putting the device again in a HRS ($10^4 \Omega$), which is lower than the pristine resistance due to the structural changes that happened during forming. The following Set (8.2 V; step 3) and Reset (-0.9 V; step 4) occur at voltages similar to the ones of the structures above.

3.2.4 Discussion

Table 3.3 shows the resistive switching parameters of the three structures. Note that the structure with the largest initial resistance ($10^{10} \Omega$) is the one with a vacuum break after the MgO layer deposition (sample C), indicating a possible contamination (e.g. oxygen) that resulted in the increase of the oxide resistance. Considering that the structure without vacuum breaks (B) better represents the intrinsic MgO layer resistance ($10^8 \Omega$), for negligible Pt resistivity, it seems that the contamination at the bottom Pt/MgO (e.g. carbon) may have decrease the initial resistance ($10^7 \Omega$). This high initial resistance explains the need for a forming voltage only for structure C and, consequently, the permanent and abrupt structural change occurring at high energy that resulted

Table 3.3 – Resistive switching parameters resume for the three structures with vacuum breaks at different interfaces.

Stack	$R_{initial}$ (Ω)	$V_{Forming}$ (V)	V_{Set} (V)	V_{Reset} (V)	R_{ON} (Ω)	R_{OFF} (Ω)
A	10^7	–	5.1	1.6	10	10^8
B	10^8	–	6.7	3.7	10^2	10^8
C	10^{10}	14.6	8.2	3.7	10^2	10^4

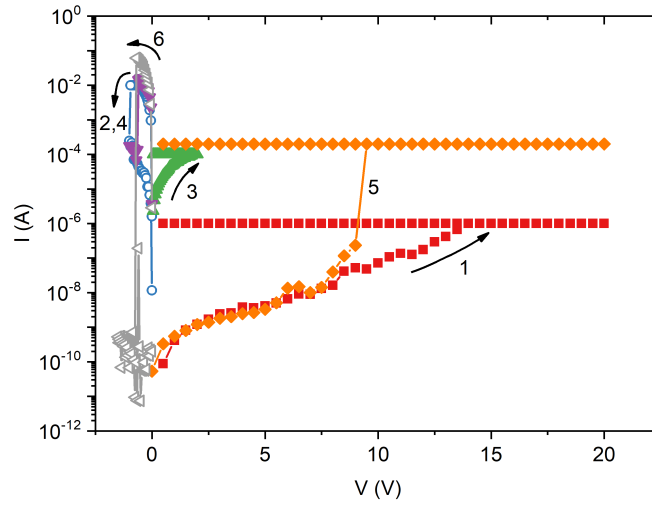


Figure 3.21 – I – V characteristics of a Pt/MgO/Al/Ru device showing the first Set and Reset steps.

in the lowest OFF resistance of the three structures ($10^4 \Omega$ versus $10^8 \Omega$). Regarding the Set voltage, *A* and *B* have similar values, whereas the value for *C* is slightly larger. The explanation for this must involve the contamination at the bottom electrode, since it is the differentiating factor between the two groups. Possibly, some contaminants at the bottom Pt/MgO interface increase the threshold energy needed to grow the conductive filament. From the values of the Reset voltage and the ON resistance, we observe that the Reset power is the same for both structures *B* and *C* (~ 0.14 W).

3.3 Influence of Top Electrodes on Resistive Switching

Different materials (Al, Ag, Cu) were studied to replace Ta (same thickness) as top electrode and to analyze the influence of the insulator/metal interface on the MgO RS behavior. To complete the stack and prevent oxidation, a 5 nm Ru layer was subsequently deposited on top. The MgO and Ag layers were deposited using magnetron sputtering (Sections 2.1.1.1 and 2.1.1.2), while Al, Cu and Ru were deposited by Ion Beam Deposition (Sections 2.1.2.1 and 2.2.2.1). Note that for the samples with Ag and Al there was a vacuum break before and after the top contact (Ru) deposition. Therefore, before Ru deposition there was a soft etch step (Section 2.2.2.1) to remove any residual oxide at the surface of the top electrode.

Figure 3.21 shows the electrical characterization of the Pt/MgO/Al structure. The devices start in a high resistance state ($\sim 10^8 \Omega$) and switch to a low resistance state ($\sim 10 \Omega$) at around 13.5 V (step 1) under a current compliance of 1 μ A. The new high resistance state ($\sim 10^4 \Omega$) is achieved at -0.7 V (step 2). The following cycle with a Set at a current compliance of 0.1 mA (step 3) also results in a OFF state of $\sim 10^4 \Omega$ at -0.6 V (step 4). However, when the compliance is increased for 0.2 mA (step 5), the next OFF state has a considerably higher resistance, similar

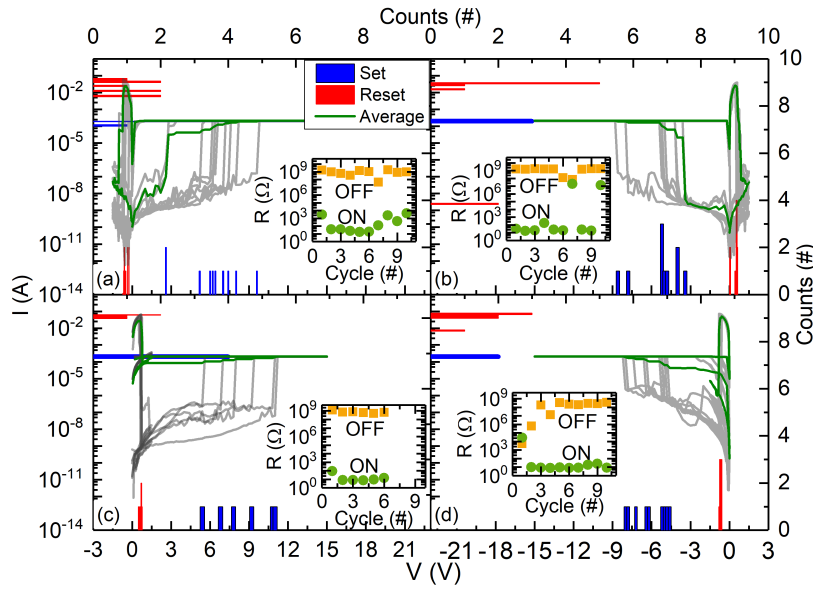


Figure 3.22 – I – V characteristics for the four voltage polarity combinations with Al electrodes, each over 10 cycles: (a) (+,-), (b) (-,+), (c) (-,+) and (d) (-,-). The right (top) axis denotes the voltage (current) distribution. The insets show the resistance values over the cycles.

to the pristine value ($\sim 10^9 \Omega$). This may be justified by the higher current resulting in a stronger filament that easily overheats during the Reset process and completely breaks it, originating a very large OFF resistance. We do not consider the first Set step as an electroforming process, since the amplitude of the following operating voltages, within a certain variability, falls into the same values. The statistical study of the unipolar RS in the four operation modes, each over 10 sweeping cycles, is shown in Fig. 3.22. Unlike the Pt/MgO/Ta/Ru stack, there seems to be no influence of the operation mode on the RS behavior. The voltage sweeps were performed in the ranges $0 \text{ V} \rightarrow 15 \text{ (-15) V} \rightarrow 0 \text{ V}$ for Set and $0 \text{ V} \rightarrow 1.5 \text{ (-1.5) V} \rightarrow 0 \text{ V}$ for Reset, with a voltage step of 0.2 and 0.05 V, respectively, imposing a current compliance of 0.2 mA during Set.

The Pt/MgO/Cu/Ru structure also shows unipolar RS behavior, starting in a HRS ($\sim 10^9 \Omega$) and switching to a LRS ($\sim 10 \Omega$), without the need of a forming step at 8 V (step 1), as seen in Fig. 3.23(a). The switching back to the HRS ($\sim 10^9 \Omega$) occurs at -1.3 V (step 2). A comparable negative voltage (-9.2 V; step 3) is also able to induce Set, followed by a negative Reset around the same value (-0.95 V; step 4) for a different device. The variability involved in the switching parameters over 50 cycles is shown in Fig. 3.23(b) for the (+,-) mode. The Reset voltage has a high variability, as well as the ON ($\sim 10 \Omega$) and OFF ($\sim 10^9 \Omega$) resistances, almost overlapping for some cycles.

When using Ag as top electrode, the behavior is completely different. The resistive switching in these structures is bipolar, starting in a comparatively lower OFF state ($\sim 10^5 \Omega$) and switching to the ON state ($\sim 10 \Omega$) only at positive voltages [3.8 V, step 1; Fig. 3.24(a)]. The Reset back to the OFF state occurs at -0.75 V (step 2). The amplitude of the voltages involved is also much smaller, as it is typical for bipolar RS. However, the device endurance is not very high, as can be seen in the insets of Fig. 3.24(a). Nevertheless, the study over time of the resistance states showed

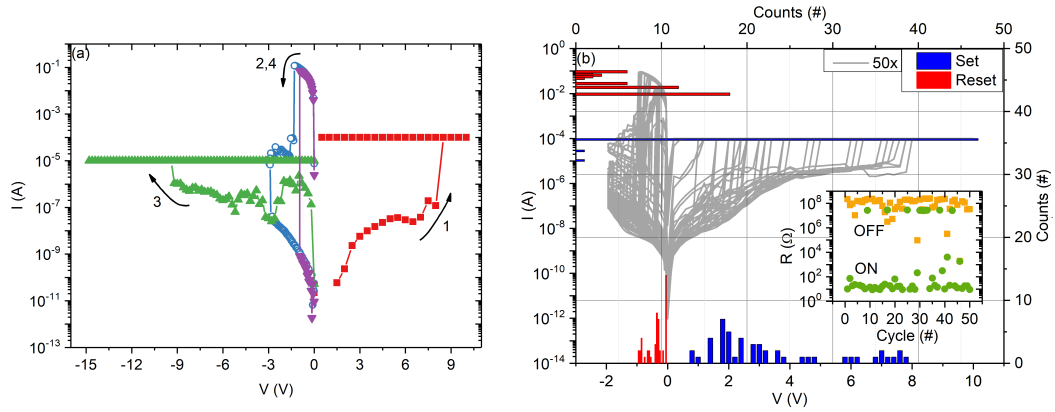


Figure 3.23 – (a) I – V characteristics of a Pt/MgO/Cu/Ru pristine device showing the first Set and Reset steps for two different devices (1, 2 and 3,4). (b) I – V characteristics for the (+,-) mode. The right (top) axis denotes the voltage (current) distribution. The inset shows the resistance values over the cycles.

stability up to 10^4 s under a reading voltage of 1 mV, as shown in Fig. 3.24(b). Zhang *et al.* studied a similar stack with a thicker (70 nm) Ag layer and obtained a volatile resistive switching behavior that was used to mimic synaptic plasticity [185].

3.3.1 Discussion

The parameters involved in the resistive switching of the different structures are shown in Table 3.4. Interestingly, although Cu and Al are reactive and mobile metals as Ag, the RS in the former remains unipolar. This suggests that the oxide formed at the MgO/metal interface is crucial for the phenomenon. This may also explain the difference in the initial resistance ($10^8 \Omega$ and $10^9 \Omega$ versus $10^5 \Omega$). Moreover, they were deposited by a less energetic method than Ag (IBD versus sputtering). For the case of Ag, only bipolar behavior was observed, suggesting a different RS mechanism, originating in the diffusion of Ag^+ ions inside the MgO matrix. The resistance ratio is also smaller (4 orders of magnitude versus 7) as it is typical of the bipolar behavior. Note

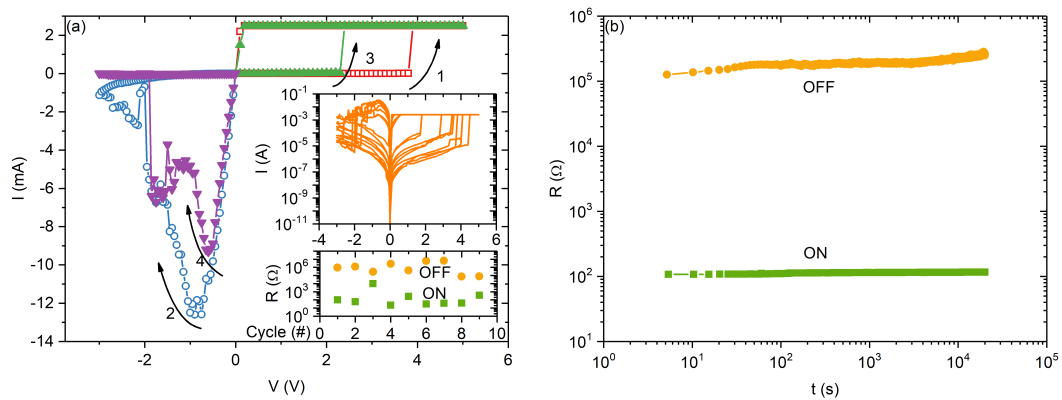


Figure 3.24 – (a) I – V characteristics of a Pt/MgO/Ag/Ru pristine device showing the first Set and Reset steps. The top inset shows I – V characteristics over 9 consecutive sweeping cycles and the bottom inset the corresponding resistance states. (b) Retention time for the OFF and ON resistance states up to 10^4 s, measured with 1 mV every 5 s.

Table 3.4 – Resistive switching parameters resume for the three structures with different top electrodes.

Top Electrode	Resistive Switching	$R_{initial}$ (Ω)	$V_{Forming}$ (V)	V_{Set} (V)	V_{Reset} (V)	R_{ON} (Ω)	R_{OFF} (Ω)
Al	unipolar	10^8	–	6.1	0.5	10	10^8
Cu		10^9		3.4	0.4	10	10^8
Ag	bipolar	10^5		3.4	1.2	10	10^5

that although the Reset voltage is higher for Ag, the Reset power involved is considerably lower (~ 100 mW versus ~ 1 mW), since the Reset current is smaller (~ 10 mA versus ~ 100 mA). Furthermore, the higher Set voltage observed for the Al top electrode may be explained by a lower carrier mobility.

3.4 Resistive Switching in Al_2O_3 /MgO Double Layer

Double layer structures of MgO/ Al_2O_3 were investigated with the aim of reducing the device variability comparatively to a MgO single layer, if the random formation and rupture of conducting filaments is limited within the Al_2O_3 film [186]. Furthermore, the Al_2O_3 layer will increase the resistance and prevent the permanent break-down of devices [187]. Al_2O_3 was adopted because of its CMOS compatibility, high break-down voltage and easy formation of a stable oxide thin film at low temperatures [188]. It is a material increasingly studied in double layer ReRAMs for showing improved properties together with TiO_2 [189, 190, 187, 191, 192, 193], HfO_2 [186, 187, 191, 194, 195], NbO [196] and itself [197]. Stathopoulos *et al.* tested different double layers with fixed TiO_2 and observed a better performance with Al_2O_3 [192]. Furthermore, its resistive switching behavior in single layer devices was also already reported [198, 199, 200]. Several other works report performance improvements with different double oxide layers [201, 202, 203, 204, 205, 206, 207].

Aiming to study the influences of the Al_2O_3 layer on the resistive switching behavior, structures with different Al_2O_3 thicknesses (0.5, 1, 2, 5 and 10 nm) for a fixed MgO thickness of 30 nm were fabricated. The samples were deposited using Ion Beam Deposition (Section 2.1.2.1) and 300 μ m circular pillars were defined using a single lithography and physical etch steps (Section 2.3.1). Platinum (150 nm) was used as bottom electrode and Tantalum (25 nm) as top. The thin films were deposited subsequently, without vacuum break, ensuring better adhesion and interfaces quality. Note that, as we verified, if there is a vacuum break between the deposition of the two oxides during deposition no reliable resistive switching behavior is observed for any of the thicknesses.

3.4.1 Structural Characterization

Transmission Electro Microscopy (TEM) analysis were performed at the International Iberian Nanotechnology Laboratory (INL). The lamellas for TEM/STEM analysis were prepared using a Helios

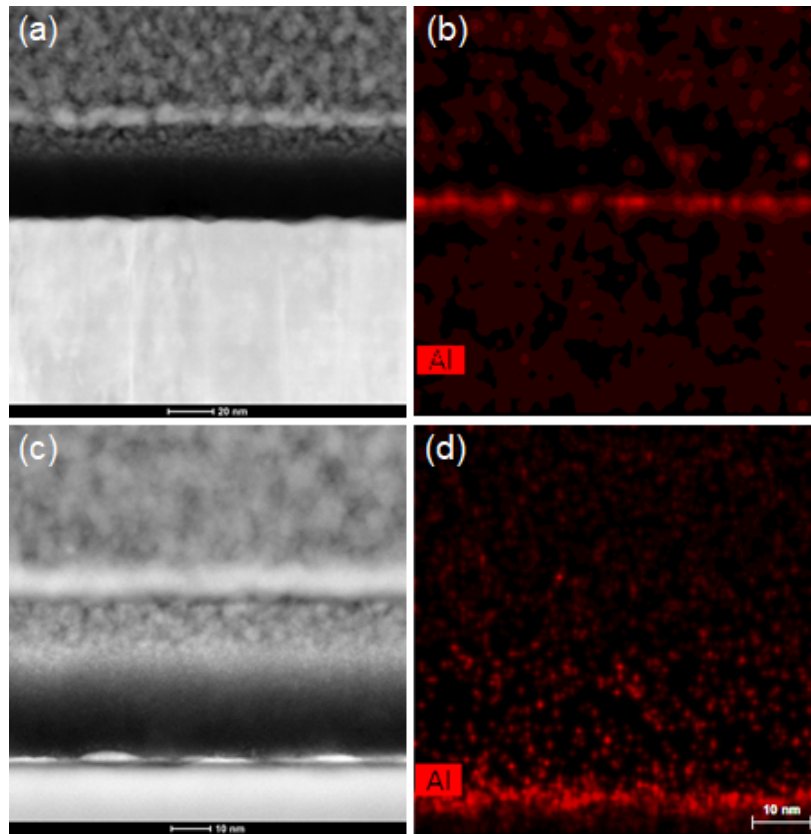


Figure 3.25 – (a) HAADF and (b) STEM EDX images of the double layer structures with 0.5 nm Al_2O_3 thickness, and (c) and (d) with 1 nm.

NanoLab 450S dual beam Focused Ion Beam (FIB) instrument. The TEM/STEM analysis of the FIB-lamellas was carried out with a Titan Themis double Cs corrected microscope (HV-200 kV), equipped with a Super-X EDX System for the chemical analysis.

The high resolution HAADF analysis for the structures with 5 and 1 nm of Al_2O_3 reveals a rough Pt surface at the interface with the Al_2O_3 layer, see Figs. 3.25(a) and (c), respectively. The STEM EDX maps showing Al K indicate some discontinuity in the 0.5 nm Al_2O_3 present between Pt and MgO [Fig. 3.25(b)] and a continuous (or nearly continuous) layer for 1 nm of Al_2O_3 [Fig. 3.25(d)].

3.4.2 Resistive Switching

As shown in Section 3.1, the single layer MgO structure shows unipolar resistive switching. Here, for a single 30 nm MgO layer deposited using Ion Beam Deposition and a vacuum break before Ta deposition, the devices start in a HRS ($\sim 10^8 \Omega$) and need a forming step of around 3.2 V (step 1) to switch to the LRS ($\sim 10^3 \Omega$), as shown in Fig. 3.26(a). A negative voltage of -2 V (step 2) takes it back to the HRS ($\sim 10^5 \Omega$). The following complete cycle has Set and Reset voltages of 1 V (step 3) and -0.3 V (step 4), respectively, and occurs between $\sim 10^3 \Omega$ (ON) and $\sim 10^4 \Omega$ (OFF) resistance states. These small operation voltages and OFF/ON resistance ratio are typical of bipolar RS, suggesting this behavior from the structure. The operation in the pulsed mode is

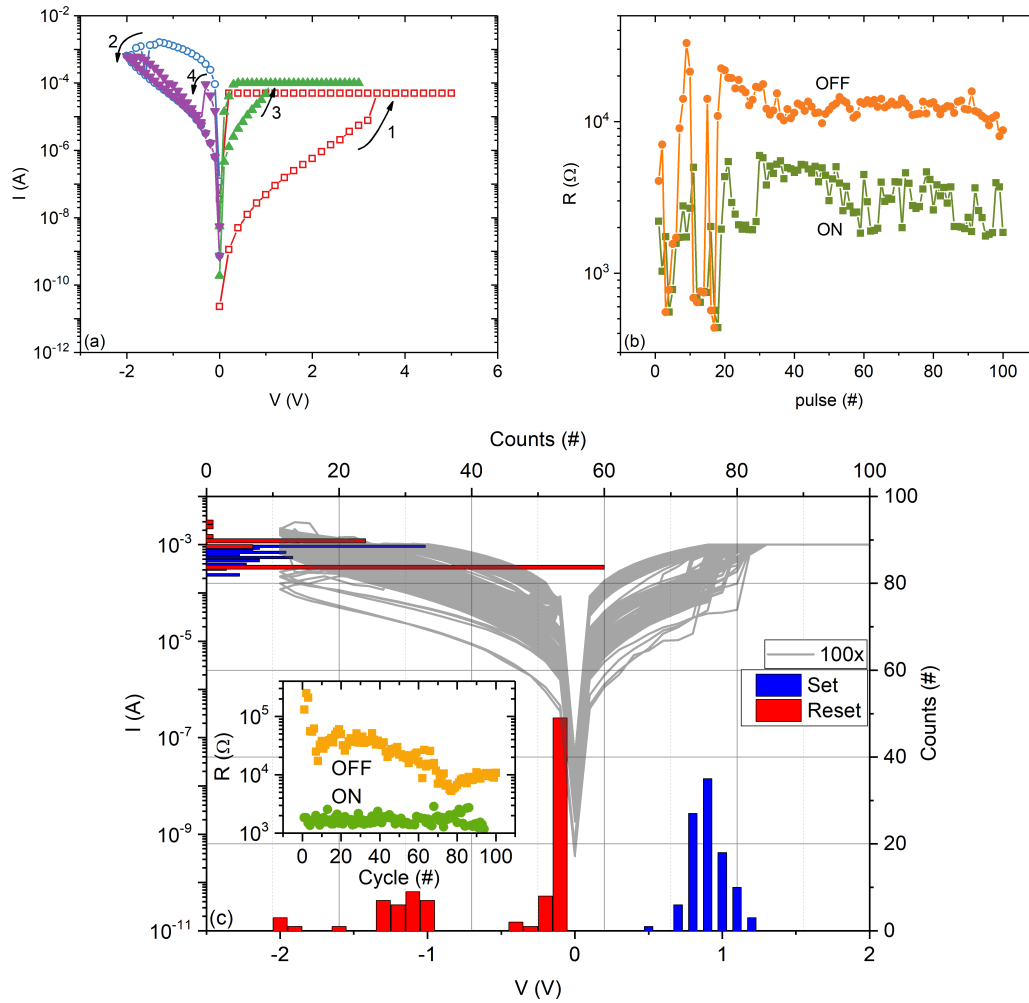


Figure 3.26 – I – V characteristics of a Pt/MgO/Ta pristine device showing forming (step 1) and first Reset (step 2) and Set (Step 3). (b) Resistance states over 100 pulses ($V_{\text{Set}} = 2$ V, $I_C = 1$ mA, $V_{\text{Reset}} = -2$ V, $t_{\text{pulse}} = 0.5$ s). (c) I – V characteristics for the (+,-) mode over 100 cycles. The right (top) axis denotes the voltage (current) distribution. The inset shows the resistance values over the cycles.

not successful for the first 20 pulses, specially for the OFF state, but then the device converges to $\sim 10^3 \Omega$ for ON and $\sim 10^4 \Omega$ for OFF for the remaining 80 pulses [Fig. 3.26(b)]. Figure 3.26(c) shows the device performance over 100 sweep cycles, with 94 successful switchings for average values of (0.9 ± 0.1) V for Set voltage and (-0.5 ± 0.6) V for Reset. Note that the device eventually fails due to the decrease of the OFF resistance (close to the ON resistance).

When introducing the Al_2O_3 layer, initially, all devices also start in a high resistance state, with no dependence on the Al_2O_3 layer for this small range, except for the 10 nm stack that shows an increase in the resistance (Fig. 3.27). Furthermore, if the initial resistance is higher than $5 \times 10^8 \Omega$, the device will probably not show resistive switching. Therefore, the sample with 10 nm of Al_2O_3 does not show reliable switching due to the too thick insulating layer.

For a thin layer (0.5 nm) of Al_2O_3 , the devices start in the OFF state ($\sim 10^6 \Omega$) and switch to the ON state ($\sim 10^1 \Omega$) under a voltage of 11.5 V (step 1) [Fig. 3.28(a)]. The same magnitude OFF state is recovered for -0.5 V (step 2). We conclude that there is no forming process both since

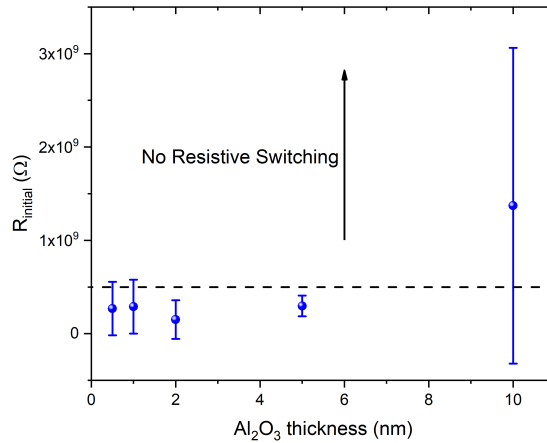


Figure 3.27 – Initial resistance for the double layer structures as a function of Al_2O_3 thickness.

the OFF state is the same after the first cycle and the Set voltage at the third cycle (step 5) has a similar value as the first one. The inset of Fig. 3.28(a) shows the unipolar behavior of the structure, as, in a different device, the first Set occurs at -8 V (step 1) and the Reset also at -0.5 V (step 2). Applying positive voltage for the following Set (9 V; step 3) no evident differences were observed.

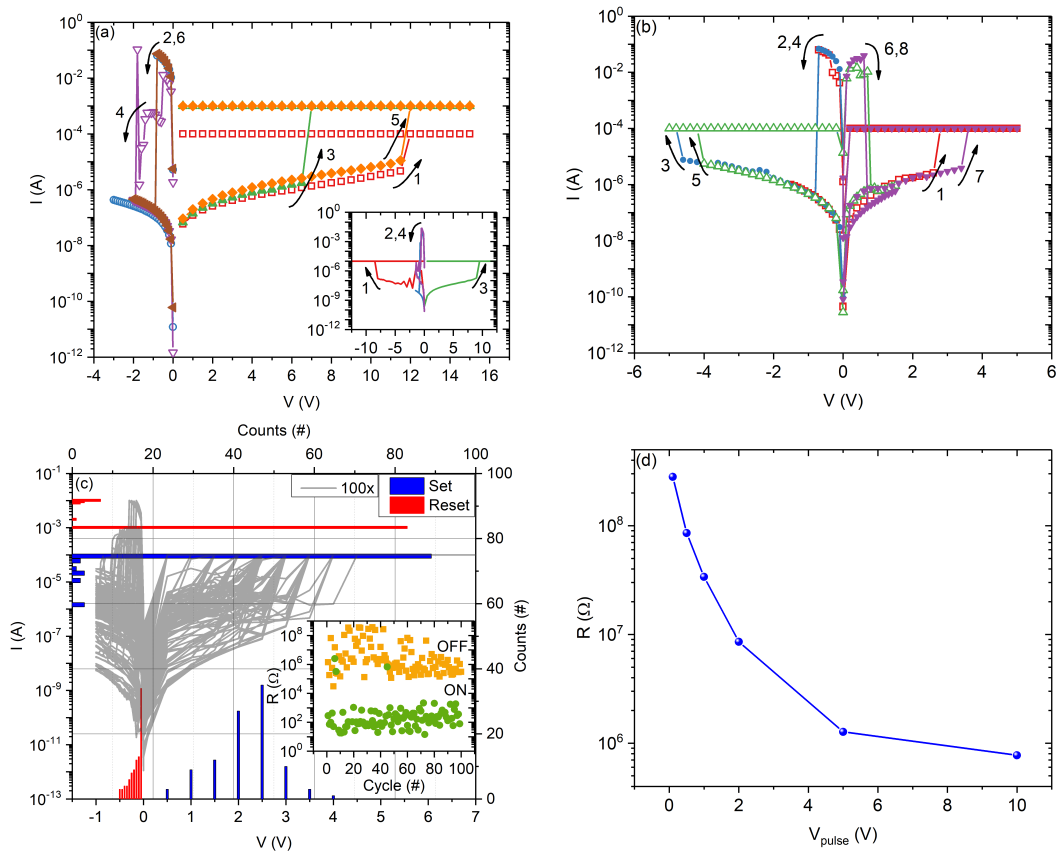


Figure 3.28 – I – V characteristics for 0.5 nm of Al_2O_3 . (a) In the pristine state (the inset shows a different device) and (b) for the four polarity modes. (c) I – V characteristics for the (+, -) mode over 100 voltage sweep cycles. The right (top) axis denotes the voltage (current) distribution. The inset shows the resistance values over the cycles. (d) Evolution of the resistance under incremental voltage pulses (the line is a guide to the eye).

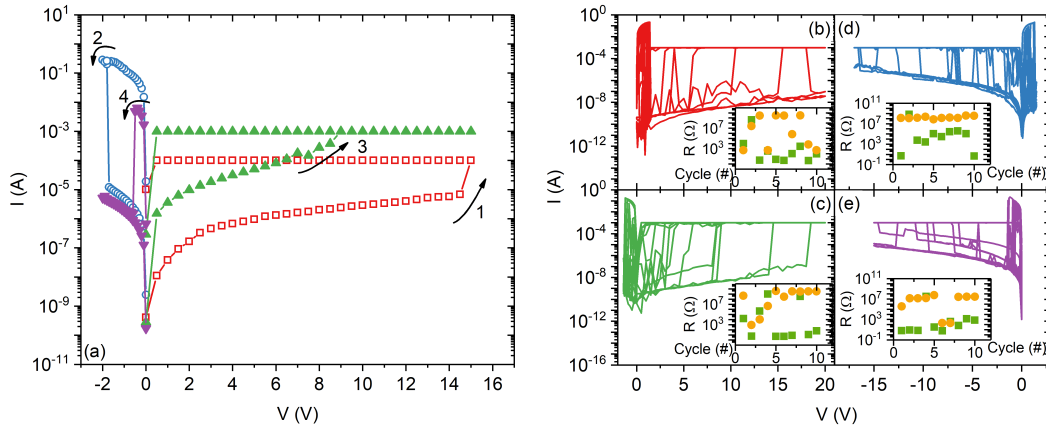


Figure 3.29 – (a) Initial I – V characteristics and for the four voltage polarity combinations over 10 cycles: (b) (+,+), (c) (+,-), (d) (-,+) and (e) (-,-) for 1 nm of Al_2O_3 . The insets show the resistance states over the cycles.

The four polarity operation modes were observed and are shown in Fig. 3.28(b): (+,-) steps 1 and 2; (-,-) steps 3 and 4; (-,+) steps 5 and 6; (+,+) steps 7 and 8. The statistical analysis of the (+,-) mode distribution gives 96/100 successful switchings [Fig. 3.28(c)] and shows a large variability of the Set voltage [(2.2 ± 0.7) V] and both resistance states, specially at the OFF state ($\sim 10^4 \Omega$ - $10^8 \Omega$ / $10^2 \Omega$). Studies under pulsed mode revealed the possibility to obtain an incremental OFF resistance decrease by incrementally increasing the positive voltage amplitude. The resulting resistance after each voltage pulse is shown in Fig. 3.28(d). Note that if more pulses are applied at each voltage increment no resistance changes are observed, which means that only one pulse (the first) is responsible for this change. The pulse duration is around the SourceMeter temporal resolution (~ 200 ms).

As shown in Fig. 3.29(a), for 1 nm of Al_2O_3 the device starts in a HRS ($\sim 10^8 \Omega$) and needs a voltage of around 14.5 V (step 1) to switch to a LRS (10Ω). The OFF state ($\sim 10^5 \Omega$) is recovered at -1.8 V (step 2) and the following complete Set and Reset cycle at 9 V (step 3) and -0.5 V (step 4), respectively. The four polarity modes are observed, showing the unipolar behavior of the structure, although with poor reliability and very high Set voltages in all modes [Fig. 3.29(b)-(e)]. The resistance states are similar for the four cases, keeping a separation ratio of 6 orders of magnitude [$\sim 10^7$ - $10^8 \Omega$ / ~ 10 - $10^2 \Omega$]. Furthermore, as the OFF state magnitude is comparable with the pristine state and the first Set value is within the statistical distribution, we conclude that there was no forming process.

The unipolar RS continues to be observed for 2 nm of Al_2O_3 , as shown in Fig. 3.30. The initial high resistance ($\sim 10^6 \Omega$) switches to a low resistance (54Ω) at 5.3 V (step 1) and is recovered at 1.8 V (step 2). As the next complete cycle has very similar values (5 V, step 3; 1.7 V, step 4), we conclude that no forming process is needed for this structure. The statistical analysis of the four modes each over 100 cycles shown in Fig. 3.31 shows Set and Reset voltages (~ 6 V and 1.5 V, respectively) independent of the operation mode, as well as well separated ON ($\sim 10^1 \Omega$) and OFF ($\sim 10^8 \Omega$) resistances. Regarding the distributions, no particular dependence is observed.

For 5 nm of Al_2O_3 , the initial resistance is around $10^8 \Omega$, switches to the LRS ($\sim 10^2 \Omega$) at 6 V

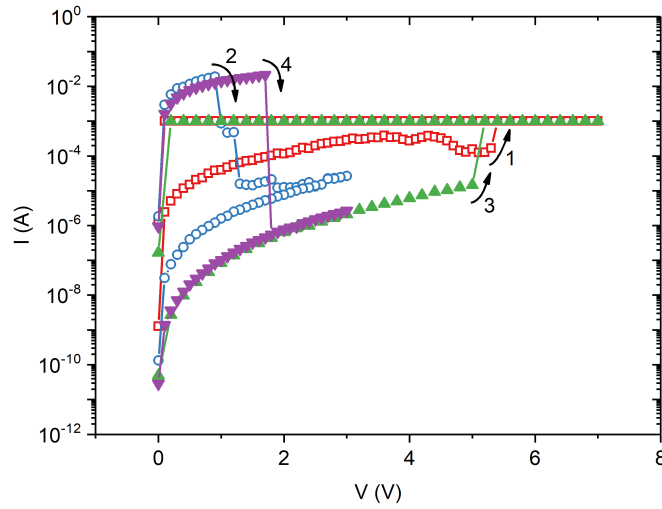


Figure 3.30 – I – V characteristics for 2 nm of Al_2O_3 pristine state showing the forming process (step 1) and the switchings between the two resistance states (steps 2-4) in the (+,+) operation mode.

(step 1) and back to the same HRS at -3 V (step 2), as shown in Fig. 3.32(a). No forming process was needed, as confirmed by the second Set step (step 3). The unipolar behavior of the device is stated by the negative Set (-9.8 V; step 5) in the following cycle, with the corresponding Reset (-3.6 V; step 6). However, the attempts to perform Reset with positive polarity on the top electrode are not successful. In other words, the behavior is unipolar but only with two feasible operation modes [(+,-) and (-,-)], since for positive Reset the process is incomplete and the OFF state is not recovered. As shown in Fig. 3.32(b), the (+,-) and (-,-) modes are complete, but in the (+,+) mode

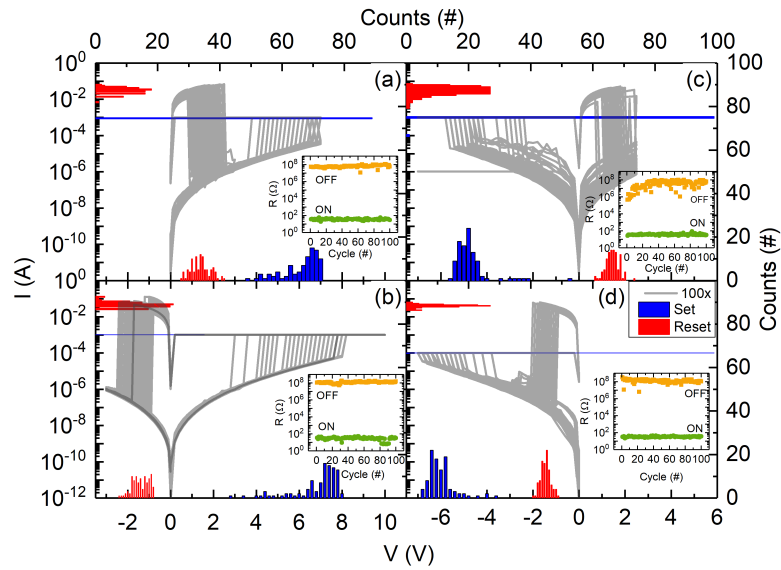


Figure 3.31 – I – V characteristics for 2 nm of Al_2O_3 over 100 cycles for the four voltage polarity combinations: (a) (+,+), (b) (+,-), (c) (-,+), and (d) (-,-). The right (top) axis denotes the voltage (current) distribution. The insets show the resistance values over the cycles.

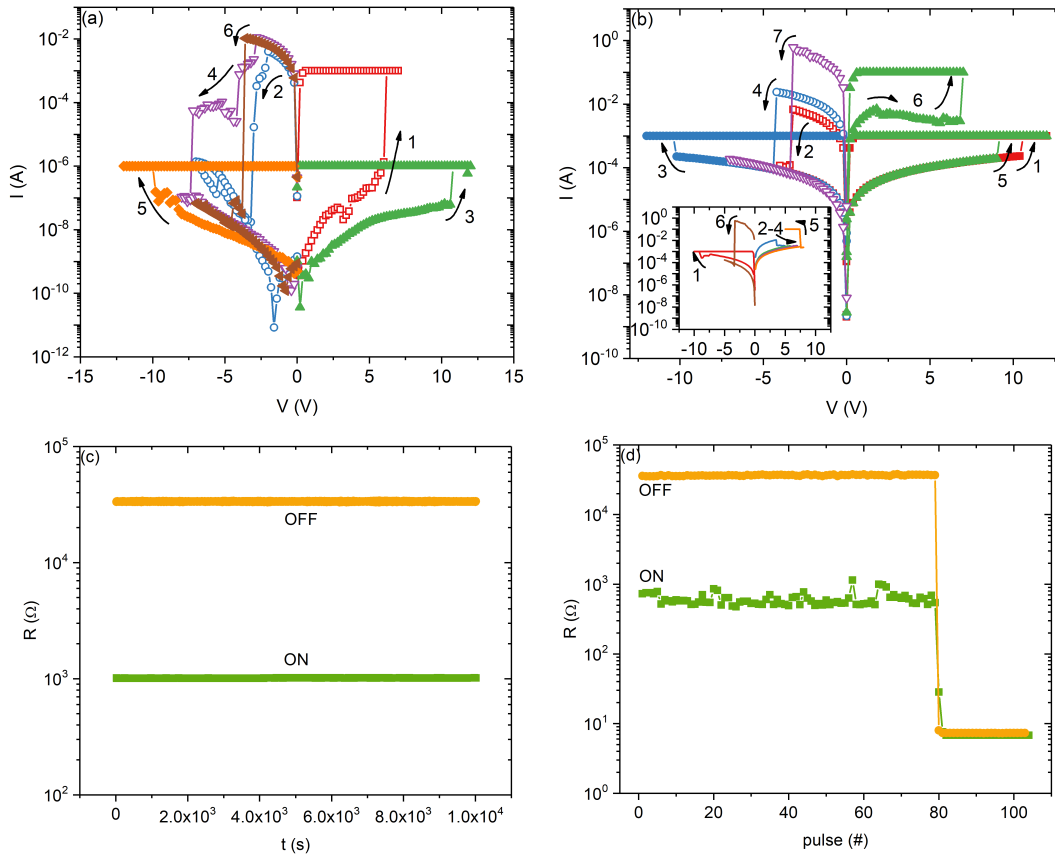


Figure 3.32 – I – V characteristics for 5 nm of Al_2O_3 (a) in the pristine state (step 1) and unipolar behavior: mode (+,-) steps 3 and 4 and mode (-,-) steps 5 and 6. (b) I – V showing complete (+,-) and (-,-) modes (steps 1-2 and 3-4, respectively), incomplete (+,+) mode (steps 5-6) and final negative Reset (step 7). The inset shows an incomplete (-,+) mode for a different device. (c) Retention time for the OFF and ON resistance states up to 10^4 s, measured with 1 mV every 5 s and (d) resistance states separation under pulsed operation mode ($V_{\text{Set}} = 10$ V, $I_C = 1$ mA, $V_{\text{Reset}} = -5$ V, $t_{\text{Set}} = 200$ ms, $t_{\text{Reset}} = 500$ ms and $V_{\text{read}} = 1$ mV).

mode, after the Set (step 5), the supposed Reset cycle ends being a Set (step 6) at high current (100 mA), which results in a lower ON state ($10^2 \Omega$ instead of $10^3 \Omega$). The same is shown in the inset of Fig. 3.32(b) for another device, when the voltage is increased to force Reset (steps 2-4) and the Set value is reached, the device switches to the LRS (step 5). Therefore, positive Reset switchings are not practicable, since Set can occur instead although without a current compliance and the device becomes permanently damaged. The retention study showed resistance states with a well defined separation ($10^4 \Omega / 10^3 \Omega$) up to 10^4 s [Fig. 3.32(c)] and the pulsed operation mode was successful for the same two states up to a maximum of 80 pulses [Fig. 3.32(d)]. The statistical study of the two modes (Fig. 3.33) shows no evident difference between them, both operating between $10^2 \Omega$ and $10^4 \Omega$. For the (+,-) mode [Fig. 3.33(a)] we obtained average values of (8 ± 2) V for Set voltage and (-2.3 ± 0.6) V for Reset, and (-9 ± 4) V and (-4 ± 1) V for the (-,-) mode [Fig. 3.33(b)].

We further observed that for this structure (sometimes) the Reset switching is not abrupt. As seen in Fig. 3.34(a), these gradual Resets can even be smooth (step 2) or by steps (step 4). To study this effect, we did the Reset using incremental cycles as shown in Fig. 3.34(b) to obtain

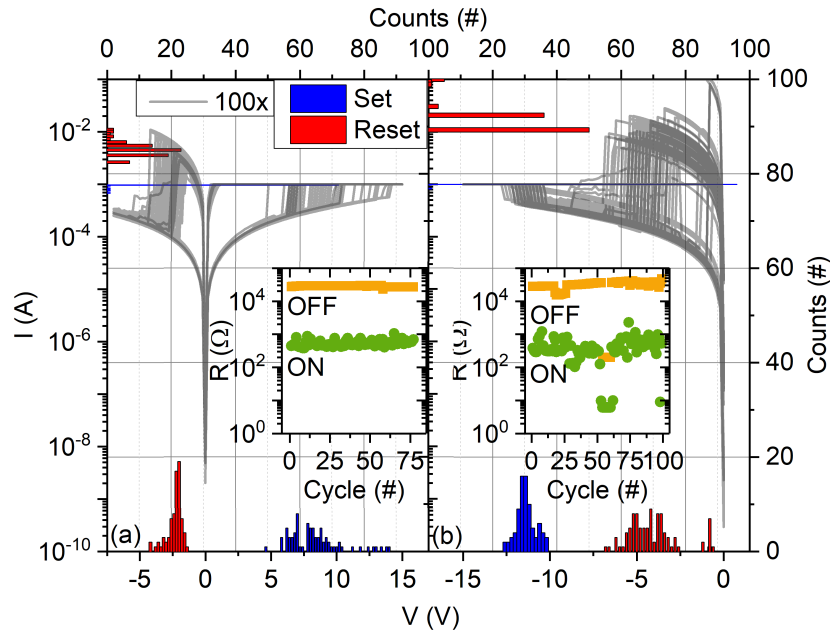


Figure 3.33 – I – V characteristics for 5 nm of Al_2O_3 for the two voltage polarity combinations over 100 cycles: (a) (+,-) and (b) (-,-). The right (top) axis denotes the voltage (current) distribution. The insets show the resistance values over the cycles.

the intermediate resistance values at the end of each cycle [inset of Fig. 3.34(b)]. The resistance levels averaged over 50 repetitions for incremental Reset cycles ($-1 \text{ V} \rightarrow -1.25 \text{ V} \rightarrow -1.5 \text{ V} \rightarrow -1.75 \text{ V} \rightarrow -2 \text{ V} \rightarrow -2.5 \text{ V} \rightarrow -3 \text{ V} \rightarrow -3.5 \text{ V} \rightarrow -4 \text{ V} \rightarrow -4.5 \text{ V} \rightarrow -5 \text{ V}$) after a Set cycle up to 10 V under a current compliance of 1 mA are shown in Fig. 3.34(c). This result shows the possibility of operating a multilevel resistance device if the Reset cycle is properly tuned.

As already stated, the structure with 10 nm of Al_2O_3 does not show reliable RS. For devices that do not start in a large HRS ($\sim 10^8 \Omega$), switching to a LRS ($\sim 10 \Omega$) at around 16 V (step 1) and

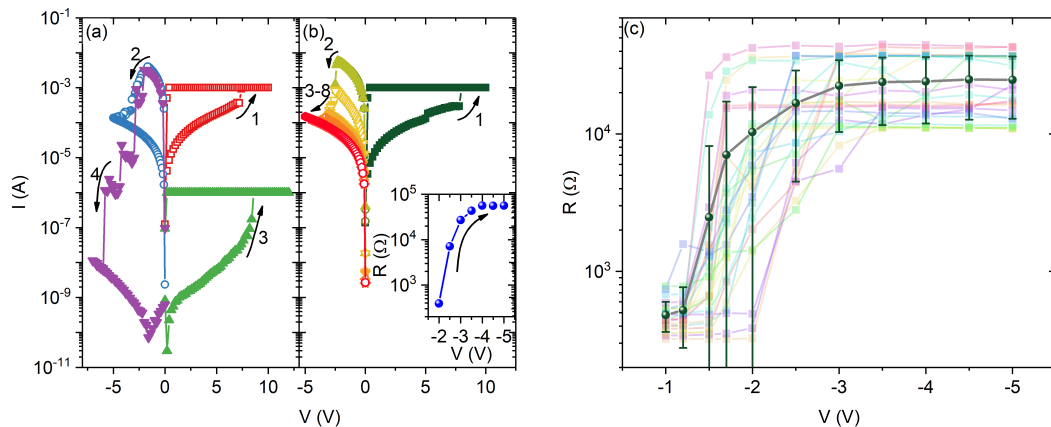


Figure 3.34 – (a) I – V for 5 nm of Al_2O_3 showing gradual Reset (smooth - step 2; by steps - step 4). (b) Incremental Reset cycle amplitude (steps 2-8). The inset shows the resistance value at the end of each cycle. (c) Resistance dependence on the maximum negative voltage averaged over 50 repetitions. Incremental Reset cycles ($-1 \text{ V} \rightarrow -1.25 \text{ V} \rightarrow -1.5 \text{ V} \rightarrow -1.75 \text{ V} \rightarrow -2 \text{ V} \rightarrow -2.5 \text{ V} \rightarrow -3 \text{ V} \rightarrow -3.5 \text{ V} \rightarrow -4 \text{ V} \rightarrow -4.5 \text{ V} \rightarrow -5 \text{ V}$) after a Set cycle up to 10 V under a I_C of 1 mA.

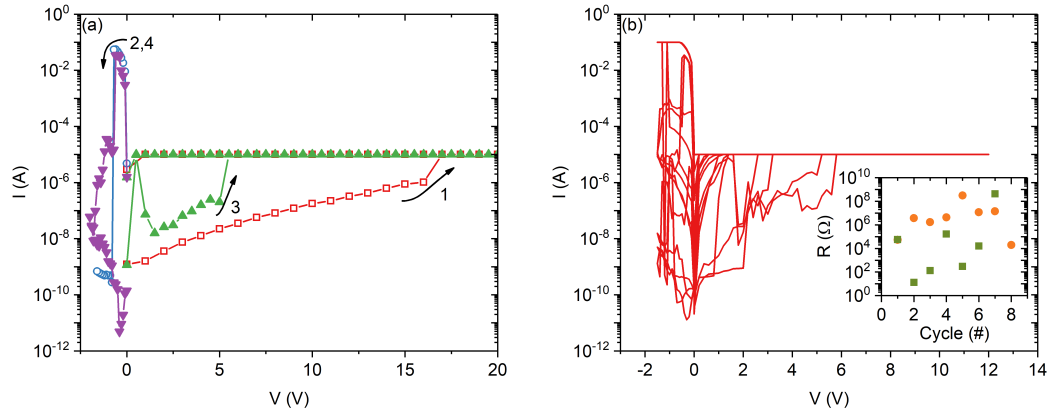


Figure 3.35 – I – V characteristics for 10 nm of Al_2O_3 (a) in the pristine state (step 1) and following cycles (steps 2-4). (b) I – V for 10 repetitions. The inset shows the resistance states over the cycles.

back ($\sim 10^8 \Omega$) at -0.6 V (step 2) is still possible, as shown in Fig. 3.35(a). However, even these devices do not show more than 10 consecutive cycles [Fig. 3.35(b)]. Furthermore, the variability of the voltages and, mainly, the resistance states is very high, as shown in the inset of Fig. 3.35(b).

On the other limit, a reference structure with an oxide layer constituted by 10 nm of Al_2O_3 , and a vacuum break before Ta deposition, only starts in a lower OFF state ($\sim 10^7 \Omega$) and switches to the ON state ($\sim 10^2 \Omega$) at 1.8 V (step 1), as shown in Fig. 3.36(a). The Reset to $10^5 \Omega$ occurs at -3 V (step 2). Similar values are involved in the following cycle (steps 3 and 4). Note that the Reset voltage being larger than the Set voltage suggests a bipolar RS behavior, as well as the lower resistance ratio. The voltage values are considerably smaller than the previous stacks, although a low endurance is seen [9/20 cycles; Fig. 3.36(b)].

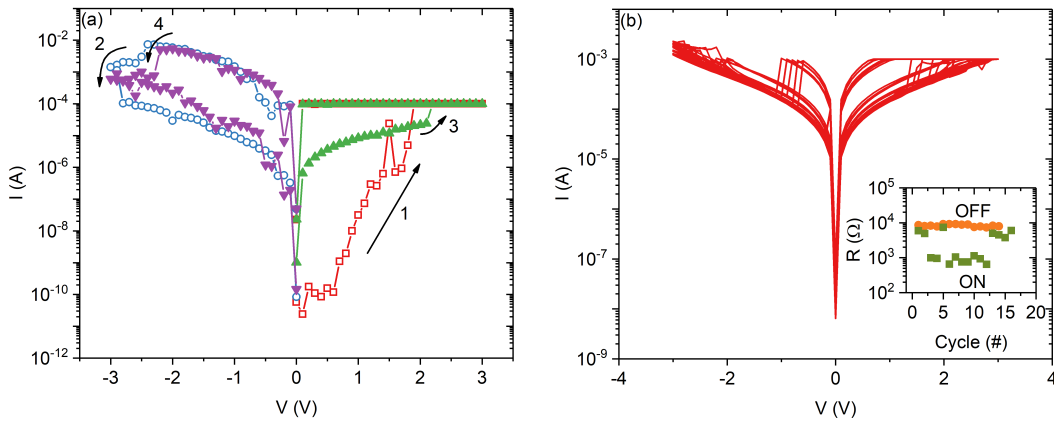


Figure 3.36 – I – V characteristics for only 10 nm of Al_2O_3 (a) in the pristine state (step 1) and following cycles (steps 2-4). (b) I – V for 20 repetitions. The inset shows the resistance states over the cycles.

Table 3.5 – Resistive switching parameters resume as a function of Al_2O_3 thickness.

Al_2O_3 thickness (nm)	Resistive Switching	R_{initial} (Ω)	V_{Forming} (V)	V_{Set} (V)	V_{Reset} (V)	R_{ON} (Ω)	R_{OFF} (Ω)	I_{C} (A)
0	bipolar	10^8	3.2	0.9	0.5	10^3	10^4	10^{-3}
0.5		10^6	–	2.2	0.2	10^2	10^6	10^{-4}
1		10^8	14.5	7	0.9	10	10^8	10^{-3}
2	unipolar	10^6	–	6.9	1.4	10	10^8	10^{-3}
5		10^8	–	8.3	2.3	10^2	10^4	10^{-5}
10		10^7	–	1.5	0.7	10^2	10^6	10^{-3}
10 (no MgO)	bipolar	10^7	–	1.9	1.2	10^3	10^4	10^{-3}

3.4.3 Discussion

The parameters of the resistive switching for all the structures with a double insulating layer $\text{Al}_2\text{O}_3/\text{MgO}$ and single MgO or Al_2O_3 layers are summarized in Table 3.5. The bipolar behavior of the single layer Al_2O_3 structure may be attributed to the vacuum break experienced after the oxide deposition. It shows the same resistance levels ($10^4 \Omega$ / $10^3 \Omega$) of the single layer MgO structure that also had the vacuum break and, besides the forming voltage, shows small operation voltages typical of bipolar behavior. The initial resistance is larger for the ticker oxide ($10^8 \Omega$ versus $10^7 \Omega$) and a forming voltage is needed (3.2 V), although with final Set and Reset voltages (0.9 V and 0.5 V, respectively) lower than those of the thinner oxide (1.9 V and 1.2 V, respectively).

The structures without a vacuum break all show unipolar behavior, but only for 1 nm there is the need of a forming step, maybe due to the high initial resistance. Interestingly, the thinner (0.5 nm) and the thicker (10 nm) structure have the smallest Set and Reset voltages, although the last sometimes shows extremely large initial resistances that do not lead to resistive switching. Both

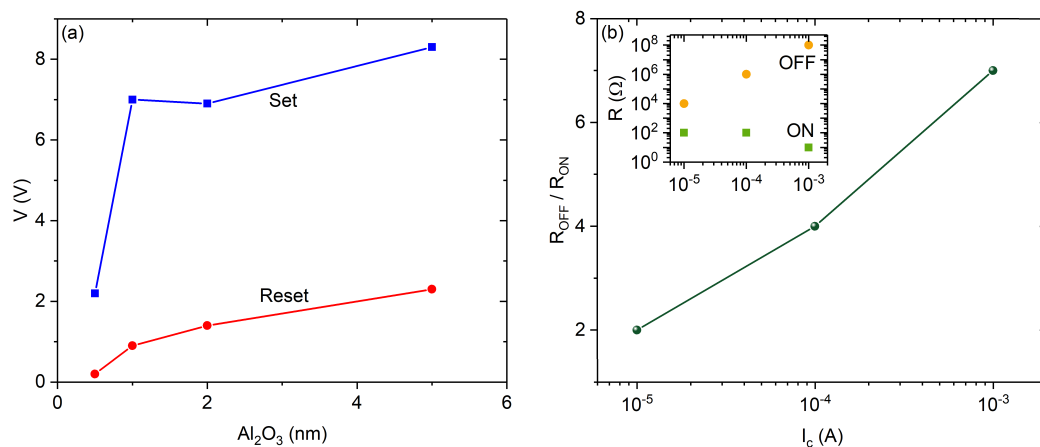


Figure 3.37 – (a) Set and Reset voltages for the double layer structures as a function of Al_2O_3 thickness. (b) Resistance ratio for the double layer structures as a function of the current compliance. The inset shows ON and OFF resistances as a function of the current compliance.

Set and Reset voltages increase with Al_2O_3 thickness, as can be seen in Fig. 3.37(a). This is understandable since the filament grows and ruptures across a longer distance. The differences in the resistance ratio are explained by the current compliance used during the measurements, as shown in Fig. 3.37(b). It is expected that the ON resistance decreases with the increase of the current compliance, due to the resulting stronger conductive filament [inset of Fig. 3.37(b)]. However, we also observed an increase of the OFF resistance, that represents a more complete filament rupture and may be indirectly explained by a higher current compliance (1 mA) originating a higher Reset current (100 mA) that through Joule heating better dissolves the filament ($10^8 \Omega$).

3.5 Influence of MgO Thickness on Resistive Switching

In previous works by our group, structures with different MgO thicknesses (15 nm [170], 22.5 nm, 30 nm and 40 nm [208]) were also electrically characterized. The measurements were performed by methods similar to the ones already described here and the results regarding the dependence of the characteristic voltages on the thin film thickness can be seen in Fig. 3.38(a). It is observed that for 15 nm of MgO there is no forming voltage and, for thicker layers, the forming voltage increases with the MgO thickness, while the Set and Reset voltages are mostly thickness independent. This reinforces the idea that, in this type of devices, resistive switching occurs due to the formation and rupture of metallic filaments inside the oxide layer. In other words, a thicker oxide needs a higher voltage to start the resistive switching process, but since the filament only suffers a partial rupture, the following switching voltages are independent of the total thickness [Fig. 3.38(b)]. This behavior was also observed by Waser *et al.* for a variable oxide thickness in a Cu/SiO₂ cell, with the forming voltage linearly increasing with thickness and the Set voltage being independent of the thickness [11]. Mao *et al.* and Yang *et al.* further observed the Reset voltage independence on the thickness of ZnO thin films [209, 210], while Kang *et al.* reported the independence of the Reset voltage on the ZnO thickness, but a linear dependence of the Set voltage [211].

Having the oxide thickness as a variable, it is interesting to understand how it affects the switching parameters. For this purpose, a numerical simulation using the Random Circuit Breaker Model [212, 213, 214] was implemented in *Python*.

3.5.1 Random Circuit Breaker Model

The identification and control of RS parameters is one of the key points in this area. Admitting that the switching phenomenon is attributed to the formation and rupture of conducting filaments, the Random Circuit Breaker Model (RCB) is a good model to describe unipolar reversible resistive switching, allowing to simulate what is happening inside an actual device. The RCB is a percolation model that assumes the insulator layer to be composed of a lattice network of circuit breakers (resistors), as shown in Fig. 3.39(a). Each circuit breaker can have either one of two changeable resistance values: R_H (high resistance/OFF state; grey) or R_L (low resistance/ON state; green), where $R_H \gg R_L$ [212]. The lattice can then be compared to a metal-insulator mixture. In response

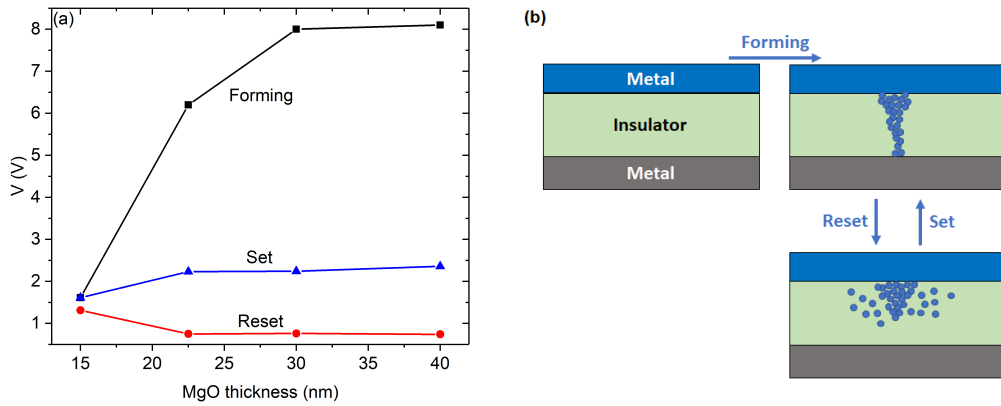


Figure 3.38 – (a) Forming, Set and Reset voltages as a function of MgO thickness (Adapted from Refs. [170] and [208]). (b) Simplified schematic of filament complete growth and partial rupture in a MIM structure.

to an external voltage, the network will reconfigure in a similar way to physical MIM structures. In other words, ON and OFF states in unipolar RS can be viewed as the formation and rupture of a percolation cluster in a network. This model yields a quantitative tool to understand and control the RS phenomenon, yielding strategies to reduce switching parameter distributions. Note that this model explains both I–V curves and resistance fluctuations [215]. Another advantage of this model is that it is material-independent, focusing only on the overall behavior of the circuit breakers. Furthermore, the RCB network model explains that the wide distributions of switching voltages is due to the randomly turning *on* or *off* of circuit breakers in the network which corresponds to the formation and rupture of a small segment of the conductive filaments.

However, this model has the disadvantage of only simulating 2D structures with orthogonal current flow [216], being a more accurate approach to consider 3D cubes, for instance [217].

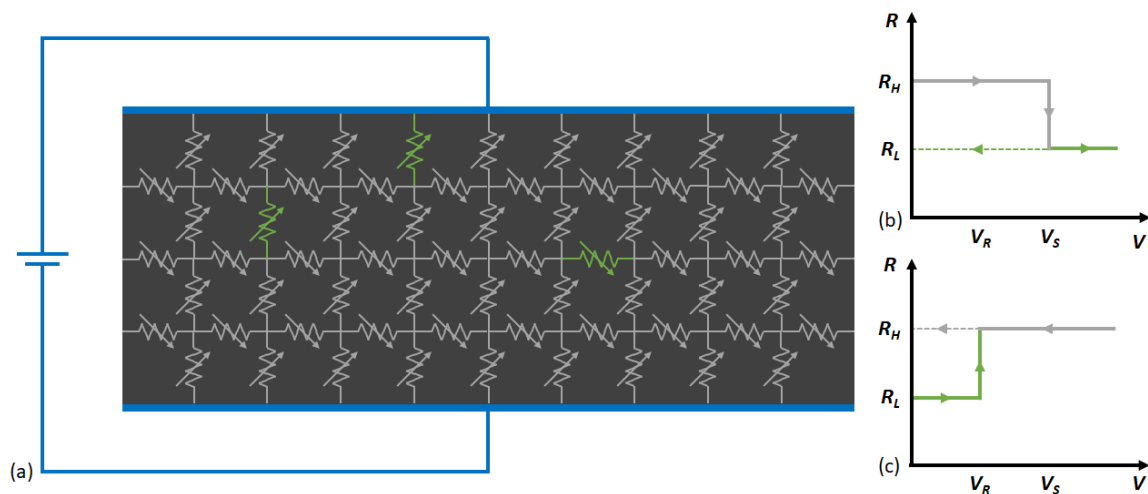


Figure 3.39 – (a) Schematic of a network model composed of circuit breakers (resistors) in between two parallel electrodes (blue). Grey resistors stand for R_H and green ones for R_L . Transitions between (b) R_H to R_L and (c) R_L to R_H resistance states for each circuit breaker in the network when subjected to a critical (switching) ΔV .

However, that is also a much more complex numerical problem, whereas if one restricts to the transverse plane of the filament formation/rupture, a satisfactory solution is already obtained. Furthermore, the standard RCB model does not include migration and temperature effects. For this considerations please see Refs. [215], [218] and [219].

3.5.1.1 Principle of operation

In order to operate the network, an external voltage V_{ext} is applied across the two parallel electrodes and the corresponding voltage drop (ΔV) is calculated at each resistor. To emulate the natural presence of defects in as-grown devices (e.g. oxygen vacancies affecting transport properties) and not to have a deterministic result, a fraction of the circuit breakers is randomly set to the ON state with a probability p_{ini} at the initial stage of the simulation.

The resistance of the network depends on the circuit breaker resistances, which switch depending on the magnitude of the voltage ΔV applied across each one by solving Kirchhoff's equations: 1) a local Set process occurs if $\Delta V > V_S$ and $R = R_H$ [Fig. 3.39(b)]; 2) a local Reset occurs if $\Delta V > V_R$ and $R = R_L$ [Fig. 3.39(c)], where $V_S \gg V_R$ and $R_H \gg R_L$. Thus, if a resistor is in the low resistance state and the local voltage is higher than a certain value V_S , it switches to the high resistance state. If it is in the high resistance state and the voltage is sufficiently high (V_R), it changes to the low resistance state. If there are no changes, the voltage in the lattice is increased. The iteration process is followed until the system attains a metastable state. Otherwise, the new resistance is calculated and the algorithm stops when the ratio with the initial resistance is above a certain value. In physical terms, this corresponds to the formation and rupture of small conductive segments inside the network. The pseudo code is shown in Algorithm 3.1, while the complete code can be seen in Appendix C.

Algorithm 3.1 RCB Model Pseudo Code

```

while  $V_{ext} < V_{max}$  do
  apply  $V_{ext}$ 
  calculate the set of  $\Delta V$ 
  calculate  $I$ 
  if  $R/R_{ini} > ratio$  then
    Stop
  else
    if  $R = R_L$  and  $\Delta V > V_R$  then
       $R \leftarrow R_H$ 
    else if  $R = R_H$  and  $\Delta V > V_S$  then
       $R \leftarrow R_L$ 
    else
       $V_{ext} \leftarrow V_{ext} + \Delta V$ 
    end if
  end if
end while

```

Table 3.6 – *RCB model simulations parameters.*

columns	lines	R_H (Ω)	R_L (Ω)	V_R (V)	V_S (V)	V_{max} (V)	ΔV (V)	I_C (A)	p_{ini} (%)
50	20	1000	1	0.01	0.2	3	0.05	0.5	0.5

For convergence purposes we made the assumption that, if a resistor changes from R_H to R_L , it cannot switch back before the full Set of the structure occurs. This assumption is based on the experimental knowledge that filament rupture occurs below the microsecond range and forming at the nanosecond range. Moreover, continuity (boundary) conditions are imposed to the network, meaning that the left and right borders are connected. Table 3.6 summarizes the typical values used during the simulations. Note that the ratio between the dimensions is not proportional with a real device, since it would be of the order of $300 \mu\text{m} / 30 \text{ nm} \sim 10^4$ (for our case). However, a rectangular matrix is sufficient to understand the phenomenon. Moreover, the results will only be qualitatively analyzed, since to obtain more reliable results, larger values of R_H/R_L , as well as 3D simulations, should be used, at the expense of much longer simulation times.

3.5.1.2 Results

Figure 3.40 shows a typical forming-Reset-Set unipolar cycle simulated in a 25×50 lattice. The network starts in the pristine state and, at 2.95 V, a conductive filament is formed in an avalanche

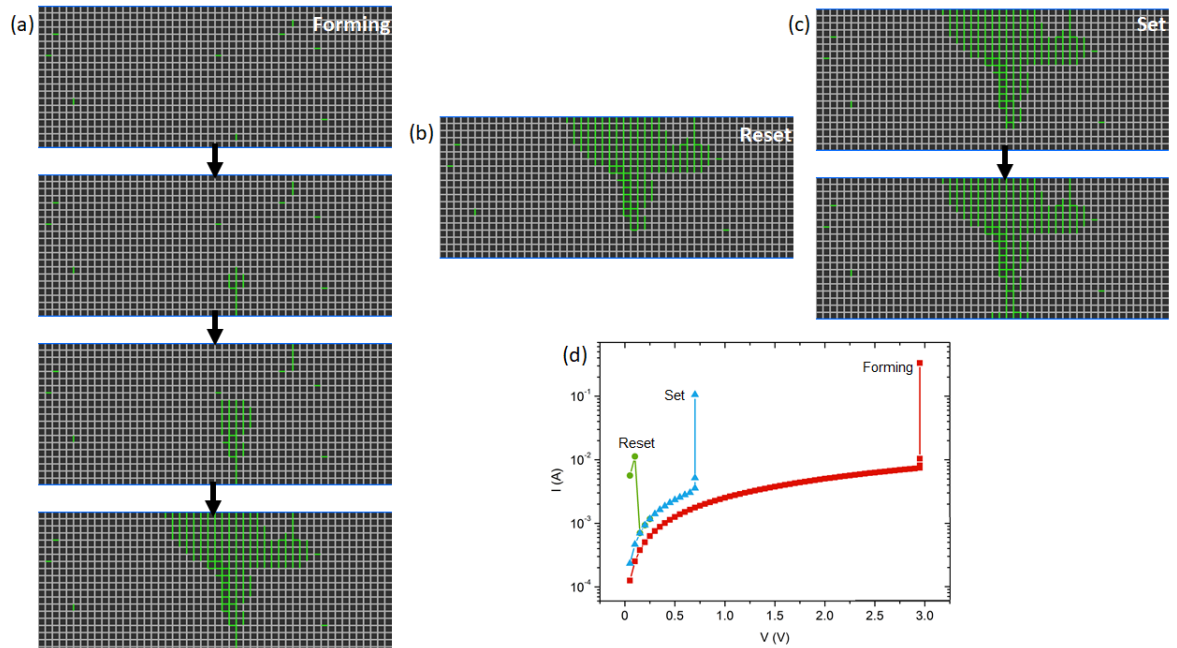


Figure 3.40 – (a) Dendritic evolution of the conductive filament in the forming operation, starting from the pristine state with a small number of circuit breakers in the ON state ($p_{ini} = 0.5\%$), then the generation of a conductive channel and finally the percolated state connecting the two electrodes (ON). The growth direction of the filament is parallel to the electric field established by the external bias in an avalanche process (3 iterations). (b) One-iteration Reset process with partial filament rupture and (c) two-iterations Set process ending again with the formation of a complete filament. (d) Corresponding I – V data for the processes occurring in (a)–(c).

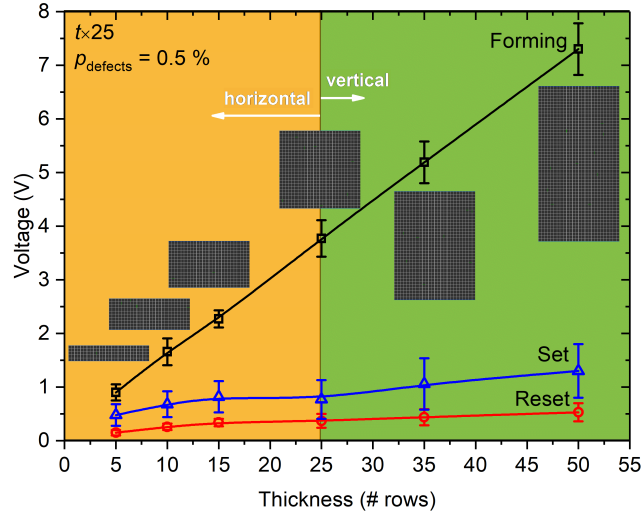


Figure 3.41 – Forming, Set and Reset voltages in a 2D simulation as a function of thickness, for fixed width, an initial probability of defects of 0.5% and averaged over 100 simulations.

process [Fig. 3.40(a)]. Then, this filament is partially broken at 0.15 V [Reset; Fig. 3.40(b)]. The missing filament part is grown again instantly at 0.7 V [Set; Fig. 3.40(c)]. The representation on the typical I–V curve is shown in Fig. 3.40(d). We observed that defect location is the critical parameter determining the filament grown direction. In other words, the filament will start to grow from the electrode with the closest defect. This corresponds to the bottom electrode in the case shown in Fig. 3.40(a).

Insulator thickness dependence. If we fix the lattice width and vary the height, we can study how the voltage distribution depends on insulator thicknesses. These simulations were performed in a 2D lattice with fixed width (25 columns), an initial probability of defects (ON states) of 0.5% and averages over 100 repetitions. Figure 3.41 shows the switching voltages obtained for variable thickness. The forming voltage shows a linear dependence on the thickness, almost being suppressed for small thicknesses as experimentally observed ($V_{Forming} \sim V_{Set}$), while Set and Reset voltages show no dependence on the insulator thickness for the horizontal configuration. There is only a small voltage increase in the vertical configuration. This may be explained by the Reset process involving one incomplete dissolution of conductive filaments at the electrode/dielectric interface, and the subsequent Set process only needing to connect this local area and not the whole filament [as seen in Figs. 3.40(a)-(c)]. Hence, Set and Reset can be considered local effects, whereas forming has a "bulk" behavior. These results are in good agreement with the experimental data for MgO [Fig. 3.38], with a linear dependence of the forming voltage on the thickness and no dependence from the Set and Reset voltages.

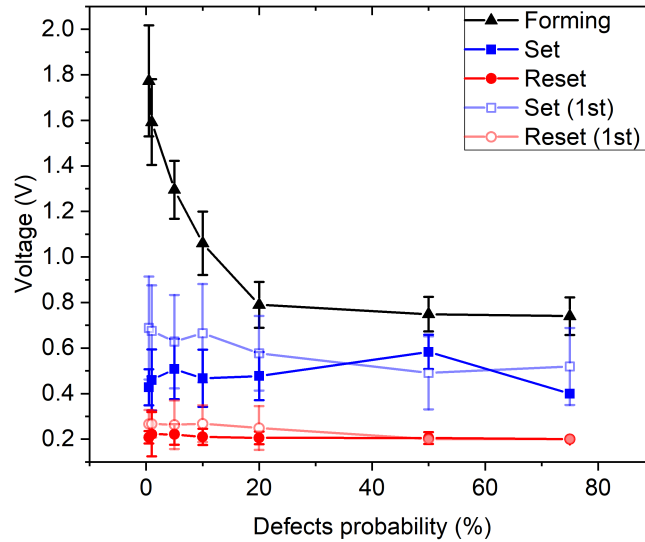


Figure 3.42 – Voltage needed for switching in a 2D device as a function of initial defects percentage, averaged over 100 repetitions.

Defects percentage. We can also study how the percentage of initial defects in the lattice affects the switching voltages by varying its value for a fixed lattice size. The Set and Reset voltages seem to be once again independent on the initial defect concentration, as can be seen in Fig. 3.42, either considering 100 consecutive cycles after the same forming step (full symbols) or only the first Set and Reset cycles for 100 different forming steps (open symbols). On the other hand, the forming voltage decreases almost linearly with the defects percentage up to 20% and becomes constant for higher values. As the number of ON defects increases, so does the number of conductive filaments possibilities as well as their initial size, which leads to a decrease of the voltage needed for their completion.

The detailed study of RCB networks configuration helped understanding forming, Reset and Set processes, as well as the influence of defects, seed layers and geometry parameters on the RS behavior. From a scale analysis, the percolation structures can be seen as a fractal: a memristor described as a network of memristors.

3.6 Conclusions

We studied the resistive switching behavior of MgO based structures. For Pt/MgO/Ta/Ru devices we obtained unipolar resistive switching after a forming step. This behavior was observed with all voltage polarity combinations and we found that operation is better (lower variability and operating voltages) for positive Set voltages. The best operating mode is the (+,-) with bipolar-like properties. We also studied the conduction mechanisms involved in the switching and attributed it to the formation and rupture of oxygen vacancy filaments, from the Ta to the Pt electrode. Knowing

Table 3.7 – Resume of resistive switching parameters for all MgO structures discussed in this chapter. The initial parameters are taken from different devices and the other values from different cycles of a single device.

Stack	comments		Resistive Switching	$R_{initial}$ (Ω)	$V_{Forming}$ (V)	V_{Set} (V)	V_{Reset} (V)	R_{ON} (Ω)	R_{OFF} (Ω)	ratio	mode
Pt/MgO/Ta/Ru	magnetron	300 μm	unipolar	10^{10}	7.5	1	1.7	10^2	10^5	3	(+,+)
	sputtering	$10 \times 10 \mu\text{m}^2$		10^9	9.6	1.1	0.4	10^2	10^4	2	(+,-)
Pt/MgO/Pt	IBD	A	unipolar	10^7	–	5.1	1.6	10	10^8	7	(-,+)
		B		10^8	–	6.7	3.7	10^2	10^8	6	(+,-)
		C		10^{10}	14.6	8.2	3.7	10^2	10^4	2	
Pt/MgO/Al/Ru	magnetron sputtering / IBD		unipolar	10^8	–	6.1	0.5	10	10^8	7	(+,-)
Pt/MgO/Cu/Ru				10^9	–	3.4	0.4	10	10^8	7	
Pt/MgO/Ag/Ru	magnetron sputtering		bipolar	10^5	–	3.4	1.2	10	10^5	4	
Pt/MgO/Al ₂ O ₃ /Ta	IBD	0 nm	bipolar	10^8	3.2	1	2	10^3	10^5	2	(+,-)
		0.5 nm	unipolar	10^6	–	2.2	0.2	10^2	10^6	4	
		1 nm		10^8	14.5	7	0.9	10	10^8	7	
		2 nm		10^6	–	6.9	1.4	10	10^8	6	
		5 nm		10^8	–	8.3	2.3	10^2	10^4	2	
		10 nm		10^7	–	1.5	0.7	10^2	10^6	4	
Pt/Al ₂ O ₃ /Ta		10 nm	bipolar	10^7	–	1.9	1.2	10^3	10^4	1	

the influence of the operation mode on the parameters variability, our results open the prospect to improve switching performance in other resistive switching systems. The influence of vacuum breaks at the metal/insulator interfaces in MIM structures was analyzed using the inert metal Pt for both bottom and top interfaces. The studies with different top electrodes showed also a unipolar resistive switching for Cu and Al, and bipolar for Ag. Furthermore, we used the RCB model to study the influence of initial defects and network geometry on the switching parameters. We also studied Al₂O₃/MgO double layer structures with different Al₂O₃ thicknesses.

Table 3.7 resumes the resistive switching parameters of all the structures discussed in this chapter. The resistive behavior of the $10 \times 10 \mu\text{m}^2$ devices is comparable to the 300 μm , as can be seen by the similar operation voltages and resistance states. When using a Pt electrode deposited by IBD and a vacuum break just after the Pt bottom electrode as in the Ta electrode case (structure A), a considerable increase of the Set voltage and of the OFF resistance are observed. We do not have enough data to conclude if this is due to the Pt electrode or the deposition method. The same magnetron sputtering deposited MgO layer but with Al, Cu and Ag top electrodes after a vacuum break also shows an increase of the Set voltage and decrease of the Reset voltage for the first two cases. For Al and Cu the resistance ratio is also higher (7 versus 3) since the OFF resistance is larger ($10^8 \Omega$ versus $10^5 \Omega$), whereas for Ag the behavior changes to bipolar. The single layer IBD deposited MgO layer with a vacuum break before the Ta top electrode deposition shows bipolar resistive switching and voltages and resistance states similar to the initial MgO/Ta stack. Comparing to structure C, with Pt but also deposited by IBD and the vacuum breaks at

the same interfaces, the influence of Ta is evident. The oxygen reservoir created at the MgO/Ta interface considerably decreases the operating voltages (forming, Set and Reset). It can also be compared to the single layer Al_2O_3 structure, displaying similar results for 30 nm of MgO and 10 nm of Al_2O_3 . The double layer stacks show unipolar resistive switching mostly without the need of a forming process and showing higher Set voltages and larger OFF resistances. Looking at the forming voltage column, we may infer that the deposition technique influences the forming step, since most of the sample fabricated with this technique do not need one. Also, the existence of a vacuum break after the oxide layer seems to have a similar effect.

CHAPTER 4

Resistive Switching in Si/Ag structures

Silicon, as the most widely used material in the semiconductor industry, is the ideal choice to integrate new devices and systems that would take full advantage of a mature technology and easily adapted processes. From the electrochemical metallization mechanism category, Si based devices have the advantage of continuous (analog) switching, by the gradual change of amplitude or duration of the electrical bias [220]. A typical Si-based device consists of a layered metal/Si/metal structure, where Si is the storage medium [221]. In order to obtain reliable resistive switching in silicon-based devices, one needs to combine it with materials, such as Ag, Cu or Al, that can diffuse within its bulk [221, 220, 222]. Several reports are present in the literature of resistive switching in Si/Ag structures. For instance, the works of Jo *et al.* and Kim *et al.* showed resistive switching for Set voltages of 3.5 V and 1.5 V, respectively [221, 223]. Jo *et al.* also showed that this system is well suited for memory or logic operations [224], crossbar array integration [225] and reported neuromorphic properties [18]. Si nanowires have also been used aiming flexible applications, showing average Set voltages of 2.9 V [226, 227]. Different metal interfaces were also reported, such as W [228]. Other studies further approach the combination of amorphous (a-Si) and p-type crystalline (p-Si) silicon as the bottom electrode [221, 225, 229], from which light-activated devices can even be obtained [230, 231]. In addition, resistive switching properties have been observed in silicon oxide (SiO_x) since 1962 [26] to more recent reports describing SiO_x as the active switching medium [232, 144, 233, 234, 235, 236]. Metal doping (Al, Cu or Ni, for instance) of SiO_x also showed successful resistive switching [201, 237, 238, 239], as well as the use of nanoporous SiO_x [240]. Neuromorphic capabilities have also been observed in Si-rich SiO_x [241, 106], together with the integration of SiO_x resistive switching devices with Si diodes [242].

4.1 Resistive Switching

Here, we studied the resistive switching of Si / SiO_2 / Ti (25) / Pt (150) / Si (20) / Ag (5) / TiW (100) (nm) thin films with circular top electrodes of 300 μm in diameter and observed ultra-low operation voltage (< 0.6 V). Figure 4.1 shows the first resistive switching curve of one of the fabricated devices. The device starts in a high resistive state (OFF; $3.7 \times 10^3 \Omega$) but, with increasing positive voltage, switches to a low resistance state (ON; 490 Ω) at around 0.35 V (Set; step 1). No forming process is needed, as the first switching already occurs at a low voltage. Then, with increasing

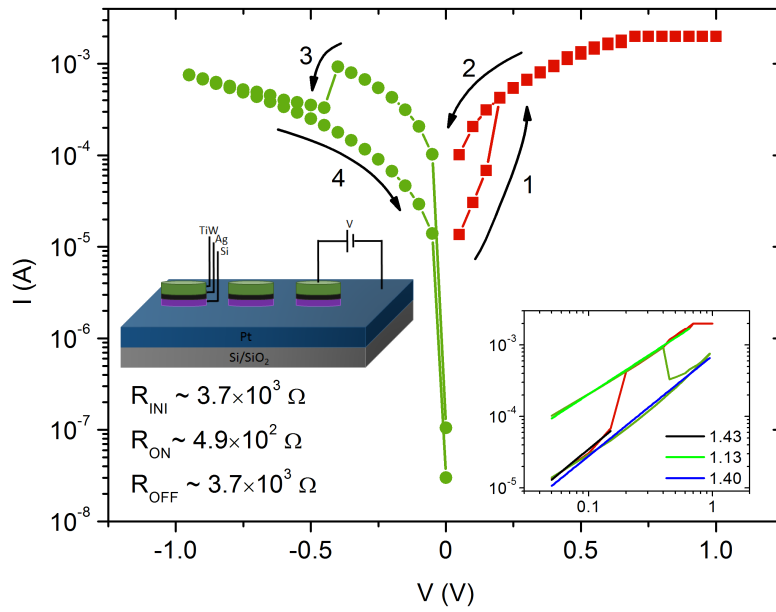


Figure 4.1 – I – V characteristics of the Pt/Si/Ag/TiW device. The left inset shows the schematic diagram of the device and measurement set up. The right inset (in a log-log scale) shows the transport mechanisms involved.

negative voltage, the device switches back to the high resistance state at approximately -0.4 V (Reset; step 3). As Set and Reset occur at opposite voltage polarities, switching is bipolar. This is further confirmed by the fact that the magnitude of the Reset voltage is higher than that of the Set. The right inset of Fig. 4.1 depicts the measured curves in a log-log scale with the linear fits to the small voltage area showing the conduction mechanisms involved in both resistance states: ohmic for the ON state (unitary slope) and space charge limited current for the OFF state. The resistive switching phenomenon is then attributed to the formation/rupture of metallic Ag filaments inside the Si layer. When a positive voltage is applied to the TiW electrode (negative at Pt), Ag ions drift from the Ag to the Si layer, creating a conduction path between top and bottom electrodes (low resistance/ON state). If a negative voltage is then applied, the Ag ions move back towards the Ag layer and the filament is ruptured (high resistance/OFF state).

Figure 4.2 shows the statistical analysis of the resistive switching behavior for 100 consecutive and successful cycles. The applied voltage was swept in the $0 \text{ V} \rightarrow 1 \text{ V} \rightarrow 0 \text{ V} \rightarrow -1 \text{ V} \rightarrow 0 \text{ V}$ range, with a voltage step of 0.05 V and a current compliance of 1 mA for Set. The bar plots for Set and Reset voltages and currents are also displayed in the bottom and left axis, respectively. Despite some curve shape variability, the operating voltages show a Gaussian distribution with small deviation [$G_{Set}(0.233, 0.005)$, $G_{Reset}(-0.214, 0.002)$]. The inset shows the separation between the two resistance states over the 100 cycles, confirming that a separation of at least one order of magnitude is obtained ($10^3 \Omega / 10^2 \Omega$). The same conclusion can be taken from the cumulative probability of the ON and OFF resistances [Fig. 4.3(b)].

The analysis of the cumulative probability of the Set and Reset voltages shows that the distribution of these parameters is small and that the operation is always below 0.4 V for Set and -0.6

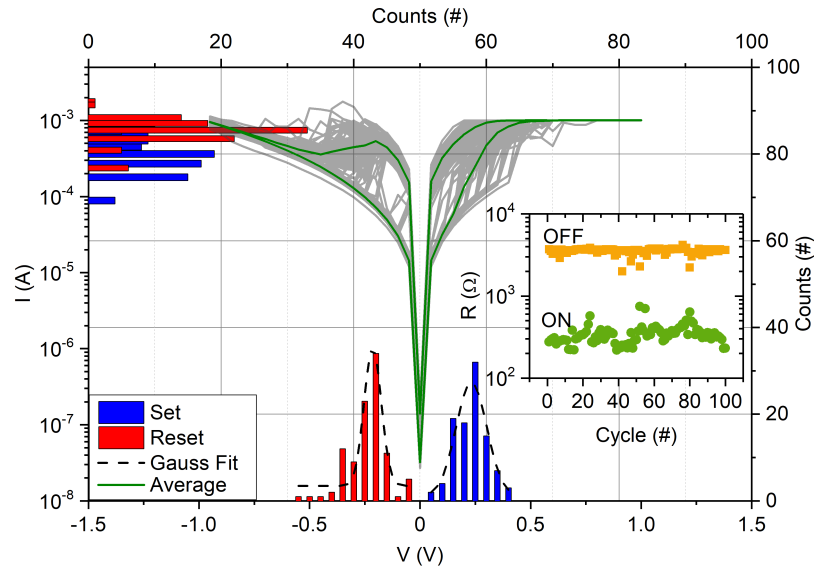


Figure 4.2 – I – V characteristics for 100 consecutive switching cycles and their average. The inset shows the variation of the resistance of both ON and OFF states for each cycle, measured at 0.1 V. The distribution and Gaussian fit of the Set and Reset voltages and currents are shown in the bottom and left axis, respectively.

V for Reset [Fig. 4.3(a)]. Using these values to calculate the power consumption, we obtain in average (0.13 ± 0.09) mW and (0.2 ± 0.1) mW for Set and Reset, respectively. Furthermore, power consumption is only slightly higher for the Reset transition (filament rupture) than for Set (filament formation). This implies that Reset is mainly driven by ionic drift rather than Joule heating, which involves high currents.

The evolution of both resistance states was measured each 5 s over 10 h with a small reading voltage (1 mV) in an attempt not to change the resistance states. For this, Set was first performed in the same conditions as for Fig. 4.2 and the ON state measured as a function of time. A similar process was performed to Reset the device and measure the evolution of the OFF state. Figure 4.4 shows that the resistances keep a good separation of up to 2 orders of magnitude. The higher variability of the OFF resistance compared to the ON resistance is again characteristic to these

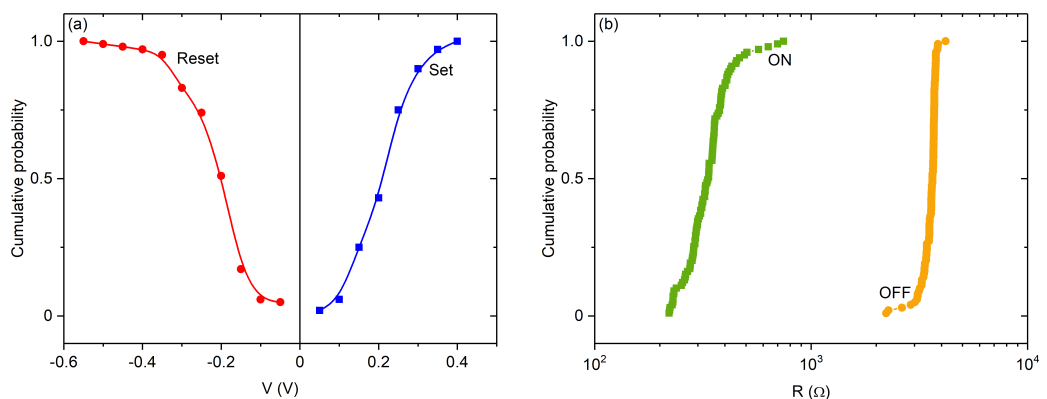


Figure 4.3 – Cumulative probability for (a) Set and Reset voltages (the lines are guides to the eye) and (b) ON and OFF resistances over the 100 cycles shown in Fig. 4.2.

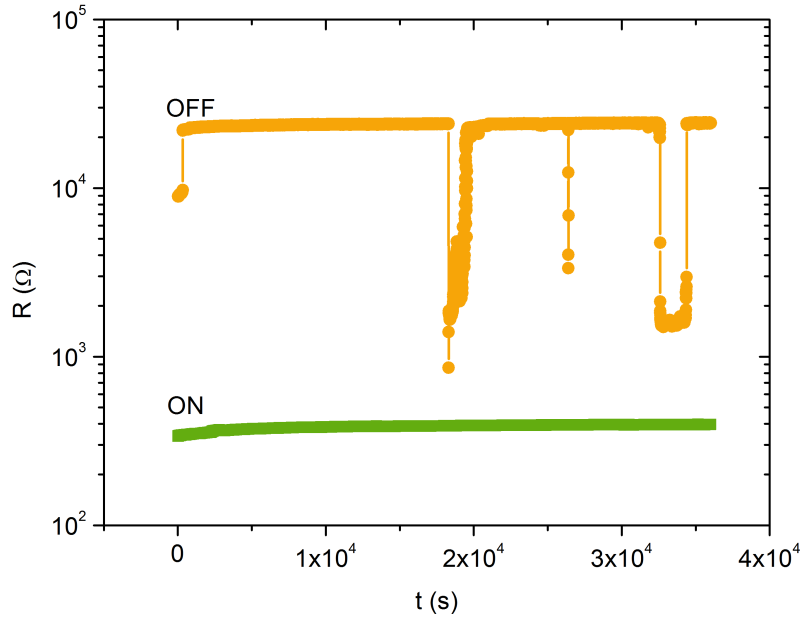


Figure 4.4 – Evolution of both ON and OFF resistance states over 10 h with a reading voltage of 1 mV.

type of resistive switching devices [181]. The observed fluctuations after 1.5×10^4 s show that even a voltage as small as 1 mV is enough to influence the resistance states. Note also that this can be explained by the flux that has flown through the device.

The pulsed switching mode (using consecutive write, read, erase, and read steps) was also successfully operated for 50 pulses with $V_{Set} = 1$ V, $V_{Read} = 1$ mV, $V_{Reset} = -1$ V, $\Delta t = 1$ s and $I_C = 1$ mA [Fig. 4.5(a)]. The separation between the resistance states ($R_{OFF} \approx 10^4 \Omega$ and $R_{ON} \approx 10^3 \Omega$) is kept, as shown in Fig. 4.5(b). Note that the oscillations of the resistances in the initial 20 cycles look like an adaptation of the device to the operation mode and parameters that then stabilize over cycling.

We further observed an inverse dependence of the ON resistance on the current compliance

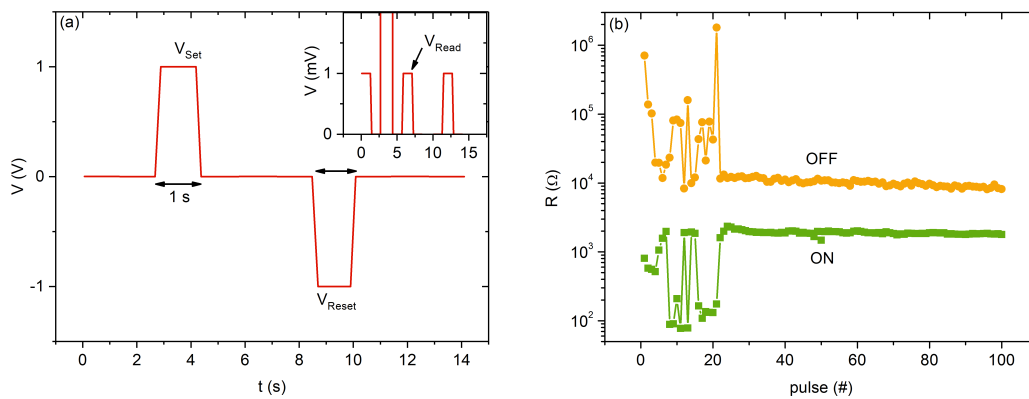


Figure 4.5 – (a) Applied voltage over time in the pulsed mode [$V_{Set} = 1$ V, $V_{Reset} = -1$ V, $V_{Read} = 1$ mV (inset), $\Delta t = 1$ s and $I_C = 1$ mA] and (b) resistance states over pulse number for the pulsed switching mode.

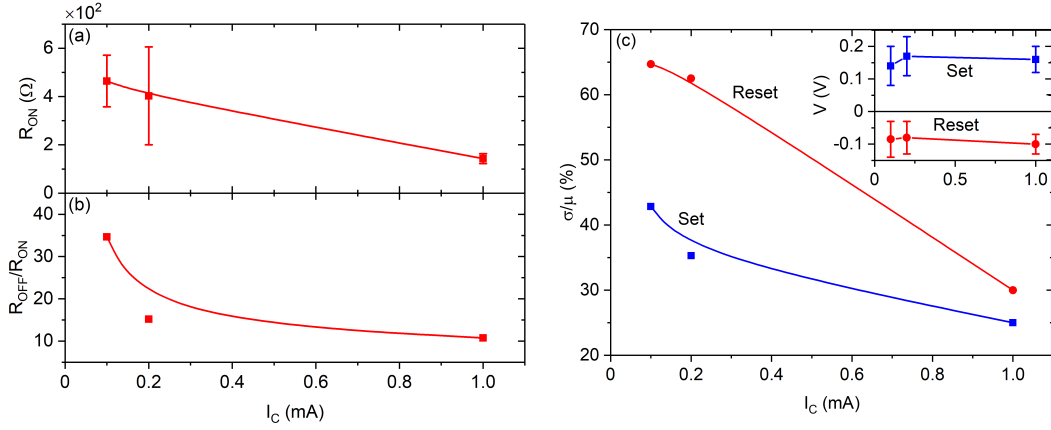


Figure 4.6 – Dependence of (a) the ON resistance, (b) resistance ratios and (c) σ/μ (in percentage; Set and Reset voltages in the inset) on the current compliance used during Set (the lines are guides to the eye).

[Fig. 4.6(a)]. We can infer that, the higher the current given for filament formation, the larger the filament will be, since the final ON conductivity is higher.

To estimate the size of the conductive filament (circular constriction of radius r), which separates the two electrodes characterized by the mean free path ℓ , in the ON state, we considered the resistance defined from the electron transport through an orifice (point contact). This resistance includes the Maxwell (diffusive regime, $\ell \ll r$) and Sharvin (ballistic regime, $\ell \gg r$) resistances and is given by

$$R(\ell/r) = R_{Sharvin} + R_{Maxwell} = \frac{4\rho\ell}{3\pi r^2} + \gamma(\ell/r)\frac{\rho}{2r}, \quad (4.1)$$

where ρ is the resistivity and γ a function numerically calculated in Ref. [243] as

$$\gamma = \frac{1 + 0.83\ell/r}{1 + 1.23\ell/r}. \quad (4.2)$$

Considering the case of pure Ag ($\ell \sim 20$ nm; $\rho \sim 1.59 \times 10^{-8}$ $\Omega \cdot m$), one obtains $r = 0.54, 0.59$ and 0.99 nm for the ON resistances shown in Fig. 4.6. Knowing that the ionic radius Ag(I) is around 129 pm, these filaments are formed by around 8, 9 and 15 Ag ions, respectively.

These results also reveal the possibility of multilevel operation if the current compliance is properly chosen. However, the ratio between the OFF and ON resistances also decreases with the increase of the current compliance [Fig. 4.6(b)]. Therefore, the resistance states separation is better for smaller current compliances. Furthermore, we calculated the ratio between the standard deviation (σ) and the average value (μ) of Set and Reset voltages for different current compliances [for 100 cycles; Fig. 4.6(c)]. We observed that the higher the current compliance, the lower the voltage variability in both cases. Higher compliance currents result in the formation of stronger and more robust filaments and thus smaller parameter fluctuations. Note that the actual values of the voltages do not show a dependence on the current compliance [inset of Fig. 4.6(c)]. These results indicate

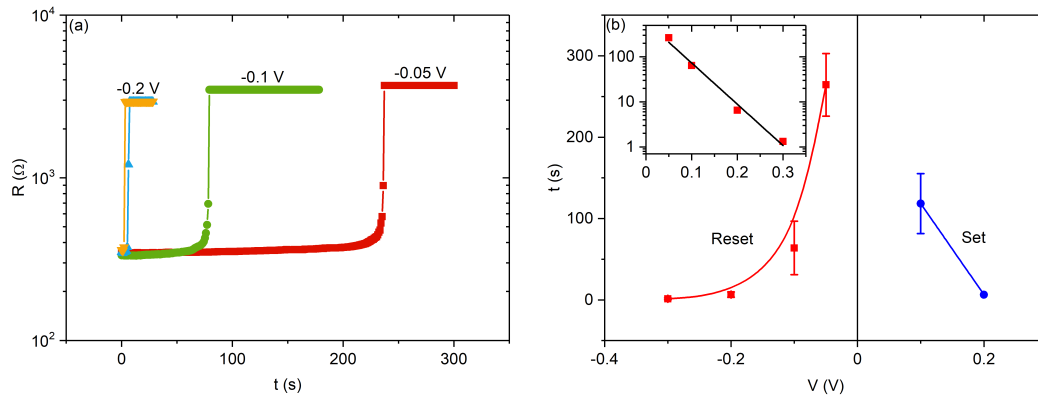


Figure 4.7 – (a) Resistance evolution over time for constant applied voltage. (b) Dependence of the switching time on the amplitude of the constant applied voltage. The inset shows the linear fit for the Reset dependence on a semi-log scale.

that there must be a compromise between higher resistance ratios or smaller voltage distributions, when choosing the Set current compliance.

Furthermore, resistive switching was also achieved when applying a constant voltage over time, as shown in Fig. 4.7(a) for the case of Reset at different voltages. As can be observed, the higher the voltage amplitude, the shorter the time needed for switching to occur (~ 5 s, 79 s and 237 s for -0.2 V, -0.1 V and -0.05 V, respectively). Figure 4.7(b) shows this time dependence on the constant voltage amplitude for both Set and Reset. This result reinforces the idea of a filament being formed or ruptured by a diffusion of ions, that is faster, the higher is the electric potential.

4.2 Charge-Flux Model

To further understand our results, we analyzed them using the charge–flux model [244, 245, 246, 247] that uses charge and flux as the main variables instead of the classical current and voltage representation. As seen in Section 1.1, the charge (q) is defined as the first momentum of the current (I), and the flux (φ) is defined accordingly for the voltage (V):

$$q(t) = \int_{-\infty}^t I(\tau) d\tau, \quad (4.3)$$

$$\varphi(t) = \int_{-\infty}^t V(\tau) d\tau. \quad (4.4)$$

The following analysis is performed according to the piecewise model developed by Al Chawa *et al.* for bipolar devices [248]. Here the model is implemented in a Ti (25) / Pt (150) / Si (20) / Ag (10) / TiW (100) (nm) stack. The characterization in the q – φ space [Fig. 4.8(a)] was performed by numerically integrating the I – V measurements [Fig. 4.8(b)], considering the staircase signal as a ramp input [$V(t) = \alpha \cdot t$]. The cycle corresponding to the Set transition is described by three equations, one before the Set and two after. The Set point, defining the beginning of the filament

formation, corresponds to the maximum of the second derivative of the charge, as shown in the inset of Fig. 4.8. Another point is defined, as the complete (*com*) filament formation, which is calculated as the first point at maximum (positive) current (compliance). After this, the device is defined as a resistor (ohmic behavior). The electrical charge is shown in Fig. 4.8(a) and fitted by:

$$q(\varphi) = \begin{cases} q_{Set} \cdot \left(\frac{\varphi}{\varphi_{Set}}\right)^k & (0 \leq \varphi \leq \varphi_{Set}) & (4.5a) \\ q_{Set} \cdot e^{z \cdot \left(\frac{\varphi}{\varphi_{Set}} - 1\right)} & (\varphi_{Set} \leq \varphi \leq \varphi_{com}) & (4.5b) \\ \frac{q_{end} - q_{Set}}{\varphi_{end} - \varphi_{Set}} \cdot (\varphi - \varphi_{Set}) + q_{Set} & (\varphi \geq \varphi_{com}) & (4.5c) \end{cases}$$

where $k = 1.01$ is a constant and

$$z = \frac{\ln(q_{com}/q_{Set})}{(\varphi_{com} - \varphi_{Set})/\varphi_{Set}}. \quad (4.6)$$

As our devices show an abrupt Set transition, here we consider complete filament formation at the point just after the Set point and therefore do not use Eq. (4.5b) and set the range of Eq. (4.5c) as $\varphi \geq \varphi_{Set}$.

For the Reset step, four equations are defined. The first extracted point is the Reset, the point with maximum (negative) current in the I–V space. The total filament rupture is defined by the break point (*brk*), that is calculated as the maximum of the second derivative of the current. Another equation is written for the voltage decrease sweep after the maximum absolute value [*max*; Fig. 4.8(b)]. The charge for the Reset cycle can then be defined as:

$$q(\varphi) = \begin{cases} q_{Reset} \cdot \left(\frac{\varphi}{\varphi_{Reset}}\right)^n & (0 \leq \varphi \leq \varphi_{Reset}) & (4.7a) \\ q_{Reset} \cdot \left(1 + \ln\left(\frac{\phi}{\phi_{Reset}}\right)^m\right) & (\varphi_{Reset} \leq \varphi \leq \varphi_{brk}) & (4.7b) \\ \frac{q_d - q_{brk}}{\varphi_d - \varphi_{brk}} \cdot (\varphi - \varphi_{brk}) + q_{brk} & (\varphi_{brk} \leq \varphi \leq \varphi_d) & (4.7c) \\ q_{max} \cdot \left(\frac{\varphi}{\varphi_{max}}\right)^a & (\varphi_d \leq \varphi \leq \varphi_{max}) & (4.7d) \end{cases}$$

where $n = 1$ is a constant,

$$m = \frac{(q_{brk} - q_{Reset})/q_{Reset}}{\ln(\varphi_{brk}/\varphi_{Reset})} \quad (4.8)$$

and

$$a = \frac{\ln(q_d/q_{max})}{\ln(\varphi_d/\varphi_{max})}. \quad (4.9)$$

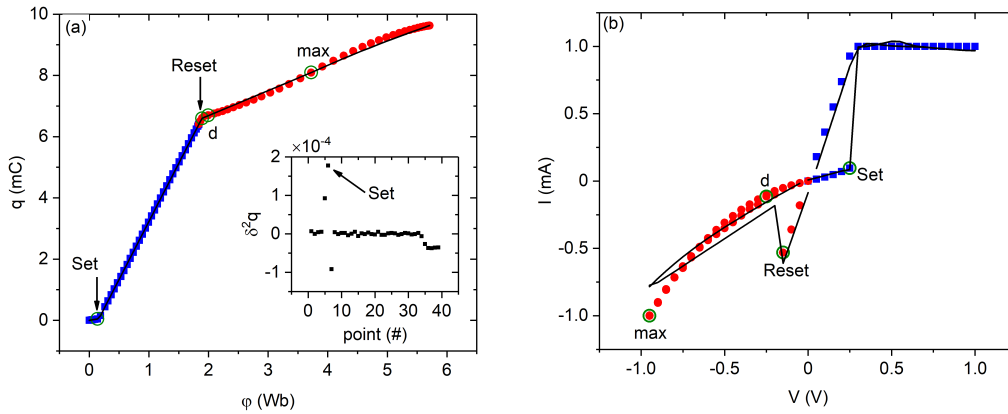


Figure 4.8 – Set and Reset transitions in (a) q – ϕ (the inset shows $\delta^2 q$ used to calculate Set point) and (b) I – V spaces. The lines represent the fitting using calculated points, which are highlighted with circles.

For these devices the Reset point corresponds to the break point and thus m [Eq. (4.8)] has no meaning and therefore Eq. (4.7b) is not considered.

The modeling of the Set and Reset parts of the I – V curve [Fig. 4.8(b)] is then given by the time derivative of the charge [Eqs. (4.5) and (4.7)]. Note that the last and first part of Eqs. (4.5) and (4.7), respectively, correspond to the ON state with an ohmic behavior. The switching voltages variability [Fig. 4.9(a)] is also visible in this space, translating in flux variability [Fig. 4.9(b)].

Using this representation, one can also compare the dependences of the Reset voltage [Fig. 4.10(a)] and Reset flux [Fig. 4.10(b)] on the time needed for Reset. In this case, we can calculate in a straightforward manner the relation between both variables. If the input voltage is a ramp [$V(t) = \alpha \cdot t$], then the flux at the Reset point will be:

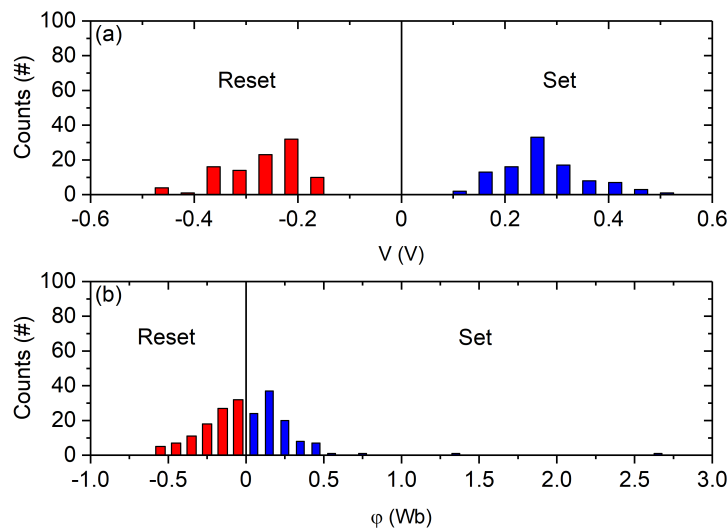


Figure 4.9 – Statistical distribution of the (a) voltage and (b) flux for 100 cycles.

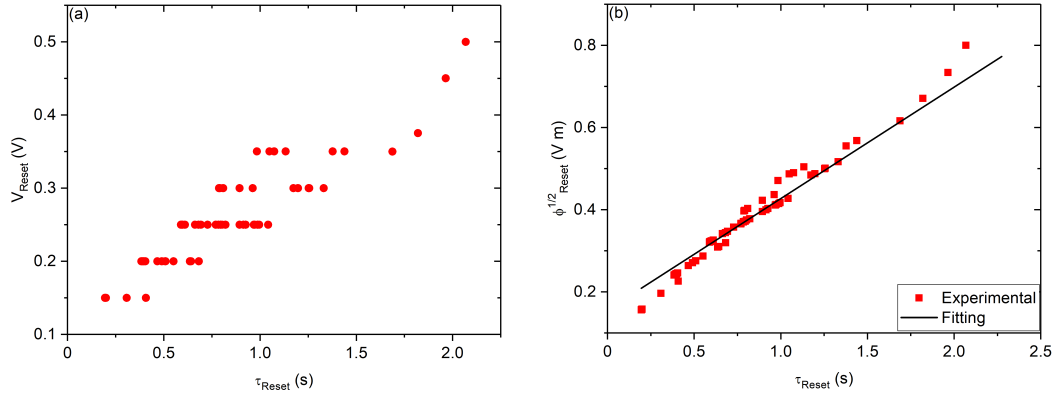


Figure 4.10 – Dependence of the (a) Reset voltage and (b) square root of the flux on the time needed for the Reset.

$$\varphi_{Reset} = \int_0^{\tau_{Reset}} \alpha \cdot t dt = \frac{1}{2} \alpha \cdot \tau_{Reset}^2. \quad (4.10)$$

This relation is shown in Fig. 4.10(b), and predicts fairly well the observed behavior. We can also calculate the Reset voltage as:

$$V_{Reset} = \alpha \cdot \tau_{Reset} = \sqrt{2 \cdot \alpha \cdot \varphi_{Reset}}. \quad (4.11)$$

Thus, using a fairly simple model, we can relate the Reset time with the Reset voltage. This behavior is different from the one in Fig. 4.7 since they correspond to different operation modes.

In summary, this analysis reinforces the idea that the conductance during resistive switching is a function of the flux, in other words, the magnitude, polarity and duration of the applied voltage. Furthermore, the different regions considered by the model have a physical meaning related with the different states of the device and can help to understand the involved processes. Models like these can then be integrated in a circuit simulator such as *Spice* to allow the study of the transient response of circuits including memristive devices.

4.3 Stochastic Resistive Switching

A resistive switching device is inherently stochastic, as shown in the previous sections, and as has been widely observed during the dynamic switching process and in the large variations of the switching parameters [249, 250, 251]. Such variations are spatiotemporal, as they occur from device to device and even cycle to cycle. This randomness is related with the stochastic nature of filament formation, which is responsible for the RS phenomenon [251]. Medeiros-Ribeiro *et al.* attributed their distribution to the nonlinear drift/diffusion behavior of the oxygen vacancies in TiO_2 [249]. This issue is an obstacle to RS devices successful commercialization, since extra energy and time are required to make a deterministic application based on memristors. However, instead of enforcing determinism, why not take advantage of the inherent variability for a stochastic

computing paradigm [251, 252, 253]? In fact, randomness is a valuable resource in computation for areas such as cryptography (security), communication (encryption), computational biology and quantum physics [252, 253].

Stochastic computing was first proposed in 1967 as a low cost computing paradigm based on probabilistic bit streams. Numbers are represented by the probability that the bit 1 is in the given bit stream. For example, the number 0.5 can be represented by a stream of 8 bits {0, 1, 1, 0, 1, 0, 0, 1}, where the probability of finding 1 in the sequence is 50% [251, 254]. This architecture is much more tolerant to soft errors (bit flips), being suited for applications that do not require high precision. Furthermore, these systems can be very simple, since memristors stochasticity is built-in and needs no extra circuitry to maintain [255, 254, 251].

Regarding security application, the intrinsic variability of RS devices enables mechanisms for computing tasks such as physical unclonable function [256], key destruction [257] and random number generator (RNG) [252]. Scalable, low-power RNGs are essential for encryption in today's communication systems for the era of the IoT. Balatti *et al.* demonstrated a RNG based on (cycle to cycle) Set variability in a single RS device, which is repeatedly programmed at a constant voltage (close to the Set voltage) being the resistance distribution converted into a digital (0/1) output voltage [258]. Other authors also proposed RNGs based on the stochastic behavior of memristors [251, 259, 253].

Furthermore, biological noise has been proven to be quite beneficial for learning, information processing and decision making in the brain [260]. As the brain is a highly stochastic system that operates using noisy elements, the variability of memristors allows to emulate the stochastic nature of the opening and closing of ion channels in biological synapses and develop brain-inspired probabilistic computation [98]. Moreover, it can also be used to implement stochastic neurons [250]. Traditionally, stochasticity is added into neural networks through injected background noise [260]. Bill *et al.* concluded that the stochasticity of combined memristors allows to define one synapse [261]. Yu *et al.* proposed using the Set variability to realize the stochastic learning rule in synapses [262]. Al-Shedivat *et al.* proposed a neural soma circuit that uses RS for triggering spike events [263, 264] and Feali *et al.* showed that the stochastic nature of memristors leads to a higher reliability in response to a fluctuating stimulus, similar to biological neurons [265]. Naous *et al.* tested memristor-modeled stochastic neurons and synapses with MNIST (Modified National Institute of Standards and Technology) data for classification applications [260, 266].

4.3.1 Time-Voltage Stochasticity

As was clearly shown in the previous results, our resistive switching devices exhibit significant stochasticity in both Set and Reset transitions. This can be explained by the randomness of the silver ions dissolution and migration. Based on nanoparticle dynamic simulation and analytical estimations, Jiang *et al.* attributed the stochasticity in the switching delay time to the probabilistic detachment of Ag particles from the electrode [253].

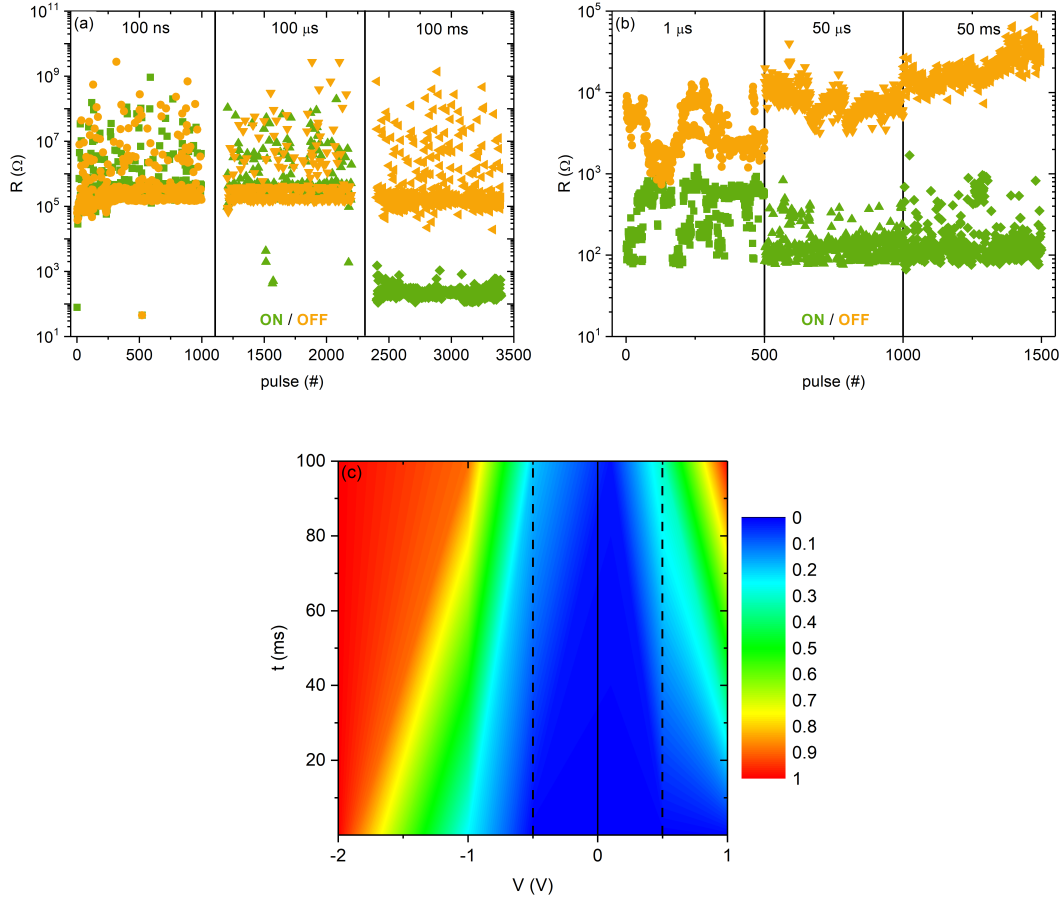


Figure 4.11 – (a) ON/OFF resistance states after each Set/Reset pulse for fixed 1 V and 100 ns, 100 μs and 100 ms of duration (from left to right) followed by a hard Reset of -2 V and 100 ms, over 500 repetitions. (b) ON/OFF resistance states after each Set/Reset pulse for fixed -2 V and 1 μs, 50 μs and 50 ms of duration (from left to right) preceded by a hard Set of 1 V and 100 ms, over 500 repetitions. (c) Switching probability distribution over pulse amplitude and duration for both Set ($V > 0$) and Reset ($V < 0$) transitions.

Here, we studied Set and Reset probabilities in a Si / SiO₂ / Ti / (25) / Pt (150) / Si (15) / Ag (5) / TiW (100) (nm) stack by tuning the applied voltage and pulse width. For that, we used a weak programming condition, which consists in applying a pulse amplitude/time smaller than the nominal switching amplitude/time, that ensures 100% switching probability. Note that a hard Set/Reset is implemented to switch the device to a complete ON/OFF state before the next cycle. We observed, as expected, that with the increase of the Set pulse duration from 100 ns to 100 ms at a fixed 1 V amplitude, the switching probability increases from 0.2% to 100%, as shown in Fig. 4.11(a). The resistance remains constant at a high resistance state ($\sim 10^6 \Omega$) for most of the pulses with duration below 100 ms and a well separated low resistance state ($\sim 10^2 \Omega$) for all Set pulses of 100 ms. A hard Reset of -2 V and 100 ms is implemented in this case. A similar behavior was observed for the Reset pulse duration [Fig. 4.11(b)]. For a fixed amplitude of -2 V and a duration of 1 μs the high resistance state is not clearly separated from the low resistance state ($\sim 10^2 \Omega$), while for 50 μs and 50 ms the separation is really well defined ($\sim 10^4 \Omega / \sim 10^2 \Omega$). These Reset pulses are preceded by a hard Set of 1 V and 100 ms.

The heat map in Fig. 4.11(c) presents the result of this study for different voltage amplitudes and durations, where the probability increases from cold (blue) to hot (red) colors. The higher the pulse amplitude and duration, the higher the switching probability. The behavior is almost symmetric regarding the voltage polarity. For example, if we look at the amplitude of 0.5 V (dashed vertical lines), for the same pulse duration the probability of switching is always higher for Set (positive) than for Reset (negative), which can be seen by the bigger proximity of the light blue band to the zero vertical axis on the right pane. This is also visible for pulses of 100 ms and 1 V amplitude, at which the probability for Set is 99.8% (red color) and 89.4% (orange color) for Reset. There seems to exist one practical limit from which the applied pulse does not result in a well defined separation of resistance states. It corresponds to very small voltages (< 0.1 V), at which the pulse duration gets too long (hundreds of ms). On the other hand, pulses of amplitude of -2 V almost guarantee a full switching (99.4% probability) even for the ultra short regime (< 100 ns).

4.4 Flexible Substrates

Additional demands of next-generation electronic devices include portability, wearability, transparency and lightweight. Therefore, novel flexible, nonvolatile, fast, compact and reliable data storage devices are being pursued [267]. Another possible application of nonvolatile memory devices for the IoT is as single-use disposable and biodegradable devices [268]. Flexible electronics is an emerging research field, which is being intensively investigated [269]. Memristive devices, as scalable two terminal devices, are highly promising for this type of applications.

Some of the popular choices for flexible and stretchable substrates include polyethylene terephthalate (PET) [270, 271, 272, 273, 274], plastic [275], paper [269, 268, 276, 277], polyimide (PI) [278, 279], metal foil [280], polyethersulfone (PES) [281, 282], parylene-C [283], textile [199] and muscovite [284]. As switching medium, different additional materials can also be used, such as polymers (PEDOT:PSS [285, 286, 287], pEGDMA [277, 288, 289] and PS-PMMA [290] for example), metal nanoparticles, 2D materials, organic small molecules, ferroelectric materials and many others [267]. Kim *et al.* were able to successfully fabricate a memristive memory array on top of a plastic substrate [275], while Wu *et al.* showed 3D artificial synapse networks on a PET substrate [291]. Furthermore, Lin *et al.* developed a memristive synapse transferable to different flexible substrates (e.g. PMMA, PEN, printing paper, glass dome hemisphere, pectin and PDMS), through a NaCl sacrificial substrate [292].

Here, we studied the Si-Ag system on three different flexible substrates: commercial and bacterial cellulose, and PET. Figure 4.12(a) shows the schematic representation of our devices, always with the Si/Ag/TiW stack on top of a flexible substrate. A curvature radius (r) of 3.5 mm was used to study the behavior on the bending mode [Fig. 4.12(b)]. The devices on the PET substrate were fabricated following the same process as that of the Si rigid substrate, although the deposition and etching steps were performed at a lower power not to damage the substrate. Note that, as the single step process is used and due to the thick bottom electrode, the transparency of the PET

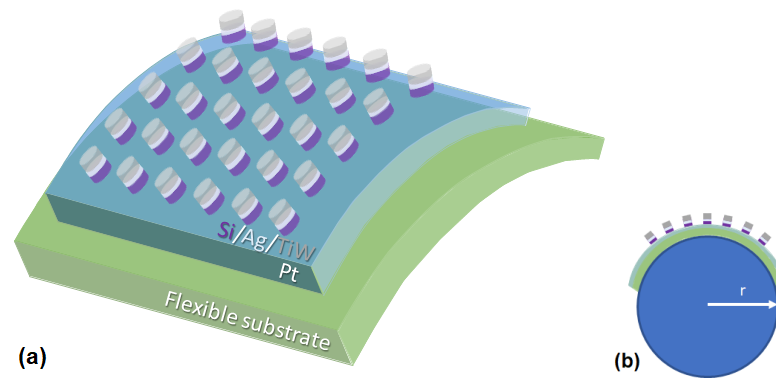


Figure 4.12 – (a) Schematic of the Pt/Si/Ag/TiW stack on a flexible substrate. The measuring bottom tip is placed on the Pt bottom layer close to the pillar and the top one directly on the pillar. (b) Radius of curvature (r) between two edges of the substrate. For a support of 7 mm in diameter, the radius is 3.5 mm.

substrate is not available. On the other hand, in the case of the cellulose substrate, no chemical solutions were used in the whole microfabrication process not to damage the substrates. The deposition was performed by IBD (Pt) and magnetron sputtering (Si, Ag and TiW), and the top electrodes with 300 μm in diameter were defined by a physical shadow mask.

4.4.1 Cellulose

A paper-based memory device is one of the most promising options for flexible electronics because cellulose is the most abundant renewable material. Cellulose is an environment-friendly, disposable substrate due to its biodegradability [268]. However, the choice of paper and compatible development process are the most crucial considerations for successful paper electronics. Difficulties regarding the use of paper include its rough and porous surface due to the fibrous nature. This is a major obstacle to obtain thin (microscale) and uniform devices, as well as the inability for ordinary paper to accommodate a conventional silicon process based on high temperature, wet cleaning and intense chemical treatment [277, 293]. One possible solution consists in fabricating the entire device on a silicon substrate and then transfer it to a paper substrate [277, 294].

ReRAM is one of the most suitable solutions for paper-related applications [293]. Celano *et al.* demonstrated a nonvolatile resistive memory composed of a 500 nm nanocellulose layer between ITO and Ag electrodes on top of a nanopaper substrate [268]. Nagashima *et al.* then showed an ultra flexible resistive memory based on Ag-decorated cellulose nanofiber paper [269] and Lien *et al.* demonstrated a resistive switching memory printed on commercial copy paper with titanium oxide as the switching layer [276].

4.4.1.1 Commercial cellulose

We tested the Ti (25) / Pt (100) / Si (20) / Ag (10) / TiW (100) (nm) stack on commercial paper for laser printers as substrate. The roughness of this substrate is high [Fig. 4.13(a)], so that 25/100 nm layers of Ti/Pt were deposited to guarantee a resistivity of $\sim 10^{-5} \Omega\cdot\text{m}$ [$(88 \pm 7) \Omega$ for 3.5

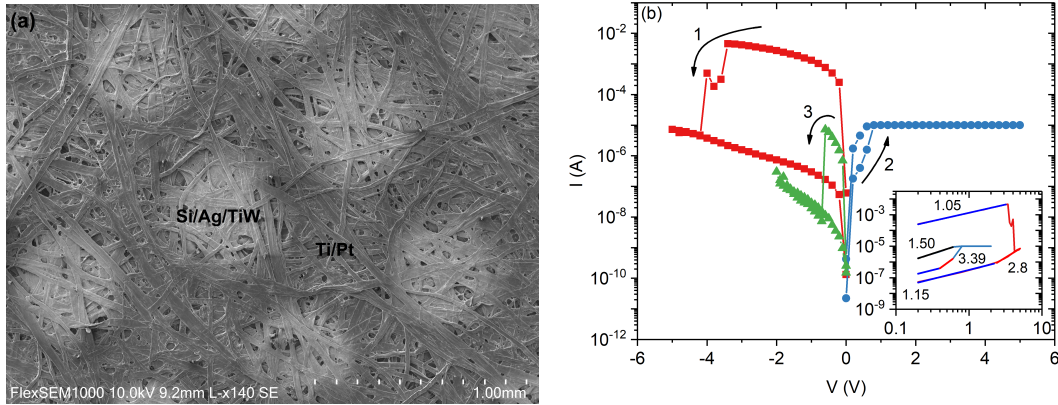


Figure 4.13 – (a) SEM image of the Pt/Si/Ag/TiW stack on a paper flexible substrate. (b) First electrical response of a measured device. The inset (in a log-log scale) shows the involved transport mechanisms.

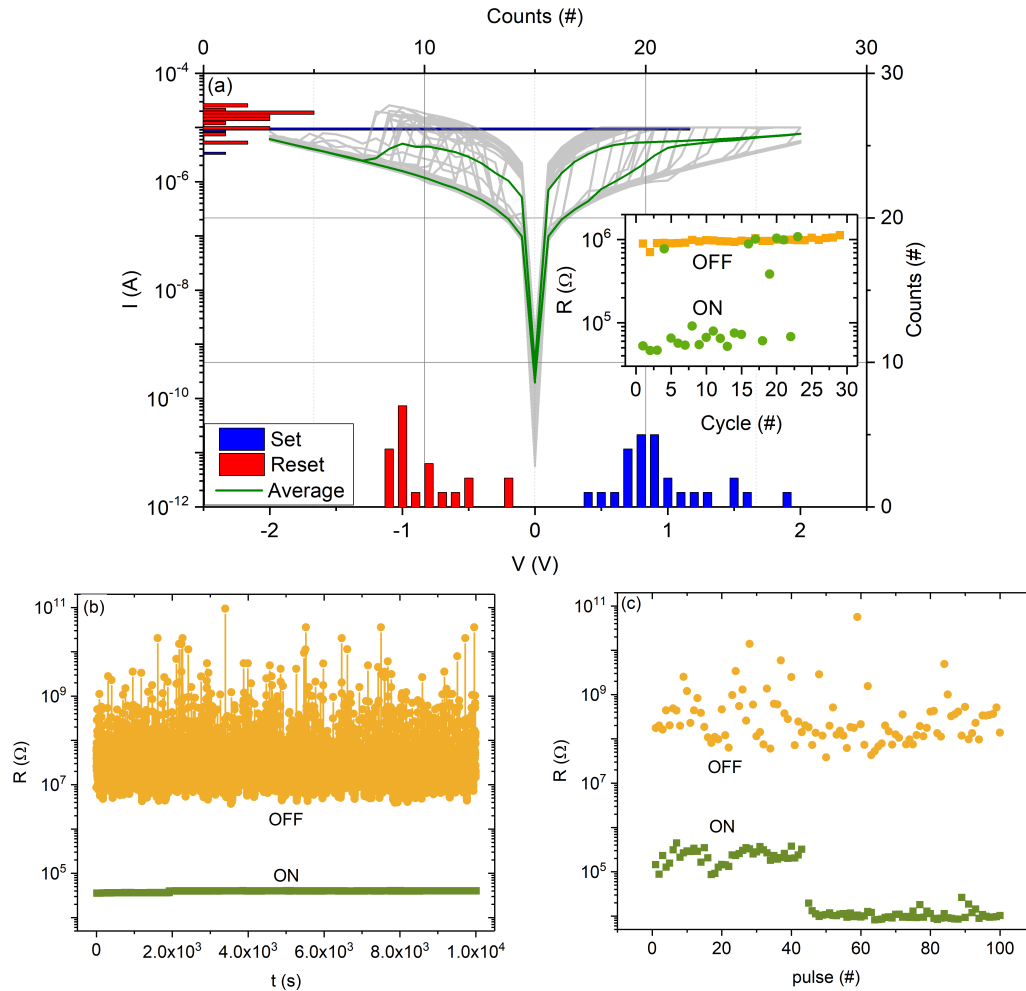


Figure 4.14 – (a) Consecutive I – V cycles in the flat configuration. The right (top) axis denotes the voltage (current) distribution. The inset shows the variation of the resistance of both ON and OFF states for each cycle, measured at 0.05 V. (b) Retention time for the OFF and ON resistance states up to 10^4 s, measured with 1 mV every 1 s. (c) Resistance states separation under pulsed operation mode ($V_{Set} = 2$ V, $I_C = 10$ μ A, $V_{Reset} = -2$ V, $t_{pulse} = 0.5$ s and $V_{read} = 10$ mV).

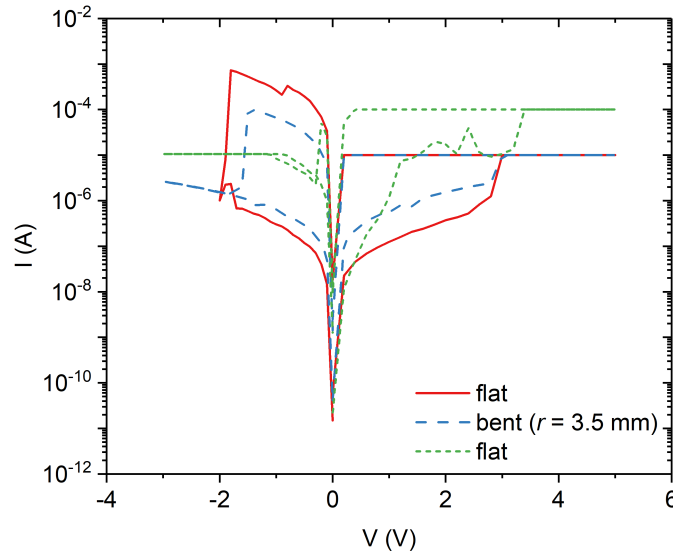


Figure 4.15 – I – V electrical response when the substrate is flat (red), bent (blue) in a curvature radius of 3.5 mm (orange) and again flat (green).

mm of parallel Au tips separation] versus $\sim 10^{-7} \Omega \cdot \text{m}$ [$(0.32 \pm 0.01) \Omega$] in a Si rigid substrate. During the RS measurements, the bottom tip is placed next to the top electrode to account for this roughness (poor conductivity). The devices show bipolar RS behavior without the need of a forming step. Unlike the case of Si substrates, the devices start in a low resistance state ($\sim 10^2 \Omega$) and switch to a high resistance state ($\sim 10^8 \Omega$) when a negative voltage (-3.4 V; step 1) is applied to the TiW electrode [Fig. 4.13(b)]. The high resistance state is recovered for positive voltages (0.6 V; step 2) and, after that, the Reset occurs at -0.6 V (step 3). The conduction mechanisms involved are Ohmic ($I \propto V$) for the ON state and space charge limited current ($I \propto V^m$, $2 \leq m \leq 4$) for the OFF state [inset of Fig. 4.13(b)]. The device only shows up to 20 voltage sweep cycles, with switching voltages below 2 V [$(0.96 \pm 0.35) \text{ V}$ for Set and $(-0.83 \pm 0.27) \text{ V}$ for Reset], as shown in Fig. 4.14(a). Our retention study demonstrated resistance states with a well defined separation ($10^7 \Omega / 10^4 \Omega$) up to 10^4 s [Fig. 4.14(b)]. Furthermore, pulsed operation mode, with $V_{\text{Set}} = 2 \text{ V}$, $I_C = 10 \mu\text{A}$, $V_{\text{Reset}} = -2 \text{ V}$, $t_{\text{pulse}} = 0.5 \text{ s}$ and $V_{\text{read}} = 10 \text{ mV}$, was successfully accomplished ($10^7 \Omega / 10^5 \Omega$) for at least 100 pulses [Fig. 4.14(c)].

Figure 4.15 shows the I – V behavior for both flat (before and after bending) and bent over a curvature radius of 3.5 mm configurations. The response is similar in both voltage and resistance values. The Set in the flat configuration after being bent was performed at $100 \mu\text{A}$ instead of the previous $10 \mu\text{A}$, since it would be volatile otherwise. Furthermore, the Reset occurs at a smaller voltage after bending. The first can be related with the device degradation over measurements and the second with the device variability, instead of directly with the bending process. Consecutive bending measurements were not performed, since each time the tip was disconnected from the top electrode, even in the flat configuration, the next measurement always started in the low resistance state ($\sim 10^2 \Omega$). This issue needs to be further investigated.

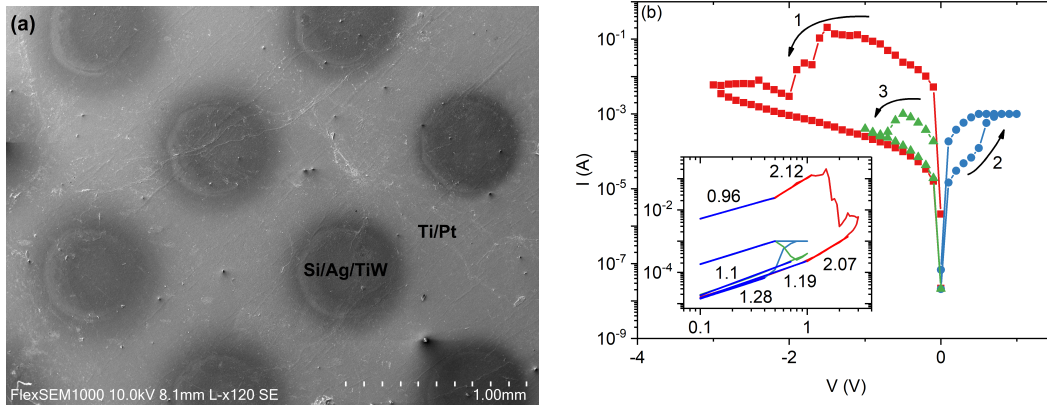


Figure 4.16 – (a) SEM image of the Pt/Si/Ag/TiW stack on a cellulose flexible substrate. (b) First electrical response of a measured device. The inset (in a log-log scale) shows the transport mechanisms involved.

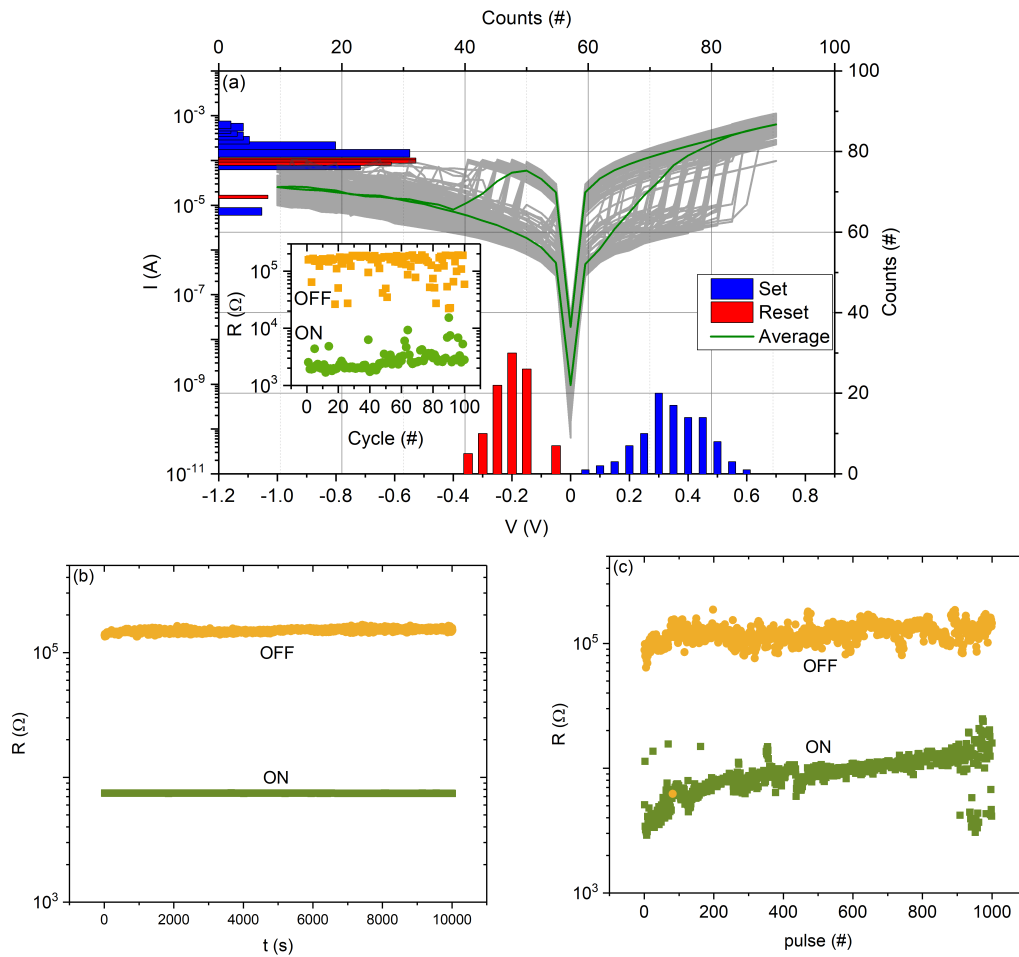


Figure 4.17 – (a) I – V cycles for Pt/Si/Ag/TiW on a cellulose flexible substrate over 100 voltage sweep cycles in the flat configuration. The right (top) axis denotes the voltage (current) distribution. The inset shows the variation of the resistance of both ON and OFF states for each cycle, measured at 0.05 V. (b) Retention time for the OFF and ON resistance states up to 10^4 s, measured with 1 mV every 1 s. (c) Resistance states separation under pulsed operation mode ($V_{Set} = 3$ V, $I_C = 1$ mA, $V_{Reset} = -3$ V, $t_{pulse} = 0.5$ s and $V_{read} = 1$ mV).

4.4.1.2 Bacterial cellulose

The same stack was studied on top of (nanofibrous) bacterial cellulose due to its biocompatibility and lower roughness ($\sim 2 \mu\text{m}$). The same Ti/Pt layers were deposited and a resistivity of $\sim 10^{-6} \Omega\cdot\text{m}$ [$(6 \pm 4) \Omega$ for 3.5 mm of parallel Au tips separation] was achieved. Figure 4.16(a) shows the surface of the stack on top of the bacterial cellulose. The bottom tip was placed next to the top electrode and tip. As before, the devices start in a low resistance state ($\sim 10 \Omega$) and switch to a high resistance state ($\sim 10^3 \Omega$) when a negative voltage (-1.5 V; step 1) is applied to the TiW electrode. The low resistance state is recovered for positive voltage (0.5 V; step 2), although it has a higher value ($\sim 10^3 \Omega$) than the pristine state, and the following Reset occurs at -0.5 V [step 3; Fig. 4.16(b)]. The conduction mechanisms observed for the RS are Ohmic for both ON and OFF states in Set and Reset cycles, except for higher voltages in the first cycle (step 1), where SCLC plays a role [inset of Fig. 4.16(b)]. Despite the small separation between the resistance states, the device supports at least 100 voltage sweep cycles, showing switching voltages below 1 V (0.35 ± 0.11 V for Set and -0.2 ± 0.07 V for Reset), as shown in Fig. 4.17(a). A retention study showed well defined resistance states, although with small separation ($\sim 10^5 \Omega / 10^4 \Omega$), up to 10^4 s [Fig. 4.17(b)] and the pulsed operation mode was successful ($\sim 10^5 \Omega / 10^4 \Omega$) for 999/1000 pulses [Fig. 4.17(c)]. As in the previous case, each time the tip is disconnected from the top electrode, even in the flat configuration, the next measurement starts in the low resistance state ($\sim 10^2 \Omega$).

Figure 4.18(a) shows the I–V behavior averaged over 10 consecutive sweep cycles for both flat (full line) and bent (dashed line; over a curvature radius of 3.5 mm) configurations. Although higher switching voltages are needed in the bent mode, the response in resistance is similar, as it is also shown in the inset for the resistance states over the 10 cycles. Besides the higher voltages in the bent mode, their distribution is also larger [Fig. 4.18(b)]. This difference in the switching voltages may be explained by a decrease in the conductivity when the substrate is not flat. Furthermore, note that a metal cylindrical bending support had to be used to dissipate the generated heat since, when a plastic one was used, the substrate degraded (melted). This is an issue to take into consideration in the future, since the substrate may be in contact with less conductive supports in real applications.

4.4.2 Polyethylene Terephthalate

We deposited our Si/Ag/TiW stacks both directly on polyethylene terephthalate (PET), after Ti (5) / Pt (25) nm (PET/Pt), or on top of an indium tin oxide (ITO) conducting layer on the PET substrate, with (PET/ITO/Pt) and without (PET/ITO) the Ti/Pt layers below. Shang *et al.* observed an extension on the mechanical failure threshold when replacing the Pt electrode by ITO [274]. However, in our case, due to adhesion problems (ITO peeling), the PET/ITO and PET/ITO/Pt devices showed poor reliability. Figure 4.19(a) shows several arrays on the PET substrate in the bending mode. All the devices show bipolar resistive switching.

For an ITO bottom electrode [Fig. 4.19(b)], the devices start in a low resistance state ($\sim 10^2$

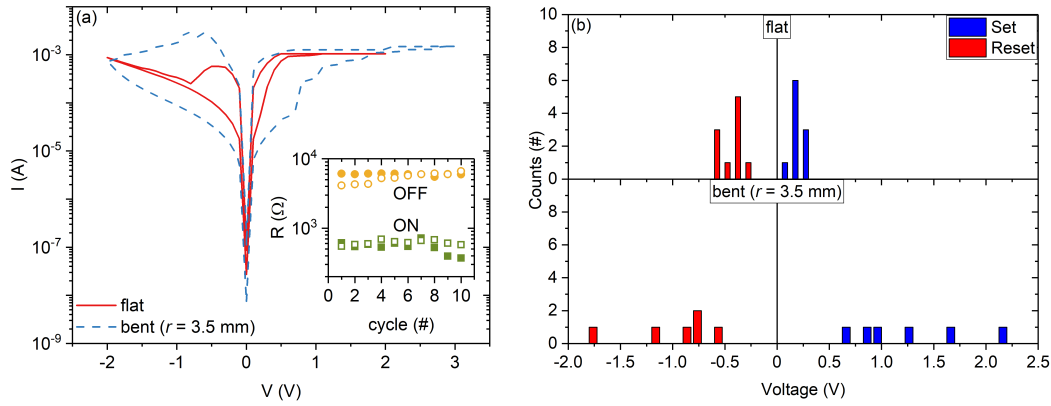


Figure 4.18 – (a) I - V characteristic averaged from 10 consecutive measurements when the substrate is flat (red) or bent (tension) under a curvature radius of 3.5 mm (blue). The inset shows the resistance states over 10 voltage sweep cycles for both flat and bent cases (filled and open symbols, respectively). (b) Distribution of Set and Reset voltages for 100 consecutive cycles in flat (top) and 10 in bent (down) modes.

Ω) and switch to a high resistance state ($\sim 10^3 \Omega$) when a negative voltage (-3.8 V; step 1) is applied to the TiW electrode. The low resistance state is recovered for positive voltage (0.25 V; step 2), although higher than the pristine state, and then Reset at -0.3 V (step 3). Regarding the conduction mechanisms, the cycles are always in the Ohmic regime [inset of Fig. 4.19(b)]. Note that although technically no electroforming step was needed, as the device was already in the ON state, the first switching voltage is considerably higher than the following ones. This may indicate some initial and permanent change in the device. Consecutive voltage sweep cycles (50) show switching voltages below 1 V [(0.37 ± 0.15) V for Set and (-0.37 ± 0.22) V for Reset], as shown in Fig. 4.20.

When using Pt as bottom electrode [Fig. 4.19(c)], the devices also start in a low resistance state ($\sim 10^2 \Omega$) and switch to a high resistance state ($\sim 10^7 \Omega$) when a negative voltage (-4.4 V; step 1) is applied to the TiW electrode. The low resistance state is recovered for positive voltage (2 V; step 2), although higher ($\sim 10^4 \Omega$) than the pristine state, and the following Reset occurs at -1 V (step 3). Unfortunately, the operation is not satisfactory and only a few cycles are achieved in some devices.

Interestingly, for the case of ITO/Pt bottom electrodes [Fig. 4.19(d)], the devices start in a high resistance state ($\sim 10^5 \Omega$) and switch to a low resistance state ($\sim 10^4 \Omega$) when a positive voltage (1 V; step 1) is applied to the TiW electrode. The high resistance state ($\sim 10^5 \Omega$) is then recovered for negative voltages (-0.4 V; step 2). This is also the configuration showing poorer results, likely due to the thicker stack used that resulted in lower adhesion. A further improvement of the fabrication process is thus needed.

4.4.3 Discussion

Table 4.1 summarizes the parameters involved for all types of substrates studied. The substrate showing the most similar results with the rigid Si substrate is the bacterial cellulose in both operating

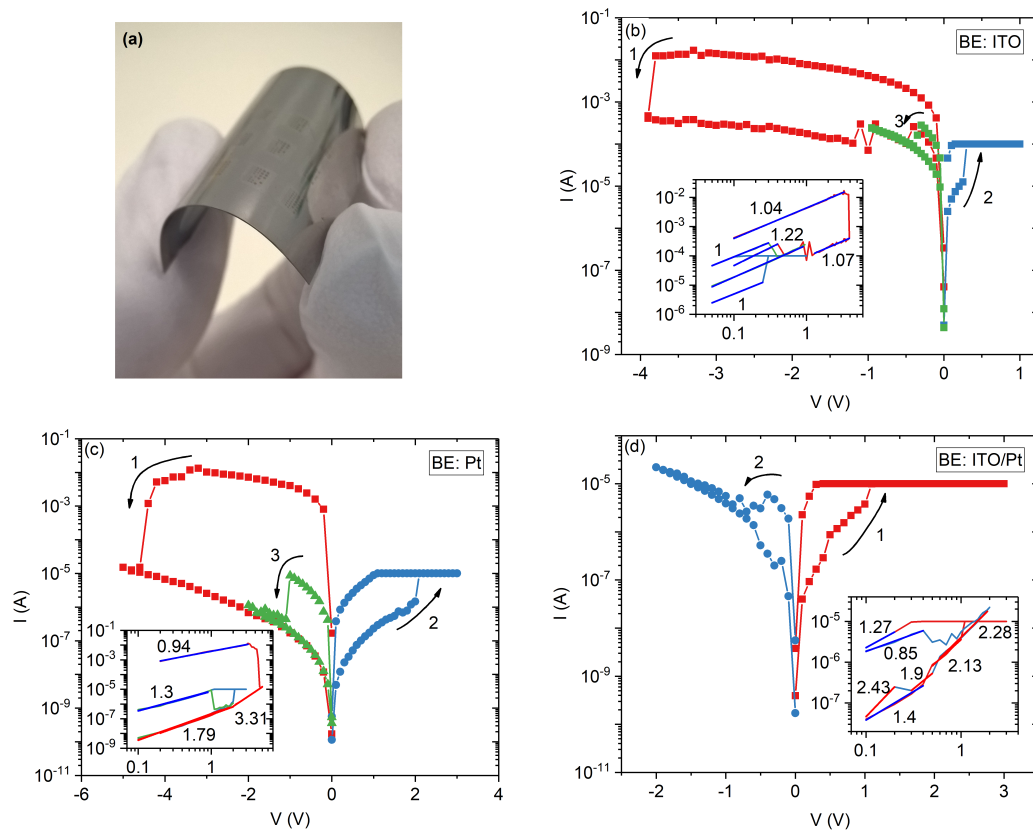


Figure 4.19 – Si/Ag/TiW stack (a) on a PET flexible substrate and first electrical response for (b) ITO, (c) Pt and (d) ITO/Pt bottom electrodes. The insets (in a log-log scale) show the mechanisms involved in the electrical transport.

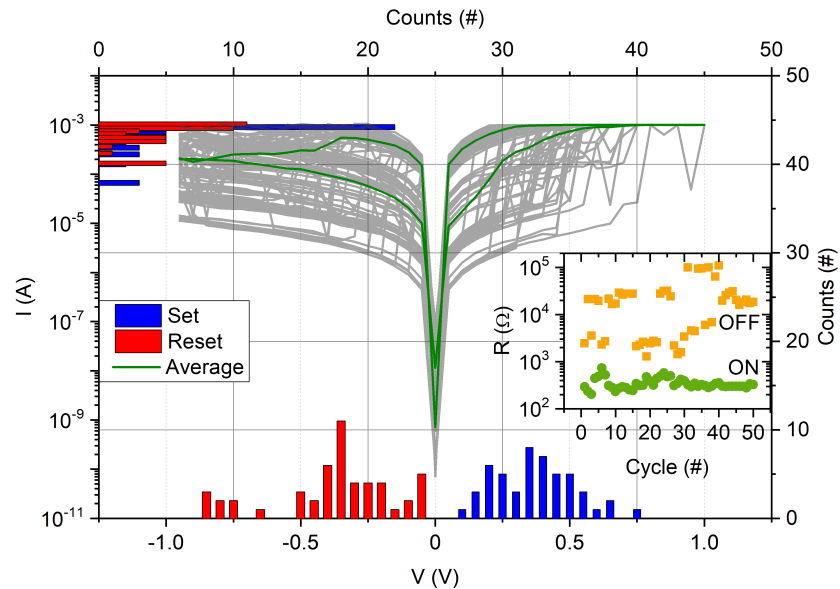


Figure 4.20 – Repetition over 50 voltage consecutive cycles for ITO bottom electrode. The right (top) axis denotes the voltage (current) distribution. The inset shows the variation of the resistance of both ON and OFF states for each cycle, measured at 0.05 V.

Table 4.1 – Main resistive switching parameters (first cycle) for the Si/Ag/TiW stack on different substrates.

Substrate	Initial Resistance (Ω)	$V_{Initial}$ (V)	V_{Set} (V)	V_{Reset} (V)	R_{ON} (Ω)	R_{OFF} (Ω)
Si/Pt	3.7×10^3	-	0.4	-0.45	490	3.7×10^3
commercial cellulose/Pt	801	-3.4	0.6	-0.6	1.2×10^5	1.0×10^8
bacterial cellulose/Pt	19	-1.5	0.5	-0.5	543	6.3×10^3
PET/ITO	240	-3.8	0.25	-0.3	1.1×10^3	5.3×10^3
PET/Pt	250	-4.4	2	-1	2.5×10^5	2.0×10^7
PET/ITO/Pt	1.1×10^5	-	1	-0.4	4.4×10^4	9.0×10^5

voltages and resistance states, despite the initial low resistance state ($10^1 \Omega$ versus $10^3 \Omega$). Furthermore, all of the other substrates show both low and high resistance states higher than the rigid Si substrate case. Commercial cellulose shows the largest resistance ratio ($10^8 \Omega / 10^5 \Omega$) and the initial voltage needed in the case of cellulose is usually lower than the PET one. Looking at the bottom electrode in the PET substrate, ITO needs lower operation voltages (<0.5 V), while Pt needs higher voltages (>1 V).

4.5 Conclusions

We obtained bipolar resistive switching without the need for an electroforming process in Ti (25) / Pt (150) / Si (20) / Ag (5) / TiW (100) (nm) stacks in different substrates. For rigid Si substrate, the devices operate in the sweeping and pulsed modes, and are stable over 100 cycles with a clear separation between resistance states. We also studied the dependencies of the ON resistance, resistance ratios and Set/Reset voltages variability on the current compliance. Furthermore, we used a simple model in the charge–flux representation to relate the Reset time with the Reset voltage and modeled the current–voltage curves. Regarding the stochasticity of the resistive switching behavior, we performed a study on the probability of switching under pulses in the soft mode operation. As expected, the higher the pulse duration and amplitude, the larger the probability of switching. Finally, we implemented this type of stack in flexible substrates, namely commercial and bacterial cellulose, and PET. The devices also showed bipolar resistive switching, even when bent under a curvature radius of 3.5 mm. Unlike the rigid substrate, some of the devices fabricated on top of flexible substrates start on a low resistance state and all of them recover this state every time the measuring tip is moved on the top electrode.

CHAPTER 5

Artificial Neural Networks Simulations

Knowing all the difficulties involved in a hardware implementation of memristive devices (fabrication and variability, for instance), numerical simulations are a great tool to study complex systems and try to optimize them in a more controlled environment, in a faster and cheaper way.

In this chapter we will detail the implemented simulations of memristors-based Willshaw and Perceptron Artificial Neural Networks. The first was performed on *LTspice*ⁱ while the later was implemented in *Python*.

5.1 Willshaw Network

One of the possible applications of the memristor is as a synapse in neuromorphic computation [295, 18, 296, 297, 298, 299]. Artificial Neural Networks are a popular subject within this field, and one example of such networks is the Willshaw hetero-associative memory [127]. The Willshaw network is a content-addressable associative memory system, known for its high capacity, robustness to noise and auto-completion properties, designed to model how information can be found in synapses in the nervous system. It comprises an input vector mapped into an output vector via a matrix of binary synapses [127] (here memristors), whose modification (learning) is performed in a single step. Its implementation using memristors has been considered before [121], albeit with a different aim than the one presented here.

Of particular interest when assessing a memristor-based Willshaw network is the case where defective elements are present. Nanodevices inherently have high defect rates, so that any application that makes use of them needs to be sufficiently robust to accommodate faults [300, 301]. There are some studies on the causes and consequences of defects on memristors, namely concerning the fabrication conditions of individual devices [302], crossbars with static defects as logic blocks [303, 304] and image recognition using adaptation [301, 305, 306], but not for instant-training and storage crossbar arrays. One of the most common defects, resulting from the lithographic process, is the inability to switch between resistive states, leaving the memristor permanently in the OFF (*stuck-at-0*) or in the ON (*stuck-at-1*) states. Previous studies have addressed the impact of this

ⁱAnother *Python* algorithm developed by us is made available to the public for particular testing, implementation and further development [140, 141].

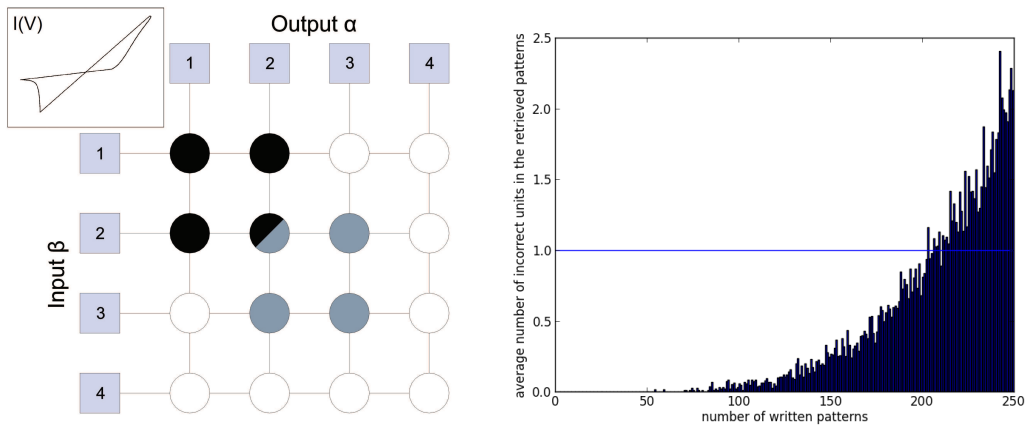


Figure 5.1 – (a) 4×4 Willshaw network arranged in a crossbar configuration; squares represent neuron units from two populations: β - input and α - output; white circles represent memristors in the OFF state and shaded circles represent memristors in the ON state. Different shades represent different patterns. Two pattern associations are depicted: $\{\beta_1, \beta_2\} \rightarrow \{\alpha_1, \alpha_2\}$ and $\{\beta_2, \beta_3\} \rightarrow \{\alpha_2, \alpha_3\}$. Each input neuron is connected to the input of all memristors along that line, and each output neuron is connected to the output of all memristors along that column. The inset shows the I–V characteristic of the used memristor model. (b) Average number of incorrect units in the retrieved patterns for 50 random repetitions.

type of defects in different contexts [301, 304, 307, 308] but Willshaw networks have so far been overlooked.

5.1.1 Principle of Operation

Here we present simulations of a memristor-based Willshaw network, both with and without defects. We study how defects affect the capacity and robustness to noise of the network, and how this determines the manner in which the network should be operated. We also address the effects of variability (distribution of values) on the most relevant switching parameters of individual memristors (threshold voltage, ON/OFF resistances) on the network's performance. The network is arranged in a nanowire crossbar configuration. Extensive studies have considered the implementation of this architecture, including additional CMOS circuitry [121, 309, 310, 311] and sneak and leakage currents issues [312, 313, 314]. While the analysis of the former falls beyond the scope of this work, the latter is inherently regarded within our simulations with the results already taking them into account. Our results show that even with relatively low OFF/ON resistance ratios (and far below those obtainable today), the related sneak path and leakage currents do not significantly impair memory performance, which attests to the resilience of this type of memory network. These results should then be seen as the lower bound for the performance of a Willshaw network in the presence of defective memristors.

The simulations were performed in *LTspice* [315], using the memristor model developed by Pino et al. [inset of Fig. 5.1(a)] [139]. This model was chosen for its well defined voltage threshold, meaning that when voltages above this threshold are applied to the memristor its state is switched from OFF (here 1.2 k Ω) to ON (160 Ω ; write operation). Voltages below threshold do not alter the memristor conductivity, thus allowing for a straightforward read operation. The network can be

reset by applying a negative voltage above threshold to all memristors.

Figure 5.1(a) shows a 4×4 Willshaw network to illustrate its operation. It comprises two neuron populations (β - input and α - output) with the same number of units, $N_\beta = N_\alpha = 4$, and a matrix of synapses arranged in a crossbar configuration. In our simulations we use voltage sources as neurons and memristors as synapses. The value of the voltage source encodes the neuron state, which is also binary: active or inactive. Each association μ can be represented as an input vector β^μ mapped onto an output vector α^μ , where the number of active units in each pattern is defined by M_β and M_α . For example, in the association $\{\beta_1, \beta_2\} \rightarrow \{\alpha_1, \alpha_2\}$, neurons $\beta_1, \beta_2, \alpha_1$ and α_2 are simultaneously active, while all others are inactive ($M_\beta = M_\alpha = 2$).

5.1.1.1 Method

The training protocol for the writing operation initiates with all memristors in the OFF state (except for the *stuck-at-1* cases). Then, for each association, the activity patterns are simultaneously applied by the appropriate (matching) units in the input and output populations, and the synapses are switched ON only at the nodes where the signals coincide. This is achieved using an activation protocol where active input neurons apply a positive voltage, below the synapse's writing threshold, while active output neurons apply a negative voltage value, symmetrical to the input neurons' voltage. The synapse in the intersection will be subject to the sum of the corresponding modules, which is above its writing threshold, so that it switches to the ON state.

After K associations ($\mu = 1, \dots, K$), the binary state of each memristor/synapse between unit b from the input population β and unit a from the output population α is thus given by $w_{ba} = \min(1, \sum_{\mu=1}^K \beta_b^\mu \alpha_a^\mu)$. A value $w = 0$ implies a high resistance R_{OFF} , while $w = 1$ corresponds to the ON state (low resistance R_{ON}).

For the reading operation, the input pattern (hereafter referred to as *cue*) is applied by the input neurons only, so that the voltage is always kept below the writing threshold. Each output neuron will receive a current that is the sum of the contribution of each synapse along that column. Synapses in the ON state, having lower resistance, yield higher current values, which allow to distinguish the neurons that belong to the association. Here one assumes that $1/R_{ON} \gg M_\beta/R_{OFF}$. An output neuron is considered to be active if the sum of the contribution of the input synapses is above a reading (current) threshold T . If V_{read} is the voltage applied in the reading operation, the value for T that maximizes capacity is $M_\beta \times V_{read}/R_{ON}$ (in amperes). Lower T values indicate that the memory system has increased robustness to spurious bits in the input population (when 1 or more bits of the cue are incorrect) and improved auto-completion properties, although at the cost of a reduced memory capacity.

In Fig. 5.1(a) the written associations were $\{\beta_1, \beta_2\} \rightarrow \{\alpha_1, \alpha_2\}$ and $\{\beta_2, \beta_3\} \rightarrow \{\alpha_2, \alpha_3\}$. The first step in our simulations is to write all the associations, and only then perform the reading operation. After the writing operation, the shaded nodes (memristors) are in the ON state, while the others remain OFF. In the reading stage, for (β_1, β_2) , only output neurons (α_1, α_2) will have two

active synapses, while for (β_2, β_3) this occurs only for (α_2, α_3) , thus recalling the correct written associations if $T = 2$ (in units of V_{read}/R_{ON}).

As we will see further ahead, there are cases where a different reading threshold should be used. If we repeat the above reading operation, but with $T = 1$, the resulting output would be: $\{\beta_1, \beta_2\} \rightarrow \{\alpha_1, \alpha_2, \alpha_3\}$ and $\{\beta_2, \beta_3\} \rightarrow \{\alpha_1, \alpha_2, \alpha_3\}$. In this case, the recalled associations are incorrect, as in each output an extra neuron was identified as being part of the pattern. The error is here defined as the number of output units with incorrect values (Hamming distance). Under this definition, the error in the above example is 1 (note that a missing neuron in the output vector also gives an error count of 1). In our simulations the output error is used to measure the performance of the network [Fig. 5.1(b)]. To improve visualization, the error values are presented in logarithmic scale, with a fixed translation factor applied to match the value 1 in the error scale to the unitary Hamming distance (i.e. a value of 1 in the error scale corresponds to an output error count of 1).

For our simulations we used a 128×128 network, with association vectors of size 7 (both input and output), that is $N_\beta = N_\alpha = 128$ and $M_\beta = M_\alpha = 7$. M_β and M_α are chosen in order to optimize memory capacity ($M = \log_2 N$) [127]. With this parameterization, the memory capacity K^{max} of the network is [127]:

$$K^{max} = \frac{N_\beta N_\alpha}{M_\beta M_\alpha} \ln 2 \approx 231, \quad (5.1)$$

which is defined as the maximum number of associations it can store, while keeping an average reading error count equal to or less than 1 when using a read out threshold of $T = M_\beta$ (in V_{read}/R_{ON} units). This standard was also used to measure the network's robustness to noise.

We are interested in studying how the capacity of the network and its robustness to noise are affected when *stuck-at-0* and *stuck-at-1* defects [301] are present in the synaptic matrix. The defects were randomly introduced in the network with different probabilities, being the patterns also generated randomly. Videos depicting the memristor-based Willshaw network dynamics under *defect-free*, *stuck-at-0* and *stuck-at-1* conditions are available in Ref. [316]. Furthermore, we tested the effect of the variability of the most relevant switching parameters of individual memristors (threshold voltage and ON/OFF resistances) on the robustness of the network, this time in the absence of defects. For statistical significance, SPICE simulations were performed ten times and an average reading error count and corresponding deviation were extracted.

5.1.2 Results

We started by assessing the capacity of the network in a *defect-free* scenario, in order to compare it with the defective cases. We found the capacity of the network to be reasonably close to the theoretical value: approximately 205 associations ($K^{max} = 231$) for a $T = 7$ reading threshold, as shown in Table 5.1. The effective capacity value approaches the theoretical one only for a very large network.

We then proceeded to test how *stuck-at-0* and *stuck-at-1* defects affect the capacity of the network (Table 5.1), studying defect percentages from 1% up to 10%. One immediately sees that

Table 5.1 – Capacity of a 128×128 network for control (defect-free) and different probabilities of both stuck-at-0 and stuck-at-1 defects. The null capacity indicates that the average error count was already above 1 for the first stored association.

	defect-free	stuck-at-0						stuck-at-1			theoretical
		1%	2%	5%	7%	9%	10%	2%	5%	10%	
$T = 7$	205 ± 2	183 ± 3	0	0	0	0	0	205 ± 3	193 ± 4	176 ± 4	231
$T = 6$	118 ± 3	123 ± 5	116 ± 4	114 ± 6	100 ± 4	70 ± 7	0	111 ± 3	104 ± 4	91 ± 3	197

a scenario of only 2% of *stuck-at-0* defects has already a drastic effect on the network's capacity as the memory system can no longer operate at $T = 7$: all associated patterns are retrieved with an average error count above 1. Nevertheless, reducing the reading threshold to $T = 6$ (gaining error correction capabilities), it is possible to recover a performance which is close to the *defect-free* condition. However, a critical point to notice is that above 9% of *stuck-at-0* defects the network is no longer viable.

For the case of *stuck-at-1* memristors one sees that the capacity of the network is close to the *defect-free* case for the considered reading thresholds up to 5% of defects. The capacity then decreases for a 10% defect percentage although, for both reading thresholds, the network remains operational. We thus conclude that the network's capacity is, to some extent, resilient to the mild presence of *stuck-at-1* defects (by still allowing $T = M_\beta$).

These results show that the type and number of defects strongly constrains the threshold setting strategy, and that this parameter is what directly determines the network's capacity.

We then tested how different probabilities of *stuck-at-0* and *stuck-at-1* defects affect a network at 25% capacity (57 patterns, calculated for $T = 7$), in order to avoid overload effects. In Fig. 5.2 we see the average error counts for different probabilities of both types of defects. As the

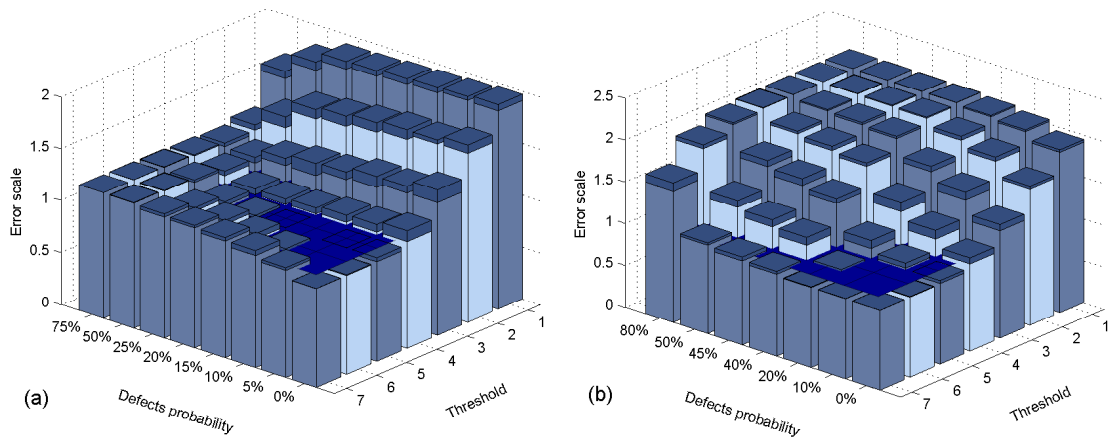


Figure 5.2 – Average error counts in the 128×128 network for different reading thresholds, as a function of defects percentage: a) percentage of stuck-at-0 and b) of stuck-at-1 defects. The standard deviations for the error counts are represented in dark on top of each bar. The blue plane helps visualize when the error count is below 1.

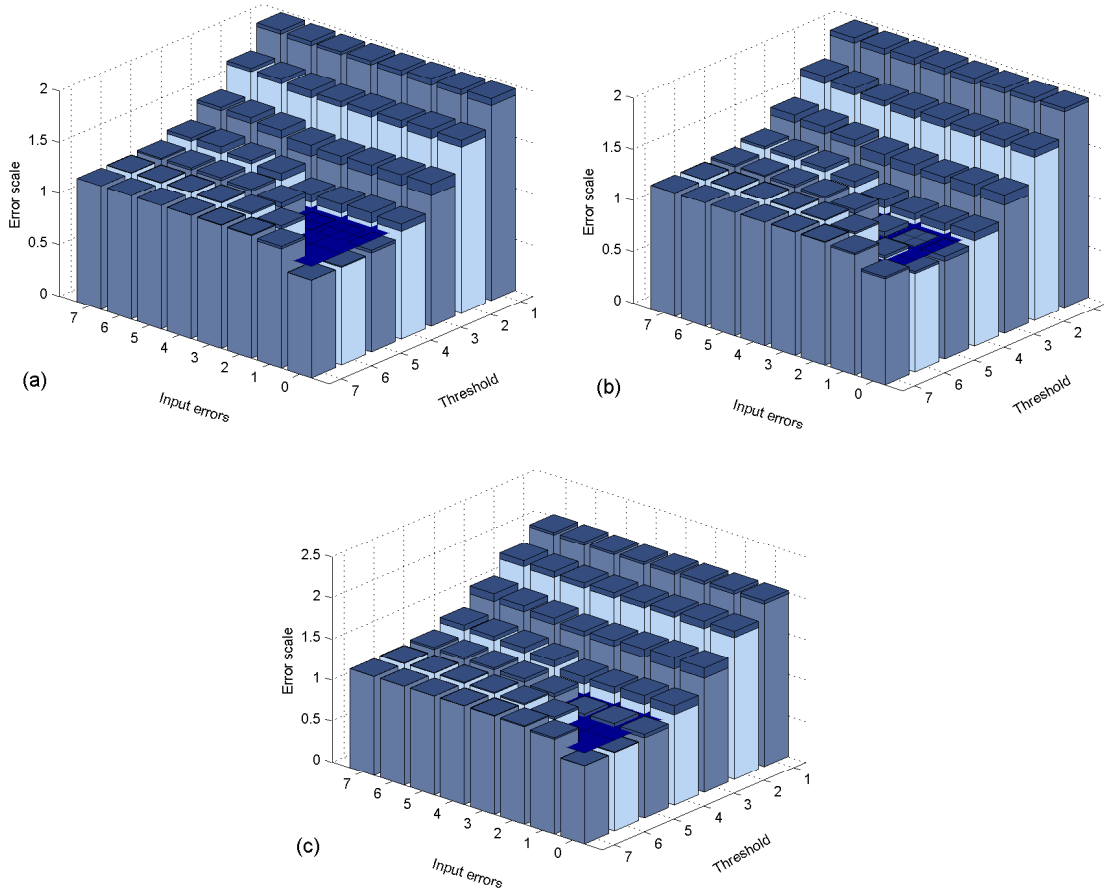


Figure 5.3 – Response of a 128×128 network to noise in the cue: a) control (defect-free), b) 5% probability of stuck-at-0 defects and c) 5% probability of stuck-at-1 defects. The standard deviations for the error counts are represented in dark on top of each bar. The blue plane helps visualize when the error count is below 1.

number of *stuck-at-0* defects increases, the reading threshold T must be decreased to reduce the reading error [Fig. 5.2(a)]. In fact, close to 20% of defects we can still have a mean error count below 1 for a reading threshold $T = 5$, which corresponds to a theoretical $K^{max} \sim 159$. For higher defect numbers the error count is always greater, and for very large defect numbers the choice of reading threshold becomes irrelevant. Note that, in accordance with Table 5.1, with 5% of defects a threshold of $T = 7$ never allows an average error count below 1. Interestingly, the network responds to *stuck-at-1* defects in quite a different way [Fig. 5.2(b)]. For a $T = 7$ threshold the network is insensitive to the defects up to some extent. This is understandable, as this is similar to the situation of using a network with previously stored associations. This holds until approximately 45% of defects, above which a large increase in the error count is seen. It is worth noting that the Willshaw network maximum capacity is reached when 50% of the synapses are activated. For all other reading thresholds the error count is quite large when compared with the *stuck-at-0* scenario.

We further tested the networks' robustness to noise in the cue for the *defect-free* and with 5% of *stuck-at-0* or *stuck-at-1* defects cases. Again the capacity was kept at 25%. The defect probability of 5% was used as an overestimation of errors in the fabrication process, as this is expected to be

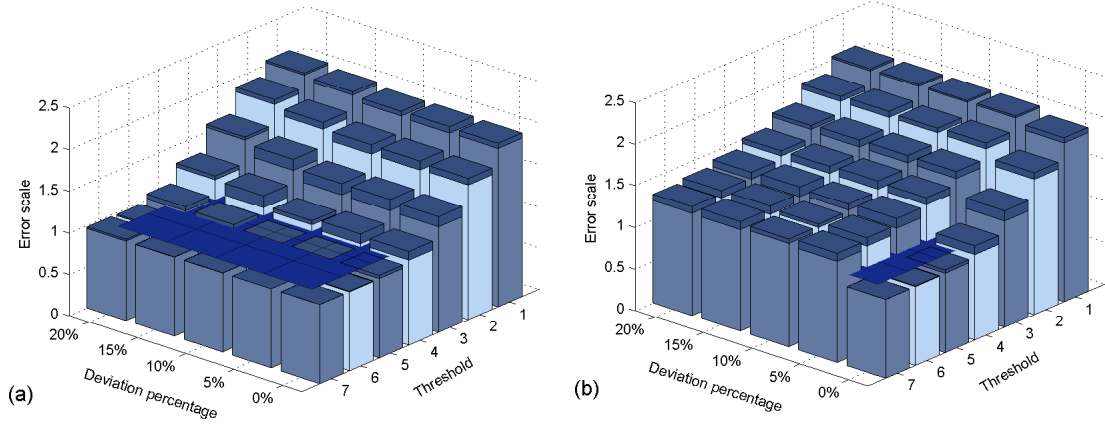


Figure 5.4 – Robustness to (a) threshold voltage and (b) ON/OFF resistances distributions of a 128×128 network. The standard deviations for the error counts are represented in dark on top of each bar. The blue plane helps visualize when the error count is below 1.

closer to 2% for a mature technology [309]. For the *defect-free* case, as seen before, a maximum reading threshold of 7 yields the lowest error count in the absence of noise [Fig. 5.3(a)]. However, when just 1 spurious bit is introduced in the cue, the output error count increases sharply for $T = 7$, and one has to reduce it to 6 to minimize the error. A maximum $T = 7$ leaves no margin to accommodate the noise, as it requires all inputs to be correct. Accordingly, as noise increases, one has to reduce the reading threshold to minimize the error count. However, with 3 spurious bits in the cue, an average error count below 1 can never be obtained.

We can see in Figs. 5.3(b) and 5.3(c) that this trend is similar for the two types of studied defects (at 5%), although the reduction of the threshold in these cases allows one to accommodate only 1 spurious bit in the cue. In the case of *stuck-at-0* defects this occurs for $T = 5$ (theoretical $K^{max} \sim 159$), while for *stuck-at-1* it occurs for $T = 6$ (theoretical $K^{max} \sim 197$). A similar study was performed for both types of defects at 2% and 10% (not shown). For 10% of *stuck-at-0* defects, an average error count below 1 is only obtained without spurious bits and a threshold of 5. Furthermore, in the case of 2% defects, the network works up to a maximum of 1 spurious bit for $T = 5$.

Finally, the effects of memristor parameters variability (threshold voltage, and ON/OFF resistances) on the robustness of the network was studied. In these simulations the parameters were individually drawn from a Gaussian distribution with a predefined standard deviation (σ). For the threshold voltage, as shown in Fig. 5.4(a), the error count only starts to increase when the variation goes above 15% and for small T values. The 1 error count criteria is maintained up to $\sigma = 20\%$ for $T = 6, 7$. On the other hand, the network is quite sensitive to the distribution of the ON and OFF resistances, being the error count higher than 1 already for $\sigma = 5\%$, remaining approximately constant up to $\sigma = 20\%$ [Fig. 5.4(b)]. This shows that, within devices, resistance rather than threshold voltage variations is the most critical parameter to control to avoid the network's deterioration. Also, the condition $1/R_{ON} \gg M_{\beta}/R_{OFF}$ plays an important role in improving the robustness to

resistances variation.

5.1.3 Discussion

Memristor-based hardware is in active development and it is necessary to understand its implications and devise strategies to cope with memristor defects and variability. We presented a study on the performance of a memristor-based Willshaw network in the presence of two common defects, *stuck-at-0* and *stuck-at-1*, and concluded that the type and estimate of the fraction of defective memristors strongly constrains the threshold setting strategy. This, in turn, sets the network's capacity and its robustness to cue noise. In summary, we observed that the impact of the two types of analyzed defects in memory performance is distinct: *stuck-at-1* defects are more amenable and can more easily be compensated through an increase in the readout current threshold, as they show a slower decrease of the network capacity with increasing defect percentage. Furthermore, we found that it is critical to control device-to-device resistance variance, more than threshold voltage variance. Our findings show that memristor defects and variability do not imply (to some extent) the catastrophic failure of a network's operation and can in fact be overcome by using a well-informed operation strategy.

In this work a static threshold mechanism was used to select the active output units, but our results can be combined with more sophisticated strategies for setting the readout threshold, leading to improvements in network performance [317, 318]. However, these strategies, such as winners-take-all or minimization of output error, require prior knowledge about size of output patterns, unit usage, number of stored patterns and noise levels in cue (and therefore impose more complex readout systems).

5.2 Perceptron

The perceptron is a neural network classifying algorithm based on the information processing mechanism of a single neural cell (neuron). As a neuron receives input signals via its dendrites, passing each other electrical signals higher than the threshold potential, the perceptron receives inputs first from the training data (examples with known solution), that are then weighted and computed into an activation equation. Using the step function as a transfer function, the output value (prediction) is then calculated, as well as the error. The weights are estimated for each input of the training data using the stochastic gradient descent (first-order iterative optimization algorithm) learning rule, which updates the weights of a neural network by trying to minimize the error in the output. In other words, this optimization procedure finds the set of weights that result in the smallest error for the training data in a finite number of steps [319]. The perceptron is the simplest algorithm with similarities with biological learning: neurons also modify their connectivity and adapt connection strengths over time [85]. The perceptron algorithm was the first to achieve Artificial Intelligence [113], being used in many practical applications such as pattern recognition (fingerprint and iris) [112, 115, 116], classification of medical images (cancer) [112], forecast ozone

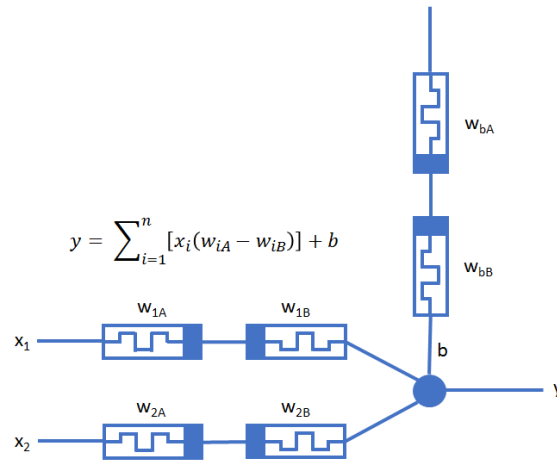


Figure 5.5 – Single-layer memristive perceptron schematics for 2 inputs (x_1 and x_2), 1 bias (b) and 1 output (y), with 4 memristors as weights (w_{1A} , w_{1B} , w_{2A} and w_{2B}). Electrical connections are simplified.

and nitrogen dioxide levels measurement in real-time [118] and many others.

The single-layer perceptron, i.e. with no hidden layers between input and output, is the simplest kind of neural network able to process information for pattern classification and decision making of linearly separable patterns. Therefore, it is a good starting point for the incorporation of memristive devices as weights, due to their reconfigurable and analogue resistance, nanoscale size and nonvolatility [112]. In hardware implementations, with memristive nanodevices as weights, bipolar pulses can be used to emulate spikes [320, 37, 321, 322, 2, 323]. Alibart *et al.* achieved pattern classification using a single-layer perceptron network implemented with a TiO_2 memristive cross-bar circuit [324] and Li *et al.* showed in-situ learning of a HfO_2 two-layer perceptron [325]. This section describes in detail the perceptron algorithm and its applicability using memristive-based devices.

5.2.1 Principle of Operation

One obstacle in the implementation of memristive-based perceptrons is the fact that the conductance is always positive, in contrast to the required positive and negative weights of the perceptron algorithm [Eq. (1.14)]. Alibart *et al.* overcome this issue by using two memristors in anti-series to reproduce the weight (Fig. 5.5) [324]. This way the resulting weight is a subtraction of conductances with normalized value ($[0, 1]$). Each weight will hence be given by $w_i = G_i^+ - G_i^-$, where $G_i^{+,-}$ is the conductance of each memristor at a given time. In hardware implementation this is equivalent to a subtraction of the two currents in the memristors. Furthermore, since we need to use continuous values for weights, the memristors must be continuous, i.e. show a large number of resistance states. The learning process of memristors (weights update process) is here implemented by using a predefined plot of the conductance change as a function of the conductance itself, one for the Set process ($\Delta G_{\text{Set}}(G)$; conductance increase) and another for the Reset process ($\Delta G_{\text{Reset}}(G)$; conductance decrease). These curves are characteristic of the used devices and should be obtained prior to the physical implementation. These plots are exemplified

in Fig. 5.6 for the case of $\text{Pt/TiO}_{2-x}/\text{Pt}$ memristors [326]. In a physical implementation, these conductance changes can be achieved applying the respective voltage pulses.

5.2.1.1 Algorithm Implementation

This subsection gives an example of an algorithm that mimics the behavior of a memristive-based perceptron. The aim is to provide an algorithm that can be used with different experimental data (Fig. 5.6) and be implemented in the training of hardware networks. In order to have normalized conductance ($G = [0, 1]$ S) and increase the conductance change ($\Delta G = [0, 10^{-2}]$ S), a normalizing factor of 10^3 is used in the experimental data. For a real circuit implementation this can be performed using an electronic amplifier. In this example each weight consists of 2 memristors, whose conductance is randomly initialized between 0 and 1. Nevertheless, these values can be given as inputs if previously read from a physical network. The conductance change (ΔG) is calculated by the perceptron learning rule for each training pattern and then the conductance of each memristor ideally changed by the same amount ($\Delta G/2$) but with opposite signs. For this purpose, voltage pulses are applied to each memristor until the desired conductance change is achieved. In fact, the conductance of analog memristors can be tuned using pulse-based programming, in which the conductance variation depends on the number and amplitude of the pulses. In this simulation the resulting conductance after each pulse is computed from the experimental curves, but in a real application it should be an input to the code. The pseudocode for one training iteration is shown in Algorithm 5.2 for an array of positive memristors (`memPos`), negative memristors (`memNeg`) and input vector (`Input`). The output `[Heaviside((memPos - memNeg) . Input))]` stands both for the prediction and reading operations. Note that, as we use the Heaviside step function, the inputs should be of the same magnitude, in order to obtain the best performance. The training data is shown more than once to the perceptron in order to have zero error on the output. Each complete training dataset defines one epoch. Regarding the Perceptron code, more details can be seen on Appendix D.

It is clear from Fig. 5.6 that both ΔG_{Set} and ΔG_{Reset} are small for the majority of the conductance range. Therefore, for time and computational purposes, we impose that each `while` loop stops at a maximum of 1000 iterations if the previous condition is not satisfied before, assuming the risk of a slower convergence. Furthermore, due to the normalization limits, after each weight update loop, the weight is truncated to 0 if it ends with a negative value and to 1 if it ends with a higher value.

5.2.2 Results

To test this memristive perceptron algorithm, an example is given below to determine if the body mass index (kg/m^2) of a person with a given weight and height is below or above the normal value (upper limit, 25). This is a simple example chosen for having a straightforward 2D representation (only 2 attributes) and therefore a straightforward interpretation of the perceptron performance. The inputs are the weight (kg) divided by a factor of 100 and height (m). The complete python

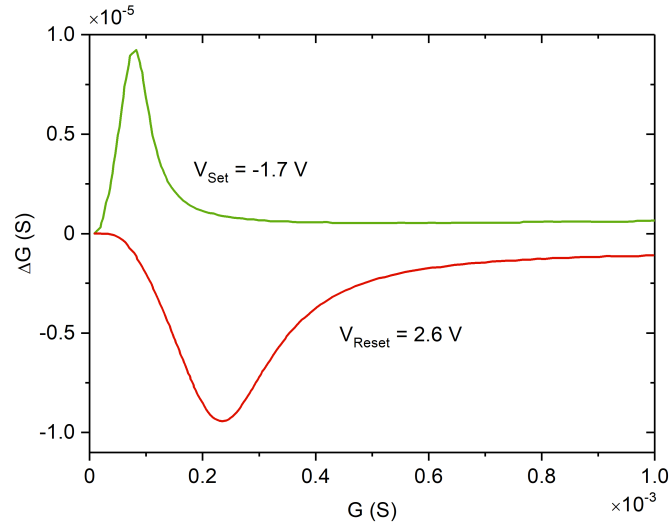


Figure 5.6 – Experimental conductance change as a function of initial conductance, when applying -1.7 V pulses for Set transitions and 2.6 V for Reset. The conductance is measured at a read bias of 0.5 V (Adapted from Ref. [326]).

code can be seen in Appendix D. Figure 5.7(a) shows the scatter plot of the 50 points used for the training (40) and test (10) dataset, and the resulting class classification (hyperplane) for a learning rate of 0.1, after 50 epochs. It is clear that 100% of the test data is classified correctly (correct side of the line). Figure 5.7(b) shows the error sum over the training process. One can observe

Algorithm 5.2 Memristive Perceptron Pseudo Code

```

error ← expected - output
for i in size(Input) do
    dG ← rate × error × input[i]
    idealGA ← memPos[i] + dG / 2
    idealGB ← memNeg[i] - dG / 2
    if error > 0 then
        while memPos[i] < idealGA do
            memPos[i] += dGSet
        end while
        while memNeg[i] > idealGB do
            memNeg[i] -= dGReset
        end while
    end if
    if error < 0 then
        while memPos[i] > idealGA do
            memPos[i] -= dGSet
        end while
        while memNeg[i] < idealGB do
            memNeg[i] += dGReset
        end while
    end if
end for

```

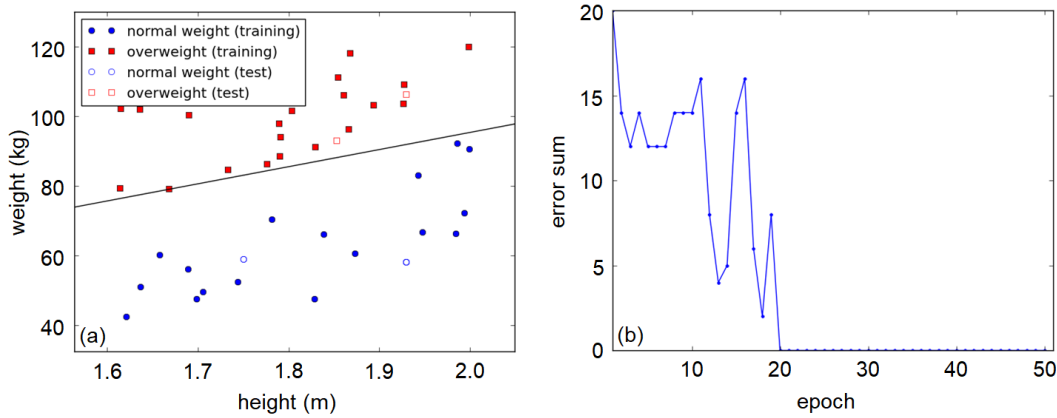


Figure 5.7 – (a) Training (36 points) and test (4 points) dataset, and resulting classification (hyperplane). Red crosses represent the over weighted class and blue dots the normal weight. (b) Error sum over the training process. Each epoch represents one complete training dataset.

that the training process results in a fully error free output after 20 epochs. The perceptron weight variations after each training data point are shown in Fig. 5.8(a) for each memristor. Note that the perceptron weight variations, and respective error, stop around 800 iterations, which corresponds to the 20 epochs observed before (20×40). The needed voltage pulses for these changes to take place are all represented together in an asynchronous way in Fig. 5.8(b). The necessary high number of pulses is related with the small conductance changes resulting from each individual pulse (Fig. 5.6).

Note that a very large training dataset results in overfitting, which translates into a non-zero error sum (the weights do not converge to a final value). This can be solved by a dynamic adjustment of the learning rate. Furthermore, as we are only implementing a single-layer perceptron (no hidden layers), we are always restrained to the classification of two linearly separable classes.

To further test the algorithm classification performance with higher number of attributes, the Sonar and Breast Cancer Wisconsin (Original) datasets from the UCI Machine Learning repository were used [327]. The sonar dataset contains 111 “mines” (metal cylinder) and 97 “rock” patterns obtained by bouncing sonar signals off a metal cylinder at various angles and under various conditions. Each pattern is a set of 60 numbers ($NA = 60$) in the range 0.0 to 1.0, representing the energy within a particular frequency band, integrated over a certain period of time. The labels associated with each record are “M” and “R” (for mines and rocks, respectively). For a 0.1 learning rate, 138 training and 69 test points (3 folds), and 20 epochs we obtained an accuracy classification value of 73% over 3 training operations. This classification performance is comparable to that of other single-layer perceptron algorithms that are known to dependent largely on the adopted training procedure [328].

The breast cancer dataset is also a two-class database, containing 699 samples with nine inputs ($NA = 9$). Some of the sample data are missing, and therefore, the actual number of samples used here is 683, of which 444 cataloged as benign cancers (label “2”) and 239 cataloged as malignant tumors (label “4”). Since each dimension is an integer value ranging from 1 to 9 and

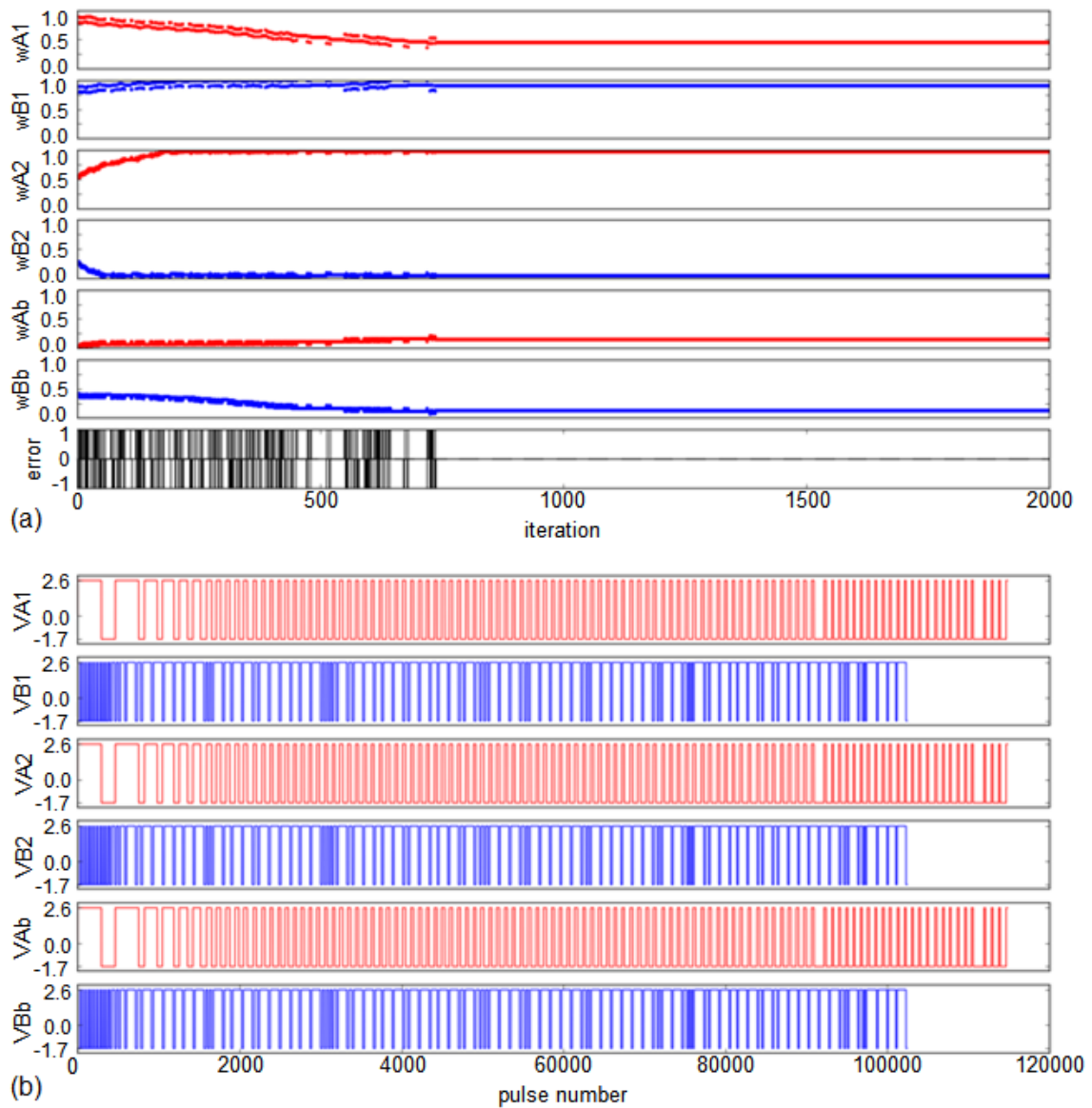


Figure 5.8 – (a) Individual weights variation over each iteration and (b) asynchronous voltage pulse application for each memristor. The label *b* stands for the bias input.

we use the Heaviside step function as transfer function, the inputs are divided by 10. Also, note that the initial patient identification number should be removed from the data before classification. For a 0.1 learning rate, 455 training and 227 test points (3 folds), and 25 epochs, we obtained an accuracy classification value of 93% over 3 training operations. These values are comparable to those obtained using multi-layer perceptron algorithms (95 - 99%), showing that, for linearly separable data, the developed single layer perceptron gives excellent results [329, 330].

Note that these two example do not result in a final null error after training, hence the accuracy is lower than 100%. This shows how more complex data needs further parameter tuning and model optimization. A natural step in these situations would be to change from a single perceptron configuration to a multi-layer architecture, well-known for its increased classification capabilities.

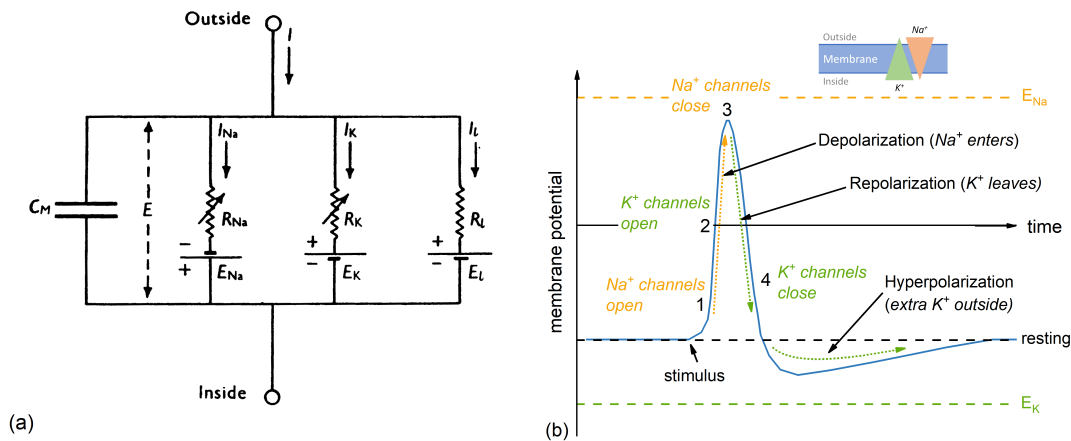


Figure 5.9 – (a) Hodgkin-Huxley model circuit (Reprinted by permission of John Wiley & Sons, Inc. [331] Copyright © 1952) and (b) schematic of the action potential of the squid giant axon.

5.3 Hodgkin-Huxley Model

The Hodgkin–Huxley model, proposed in 1952, is a mathematical description of how action potentials in the squid giant axon are initiated and propagated, using a set of nonlinear differential equations [332]. It can be described by the electrical circuit shown in Fig. 5.9(a), where sodium (Na) and potassium (K) ion channels are described by variable resistors (R_{Na} and R_K , respectively), the lipid bilayer by a capacitor (C_M) and the leak channels by a linear resistor (R_L). The voltage sources (E_{Na} , E_K and E_L) represent the electrochemical gradients responsible for the flow of ions.

Figure 5.9(b) shows the output action potential mimicked by this model. The membrane is initially at a resting potential of -70 mV, and a stimulus above the threshold of -55 mV makes it spike. When the axon is excited, the membrane potential spikes because sodium Na^+ and potassium K^+ ions flow through the membrane. Firstly the Na^+ channels open, increasing the potential up to a maximum of 58 mV (E_{Na} ; depolarization), then the Na^+ channels close and the K^+ ones open, decreasing the voltage down to a minimum of -93 mV (E_K ; repolarization). The K^+ channels then close and the membrane recovers to the resting potential (-55 mV). During the refractory period, at which the potential is lower than the resting value (hyperpolarization) the neuron does not respond to stimulus.

Based on the nonlinear dynamics of the memristor, in 2012 Chua *et al.* mathematically suggested a memristive Hodgkin–Huxley axon circuit model [333]. This circuit is composed by a potassium ion channel memristor and a sodium ion channel memristor in the place of the variable resistors, as shown in Fig. 5.10(a).

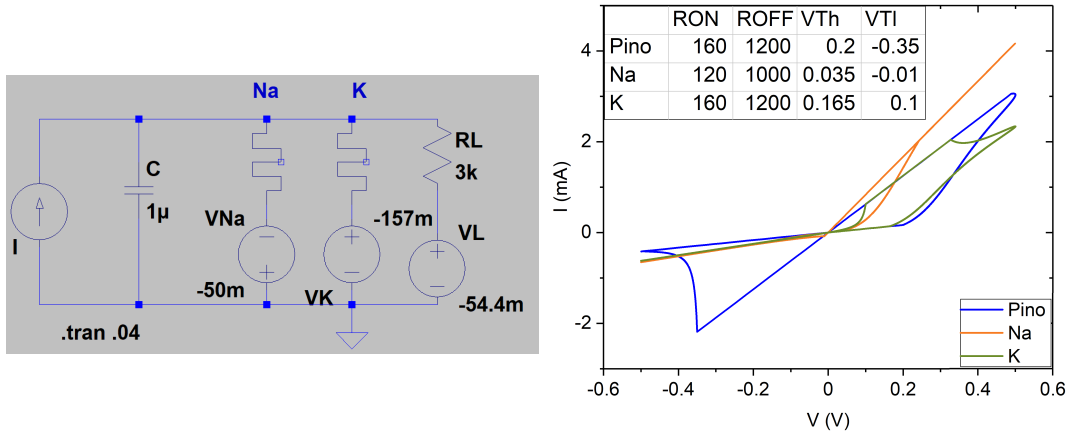


Figure 5.10 – (a) Memristor-based Hodgkin-Huxley circuit implemented in LTSpice ($V_{Na} = -50$ mV, $V_K = -157$ mV, $V_L = -54.4$ mV, $R_L = 3$ k Ω , $C_M = 1$ μ C, $I = 2$ mA, $t_{pulse} = 0.1$ ms and $t_{simulation} = 40$ ms) and (b) memristors I–V and respective model parameters ($R_{ON}^{Na} = 120$ Ω , $R_{OFF}^{Na} = 1$ k Ω , $R_{ON}^K = 160$ Ω , $R_{OFF}^K = 1.2$ k Ω , $V_{Th}^{Na} = 35$ mV, $V_{Ti}^{Na} = -10$ mV, $V_{Th}^K = 165$ mV and $V_{Ti}^K = 100$ mV).

5.3.1 Results

Preliminary studies were performed to implement the Hodgkin-Huxley neuron model in a memristor-based circuit using *LTspice*. We used Pino *et al.* model to describe the memristors [302]. The ON and OFF resistances of the model corresponding to the *Na* channel were decreased in order to agree with its higher conductance, comparatively with the *K* channel (120 Ω and 1 k Ω versus 160 Ω and 1.2 k Ω). The resulting curves can be seen in Fig. 5.10(b). Figure 5.11 shows the dynamic evolution of the circuit with $C_M = 1$ μ F, $V_{Na} = -50$ mV, $V_K = -157$ mV, $R_L = 3$ k Ω and $V_L = -54.5$ mV for a pulse stimulus of $I = 2$ mA over 0.1 ms. Both memristors Set (V_{Th}) and Reset (V_{Ti}) voltages were also adjusted for the *Na* channel (orange) to be the first to open (resistance decrease) when the voltage starts to increase (35 mV and -10 mV versus 165 mV and 100 mV, respectively). This is then followed by the opening of the *K* channel (green) and right after the closure of the first (resistance increase) and of the second [Fig. 5.11(c)]. The output voltage signal resembles an action potential spiking from a resting potential of around -47 mV, including the three stages of depolarization (up to ~ 151 mV), repolarization and hyperpolarization (down to ~ -68 mV), with a refractory period of approximately 1 ms [Fig. 5.11(e)]. However, to satisfy this result, the I–V response of the memristors is not typical, as can be seen in Figs. 5.10(b), 5.11(a) and 5.11(b). This is related with the lack of flexibility of the memristor model to changes in the parameters. Therefore, a more robust model is needed to both better describe real devices and to satisfy the criteria giving rise to an action potential. After this, a physical circuit implementation with memristive devices should be straightforward.

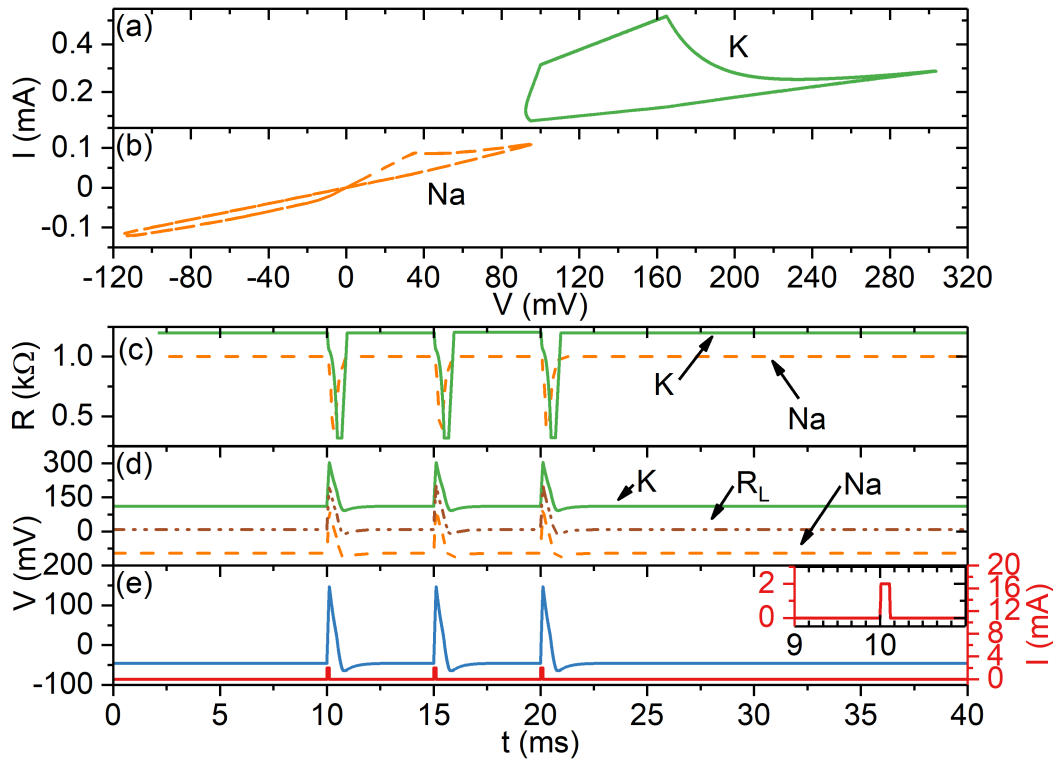


Figure 5.11 – Dynamics evolution of the circuit with the parameter described in Fig. 5.10: (a) K^+ and (b) Na^+ memristors I - V response; (c) K^+ (green) and Na^+ (orange) memristors resistance and (d) voltages across K^+ (green) and Na^+ (orange) memristors and leak resistor over time; (e) input current stimulus (red; right axis) and output action potential (blue; left axis). The inset shows the first input current pulse.

5.4 Conclusions

The fast growing machine learning field will deeply benefit from memristive devices in order to build promising and efficient neuromorphic physical systems. The main advantages in using these new circuit elements come from their nonvolatility, speed, nonlinear dynamics, low power and nanosize. Memristive devices can be both implemented as digital synapses, taking advantage of their two well separated resistance states, or as analog synapses, by using the continuous response of the conductance on the voltage. Here we have shown that the implementation of associative memories becomes straightforward using memristive-based architectures. In particular, we have numerically implemented the Willshaw network. On the other hand, artificial neural network architectures can be seen as a large number of perceptrons connected to each other. In that respect, the single-layer memristive perceptron here presented may allow to scale devices made of memristors to complex artificial neural networks. Besides synaptic mimicking, memristors can also be implemented for neuron replication, as in the case of the Hodgkin-Huxley model.

CHAPTER 6

Conclusions and Outlook

This thesis dealt with the electrical characterization of MgO and Si/Ag Metal-Insulator-Metal structures. The document can be divided in two main parts. Chapter 3 and 4 relating to experimental results and Chapter 5 to numerical simulations.

From the Pt/MgO/Ta/Ru structure, we observed that there is the formation of TaO_x at the interface, which plays an essential role in the resistive switching behavior. The resistance change was attributed to a voltage-driven oxygen vacancy motion in the MgO layer that leads to the formation and rupture of conductive filaments. A multi mode operation was observed with the performance being influenced by the polarity of the applied voltages, being the positive Set and negative Reset mode the one with lower variability and operating voltages. The importance of the Ta electrode was further confirmed by the comparison with a Pt top electrode, whose structure shows larger forming, Set and Reset voltages. Furthermore, the resistive switching was changed from unipolar to bipolar when using Ag as top electrode, revealing a change in the switching mechanism from oxygen vacancies driven to silver ions. We inferred that the existence of a forming step is a consequence of the deposition technique (magnetron sputtering) and the non-existence of a vacuum break after the MgO layer deposition. We also observed increasing Set and Reset voltages in $\text{Al}_2\text{O}_3/\text{MgO}$ double layer structures for the Al_2O_3 thickness. A maximum initial resistance, dictated by the total oxide layer thickness, was obtained for reliable resistive switching behavior. Using the Random Circuit Breaker model, we observed that the thickness of the insulator layer in a metal-insulator-metal structure mainly affects the forming voltage and not the Set or Reset ones. This implies that, after the initial conductive filament formation, the resistive switching takes places at a thinner section close to the interface, therefore being independent of the total thickness. The initial percentage of defects also only affects the voltage magnitude needed for the forming step, facilitating its occurrence.

The Si/Ag system was intensively studied using the Pt/Si/Ag/TiW stack. Resistive switching was successfully achieved using both Si rigid substrates, and cellulose and PET flexible substrates, including in the bent configuration. The observed phenomenon was explained by the formation/rupture of metallic Ag filaments in the otherwise insulating Si host layer. Concerning the flexible substrates, a bottom electrode of ITO on top of PET was also considered and showed lower operation voltages than Pt. Furthermore, we used a model in the charge–flux space to describe the current–voltage hysteretic curves. The intrinsic stochastic behavior of the resistive switch-

ing processes was explored in the time–voltage space aiming the future replication of neuronal stochasticity. We observed, as expected, that the longer is the input pulse duration and voltage amplitude, the higher is the switching amplitude.

Finally, the numerical simulations enabled us to understand the behavior of memristor-based artificial neural networks without the necessity to fabricate a physical device. The memristive devices were implemented both as artificial synapses (in the case of the Willshaw memory and the Perceptron) and neurons (ion channels) using the Hodgkin-Huxley model. For the first and last cases a *Spice* model was used, whereas for the Perceptron, experimental data is used in *Python* to described the memristor behavior. We tested the performance/tolerance of a memristor-based Willshaw network under two types of defects. We found that *stuck-at-1* defects are more amenable and can more easily be compensated through an increase in the readout current threshold. We also tested device parameter variations and found that device-to-device resistance variance are more critical to control than threshold voltage variability. A memristive Perceptron was successfully trained to classify three data cases: body height and weight (body mass index), rock and metal (sonar), and benign and malignant breast cancer (Wisconsin database). Preliminary studies performed in a Hodgkin-Huxley neuron model using memristors as ion channels showed an output voltage signal resembling an action potential spike.

The work developed showed some of the possible parameters to explore in the optimization of these type of devices and several questions were left open. Studies on the temperature dependence of the electrical resistance and resistive switching hysteresis cycle should be performed to better understand the conduction mechanisms involved. Also, a deeper study of the structural properties of the stacks at different interfaces and resistance states would be fruitful. The origin of the low resistance initial state observed for the devices on top of the flexible substrates must be investigated.

Since CMOS processes are not optimized for the patterning of inert metals (e.g. Pt or Pd), the effect on resistive switching of the substitution of the bottom electrode by TiN and TaN, for example, should be pursued. After this, the downsizing of individual devices and their interconnections in crossbar configurations should become more practical.

Aiming to take full advantage of the stochastic properties of the memristive systems to mimic learning behaviors, the voltage-time space must be characterized and the connection with biological components should be attempted. Furthermore, the full capacities of the bacterial cellulose substrates may be explored from its malleability and ionic conduction when in contact with water. This would increase the range of applications to environments with moisture (e.g. *in-vivo* applications).

Regarding the implementation of the Hodgkin-Huxley neuron, memristor model improvements are needed to better understand the parameters and therefore succeed in the mimicking of neuronal behavior through the connection of two real metal-insulator-metal devices in the electric circuit.

References

- [1] Y. Liu, T. P. Chen, Z. Liu, Y. F. Yu, Q. Yu, P. Li, S. Fung, Self-learning ability realized with a resistive switching device based on a Ni-rich nickel oxide thin film, *Applied Physics A* 105 (4) (2011) 855–860. doi:10.1007/s00339-011-6605-8. [Cited on pages 1, 2, and 18.]
- [2] S. Yu, Y. Wu, R. Jeyasingh, An electronic synapse device based on metal oxide resistive switching memory for neuromorphic computation, *IEEE Transactions on Electron Devices* 58 (8) (2011) 2729–2737. doi:10.1109/TED.2011.2147791. [Cited on pages 1, 2, and 103.]
- [3] D. Ielmini, Resistive switching memories based on metal oxides: mechanisms, reliability and scaling, *Semiconductor Science and Technology* 31 (6) (2016) 063002. doi:10.1088/0268-1242/31/6/063002. [Cited on pages 1, 6, 7, 10, 11, 13, 14, 15, and 24.]
- [4] M. Versace, B. Chandler, Meet MoNETA—The brain-inspired chip that will outsmart us all, *Spectrum*, *IEEE* 47 (12) (2010) 30–37. [Cited on page 1.]
- [5] R. J. Douglas, K. A. Martin, Mapping the Matrix: The Ways of Neocortex, *Neuron* 56 (2) (2007) 226–238. doi:10.1016/j.neuron.2007.10.017. [Cited on pages 1 and 2.]
- [6] T. Chang, Y. Yang, W. Lu, Building Neuromorphic Circuits with Memristive Devices, *IEEE Circuits and Systems Magazine* 13 (2) (2013) 56–73. doi:10.1109/MCAS.2013.2256260. [Cited on pages 1 and 2.]
- [7] M. M. Waldrop, The chips are down for Moore's law, *Nature* 530 (7589) (2016) 144–147. doi:10.1038/530144a. [Cited on page 1.]
- [8] R. S. Williams, What's Next? [The end of Moore's law], *Computing in Science & Engineering* 19 (2) (2017) 7–13. doi:10.1109/MCSE.2017.31. [Cited on page 1.]
- [9] E. Track, N. Forbes, G. Strawn, The End of Moore's Law, *Computing in Science & Engineering* 19 (2) (2017) 4–6. doi:10.1109/MCSE.2017.25. [Cited on page 1.]
- [10] W. Lu, D. S. Jeong, M. Kozicki, R. Waser, Electrochemical metallization cells—blending nanoionics into nanoelectronics?, *MRS Bulletin* 37 (2) (2012) 124–130. doi:10.1557/mrs.2012.5. [Cited on pages 1, 6, 8, and 13.]
- [11] R. Waser, R. Dittmann, G. Staikov, K. Szot, Redox-Based Resistive Switching Memories - Nanoionic Mechanisms, Prospects, and Challenges, *Advanced Materials* 21 (25-26) (2009) 2632–2663. doi:10.1002/adma.200900375. [Cited on pages 1, 8, 9, 10, and 66.]
- [12] I. Valov, R. Waser, J. R. Jameson, M. N. Kozicki, Electrochemical metallization memories—fundamentals, applications, prospects, *Nanotechnology* 22 (28) (2011) 289502. doi:10.1088/0957-4484/22/28/289502. [Cited on pages 1, 7, 9, 11, and 15.]
- [13] R. Waser, M. Aono, Nanoionics-based resistive switching memories, *Nature Materials* 6 (11) (2007) 833–840. doi:10.1038/nmat2023. [Cited on pages 1, 4, 6, 7, 9, 15, and 24.]

- [14] S. Larentis, S. Member, F. Nardi, S. Member, S. Balatti, S. Member, D. C. Gilmer, D. Ielmini, S. Member, A. Resistive-switching, Resistive Switching by Voltage-Driven Ion Migration in Bipolar RRAM — Part II : Modeling, *IEEE Transactions on Electron Devices* 59 (9) (2012) 2468–2475. [Cited on page 1.]
- [15] J. Meena, S. Sze, U. Chand, T.-Y. Tseng, Overview of emerging nonvolatile memory technologies, *Nanoscale Research Letters* 9 (1) (2014) 526. doi:10.1186/1556-276X-9-526. [Cited on page 1.]
- [16] F. Pan, S. Gao, C. Chen, C. Song, F. Zeng, Recent progress in resistive random access memories: Materials, switching mechanisms, and performance, *Materials Science and Engineering: R: Reports* 83 (9) (2014) 1–59. doi:10.1016/j.mser.2014.06.002. [Cited on pages 1, 10, and 37.]
- [17] T. Chang, S.-H. Jo, W. Lu, Short-Term Memory to Long-Term Memory Transition in a Nanoscale Memristor, *ACS Nano* 5 (9) (2011) 7669–7676. doi:10.1021/nn202983n. [Cited on pages 2, 18, and 24.]
- [18] S. H. Jo, T. Chang, I. Ebong, B. B. Bhadviya, P. Mazumder, W. Lu, Nanoscale Memristor Device as Synapse in Neuromorphic Systems, *Nano Letters* 10 (4) (2010) 1297–1301. doi:10.1021/nl904092h. [Cited on pages 2, 6, 12, 16, 17, 18, 19, 75, and 95.]
- [19] K. D. Cantley, A. Subramaniam, H. J. Stiegler, R. A. Chapman, E. M. Vogel, Hebbian Learning in Spiking Neural Networks With Nanocrystalline Silicon TFTs and Memristive Synapses, *IEEE Transactions on Nanotechnology* 10 (5) (2011) 1066–1073. doi:10.1109/TNANO.2011.2105887. [Cited on page 2.]
- [20] R. Kozma, R. E. Pino, G. E. Paziienza, *Advances in Neuromorphic Memristor Science and Applications*, Springer Netherlands, Dordrecht, 2012. doi:10.1007/978-94-007-4491-2. [Cited on page 2.]
- [21] D. B. Strukov, G. S. Snider, D. R. Stewart, R. S. Williams, The missing memristor found, *Nature* 453 (2008) 80–83. doi:10.1038/nature06932. [Cited on pages 3, 24, and 37.]
- [22] L. Chua, Memristor-The missing circuit element, *IEEE Transactions on Circuit Theory* 18 (5) (1971) 507–519. doi:10.1109/TCT.1971.1083337. [Cited on page 2.]
- [23] L. Chua, S. Kang, Memristive devices and systems, *Proceedings of the IEEE* 64 (2) (1976) 209–223. doi:10.1109/PROC.1976.10092. [Cited on pages 2 and 24.]
- [24] Y. N. Joglekar, S. J. Wolf, The elusive memristor: properties of basic electrical circuits, *European Journal of Physics* 30 (4) (2009) 661–675. doi:10.1088/0143-0807/30/4/001. [Cited on pages 2, 4, and 15.]
- [25] Y. V. Pershin, M. Di Ventra, Memory effects in complex materials and nanoscale systems, *Advances in Physics* 60 (2) (2011) 145–227. doi:10.1080/00018732.2010.544961. [Cited on pages 2 and 3.]
- [26] T. W. Hickmott, Low-frequency negative resistance in thin anodic oxide films, *Journal of Applied Physics* 33 (9) (1962) 2669–2682. doi:10.1063/1.1702530. [Cited on pages 3 and 75.]
- [27] J. Gibbons, W. Beadle, Switching properties of thin NiO films, *Solid-State Electronics* 7 (11) (1964) 785–790. doi:10.1016/0038-1101(64)90131-5. [Cited on page 3.]

- [28] W. R. Hiatt, T. W. Hickmott, Bistable switching in niobium oxide diodes, *Applied Physics Letters* 6 (6) (1965) 106–108. doi:10.1063/1.1754187. [Cited on page 3.]
- [29] K. L. Chopra, Avalanche-induced negative resistance in thin oxide films, *Journal of Applied Physics* 36 (1) (1965) 184–187. doi:10.1063/1.1713870. [Cited on page 3.]
- [30] H. J. Hovel, J. J. Urgell, Switching and memory characteristics of ZnSe - Ge heterojunctions, *Journal of Applied Physics* 42 (12) (1971) 5076–5083. doi:10.1063/1.1659895. [Cited on page 3.]
- [31] Y. Hirose, H. Hirose, Polarity-dependent memory switching and behavior of Ag dendrite in Ag-photodoped amorphous As₂S₃ films, *Journal of Applied Physics* 47 (6) (1976) 2767–2772. doi:10.1063/1.322942. [Cited on page 3.]
- [32] M. Bloor, H. Sampson, S. Baker, D. Walters, K. Dahlgren, E. Wadsworth, P. James, Room for Manoeuvre? Regulatory Compliance in the Global Shipping Industry, *Social & Legal Studies* 22 (2) (2013) 171–189. doi:10.1177/0964663912467814. [Cited on page 3.]
- [33] F. Corinto, A. Ascoli, M. Gilli, Class of all i-v dynamics for memristive elements in pattern recognition systems, in: *The 2011 International Joint Conference on Neural Networks, IEEE, 2011*, pp. 2289–2296. doi:10.1109/IJCNN.2011.6033514. [Cited on pages 3 and 4.]
- [34] T. Hasegawa, K. Terabe, T. Tsuruoka, M. Aono, Atomic Switch: Atom/Ion Movement Controlled Devices for Beyond Von-Neumann Computers, *Advanced Materials* 24 (2) (2012) 252–267. doi:10.1002/adma.201102597. [Cited on pages 4, 11, and 17.]
- [35] R. Waser, D. Ielmini, H. Akinaga, H. Shima, H.-S. P. Wong, J. J. Yang, S. Yu, Introduction to Nanoionic Elements for Information Technology, in: *Resistive Switching*, Wiley-VCH Verlag GmbH & Co. KGaA, Weinheim, Germany, 2016, pp. 1–30. doi:10.1002/9783527680870.ch1. [Cited on pages 4, 5, 6, 7, 10, 14, and 24.]
- [36] H.-S. P. Wong, H.-Y. Lee, S. Yu, Y.-S. Chen, Y. Wu, P.-S. Chen, B. Lee, F. T. Chen, M.-J. Tsai, Metal–Oxide RRAM, *Proceedings of the IEEE* 100 (6) (2012) 1951–1970. doi:10.1109/JPROC.2012.2190369. [Cited on pages 4, 5, 10, 14, 15, and 37.]
- [37] S. D. Ha, S. Ramanathan, Adaptive oxide electronics: A review, *Journal of Applied Physics* 110 (7) (2011) 071101. doi:10.1063/1.3640806. [Cited on pages 4, 17, 19, 37, and 103.]
- [38] T. Tsuruoka, T. Hasegawa, K. Terabe, M. Aono, Conductance quantization and synaptic behavior in a Ta₂O₅ -based atomic switch, *Nanotechnology* 23 (43) (2012) 435705. doi:10.1088/0957-4484/23/43/435705. [Cited on pages 4, 17, and 18.]
- [39] A. Chen, Ionic Memory Technology, in: *Solid State Electrochemistry II*, 1st Edition, Wiley-VCH Verlag GmbH & Co. KGaA, Weinheim, Germany, 2011, Ch. 1, pp. 1–30. doi:10.1002/9783527635566.ch1. [Cited on pages 5, 6, 7, 8, 9, 10, 11, and 15.]
- [40] C. Kögeler, R. Rosezin, E. Linn, R. Bruchhaus, R. Waser, Materials, technologies, and circuit concepts for nanocrossbar-based bipolar RRAM, *Applied Physics A* 102 (4) (2011) 791–809. doi:10.1007/s00339-011-6287-2. [Cited on pages 5, 6, 11, 12, and 19.]
- [41] L. Goux, Y.-Y. Chen, L. Pantisano, X.-P. Wang, G. Groeseneken, M. Jurczak, D. J. Wouters, On the Gradual Unipolar and Bipolar Resistive Switching of TiN\HfO₂\Pt Memory Systems, *Electrochemical and Solid-State Letters* 13 (6) (2010) G54–G56. doi:10.1149/1.3373529. [Cited on page 6.]

- [42] D. S. Jeong, H. Schroeder, R. Waser, Coexistence of Bipolar and Unipolar Resistive Switching Behaviors in a Pt/TiO₂/Pt Stack, *Electrochemical and Solid-State Letters* 10 (8) (2007) G51–G53. doi:10.1149/1.2742989. [Cited on page 6.]
- [43] X. Sun, G. Li, X. Zhang, L. Ding, W. Zhang, Coexistence of the bipolar and unipolar resistive switching behaviours in Au/SrTiO₃/Pt cells, *Journal of Physics D: Applied Physics* 44 (12) (2011) 125404. doi:10.1088/0022-3727/44/12/125404. [Cited on page 6.]
- [44] J. Suñé, N. Raghavan, K. L. Pey, Dielectric Breakdown Processes, in: *Resistive Switching*, Wiley-VCH Verlag GmbH & Co. KGaA, Weinheim, Germany, 2016, pp. 225–252. doi:10.1002/9783527680870.ch8. [Cited on page 6.]
- [45] H.-C. Tseng, T.-C. Chang, Y.-C. Wu, S.-W. Wu, J.-J. Huang, Y.-T. Chen, J.-B. Yang, T.-P. Lin, S. M. Sze, M.-J. Tsai, Y.-L. Wang, A.-K. Chu, Impact of Electroforming Current on Self-Compliance Resistive Switching in an ITO/Gd:SiO_x/TiN Structure, *IEEE Electron Device Letters* 34 (7) (2013) 858–860. doi:10.1109/LED.2013.2259135. [Cited on page 6.]
- [46] K. M. Kim, D. S. Jeong, C. S. Hwang, Nanofilamentary resistive switching in binary oxide system; a review on the present status and outlook, *Nanotechnology* 22 (25) (2011) 254002. doi:10.1088/0957-4484/22/25/254002. [Cited on pages 6, 7, 10, and 15.]
- [47] I. Valov, T. Tsuruoka, Effects of moisture and redox reactions in VCM and ECM resistive switching memories, *Journal of Physics D: Applied Physics* 51 (41) (2018) 413001. doi:10.1088/1361-6463/aad581. [Cited on pages 6, 8, 9, 10, 11, 12, 13, 15, and 24.]
- [48] C. Bäumer, R. Dittmann, Redox-based memristive metal-oxide devices, in: *Metal Oxide-Based Thin Film Structures*, Elsevier, 2018, pp. 489–522. doi:10.1016/B978-0-12-811166-6.00020-0. [Cited on page 7.]
- [49] R. Muenstermann, T. Menke, R. Dittmann, R. Waser, Coexistence of filamentary and homogeneous resistive switching in Fe-doped SrTiO₃ thin-film memristive devices, *Advanced Materials* 22 (43) (2010) 4819–4822. doi:10.1002/adma.201001872. [Cited on page 7.]
- [50] D. Choi, C. Soo Kim, Coexistence of unipolar and bipolar resistive switching in Pt/NiO/Pt, *Applied Physics Letters* 104 (19) (2014) 193507. doi:10.1063/1.4875918. [Cited on page 7.]
- [51] C. Baeumer, R. Valenta, C. Schmitz, A. Locatelli, S. P. Rogers, A. Sala, N. Raab, S. Nemsak, M. Shim, C. M. Schneider, S. Menzel, R. Waser, R. Dittmann, Subfilamentary Networks Cause Cycle-to-Cycle Variability in Memristive Devices, *ACS Nano* 11 (7) (2017) 6921–6929. doi:10.1021/acsnano.7b02113. [Cited on page 7.]
- [52] Y. Zhang, W. He, Y. Wu, K. Huang, Y. Shen, J. Su, Y. Wang, Z. Zhang, X. Ji, G. Li, H. Zhang, S. Song, H. Li, L. Sun, R. Zhao, L. Shi, Highly Compact Artificial Memristive Neuron with Low Energy Consumption, *Small* 14 (51) (2018) 1802188. doi:10.1002/smll.201802188. [Cited on page 7.]
- [53] S. Gao, G. Liu, Q. Chen, W. Xue, H. Yang, J. Shang, B. Chen, F. Zeng, C. Song, F. Pan, R. W. Li, Improving Unipolar Resistive Switching Uniformity with Cone-Shaped Conducting Filaments and Its Logic-In-Memory Application, *ACS Applied Materials and Interfaces* 10 (7) (2018) 6453–6462. doi:10.1021/acsaami.7b19586. [Cited on page 7.]

- [54] X.-J. Zhu, J. Shang, G. Liu, R.-W. Li, Ion transport-related resistive switching in film sandwich structures, *Chinese Science Bulletin* 59 (20) (2014) 2363–2382. doi:10.1007/s11434-014-0284-8. [Cited on page 7.]
- [55] R. Yang, K. Terabe, Y. Yao, T. Tsuruoka, T. Hasegawa, J. K. Gimzewski, M. Aono, Synaptic plasticity and memory functions achieved in a WO₃-x-based nanoionics device by using the principle of atomic switch operation, *Nanotechnology* 24 (38) (2013) 384003. doi:10.1088/0957-4484/24/38/384003. [Cited on pages 7 and 9.]
- [56] R. A. De Souza, Ion Transport in Metal Oxides, in: *Resistive Switching*, Wiley-VCH Verlag GmbH & Co. KGaA, Weinheim, Germany, 2016, pp. 125–164. doi:10.1002/9783527680870.ch5. [Cited on page 7.]
- [57] L. Goux, S. Spiga, Unipolar Resistive-Switching Mechanisms, in: *Resistive Switching*, Wiley-VCH Verlag GmbH & Co. KGaA, Weinheim, Germany, 2016, pp. 363–394. doi:10.1002/9783527680870.ch13. [Cited on pages 7, 12, and 14.]
- [58] I. Valov, Interfacial interactions and their impact on redox-based resistive switching memories (ReRAMs), *Semiconductor Science and Technology* 32 (9) (2017) 093006. doi:10.1088/1361-6641/aa78cd. [Cited on page 8.]
- [59] J. B. Yun, S. Kim, S. Seo, M. J. Lee, D. C. Kim, S. E. Ahn, Y. Park, J. Kim, H. Shin, Random and localized resistive switching observation in Pt/NiO/Pt, *Physica Status Solidi - Rapid Research Letters* 1 (6) (2007) 280–282. doi:10.1002/pssr.200701205. [Cited on page 7.]
- [60] M. Janousch, G. I. Meijer, U. Staub, B. Delley, S. F. Karg, B. P. Andreasson, Role of Oxygen Vacancies in Cr-Doped SrTiO₃ for Resistance-Change Memory, *Advanced Materials* 19 (17) (2007) 2232–2235. doi:10.1002/adma.200602915. [Cited on page 7.]
- [61] Y. Yang, P. Gao, S. Gaba, T. Chang, X. Pan, W. Lu, Observation of conducting filament growth in nanoscale resistive memories, *Nature Communications* 3 (1) (2012) 732. doi:10.1038/ncomms1737. [Cited on pages 7 and 37.]
- [62] Y. Yang, P. Gao, L. Li, X. Pan, S. Tappertzhofen, S. Choi, R. Waser, I. Valov, W. D. Lu, Electrochemical dynamics of nanoscale metallic inclusions in dielectrics, *Nature Communications* 5 (1) (2014) 4232. doi:10.1038/ncomms5232. [Cited on page 7.]
- [63] F. Yuan, Z. Zhang, C. Liu, F. Zhou, H. M. Yau, W. Lu, X. Qiu, H.-S. P. Wong, J. Dai, Y. Chai, Real-Time Observation of the Electrode-Size-Dependent Evolution Dynamics of the Conducting Filaments in a SiO₂ Layer, *ACS Nano* 11 (4) (2017) 4097–4104. doi:10.1021/acsnano.7b00783. [Cited on page 7.]
- [64] M. Arita, A. Tsurumaki-Fukuchi, Y. Takahashi, Nanoscale Switching and Degradation of Resistive Random Access Memory Studied by In Situ Electron Microscopy, in: *Memristor and Memristive Neural Networks*, InTech, 2018, pp. 63–91. doi:10.5772/intechopen.69024. [Cited on page 7.]
- [65] R. Yang, K. Terabe, G. Liu, T. Tsuruoka, T. Hasegawa, J. K. Gimzewski, M. Aono, On-Demand Nanodevice with Electrical and Neuromorphic Multifunction Realized by Local Ion Migration, *ACS Nano* 6 (11) (2012) 9515–9521. doi:10.1021/nn302510e. [Cited on page 7.]

- [66] I. Valov, Redox-Based Resistive Switching Memories (ReRAMs): Electrochemical Systems at the Atomic Scale, *ChemElectroChem* 1 (1) (2014) 26–36. doi:10.1002/ce1c.201300165. [Cited on pages 8, 9, 10, 12, 13, 14, and 15.]
- [67] R. Soni, P. Meuffels, A. Petraru, M. Hansen, M. Ziegler, O. Vavra, H. Kohlstedt, D. S. Jeong, Bipolar switching polarity reversal by electrolyte layer sequence in electrochemical metallization cells with dual-layer solid electrolytes, *Nanoscale* 5 (24) (2013) 12598. doi:10.1039/c3nr03993e. [Cited on page 9.]
- [68] S. Menzel, J.-H. Hur, Modeling the VCM- and ECM-Type Switching Kinetics, in: *Resistive Switching*, Wiley-VCH Verlag GmbH & Co. KGaA, Weinheim, Germany, 2016, pp. 395–436. doi:10.1002/9783527680870.ch14. [Cited on pages 9 and 13.]
- [69] S. Menzel, U. Böttger, M. Wimmer, M. Salanga, Physics of the Switching Kinetics in Resistive Memories, *Advanced Functional Materials* 25 (40) (2015) 6306–6325. doi:10.1002/adfm.201500825. [Cited on page 10.]
- [70] D. S. Jeong, B. J. Choi, C. S. Hwang, Electroforming Processes in Metal Oxide Resistive-Switching Cells, in: *Resistive Switching*, Wiley-VCH Verlag GmbH & Co. KGaA, Weinheim, Germany, 2016, pp. 289–316. doi:10.1002/9783527680870.ch10. [Cited on page 10.]
- [71] D. Kuzum, S. Yu, H.-S. Philip Wong, Synaptic electronics: materials, devices and applications, *Nanotechnology* 24 (38) (2013) 382001. doi:10.1088/0957-4484/24/38/382001. [Cited on page 10.]
- [72] M. Lanza, A Review on Resistive Switching in High-k Dielectrics: A Nanoscale Point of View Using Conductive Atomic Force Microscope, *Materials* 7 (3) (2014) 2155–2182. doi:10.3390/ma7032155. [Cited on page 10.]
- [73] M. Lübben, P. Karakolis, V. Ioannou-Sougleridis, P. Normand, P. Dimitrakis, I. Valov, Graphene-Modified Interface Controls Transition from VCM to ECM Switching Modes in Ta/TaOx Based Memristive Devices, *Advanced Materials* 27 (40) (2015) 6202–6207. doi:10.1002/adma.201502574. [Cited on pages 10 and 15.]
- [74] A. Wedig, M. Luebben, D.-Y. Cho, M. Moors, K. Skaja, V. Rana, T. Hasegawa, K. K. Adepalli, B. Yildiz, R. Waser, I. Valov, Nanoscale cation motion in TaOx, HfOx and TiOx memristive systems, *Nature Nanotechnology* 11 (1) (2016) 67–74. doi:10.1038/nnano.2015.221. [Cited on page 10.]
- [75] D.-Y. Cho, M. Luebben, S. Wiefels, K.-S. Lee, I. Valov, Interfacial Metal–Oxide Interactions in Resistive Switching Memories, *ACS Applied Materials & Interfaces* 9 (22) (2017) 19287–19295. doi:10.1021/acsami.7b02921. [Cited on page 10.]
- [76] C.-c. Hsieh, Y.-F. Chang, Y.-C. Chen, X. Wu, M. Guo, F. Zhou, S. Kim, B. Fowler, C.-y. Lin, C.-h. Pan, T.-c. Chang, J. C. Lee, Review of Recently Progress on Neural Electronics and Memcomputing Applications in Intrinsic SiOx-Based Resistive Switching Memory, in: *Memristor and Memristive Neural Networks*, InTech, 2018, pp. 227–248. doi:10.5772/intechopen.68530. [Cited on page 11.]
- [77] W. Chen, N. Chamele, Y. Gonzalez-Velo, H. J. Barnaby, M. N. Kozicki, Low Temperature Characterization of Cu-Cu:silica Based Programmable Metallization Cell, *IEEE Electron Device Letters* 38 (9) (2017) 1–1. doi:10.1109/LED.2017.2734743. [Cited on page 11.]

- [78] W. Chen, R. Fang, H. J. Barnaby, M. B. Balaban, Y. Gonzalez-Velo, J. L. Taggart, A. Mahmud, K. Holbert, A. H. Edwards, M. N. Kozicki, Total-Ionizing-Dose Effects on Resistance Stability of Programmable Metallization Cell Based Memory and Selectors, *IEEE Transactions on Nuclear Science* 64 (1) (2017) 269–276. doi:10.1109/TNS.2016.2618359. [Cited on page 11.]
- [79] J. J. Yang, D. B. Strukov, D. R. Stewart, Memristive devices for computing, *Nature Nanotechnology* 8 (1) (2013) 13–24. doi:10.1038/nnano.2012.240. [Cited on pages 11, 20, and 40.]
- [80] M. Prezioso, F. Merrih-Bayat, B. D. Hoskins, G. C. Adam, K. K. Likharev, D. B. Strukov, Training and operation of an integrated neuromorphic network based on metal-oxide memristors, *Nature* 521 (2015) 61–64. doi:10.1038/nature14441. [Cited on page 11.]
- [81] Z. Wang, S. Joshi, S. Savel'ev, W. Song, R. Midya, Y. Li, M. Rao, P. Yan, S. Asapu, Y. Zhuo, H. Jiang, P. Lin, C. Li, J. H. Yoon, N. K. Upadhyay, J. Zhang, M. Hu, J. P. Strachan, M. Barnell, Q. Wu, H. Wu, R. S. Williams, Q. Xia, J. J. Yang, Fully memristive neural networks for pattern classification with unsupervised learning, *Nature Electronics* 1 (2) (2018) 137–145. doi:10.1038/s41928-018-0023-2. [Cited on pages 11 and 19.]
- [82] F. Caravelli, J. Carbajal, Memristors for the Curious Outsiders, *Technologies* 6 (4) (2018) 118. doi:10.3390/technologies6040118. [Cited on pages 11 and 12.]
- [83] E. Linn, R. Rosezin, S. Tappertzhofen, U. Böttger, R. Waser, Beyond von Neumann—logic operations in passive crossbar arrays alongside memory operations, *Nanotechnology* 23 (30) (2012) 305205. doi:10.1088/0957-4484/23/30/305205. [Cited on pages 11 and 19.]
- [84] N. K. Upadhyay, H. Jiang, Z. Wang, S. Asapu, Q. Xia, J. Joshua Yang, Emerging Memory Devices for Neuromorphic Computing, *Advanced Materials Technologies* 1800589 (2019) 1800589. doi:10.1002/admt.201800589. [Cited on page 11.]
- [85] H. Daumé III, The Perceptron, in: *A course in Machine Learning*, 2012, pp. 37–50. [Cited on pages 12, 20, and 102.]
- [86] Y. Deng, P. Huang, B. Chen, X. Yang, B. Gao, J. Wang, L. Zeng, G. Du, J. Kang, X. Liu, RRAM crossbar array with cell selection device: A device and circuit interaction study, *IEEE Transactions on Electron Devices* 60 (2) (2013) 719–726. doi:10.1109/TED.2012.2231683. [Cited on page 13.]
- [87] I. Valov, R. Waser, Physics and Chemistry of Nanoionic Cells, in: *Resistive Switching*, Wiley-VCH Verlag GmbH & Co. KGaA, Weinheim, Germany, 2016, pp. 253–288. doi:10.1002/9783527680870.ch9. [Cited on pages 12 and 13.]
- [88] I. Valov, W. D. Lu, Nanoscale electrochemistry using dielectric thin films as solid electrolytes, *Nanoscale* 8 (29) (2016) 13828–13837. doi:10.1039/C6NR01383J. [Cited on pages 12 and 13.]
- [89] A. C. Torrezan, J. P. Strachan, G. Medeiros-Ribeiro, R. S. Williams, Sub-nanosecond switching of a tantalum oxide memristor, *Nanotechnology* 22 (48) (2011) 485203. doi:10.1088/0957-4484/22/48/485203. [Cited on page 13.]
- [90] Y. Yang, W. Lu, Nanoscale resistive switching devices: mechanisms and modeling, *Nanoscale* 5 (21) (2013) 10076–10092. doi:10.1039/c3nr03472k. [Cited on page 13.]

- [91] I. Valov, Interfacial interactions and their impact on redox-based resistive switching memories (ReRAMs), *Semiconductor Science and Technology* 32 (9) (2017) 093006. doi:10.1088/1361-6641/aa78cd. [Cited on page 13.]
- [92] D. J. Wouters, Y.-Y. Chen, A. Fantini, N. Raghavan, Reliability Aspects, in: *Resistive Switching*, Wiley-VCH Verlag GmbH & Co. KGaA, Weinheim, Germany, 2016, pp. 597–622. doi:10.1002/9783527680870.ch21. [Cited on page 14.]
- [93] Y. S. Kim, J. S. Kim, J. S. Choi, I. R. Hwang, S. H. Hong, S. O. Kang, B. H. Park, Resistive switching behaviors of NiO films with controlled number of conducting filaments, *Applied Physics Letters* 98 (19) (2011) 1–4. doi:10.1063/1.3589825. [Cited on pages 15 and 37.]
- [94] S. Tappertzhofen, I. Valov, T. Tsuruoka, T. Hasegawa, R. Waser, M. Aono, Generic Relevance of Counter Charges for Cation-Based Nanoscale Resistive Switching Memories, *ACS Nano* 7 (7) (2013) 6396–6402. doi:10.1021/nm4026614. [Cited on page 15.]
- [95] J. Park, W. Lee, M. Choe, S. Jung, M. Son, S. Kim, S. Park, J. Shin, D. Lee, M. Siddik, J. Woo, G. Choi, E. Cha, T. Lee, H. Hwang, Quantized conductive filament formed by limited Cu source in sub-5nm era, in: *2011 International Electron Devices Meeting, IEEE, 2011*, pp. 3.7.1–3.7.4. doi:10.1109/IEDM.2011.6131484. [Cited on page 15.]
- [96] B. Govoreanu, G. Kar, Y.-Y. Chen, V. Paraschiv, S. Kubicek, A. Fantini, I. Radu, L. Goux, S. Clima, R. Degraeve, N. Jossart, O. Richard, T. Vandeweyer, K. Seo, P. Hendrickx, G. Pourtois, H. Bender, L. Altimime, D. Wouters, J. Kittl, M. Jurczak, 10×10nm² Hf/HfO_x crossbar resistive RAM with excellent performance, reliability and low-energy operation, in: *2011 International Electron Devices Meeting, IEEE, 2011*, pp. 31.6.1–31.6.4. doi:10.1109/IEDM.2011.6131652. [Cited on page 15.]
- [97] S. Pi, C. Li, H. Jiang, W. Xia, H. Xin, J. J. Yang, Q. Xia, Memristor crossbar arrays with 6-nm half-pitch and 2-nm critical dimension, *Nature Nanotechnology* 14 (1) (2019) 35–39. doi:10.1038/s41565-018-0302-0. [Cited on page 15.]
- [98] G. Indiveri, B. Linares-Barranco, R. Legenstein, G. Deligeorgis, T. Prodromakis, Integration of nanoscale memristor synapses in neuromorphic computing architectures, *Nanotechnology* 24 (38) (2013) 384010. doi:10.1088/0957-4484/24/38/384010. [Cited on pages 15 and 84.]
- [99] Testing memory downsizing limits, *Nature Nanotechnology* 14 (1) (2019) 1–1. doi:10.1038/s41565-018-0355-0. [Cited on page 15.]
- [100] L. P. Shi, K. J. Yi, K. Ramanathan, R. Zhao, N. Ning, D. Ding, T. C. Chong, Artificial cognitive memory - changing from density driven to functionality driven, *Applied Physics A* 102 (4) (2011) 865–875. doi:10.1007/s00339-011-6297-0. [Cited on pages 16 and 19.]
- [101] Z. Q. Wang, H. Y. Xu, X. H. Li, H. Yu, Y. C. Liu, X. J. Zhu, Synaptic Learning and Memory Functions Achieved Using Oxygen Ion Migration/Diffusion in an Amorphous InGaZnO Memristor, *Advanced Functional Materials* 22 (13) (2012) 2759–2765. doi:10.1002/adfm.201103148. [Cited on pages 16 and 17.]
- [102] S.-J. Choi, G.-B. Kim, K. Lee, K.-H. Kim, W.-Y. Yang, S. Cho, H.-J. Bae, D.-S. Seo, S.-I. Kim, K.-J. Lee, Synaptic behaviors of a single metal–oxide–metal resistive device, *Applied Physics A* 102 (4) (2011) 1019–1025. doi:10.1007/s00339-011-6282-7. [Cited on pages 16, 17, and 19.]

- [103] Y. V. Pershin, M. Di Ventra, Experimental demonstration of associative memory with memristive neural networks, *Neural Networks* 23 (7) (2010) 881–886. doi:10.1016/j.neunet.2010.05.001. [Cited on page 18.]
- [104] K. Seo, I. Kim, S. Jung, M. Jo, S. Park, J. Park, J. Shin, K. P. Biju, J. Kong, K. Lee, B. Lee, H. Hwang, Analog memory and spike-timing-dependent plasticity characteristics of a nanoscale titanium oxide bilayer resistive switching device, *Nanotechnology* 22 (25) (2011) 254023. doi:10.1088/0957-4484/22/25/254023. [Cited on pages 16 and 19.]
- [105] C. Zamarreño-Ramos, L. a. Camuñas-Mesa, J. a. Pérez-Carrasco, T. Masquelier, T. Serrano-Gotarredona, B. Linares-Barranco, On Spike-Timing-Dependent-Plasticity, Memristive Devices, and Building a Self-Learning Visual Cortex, *Frontiers in Neuroscience* 5 (26). doi:10.3389/fnins.2011.00026. [Cited on pages 16 and 17.]
- [106] K. Zarudnyi, A. Mehonic, L. Montesi, M. Buckwell, S. Hudziak, A. J. Kenyon, Spike-Timing Dependent Plasticity in Unipolar Silicon Oxide RRAM Devices, *Frontiers in Neuroscience* 12 (2018) 1–8. doi:10.3389/fnins.2018.00057. [Cited on pages 17 and 75.]
- [107] T. Ohno, T. Hasegawa, T. Tsuruoka, K. Terabe, J. K. Gimzewski, M. Aono, Short-term plasticity and long-term potentiation mimicked in single inorganic synapses, *Nature Materials* 10 (8) (2011) 591–595. doi:10.1038/nmat3054. [Cited on pages 17 and 18.]
- [108] C. J. Wan, L. Q. Zhu, J. M. Zhou, Y. Shi, Q. Wan, Memory and learning behaviors mimicked in nanogranular SiO₂-based proton conductor gated oxide-based synaptic transistors, *Nanoscale* 5 (21) (2013) 10194–10199. doi:10.1039/c3nr02987e. [Cited on page 18.]
- [109] J. Schemmel, A. Grubl, K. Meier, E. Mueller, Implementing Synaptic Plasticity in a VLSI Spiking Neural Network Model, in: *The 2006 IEEE International Joint Conference on Neural Network Proceedings*, IEEE, 2006, pp. 1–6. doi:10.1109/IJCNN.2006.246651. [Cited on page 19.]
- [110] P. a. Merolla, J. V. Arthur, R. Alvarez-Icaza, a. S. Cassidy, J. Sawada, F. Akopyan, B. L. Jackson, N. Imam, C. Guo, Y. Nakamura, B. Brezzo, I. Vo, S. K. Esser, R. Appuswamy, B. Taba, a. Amir, M. D. Flickner, W. P. Risk, R. Manohar, D. S. Modha, A million spiking-neuron integrated circuit with a scalable communication network and interface, *Science* 345 (6197) (2014) 668–673. doi:10.1126/science.1254642. [Cited on page 19.]
- [111] F. Rosenblatt, *The Perceptron - A Perceiving and Recognizing Automaton*, Tech. rep., Cornell Aeronautical Laboratory, Inc (1957). [Cited on page 19.]
- [112] L. Wang, M. Duan, S. Duan, Memristive Perceptron for Combinational Logic Classification, *Mathematical Problems in Engineering* 2013 (1) (2013) 1–7. doi:10.1155/2013/625790. [Cited on pages 19, 20, 21, 102, and 103.]
- [113] H. Park, Part 2: Multilayer perceptron and natural gradient learning, *New Generation Computing* 24 (1) (2006) 79–95. doi:10.1007/BF03037294. [Cited on pages 20 and 102.]
- [114] S. Haykin, Rosenblatt 's Perceptron, in: *Neural Networks and Learning Machines*, Pearson, 2009, pp. 47–67. [Cited on pages 20 and 21.]
- [115] N. A. Mat Isa, W. M. F. W. Mamat, Clustered-Hybrid Multilayer Perceptron network for pattern recognition application, *Applied Soft Computing* 11 (1) (2011) 1457–1466. doi:10.1016/j.asoc.2010.04.017. [Cited on pages 20 and 102.]

- [116] L. Gatet, H. Tap-Beteille, F. Bony, Comparison Between Analog and Digital Neural Network Implementations for Range-Finding Applications, *IEEE Transactions on Neural Networks* 20 (3) (2009) 460–470. doi:10.1109/TNN.2008.2009120. [Cited on pages 20, 21, and 102.]
- [117] L. Bo, L. Wang, L. Jiao, Multi-layer Perceptrons with embedded feature selection with application in Cancer Classification, in: *Chinese Journal of Electronics*, 2006. [Cited on page 20.]
- [118] E. Agirre-Basurko, G. Ibarra-Berastegi, I. Madariaga, Regression and multilayer perceptron-based models to forecast hourly O₃ and NO₂ levels in the Bilbao area, *Environmental Modelling & Software* 21 (4) (2006) 430–446. doi:10.1016/j.envsoft.2004.07.008. [Cited on pages 21 and 103.]
- [119] M. Ziegler, R. Soni, T. Patelczyk, M. Ignatov, T. Bartsch, P. Meuffels, H. Kohlstedt, An Electronic Version of Pavlov's Dog, *Advanced Functional Materials* 22 (13) (2012) 2744–2749. doi:10.1002/adfm.201200244. [Cited on page 21.]
- [120] W. S. McCulloch, W. Pitts, A logical calculus of the ideas immanent in nervous activity, *The Bulletin of Mathematical Biophysics* 5 (4) (1943) 115–133. doi:10.1007/BF02478259. [Cited on page 21.]
- [121] E. Lehtonen, J. H. Poikonen, M. Laiho, P. Kanerva, Large-Scale Memristive Associative Memories, *IEEE Transactions on Very Large Scale Integration (VLSI) Systems* 22 (3) (2014) 562–574. doi:10.1109/TVLSI.2013.2250319. [Cited on pages 23, 95, and 96.]
- [122] C. Dias, L. M. Guerra, J. Ventura, P. Aguiar, Memristor-based Willshaw network: Capacity and robustness to noise in the presence of defects, *Applied Physics Letters* 106 (22) (2015) 223505. doi:10.1063/1.4922148. [Cited on page 23.]
- [123] S. Hu, Y. Liu, Z. Liu, T. Chen, J. Wang, Q. Yu, L. Deng, Y. Yin, S. Hosaka, Associative memory realized by a reconfigurable memristive Hopfield neural network, *Nature Communications* 6 (1) (2015) 7522. doi:10.1038/ncomms8522. [Cited on page 23.]
- [124] X. Guo, F. Merrikh-Bayat, L. Gao, B. D. Hoskins, F. Alibart, B. Linares-Barranco, L. Theogarajan, C. Teuscher, D. B. Strukov, Modeling and Experimental Demonstration of a Hopfield Network Analog-to-Digital Converter with Hybrid CMOS/Memristor Circuits, *Frontiers in Neuroscience* 9 (2015) 1–8. doi:10.3389/fnins.2015.00488. [Cited on page 23.]
- [125] S. Duan, Z. Dong, X. Hu, L. Wang, H. Li, Small-world Hopfield neural networks with weight salience priority and memristor synapses for digit recognition, *Neural Computing and Applications* 27 (4) (2016) 837–844. doi:10.1007/s00521-015-1899-7. [Cited on page 23.]
- [126] J. Yang, L. Wang, Y. Wang, T. Guo, A novel memristive Hopfield neural network with application in associative memory, *Neurocomputing* 227 (2017) 142–148. doi:10.1016/j.neucom.2016.07.065. [Cited on page 23.]
- [127] D. J. Willshaw, O. P. Buneman, H. C. Longuet-Higgins, Non-Holographic Associative Memory, *Nature* 222 (1969) 960–962. doi:10.1038/222960a0. [Cited on pages 23, 95, and 98.]
- [128] J. J. Hopfield, Neural networks and physical systems with emergent collective computational abilities., *Proceedings of the National Academy of Sciences* 79 (8) (1982) 2554–2558. doi:10.1073/pnas.79.8.2554. [Cited on page 23.]
- [129] D. W. Hopfield, J. J. Tank, “Neural” computation of decisions in optimization problems, *Biological Cybernetics* 52 (3) (1985) 141–152. doi:10.1007/BF00339943. [Cited on page 23.]

- [130] G. V. Wilson, G. S. Pawley, On the stability of the Travelling Salesman Problem algorithm of Hopfield and Tank, *Biological Cybernetics* 58 (1) (1988) 63–70. doi:10.1007/BF00363956. [Cited on page 23.]
- [131] P. Hollis, J. Paulos, An analog BiCMOS Hopfield neuron, *Analog Integrated Circuits and Signal Processing* 2 (4) (1992) 273–279. doi:10.1007/BF00228711. [Cited on page 23.]
- [132] K. Likharev, Neuromorphic CMOL circuits, in: 2003 Third IEEE Conference on Nanotechnology, 2003. IEEE-NANO 2003., Vol. 2, IEEE, 2003, pp. 339–342. doi:10.1109/NANO.2003.1231787. [Cited on page 23.]
- [133] A. Wu, J. Zhang, Z. Zeng, Dynamic behaviors of a class of memristor-based Hopfield networks, *Physics Letters, Section A: General, Atomic and Solid State Physics* 375 (15) (2011) 1661–1665. doi:10.1016/j.physleta.2011.02.068. [Cited on page 23.]
- [134] V. Ravichandran, C. Li, A. Banagozar, J. J. Yang, Q. Xia, Artificial neural networks based on memristive devices, *Science China Information Sciences* 61 (6) (2018) 060423. doi:10.1007/s11432-018-9425-1. [Cited on page 24.]
- [135] R. Ferreira, Ion Beam Deposited Magnetic Spin Tunnel Junctions targeting HDD Read Heads, Non-volatile Memories and Magnetic Field Sensor Applications, Phd thesis, Instituto Superior Técnico, Universidade de Lisboa (2008). [Cited on pages 28 and 30.]
- [136] A. Errokh, A. Ferraria, D. Conceição, L. Vieira Ferreira, A. Botelho do Rego, M. Rei Vilar, S. Boufi, Controlled growth of Cu₂O nanoparticles bound to cotton fibres, *Carbohydrate Polymers* 141 (2016) 229–237. doi:10.1016/j.carbpol.2016.01.019. [Cited on page 34.]
- [137] A. Instruments, ArC ONE, <http://www.arc-instruments.co.uk/products/arc-one/>. [Cited on page 35.]
- [138] G. Venturini, I. Daniher, R. Crowther, Ahkab - A Spice-like Electronic Circuit Simulator Written in Python, Ahkab v0.18, <https://ahkab.github.io/ahkab/> (2015). [Cited on page 36.]
- [139] R. Pino, J. Bohl, N. McDonald, Compact Method for Modeling and Simulation of Memristor Devices, in: *Nanoscale Architectures (NANOARCH)*, 2010, pp. 1–4. doi:10.1109/NANOARCH.2010.5510936. [Cited on pages 36 and 96.]
- [140] C. Dias, D. J. Silva, P. Aguiar, J. Ventura, Associative networks and perceptron based on memristors: fundamentals and algorithmic implementation, in: L. Chua, G. Sirakoulis, A. Adamatzky (Eds.), *Handbook of Memristor Networks*, Springer International Publishing, 2019. [Cited on pages 36 and 95.]
- [141] C. Dias, D. J. Silva, P. Aguiar, J. Ventura, Github: Memristive Networks, <https://github.com/danieljosesilva/memristivenetworks> (2018). [Cited on pages 36 and 95.]
- [142] S. G. Hu, S. Y. Wu, W. W. Jia, Q. Yu, L. J. Deng, Y. Q. Fu, Y. Liu, T. P. Chen, Review of Nanostructured Resistive Switching Memristor and Its Applications, *Nanoscience and Nanotechnology Letters* 6 (9) (2014) 729–757. doi:10.1166/nnl.2014.1888. [Cited on page 37.]
- [143] C. Ye, J. Wu, G. He, J. Zhang, T. Deng, P. He, H. Wang, Physical Mechanism and Performance Factors of Metal Oxide Based Resistive Switching Memory: A Review, *Journal of Materials Science & Technology* 32 (1) (2016) 1–11. doi:10.1016/j.jmst.2015.10.018. [Cited on page 37.]

- [144] J. Yao, L. Zhong, D. Natelson, J. M. Tour, In situ imaging of the conducting filament in a silicon oxide resistive switch, *Scientific Reports* 2 (1) (2012) 242. doi:10.1038/srep00242. [Cited on pages 37 and 75.]
- [145] H. Jiang, Q. Xia, Effect of voltage polarity and amplitude on electroforming of TiO₂ based memristive devices, *Nanoscale* 5 (8) (2013) 3257–3261. doi:10.1039/c3nr00622k. [Cited on pages 37 and 40.]
- [146] S. B. Lee, H. K. Yoo, K. Kim, J. S. Lee, Y. S. Kim, S. Sinn, D. Lee, B. S. Kang, B. Kahng, T. W. Noh, Forming mechanism of the bipolar resistance switching in double-layer memristive nanodevices, *Nanotechnology* 23 (31) (2012) 315202. doi:10.1088/0957-4484/23/31/315202. [Cited on page 37.]
- [147] S. Maikap, D. Jana, M. Dutta, A. Prakash, Self-compliance RRAM characteristics using a novel W/TaO_x/TiN structure, *Nanoscale Research Letters* 9 (1) (2014) 292. doi:10.1186/1556-276X-9-292. [Cited on page 37.]
- [148] W. Banerjee, S. Maikap, C.-S. Lai, Y.-Y. Chen, T.-C. Tien, H.-Y. Lee, W.-S. Chen, F. T. Chen, M.-J. Kao, M.-J. Tsai, J.-R. Yang, Formation polarity dependent improved resistive switching memory characteristics using nanoscale (1.3 nm) core-shell IrO_x nano-dots, *Nanoscale Research Letters* 7 (1) (2012) 194. doi:10.1186/1556-276X-7-194. [Cited on pages 37 and 40.]
- [149] A. Rodriguez, M. Gonzalez, E. Miranda, F. Campabadal, J. Suñe, Temperature and polarity dependence of the switching behavior of Ni/HfO₂-based RRAM devices, *Microelectronic Engineering* 147 (2015) 75–78. doi:10.1016/j.mee.2015.04.038. [Cited on pages 37 and 40.]
- [150] I. K. Yoo, M. J. Lee, D. H. Seo, S. J. Kim, Interpretation of set and reset switching in nickel oxide thin films, *Applied Physics Letters* 104 (22) (2014) 2012–2016. doi:10.1063/1.4880796. [Cited on page 37.]
- [151] F.-C. Chiu, W.-C. Shih, J.-J. Feng, Conduction mechanism of resistive switching films in MgO memory devices, *Journal of Applied Physics* 111 (9) (2012) 094104. doi:10.1063/1.4712628. [Cited on page 37.]
- [152] E. Miranda, J. Martin-Martinez, E. O'Connor, G. Hughes, P. Casey, K. Cherkaoui, S. Monaghan, R. Long, D. O'Connell, P. Hurley, Effects of the electrical stress on the conduction characteristics of metal gate/MgO/InP stacks, *Microelectronics Reliability* 49 (2009) 1052–1055. doi:10.1016/j.microrel.2009.06.017. [Cited on page 37.]
- [153] C. Yoshida, M. Kurasawa, Y. M. Lee, M. Aoki, Y. Sugiyama, Unipolar resistive switching in CoFeB-MgO/CoFeB magnetic tunnel junction, *Applied Physics Letters* 92 (11) (2008) 113508. doi:10.1063/1.2898514. [Cited on page 37.]
- [154] P. Krzysteczko, X. Kou, K. Rott, A. Thomas, G. Reiss, Current induced resistance change of magnetic tunnel junctions with ultra-thin MgO tunnel barriers, *Journal of Magnetism and Magnetic Materials* 321 (3) (2009) 144–147. doi:10.1016/j.jmmm.2008.08.088. [Cited on page 37.]
- [155] H.-H. Huang, W.-C. Shih, C.-H. Lai, Nonpolar resistive switching in the Pt/MgO/Pt nonvolatile memory device, *Applied Physics Letters* 96 (19) (2010) 193505. doi:10.1063/1.3429024. [Cited on page 37.]

- [156] J. M. Teixeira, J. Ventura, R. Fermento, J. P. Araujo, J. B. Sousa, P. Wisniowski, P. P. Freitas, Electroforming, magnetic and resistive switching in MgO-based tunnel junctions, *Journal of Physics D: Applied Physics* 42 (10) (2009) 105407. doi:10.1088/0022-3727/42/10/105407. [Cited on page 37.]
- [157] P. Krzysteczko, G. Reiss, A. Thomas, Memristive switching of MgO based magnetic tunnel junctions, *Applied Physics Letters* 95 (11) (2009) 112508. doi:10.1063/1.3224193. [Cited on page 37.]
- [158] P. Krzysteczko, J. Münchenberger, M. Schäfers, G. Reiss, A. Thomas, The Memristive Magnetic Tunnel Junction as a Nanoscopic Synapse-Neuron System, *Advanced Materials* 24 (6) (2012) 762–766. doi:10.1002/adma.201103723. [Cited on page 37.]
- [159] K. Jeong, Y. Do, K. Yoon, Resistive Switching Characteristics of Unique Binary-Oxide MgOx Films, *Journal of the Korean Physical Society* 48 (6) (2006) 1501–1504. [Cited on page 37.]
- [160] Fu-Chien Chiu, Jun-Jea Feng, Wen-Chieh Shih, Po-Yueh Cheng, Chih-Yao Huang, Conduction mechanisms and reliability characteristics in MgO resistive switching memory devices, in: 18th IEEE International Symposium on the Physical and Failure Analysis of Integrated Circuits (IPFA), IEEE, 2011, pp. 1–4. doi:10.1109/IPFA.2011.5992775. [Cited on page 37.]
- [161] J. Qi, M. Olmedo, J.-G. Zheng, J. Liu, Multimode Resistive Switching in Single ZnO Nanoisland System, *Scientific Reports* 3 (1) (2013) 2405. doi:10.1038/srep02405. [Cited on page 37.]
- [162] H.-B. LV, P. Zhuo, X.-F. Fu, M. Yin, Y.-L. Song, L. Tang, T.-A. Tang, Y.-y. Lin, Polarity-Free Resistive Switching Characteristics of CuxO Films for Non-volatile Memory Applications, *Chinese Physics Letters* 25 (3) (2008) 1087–1090. doi:10.1088/0256-307X/25/3/076. [Cited on page 37.]
- [163] D. S. Hong, W. X. Wang, Y. S. Chen, J. R. Sun, B. G. Shen, In-situ observation of self-regulated switching behavior in WO_{3-x} based resistive switching devices, *Applied Physics Letters* 105 (11) (2014) 113504. doi:10.1063/1.4895629. [Cited on page 37.]
- [164] S. Yuasa, D. D. Djayaprawira, Giant tunnel magnetoresistance in magnetic tunnel junctions with a crystalline MgO(0 0 1) barrier, *Journal of Physics D: Applied Physics* 40 (21) (2007) R337–R354. doi:10.1088/0022-3727/40/21/R01. [Cited on page 37.]
- [165] S. S. P. Parkin, C. Kaiser, A. Panchula, P. M. Rice, B. Hughes, M. Samant, S.-H. Yang, Giant tunnelling magnetoresistance at room temperature with MgO (100) tunnel barriers, *Nature Materials* 3 (12) (2004) 862–867. doi:10.1038/nmat1256. [Cited on page 37.]
- [166] J. M. Teixeira, J. Ventura, J. P. Araujo, J. B. Sousa, P. Wisniowski, S. Cardoso, P. P. Freitas, Resonant Tunneling through Electronic Trapping States in Thin MgO Magnetic Junctions, *Physical Review Letters* 106 (19) (2011) 196601. doi:10.1103/PhysRevLett.106.196601. [Cited on page 37.]
- [167] E. Miranda, E. O'Connor, K. Cherkaoui, S. Monaghan, R. Long, D. O'Connell, P. K. Hurley, G. Hughes, P. Casey, Electrical characterization of the soft breakdown failure mode in MgO layers, *Applied Physics Letters* 95 (1) (2009) 2009–2011. doi:10.1063/1.3167827. [Cited on page 37.]
- [168] O. Jambois, P. Carreras, A. Antony, J. Bertomeu, C. Martinez-Boubeta, Resistance switching in transparent magnetic MgO films, *Solid State Communications* 151 (24) (2011) 1856–1859. doi:10.1016/j.ssc.2011.10.009. [Cited on page 37.]

- [169] W. Lu, W. Chen, P. Thapaliya, R. O' Dell, R. Jha, Switching characteristics of MgO based self-compliant ReRAM devices, in: 2015 IEEE 58th International Midwest Symposium on Circuits and Systems (MWSCAS), IEEE, 2015, pp. 1–4. doi:10.1109/MWSCAS.2015.7282090. [Cited on page 37.]
- [170] L. M. Guerra, C. Dias, J. Pereira, H. Lv, S. Cardoso, P. P. Freitas, J. Ventura, Unipolar Nonvolatile Resistive Switching in Pt / MgO / Ta / Ru Structures Deposited by Magnetron Sputtering, *Journal of Nanoscience and Nanotechnology* 17 (1) (2017) 564–567. doi:10.1166/jnn.2017.12333. [Cited on pages 37, 66, and 67.]
- [171] M. Menghini, C. Quinteros, C.-Y. Su, P. Homm, P. Levy, J. Kittl, J.-P. Locquet, Resistive switching on MgO-based metal-insulator-metal structures grown by molecular beam epitaxy, *physica status solidi (c)* 12 (1-2) (2015) 246–249. doi:10.1002/pssc.201400192. [Cited on page 37.]
- [172] L. Pauling, The sizes of ions and the structure of ionic crystals, *Journal of the American Chemical Society* 49 (3) (1927) 765–790. doi:10.1021/ja01402a019. [Cited on page 37.]
- [173] A. Naumkin, A. Kraut-Vass, S. Gaarenstroom, C. Powell, NIST X-ray photoelectron spectroscopy database, standard reference database 20, Version 4.1. Ed. [Cited on page 38.]
- [174] M. Zhang, S. Long, G. Wang, Y. Li, X. Xu, H. Liu, R. Liu, M. Wang, C. Li, P. Sun, H. Sun, Q. Liu, H. Lü, M. Liu, An overview of the switching parameter variation of RRAM, *Chinese Science Bulletin* 59 (36) (2014) 5324–5337. doi:10.1007/s11434-014-0673-z. [Cited on page 40.]
- [175] P. S. Chen, Y. S. Chen, K. H. Tsai, H. Y. Lee, Polarity dependence of forming step on improved performance in Ti/HfO_x/W with dual resistive switching mode, *Microelectronic Engineering* 112 (2013) 157–162. doi:10.1016/j.mee.2013.04.005. [Cited on page 40.]
- [176] Y.-C. Chen, Y.-L. Chung, B.-T. Chen, W.-C. Chen, J.-S. Chen, Revelation on the Interrelated Mechanism of Polarity-Dependent and Multilevel Resistive Switching in TaO_x -Based Memory Devices, *The Journal of Physical Chemistry C* 117 (11) (2013) 5758–5764. doi:10.1021/jp311951e. [Cited on page 40.]
- [177] I. S. Park, Y. C. Jung, J. Ahn, Anode dependence of set voltage in resistive switching of metal/HfO₂/metal resistors, *Applied Physics Letters* 105 (22) (2014) 2014–2017. doi:10.1063/1.4903805. [Cited on page 40.]
- [178] E. Yalon, I. Karpov, V. Karpov, I. Riess, D. Kalaev, D. Ritter, Detection of the insulating gap and conductive filament growth direction in resistive memories, *Nanoscale* 7 (37) (2015) 15434–15441. doi:10.1039/C5NR03314D. [Cited on pages 40, 44, and 45.]
- [179] Z. Wang, H. Xu, X. Zhao, Y. Lin, L. Zhang, J. Ma, Y. Liu, Effect of reset voltage polarity on the resistive switching region of unipolar memory, *physica status solidi (a)* 212 (10) (2015) 2255–2261. doi:10.1002/pssa.201532235. [Cited on page 40.]
- [180] M. Ismail, E. Ahmed, A. M. Rana, I. Talib, M. Y. Nadeem, Coexistence of bipolar and unipolar resistive switching in Al-doped ceria thin films for non-volatile memory applications, *Journal of Alloys and Compounds* 646 (2015) 662–668. doi:10.1016/j.jallcom.2015.06.146. [Cited on page 40.]
- [181] I. Salaoru, A. Khiat, Q. Li, R. Berdan, C. Papavassiliou, T. Prodromakis, Origin of the OFF state variability in ReRAM cells, *Journal of Physics D: Applied Physics* 47 (14) (2014) 145102. doi:10.1088/0022-3727/47/14/145102. [Cited on pages 42 and 78.]

- [182] D. S. Jeong, R. Thomas, R. S. Katiyar, J. F. Scott, H. Kohlstedt, A. Petraru, C. S. Hwang, Emerging memories: resistive switching mechanisms and current status, *Reports on Progress in Physics* 75 (7) (2012) 076502. doi:10.1088/0034-4885/75/7/076502. [Cited on page 44.]
- [183] D. Kalaev, E. Yalon, I. Riess, On the direction of the conductive filament growth in valence change memory devices during electroforming, *Solid State Ionics* 276 (2015) 9–17. doi:10.1016/j.ssi.2015.03.017. [Cited on page 44.]
- [184] T. Liu, M. Verma, Y. Kang, M. K. Orlowski, Coexistence of Bipolar and Unipolar Switching of Cu and Oxygen Vacancy Nanofilaments in Cu/TaOx/Pt Resistive Devices, *ECS Solid State Letters* 1 (1) (2012) Q11–Q13. doi:10.1149/2.012201ss1. [Cited on page 45.]
- [185] Y. Zhang, S. Zhong, L. Song, X. Ji, R. Zhao, Emulating dynamic synaptic plasticity over broad timescales with memristive device, *Applied Physics Letters* 113 (20) (2018) 203102. doi:10.1063/1.5052556. [Cited on page 55.]
- [186] L. Chen, Y.-W. Dai, Q.-Q. Sun, J.-J. Guo, P. Zhou, D. W. Zhang, Al₂O₃/HfO₂ functional stack films based resistive switching memories with controlled SET and RESET voltages, *Solid State Ionics* 273 (2015) 66–69. doi:10.1016/j.ssi.2014.08.014. [Cited on page 56.]
- [187] W. Liu, L. Gao, K. Xu, F. Ma, Impact of ultrathin Al₂O₃ interlayers on resistive switching in TiOx thin films deposited by atomic layer deposition, *Journal of Vacuum Science & Technology B, Nanotechnology and Microelectronics: Materials, Processing, Measurement, and Phenomena* 35 (4) (2017) 041001. doi:10.1116/1.4985053. [Cited on page 56.]
- [188] H. Jeon, J. Park, W. Jang, H. Kim, S. Ahn, K.-J. Jeon, H. Seo, H. Jeon, Detection of oxygen ion drift in Pt/Al₂O₃/TiO₂/Pt RRAM using interface-free single-layer graphene electrodes, *Carbon* 75 (2014) 209–216. doi:10.1016/j.carbon.2014.03.055. [Cited on page 56.]
- [189] W. Banerjee, Q. Liu, H. Lv, S. Long, M. Liu, Electronic imitation of behavioral and psychological synaptic activities using TiOx/Al₂O₃ -based memristor devices, *Nanoscale* 9 (38) (2017) 14442–14450. doi:10.1039/C7NR04741J. [Cited on page 56.]
- [190] D. Kumar, R. Aluguri, U. Chand, T.-Y. Tseng, Enhancement of resistive switching properties in nitride based CBRAM device by inserting an Al₂O₃ thin layer, *Applied Physics Letters* 110 (20) (2017) 203102. doi:10.1063/1.4983465. [Cited on page 56.]
- [191] M. Trapatseli, S. Cortese, A. Serb, A. Khiat, T. Prodromakis, Impact of ultra-thin Al₂O_{3-y} layers on TiO_{2-x} ReRAM switching characteristics, *Journal of Applied Physics* 121 (18) (2017) 184505. doi:10.1063/1.4983006. [Cited on page 56.]
- [192] S. Stathopoulos, A. Khiat, M. Trapatseli, S. Cortese, A. Serb, I. Valov, T. Prodromakis, Multibit memory operation of metal-oxide bi-layer memristors, *Scientific Reports* 7 (1) (2017) 17532. doi:10.1038/s41598-017-17785-1. [Cited on page 56.]
- [193] N. Andreeva, A. Ivanov, A. Petrov, Multilevel resistive switching in TiO₂/Al₂O₃ bilayers at low temperature, *AIP Advances* 8 (2) (2018) 025208. doi:10.1063/1.5019570. [Cited on page 56.]
- [194] M. Akbari, M.-K. Kim, D. Kim, J.-S. Lee, Reproducible and reliable resistive switching behaviors of AlOx/HfOx bilayer structures with Al electrode by atomic layer deposition, *RSC Adv.* 7 (27) (2017) 16704–16708. doi:10.1039/C6RA26872B. [Cited on page 56.]

- [195] K.-c. Chuang, H.-t. Chung, C.-y. Chu, J.-d. Luo, W.-S. Li, Y.-s. Li, H.-c. Cheng, Impact of AlOx layer on resistive switching characteristics and device-to-device uniformity of bilayered HfOx-based resistive random access memory devices, *Japanese Journal of Applied Physics* 57 (6S3) (2018) 06KC01. doi:10.7567/JJAP.57.06KC01. [Cited on page 56.]
- [196] M. Hansen, M. Ziegler, L. Kolberg, R. Soni, S. Dirkmann, T. Mussenbrock, H. Kohlstedt, A double barrier memristive device, *Scientific Reports* 5 (1) (2015) 13753. doi:10.1038/srep13753. [Cited on page 56.]
- [197] K. Park, J.-S. Lee, Reliable resistive switching memory based on oxygen-vacancy-controlled bilayer structures, *RSC Advances* 6 (26) (2016) 21736–21741. doi:10.1039/C6RA00798H. [Cited on page 56.]
- [198] S.-C. Qin, R.-X. Dong, X.-L. Yan, Memristive behavior of Al₂O₃ film with bottom electrode surface modified by Ag nanoparticles, *Applied Physics A* 118 (2) (2015) 605–612. doi:10.1007/s00339-014-8765-9. [Cited on page 56.]
- [199] A. Jo, Y. Seo, M. Ko, C. Kim, H. Kim, S. Nam, H. Choi, C. S. Hwang, M. J. Lee, Textile Resistance Switching Memory for Fabric Electronics, *Advanced Functional Materials* 27 (15) (2017) 1605593. doi:10.1002/adfm.201605593. [Cited on pages 56 and 86.]
- [200] J. Molina-Reyes, L. Hernandez-Martinez, Understanding the resistive switching phenomena of stacked Al/Al₂O₃/Al thin films from the dynamics of conductive filaments, *Complexity* 2017. doi:10.1155/2017/8263904. [Cited on page 56.]
- [201] T.-m. Tsai, K.-C. Chang, R. Zhang, T.-c. Chang, J. C. Lou, J.-H. Chen, T.-f. Young, B.-h. Tseng, C.-c. Shih, Y.-C. Pan, M.-c. Chen, J.-h. Pan, Y.-e. Syu, S. M. Sze, Performance and characteristics of double layer porous silicon oxide resistance random access memory, *Applied Physics Letters* 102 (25) (2013) 253509. doi:10.1063/1.4812474. [Cited on pages 56 and 75.]
- [202] H. Wu, X. Li, M. Wu, F. Huang, Z. Yu, H. Qian, Resistive Switching Performance Improvement of Ta₂O_{5-x}/TaO_y Bilayer ReRAM Devices by Inserting AlO_d Barrier Layer, *IEEE Electron Device Letters* 35 (1) (2014) 39–41. doi:10.1109/LED.2013.2288311. [Cited on page 56.]
- [203] J. Li, Q. Duan, T. Zhang, M. Yin, X. Sun, Y. Cai, L. Li, Y. Yang, R. Huang, Tuning analog resistive switching and plasticity in bilayer transition metal oxide based memristive synapses, *RSC Advances* 7 (68) (2017) 43132–43140. doi:10.1039/C7RA07522G. [Cited on page 56.]
- [204] A. Hardtdegen, C. La Torre, F. Cuppers, S. Menzel, R. Waser, S. Hoffmann-Eifert, Improved Switching Stability and the Effect of an Internal Series Resistor in HfO₂/TiO_x Bilayer ReRAM Cells, *IEEE Transactions on Electron Devices* 65 (8) (2018) 3229–3236. doi:10.1109/TED.2018.2849872. [Cited on page 56.]
- [205] T. Tan, Y. Du, A. Cao, Y. Sun, H. Zhang, G. Zha, Resistive switching of the HfOx/HfO₂ bilayer heterostructure and its transmission characteristics as a synapse, *RSC Advances* 8 (73) (2018) 41884–41891. doi:10.1039/C8RA06230G. [Cited on page 56.]
- [206] J. Yin, F. Zeng, Q. Wan, Y. Sun, Y. Hu, J. Liu, G. Li, F. Pan, Self-Modulating Interfacial Cation Migration Induced Threshold Switching in Bilayer Oxide Memristive Device, *The Journal of Physical Chemistry C* 123 (1) (2019) 878–885. doi:10.1021/acs.jpcc.8b09793. [Cited on page 56.]

- [207] S. Kim, Y. Abbas, Y.-R. Jeon, A. S. Sokolov, B. Ku, C. Choi, Engineering synaptic characteristics of TaOx/HfO2 bi-layered resistive switching device, *Nanotechnology* 29 (41) (2018) 415204. doi: 10.1088/1361-6528/aad64c. [Cited on page 56.]
- [208] T. R. Phillip, A Study On Resistive Switching of MgO ReRAM Devices, MSc thesis, Faculty of Sciences of the University of Porto. [Cited on pages 66 and 67.]
- [209] Q. Mao, Z. Ji, J. Xi, Realization of forming-free ZnO-based resistive switching memory by controlling film thickness, *Journal of Physics D: Applied Physics* 43 (39) (2010) 395104. doi:10.1088/0022-3727/43/39/395104. [Cited on page 66.]
- [210] Y. Chao Yang, F. Pan, F. Zeng, Bipolar resistance switching in high-performance Cu/ZnO:Mn/Pt nonvolatile memories: active region and influence of Joule heating, *New Journal of Physics* 12 (2) (2010) 023008. doi:10.1088/1367-2630/12/2/023008. [Cited on page 66.]
- [211] Y. H. Kang, J. H. Choi, T. I. Lee, W. Lee, J. M. Myoung, Thickness dependence of the resistive switching behavior of nonvolatile memory device structures based on undoped ZnO films, *Solid State Communications* 151 (23) (2011) 1739–1742. doi:10.1016/j.ssc.2011.08.036. [Cited on page 66.]
- [212] S. C. Chae, J. S. Lee, S. Kim, S. B. Lee, S. H. Chang, C. Liu, B. Kahng, H. Shin, D. W. Kim, C. U. Jung, S. Seo, M. J. Lee, T. W. Noh, Random circuit breaker network model for unipolar resistance switching, *Advanced Materials* 20 (6) (2008) 1154–1159. doi:10.1002/adma.200702024. [Cited on page 66.]
- [213] S. B. Lee, J. S. Lee, S. H. Chang, H. K. Yoo, B. S. Kang, B. Kahng, M. J. Lee, C. J. Kim, T. W. Noh, Interface-modified random circuit breaker network model applicable to both bipolar and unipolar resistance switching, *Applied Physics Letters* 98 (3) (2011) 2009–2012. doi:10.1063/1.3543776. [Cited on page 66.]
- [214] J. Xing, Q. Li, X. Tian, Z. Li, H. Xu, A memristor random circuit breaker model accounting for stimulus thermal accumulation, *IEICE Electronics Express* 13 (14) (2016) 1–10. doi:10.1587/elex.13.20160376. [Cited on page 66.]
- [215] J. S. Lee, S. Lee, T. W. Noh, Resistive switching phenomena: A review of statistical physics approaches, *Applied Physics Reviews* 2 (3) (2015) 031303. doi:10.1063/1.4929512. [Cited on pages 67 and 68.]
- [216] K. Lee, J.-S. Jang, Y. Kwon, K.-H. Lee, Y.-K. Park, W. Young Choi, A unified model for unipolar resistive random access memory, *Applied Physics Letters* 100 (8) (2012) 083509. doi:10.1063/1.3688944. [Cited on page 67.]
- [217] K. Kim, S. J. Yoon, W. Y. Choi, Dual random circuit breaker network model with equivalent thermal circuit network, *Applied Physics Express* 7 (2) (2014) 024203. doi:10.7567/APEX.7.024203. [Cited on page 67.]
- [218] K. Kim, K. Lee, K.-H. Lee, Y.-K. Park, W. Y. Choi, A Finite Element Model for Bipolar Resistive Random Access Memory, *JSTS:Journal of Semiconductor Technology and Science* 14 (3) (2014) 268–273. doi:10.5573/JSTS.2014.14.3.268. [Cited on page 68.]

- [219] S. H. Chang, J. S. Lee, S. C. Chae, S. B. Lee, C. Liu, B. Kahng, D.-W. Kim, T. W. Noh, Occurrence of Both Unipolar Memory and Threshold Resistance Switching in a NiO Film, *Physical Review Letters* 102 (2) (2009) 026801. doi:10.1103/PhysRevLett.102.026801. [Cited on page 68.]
- [220] L. Gao, S. B. Lee, B. Hoskins, H. K. Yoo, B. S. Kang, Dynamic switching mechanism of conduction/set process in Cu/a-Si/Si memristive device, *Applied Physics Letters* 103 (4). doi:10.1063/1.4816327. [Cited on page 75.]
- [221] S. H. Jo, W. Lu, CMOS Compatible Nanoscale Nonvolatile Resistance Switching Memory, *Nano Letters* 8 (2) (2008) 392–397. doi:10.1021/nl073225h. [Cited on page 75.]
- [222] J. Won Seo, S. J. Baik, S. J. Kang, Y. H. Hong, J.-H. Yang, L. Fang, K. S. Lim, Evidence of Al induced conducting filament formation in Al/amorphous silicon/Al resistive switching memory device, *Applied Physics Letters* 96 (5) (2010) 053504. doi:10.1063/1.3308471. [Cited on page 75.]
- [223] K.-H. Kim, S. Hyun Jo, S. Gaba, W. Lu, Nanoscale resistive memory with intrinsic diode characteristics and long endurance, *Applied Physics Letters* 96 (5) (2010) 053106. doi:10.1063/1.3294625. [Cited on page 75.]
- [224] S. H. Jo, K.-H. Kim, W. Lu, Programmable Resistance Switching in Nanoscale Two-Terminal Devices, *Nano Letters* 9 (1) (2009) 496–500. doi:10.1021/nl803669s. [Cited on page 75.]
- [225] S. H. Jo, K.-H. Kim, W. Lu, High-Density Crossbar Arrays Based on a Si Memristive System, *Nano Letters* 9 (2) (2009) 870–874. doi:10.1021/nl8037689. [Cited on page 75.]
- [226] Y. Dong, G. Yu, M. C. McAlpine, W. Lu, C. M. Lieber, Si/a-Si Core/Shell Nanowires as Nonvolatile Crossbar Switches, *Nano Letters* 8 (2) (2008) 386–391. doi:10.1021/nl073224p. [Cited on page 75.]
- [227] T. Moon, J. Kang, Y. Han, C. Kim, Y. Jeon, H. Kim, S. Kim, Si-Based Flexible Memristive Systems Constructed Using Top-Down Methods, *ACS Applied Materials & Interfaces* 3 (10) (2011) 3957–3961. doi:10.1021/am2008344. [Cited on page 75.]
- [228] R. Ebrahim, R. Mithun Kumar, N. Badi, N. Wu, A. Ignatiev, Filamentary bipolar electric pulse induced resistance switching in amorphous silicon resistive random access memory, *Journal of Vacuum Science & Technology B, Nanotechnology and Microelectronics: Materials, Processing, Measurement, and Phenomena* 33 (3) (2015) 032205. doi:10.1116/1.4919087. [Cited on page 75.]
- [229] J. Zhang, D. Chen, S. Huang, Influence of oxygen doping on resistive-switching characteristic of a-Si/c-Si device, *Journal of Semiconductors* 38 (12) (2017) 122003. doi:10.1088/1674-4926/38/12/122003. [Cited on page 75.]
- [230] D. Li, A. Guo, Q. Song, G. Guo, Y. Jiang, W. Li, The realization of optical switching generated from the combination of Ag/a-Si/p-Si memristor and silicon waveguide, in: X. Zhang, B. Li, C. Yu (Eds.), *Proc. SPIE 10019, Optoelectronic Devices and Integration VI*, 2016, p. 1001909. doi:10.1117/12.2245695. [Cited on page 75.]
- [231] A. Mehonic, T. Gerard, A. J. Kenyon, Light-activated resistance switching in SiO_x RRAM devices, *Applied Physics Letters* 111 (23) (2017) 233502. doi:10.1063/1.5009069. [Cited on page 75.]

- [232] J. Yao, Z. Sun, L. Zhong, D. Natelson, J. M. Tour, Resistive switches and memories from silicon oxide, *Nano Letters* 10 (10) (2010) 4105–4110. doi:10.1021/nl102255r. [Cited on page 75.]
- [233] A. Mehonic, A. Vrajitoarea, S. Cuff, S. Hudziak, H. Howe, C. Labbé, R. Rizk, M. Pepper, a. J. Kenyon, Quantum Conductance in Silicon Oxide Resistive Memory Devices, *Scientific Reports* 3 (1) (2013) 2708. doi:10.1038/srep02708. [Cited on page 75.]
- [234] A. Bricalli, E. Ambrosi, M. Laudato, M. Maestro, R. Rodriguez, D. Ielmini, Resistive Switching Device Technology Based on Silicon Oxide for Improved ON–OFF Ratio—Part II: Select Devices, *IEEE Transactions on Electron Devices* 65 (1) (2018) 122–128. doi:10.1109/TED.2017.2776085. [Cited on page 75.]
- [235] A. Mehonic, S. Cuff, M. Wojdak, S. Hudziak, C. Labbé, R. Rizk, A. J. Kenyon, Electrically tailored resistance switching in silicon oxide, *Nanotechnology* 23 (45) (2012) 455201. doi:10.1088/0957-4484/23/45/455201. [Cited on page 75.]
- [236] A. Mehonic, A. L. Shluger, D. Gao, I. Valov, E. Miranda, D. Ielmini, A. Bricalli, E. Ambrosi, C. Li, J. J. Yang, Q. Xia, A. J. Kenyon, Silicon Oxide (SiO_x): A Promising Material for Resistance Switching?, *Advanced Materials* 30 (43) (2018) 1801187. doi:10.1002/adma.201801187. [Cited on page 75.]
- [237] J.-s. Huang, Y.-c. Shih, L.-m. Chen, T.-y. Lin, S.-c. Chang, T.-s. Chin, Electrical Switching of Al-Doped Amorphous SiO_x Thin Films, *IEEE Transactions on Magnetics* 50 (7) (2014) 1–3. doi:10.1109/TMAG.2014.2305721. [Cited on page 75.]
- [238] C. Schindler, S. C. P. Thermadam, R. Waser, M. N. Kozicki, Bipolar and Unipolar Resistive Switching in Cu-Doped SiO₂, *IEEE Transactions on Electron Devices* 54 (10) (2007) 2762–2768. doi:10.1109/TED.2007.904402. [Cited on page 75.]
- [239] T.-M. Tsai, K.-C. Chang, T.-C. Chang, Y.-E. Syu, S.-L. Chuang, G.-W. Chang, G.-R. Liu, M.-C. Chen, H.-C. Huang, S.-K. Liu, Y.-H. Tai, D.-S. Gan, Y.-L. Yang, T.-F. Young, B.-H. Tseng, K.-H. Chen, M.-J. Tsai, C. Sze, H. Sze, S. M. Sze, Bipolar Resistive RAM Characteristics Induced by Nickel Incorporated Into Silicon Oxide Dielectrics for IC Applications, *IEEE Electron Device Letters* 33 (12) (2012) 1696–1698. doi:10.1109/LED.2012.2217933. [Cited on page 75.]
- [240] G. Wang, Y. Yang, J. H. Lee, V. Abramova, H. Fei, G. Ruan, E. L. Thomas, J. M. Tour, Nanoporous silicon oxide memory, *Nano Letters* 14 (8) (2014) 4694–4699. doi:10.1021/nl501803s. [Cited on page 75.]
- [241] J. H. Yoon, Z. Wang, K. M. Kim, H. Wu, V. Ravichandran, Q. Xia, C. S. Hwang, J. J. Yang, An artificial nociceptor based on a diffusive memristor, *Nature Communications* 9 (1) (2018) 417. doi:10.1038/s41467-017-02572-3. [Cited on page 75.]
- [242] Y.-F. Chang, B. Fowler, Y.-C. Chen, F. Zhou, C.-H. Pan, T.-C. Chang, J. C. Lee, Demonstration of Synaptic Behaviors and Resistive Switching Characterizations by Proton Exchange Reactions in Silicon Oxide, *Scientific Reports* 6 (1) (2016) 21268. doi:10.1038/srep21268. [Cited on page 75.]
- [243] B. Nikolić, P. Allen, Electron transport through a circular constriction, *Physical Review B - Condensed Matter and Materials Physics* 60 (6) (1999) 3963–3969. doi:10.1103/PhysRevB.60.3963. [Cited on page 79.]
- [244] L. Chua, Resistance switching memories are memristors, *Applied Physics A: Materials Science and Processing* 102 (4) (2011) 765–783. doi:10.1007/s00339-011-6264-9. [Cited on page 80.]

- [245] F. Corinto, P. P. Civalleri, L. O. Chua, A theoretical approach to memristor devices, *IEEE Journal on Emerging and Selected Topics in Circuits and Systems* 5 (2) (2015) 123–132. doi:10.1109/JETCAS.2015.2426494. [Cited on page 80.]
- [246] R. Picos, J. Roldan, M. A. Chawa, F. Jimenez-Molinos, M. Villena, E. Garcia-Moreno, Exploring ReRAM-based memristors in the charge-flux domain, a modeling approach, in: 2015 International Conference on Memristive Systems (MEMRISYS), IEEE, 2015, pp. 1–2. doi:10.1109/MEMRISYS.2015.7378386. [Cited on page 80.]
- [247] R. Picos, J. B. Roldan, M. M. Al Chawa, P. Garcia-Fernandez, F. Jimenez-Molinos, E. Garcia-Moreno, Semiempirical Modeling of Reset Transitions in Unipolar Resistive-Switching based Memristors, *Radioengineering* 24 (2) (2015) 420–424. doi:10.13164/re.2015.0420. [Cited on page 80.]
- [248] M. M. Al Chawa, C. de Benito, R. Picos, A Simple Piecewise Model of Reset/Set Transitions in Bipolar ReRAM Memristive Devices, *IEEE Transactions on Circuits and Systems I: Regular Papers* 65 (10) (2018) 3469–3480. doi:10.1109/TCSI.2018.2830412. [Cited on page 80.]
- [249] G. Medeiros-Ribeiro, F. Perner, R. Carter, H. Abdalla, M. D. Pickett, R. S. Williams, Lognormal switching times for titanium dioxide bipolar memristors: origin and resolution, *Nanotechnology* 22 (9) (2011) 095702. doi:10.1088/0957-4484/22/9/095702. [Cited on page 83.]
- [250] M. Hu, Y. Wang, Q. Qiu, Y. Chen, H. Li, The stochastic modeling of TiO_2 memristor and its usage in neuromorphic system design, in: 2014 19th Asia and South Pacific Design Automation Conference (ASP-DAC), IEEE, 2014, pp. 831–836. doi:10.1109/ASPDAC.2014.6742993. [Cited on pages 83 and 84.]
- [251] P. Knag, W. Lu, Z. Zhang, A Native Stochastic Computing Architecture Enabled by Memristors, *IEEE Transactions on Nanotechnology* 13 (2) (2014) 283–293. doi:10.1109/TNANO.2014.2300342. [Cited on pages 83 and 84.]
- [252] S. Balatti, S. Ambrogio, R. Carboni, V. Milo, Z. Wang, A. Calderoni, N. Ramaswamy, D. Ielmini, Physical Unbiased Generation of Random Numbers With Coupled Resistive Switching Devices, *IEEE Transactions on Electron Devices* 63 (5) (2016) 2029–2035. doi:10.1109/TED.2016.2537792. [Cited on page 84.]
- [253] H. Jiang, D. Belkin, S. E. Savel'ev, S. Lin, Z. Wang, Y. Li, S. Joshi, R. Midya, C. Li, M. Rao, M. Barnell, Q. Wu, J. J. Yang, Q. Xia, A novel true random number generator based on a stochastic diffusive memristor, *Nature Communications* 8 (1) (2017) 882. doi:10.1038/s41467-017-00869-x. [Cited on page 84.]
- [254] S. Gaba, P. Knag, Z. Zhang, W. Lu, Memristive devices for stochastic computing, 2014 IEEE International Symposium on Circuits and Systems (ISCAS) 9 (2) (2014) 2592–2595. doi:10.1109/ISCAS.2014.6865703. [Cited on page 84.]
- [255] W. Qian, X. Li, M. D. Riedel, K. Bazargan, D. J. Lilja, An architecture for fault-tolerant computation with stochastic logic, *IEEE Transactions on Computers* 60 (1) (2011) 93–105. doi:10.1109/TC.2010.202. [Cited on page 84.]
- [256] A. Chen, Utilizing the Variability of Resistive Random Access Memory to Implement Reconfigurable Physical Unclonable Functions, *IEEE Electron Device Letters* 36 (2) (2015) 138–140. doi:10.1109/LED.2014.2385870. [Cited on page 84.]

- [257] H. Jiang, C. Li, R. Zhang, P. Yan, P. Lin, Y. Li, J. J. Yang, D. Holcomb, Q. Xia, A provable key destruction scheme based on memristive crossbar arrays, *Nature Electronics* 1 (10) (2018) 548–554. doi:10.1038/s41928-018-0146-5. [Cited on page 84.]
- [258] S. Balatti, S. Ambrogio, Z. Wang, D. Ielmini, True Random Number Generation by Variability of Resistive Switching in Oxide-Based Devices, *IEEE Journal on Emerging and Selected Topics in Circuits and Systems* 5 (2) (2015) 214–221. doi:10.1109/JETCAS.2015.2426492. [Cited on page 84.]
- [259] M. Hu, Y. Wang, W. Wen, Y. Wang, H. Li, Leveraging Stochastic Memristor Devices in Neuromorphic Hardware Systems, *IEEE Journal on Emerging and Selected Topics in Circuits and Systems* 6 (2) (2016) 235–246. doi:10.1109/JETCAS.2016.2547780. [Cited on page 84.]
- [260] R. Naous, M. AlShedivat, E. Neftci, G. Cauwenberghs, K. N. Salama, Memristor-based neural networks: Synaptic versus neuronal stochasticity, *AIP Advances* 6 (11) (2016) 111304. doi:10.1063/1.4967352. [Cited on page 84.]
- [261] J. Bill, R. Legenstein, A compound memristive synapse model for statistical learning through STDP in spiking neural networks, *Frontiers in Neuroscience* 8 (2014) 412. doi:10.3389/fnins.2014.00412. [Cited on page 84.]
- [262] S. Yu, B. Gao, Z. Fang, H. Yu, J. Kang, H.-S. P. Wong, Stochastic learning in oxide binary synaptic device for neuromorphic computing, *Frontiers in Neuroscience* 7 (2013) 186. doi:10.3389/fnins.2013.00186. [Cited on page 84.]
- [263] M. Al-Shedivat, R. Naous, E. Neftci, G. Cauwenberghs, K. N. Salama, Inherently stochastic spiking neurons for probabilistic neural computation, in: 2015 7th International IEEE/EMBS Conference on Neural Engineering (NER), IEEE, 2015, pp. 356–359. doi:10.1109/NER.2015.7146633. [Cited on page 84.]
- [264] M. Al-Shedivat, R. Naous, G. Cauwenberghs, K. N. Salama, Memristors empower spiking neurons with stochasticity, *IEEE Journal on Emerging and Selected Topics in Circuits and Systems* 5 (2) (2015) 242–253. doi:10.1109/JETCAS.2015.2435512. [Cited on page 84.]
- [265] M. S. Feali, A. Ahmadi, Realistic Hodgkin–Huxley Axons Using Stochastic Behavior of Memristors, *Neural Processing Letters* 45 (1) (2017) 1–14. doi:10.1007/s11063-016-9502-5. [Cited on page 84.]
- [266] R. Naous, M. Al-Shedivat, E. Neftci, G. Cauwenberghs, K. N. Salama, Stochastic synaptic plasticity with memristor crossbar arrays, in: 2016 IEEE International Symposium on Circuits and Systems (ISCAS), IEEE, 2016, pp. 2078–2081. doi:10.1109/ISCAS.2016.7538988. [Cited on page 84.]
- [267] L. Zhou, J. Mao, Y. Ren, S.-T. Han, V. A. L. Roy, Y. Zhou, Recent Advances of Flexible Data Storage Devices Based on Organic Nanoscaled Materials, *Small* 14 (10) (2018) 1703126. doi:10.1002/smll.201703126. [Cited on page 86.]
- [268] U. Celano, K. Nagashima, H. Koga, M. Nogi, F. Zhuge, G. Meng, Y. He, J. De Boeck, M. Jurczak, W. Vandervorst, T. Yanagida, All-nanocellulose nonvolatile resistive memory, *NPG Asia Materials* 8 (2016) e310. doi:10.1038/am.2016.144. [Cited on pages 86 and 87.]

- [269] K. Nagashima, H. Koga, U. Celano, F. Zhuge, M. Kanai, S. Rahong, G. Meng, Y. He, J. De Boeck, M. Jurczak, W. Vandervorst, T. Kitaoka, M. Nogi, T. Yanagida, Cellulose Nanofiber Paper as an Ultra Flexible Nonvolatile Memory, *Scientific Reports* 4 (1) (2015) 5532. doi:10.1038/srep05532. [Cited on pages 86 and 87.]
- [270] F. B. Fauzi, M. H. Ani, R. Othman, A. Z. A. Azhar, M. A. Mohamed, S. H. Herman, Fabrication of Flexible Au/ZnO/ITO/PET Memristor Using Dilute Electrodeposition Method, *IOP Conference Series: Materials Science and Engineering* 99 (2015) 012002. doi:10.1088/1757-899X/99/1/012002. [Cited on page 86.]
- [271] C. Zhang, Y.-T. Tai, J. Shang, G. Liu, K.-L. Wang, C. Hsu, X. Yi, X. Yang, W. Xue, H. Tan, S. Guo, L. Pan, R.-W. Li, Synaptic plasticity and learning behaviours in flexible artificial synapse based on polymer/viologen system, *Journal of Materials Chemistry C* 4 (15) (2016) 3217–3223. doi:10.1039/C6TC00496B. [Cited on page 86.]
- [272] K. N. Pham, V. D. Hoang, C. V. Tran, B. T. Phan, TiO₂ thin film based transparent flexible resistive switching random access memory, *Advances in Natural Sciences: Nanoscience and Nanotechnology* 7 (1) (2016) 015017. doi:10.1088/2043-6262/7/1/015017. [Cited on page 86.]
- [273] G. U. Siddiqui, M. M. Rehman, K. H. Choi, Enhanced resistive switching in all-printed, hybrid and flexible memory device based on perovskite ZnSnO₃ via PVOH polymer, *Polymer* 100 (2016) 102–110. doi:10.1016/j.polymer.2016.07.081. [Cited on page 86.]
- [274] J. Shang, W. Xue, Z. Ji, G. Liu, X. Niu, X. Yi, L. Pan, Q. Zhan, X.-H. Xu, R.-W. Li, Highly flexible resistive switching memory based on amorphous-nanocrystalline hafnium oxide films, *Nanoscale* 9 (21) (2017) 7037–7046. doi:10.1039/C6NR08687J. [Cited on pages 86 and 91.]
- [275] S. Kim, H. Y. Jeong, S. K. Kim, S. Y. Choi, K. J. Lee, Flexible memristive memory array on plastic substrates, *Nano Letters* 11 (12) (2011) 5438–5442. doi:10.1021/nl203206h. [Cited on page 86.]
- [276] D.-H. Lien, Z.-K. Kao, T.-H. Huang, Y.-C. Liao, S.-C. Lee, J.-H. He, All-Printed Paper Memory, *ACS Nano* 8 (8) (2014) 7613–7619. doi:10.1021/nn501231z. [Cited on pages 86 and 87.]
- [277] B.-H. Lee, D.-I. Lee, H. Bae, H. Seong, S.-B. Jeon, M.-L. Seol, J.-W. Han, M. Meyyappan, S.-G. Im, Y.-K. Choi, Foldable and Disposable Memory on Paper, *Scientific Reports* 6 (1) (2016) 38389. doi:10.1038/srep38389. [Cited on pages 86 and 87.]
- [278] C. H. Cheng, F. S. Yeh, A. Chin, Low-power high-performance non-volatile memory on a flexible substrate with excellent endurance, *Advanced Materials* 23 (7) (2011) 902–905. doi:10.1002/adma.201002946. [Cited on page 86.]
- [279] J. Zhao, M. Zhang, S. Wan, Z. Yang, C. S. Hwang, Highly Flexible Resistive Switching Memory Based on the Electronic Switching Mechanism in the Al/TiO₂/Al/Polyimide Structure, *ACS Applied Materials & Interfaces* 10 (2) (2018) 1828–1835. doi:10.1021/acsami.7b16214. [Cited on page 86.]
- [280] H. Wang, C. Zou, L. Zhou, C. Tian, D. Fu, Resistive switching characteristics of thin NiO film based flexible nonvolatile memory devices, *Microelectronic Engineering* 91 (2012) 144–146. doi:10.1016/j.mee.2011.05.037. [Cited on page 86.]
- [281] S. Kim, O. Yarimaga, S. J. Choi, Y. K. Choi, Highly durable and flexible memory based on resistance switching, *Solid-State Electronics* 54 (4) (2010) 392–396. doi:10.1016/j.sse.2009.10.021. [Cited on page 86.]

- [282] C. C. Lin, C. T. Su, C. L. Chang, H. Y. Wu, Resistive Switching Behavior of Al/Al₂O₃/ZrO₂/Al Structural Device for Flexible Nonvolatile Memory Application, *IEEE Transactions on Magnetics* 50 (7) (2014) 3–6. doi:10.1109/TMAG.2013.2296039. [Cited on page 86.]
- [283] A. Khiat, S. Cortese, A. Serb, T. Prodromakis, Resistive switching of Pt/TiO_x/Pt devices fabricated on flexible Parylene-C substrates, *Nanotechnology* 28 (2) (2017) 025303. doi:10.1088/1361-6528/28/2/025303. [Cited on page 86.]
- [284] V.-Q. Le, T.-H. Do, J. R. D. Retamal, P.-W. Shao, Y.-H. Lai, W.-W. Wu, J.-H. He, Y.-L. Chueh, Y.-H. Chu, Van der Waals Heteroepitaxial AZO/NiO/AZO/Muscovite (ANA/muscovite) Transparent Flexible Memristor, *Nano Energy* 56 (October 2018) (2018) 322–329. doi:10.1016/j.nanoen.2018.10.042. [Cited on page 86.]
- [285] J. Min Son, W. Seung Song, C. Ho Yoo, D. Yeol Yun, T. Whan Kim, Electrical stabilities and memory mechanisms of organic bistable devices fabricated utilizing a poly(3,4-ethylene-dioxythiophene): Poly(styrenesulfonate) layer with a poly(methyl methacrylate) buffer layer, *Applied Physics Letters* 100 (18) (2012) 183303. doi:10.1063/1.4709399. [Cited on page 86.]
- [286] U. S. Bhansali, M. A. Khan, D. Cha, M. N. AlMadhoun, R. Li, L. Chen, A. Amassian, I. N. Odeh, H. N. Alshareef, Metal-Free, Single-Polymer Device Exhibits Resistive Memory Effect, *ACS Nano* 7 (12) (2013) 10518–10524. doi:10.1021/nn403873c. [Cited on page 86.]
- [287] B. Huber, P. B. Popp, M. Kaiser, A. Ruediger, C. Schindler, Fully inkjet printed flexible resistive memory, *Applied Physics Letters* 110 (14) (2017) 143503. doi:10.1063/1.4978664. [Cited on page 86.]
- [288] S. M. Islam, P. Banerji, S. Banerjee, Electrical bistability, negative differential resistance and carrier transport in flexible organic memory device based on polymer bilayer structure, *Organic Electronics* 15 (1) (2014) 144–149. doi:10.1016/j.orgel.2013.10.029. [Cited on page 86.]
- [289] B.-H. Lee, H. Bae, H. Seong, D.-I. Lee, H. Park, Y. J. Choi, S.-G. Im, S. O. Kim, Y.-K. Choi, Direct Observation of a Carbon Filament in Water-Resistant Organic Memory, *ACS Nano* 9 (7) (2015) 7306–7313. doi:10.1021/acsnano.5b02199. [Cited on page 86.]
- [290] H. Jo, J. Ko, J. A. Lim, H. J. Chang, Y. S. Kim, Organic Nonvolatile Resistive Switching Memory Based on Molecularly Entrapped Fullerene Derivative within a Diblock Copolymer Nanostructure, *Macromolecular Rapid Communications* 34 (4) (2013) 355–361. doi:10.1002/marc.201200614. [Cited on page 86.]
- [291] C. Wu, T. W. Kim, H. Y. Choi, D. B. Strukov, J. J. Yang, Flexible three-dimensional artificial synapse networks with correlated learning and trainable memory capability, *Nature Communications* 8 (1) (2017) 752. doi:10.1038/s41467-017-00803-1. [Cited on page 86.]
- [292] Y. Lin, T. Zeng, H. Xu, Z. Wang, X. Zhao, W. Liu, J. Ma, Y. Liu, Transferable and Flexible Artificial Memristive Synapse Based on WO_x Schottky Junction on Arbitrary Substrates, *Advanced Electronic Materials* 4 (12) (2018) 1800373. doi:10.1002/aelm.201800373. [Cited on page 86.]
- [293] D. H. Lien, Z. K. Kao, T. H. Huang, Y. C. Liao, S. C. Lee, J. H. He, All-printed paper memory, *ACS Nano* 8 (8) (2014) 7613–7619. doi:10.1021/nn501231z. [Cited on page 87.]

- [294] J. M. Choi, M. S. Kim, M. L. Seol, Y. K. Choi, Transfer of functional memory devices to any substrate, *Physica Status Solidi - Rapid Research Letters* 7 (5) (2013) 326–331. doi:10.1002/pssr.201307084. [Cited on page 87.]
- [295] C. Mead, Neuromorphic electronic systems, *Proceedings of the IEEE* 78 (10) (1990) 1629–1636. doi:10.1109/5.58356. [Cited on page 95.]
- [296] S. Yu, Ximeng Guan, H.-S. P. Wong, On the stochastic nature of resistive switching in metal oxide RRAM: Physical modeling, monte carlo simulation, and experimental characterization, in: 2011 International Electron Devices Meeting, IEEE, 2011, pp. 17.3.1–17.3.4. doi:10.1109/IEDM.2011.6131572. [Cited on page 95.]
- [297] M. Laiho, E. Lehtonen, A. Russell, P. Dudek, Memristive synapses are becoming reality, in: *The Neuromorphic Engineer*, Institute of Neuromorphic Engineers, 2010, pp. 1–3. doi:10.2417/1201011.003396. [Cited on page 95.]
- [298] S. G. Hu, H. T. Wu, Y. Liu, T. P. Chen, Z. Liu, Q. Yu, Y. Yin, S. Hosaka, Design of an electronic synapse with spike time dependent plasticity based on resistive memory device, *Journal of Applied Physics* 113 (11) (2013) 114502. doi:10.1063/1.4795280. [Cited on page 95.]
- [299] T. Ohno, T. Hasegawa, A. Nayak, T. Tsuruoka, J. K. Gimzewski, M. Aono, Sensory and short-term memory formations observed in a Ag₂S gap-type atomic switch, *Applied Physics Letters* 99 (20) (2011) 203108. doi:10.1063/1.3662390. [Cited on page 95.]
- [300] J. R. Heath, A Defect-Tolerant Computer Architecture: Opportunities for Nanotechnology, *Science* 280 (5370) (1998) 1716–1721. doi:10.1126/science.280.5370.1716. [Cited on page 95.]
- [301] G. S. Snider, Self-organized computation with unreliable, memristive nanodevices, *Nanotechnology* 18 (36) (2007) 365202. doi:10.1088/0957-4484/18/36/365202. [Cited on pages 95, 96, and 98.]
- [302] R. E. Pino, H. H. Li, Y. Chen, M. Hu, B. Liu, Statistical memristor modeling and case study in neuromorphic computing, in: *Proceedings of the 49th Annual Design Automation Conference on - DAC '12*, ACM Press, New York, New York, USA, 2012, pp. 585–590. doi:10.1145/2228360.2228466. [Cited on pages 95 and 109.]
- [303] G. Snider, Computing with hysteretic resistor crossbars, *Applied Physics A* 80 (6) (2005) 1165–1172. doi:10.1007/s00339-004-3149-1. [Cited on page 95.]
- [304] D. Chabi, W. Zhao, D. Querlioz, J.-O. Klein, Robust neural logic block (NLB) based on memristor crossbar array, in: 2011 IEEE/ACM International Symposium on Nanoscale Architectures, IEEE, 2011, pp. 137–143. doi:10.1109/NANOARCH.2011.5941495. [Cited on pages 95 and 96.]
- [305] D. Querlioz, O. Bichler, C. Gamrat, Simulation of a memristor-based spiking neural network immune to device variations, in: *The 2011 International Joint Conference on Neural Networks*, IEEE, 2011, pp. 1775–1781. doi:10.1109/IJCNN.2011.6033439. [Cited on page 95.]
- [306] D. Querlioz, O. Bichler, P. Dollfus, C. Gamrat, Immunity to device variations in a spiking neural network with memristive nanodevices, *IEEE Transactions on Nanotechnology* 12 (3) (2013) 288–295. doi:10.1109/TNANO.2013.2250995. [Cited on page 95.]

- [307] P. Protzel, D. Palumbo, M. Arras, Performance and fault-tolerance of neural networks for optimization, *IEEE Transactions on Neural Networks* 4 (4) (1993) 600–614. doi:10.1109/72.238315. [Cited on page 96.]
- [308] R. A. Nawrocki, S. E. Shaheen, R. M. Voyles, A neuromorphic architecture from single transistor neurons with organic bistable devices for weights, in: *The 2011 International Joint Conference on Neural Networks, IEEE*, 2011, pp. 450–456. doi:10.1109/IJCNN.2011.6033256. [Cited on page 96.]
- [309] H.-S. Oh, S.-J. Lee, Y.-W. Kim, D.-W. Lee, Behavior Characteristics of Nano-Stage According to Hinge Structure, *Journal of Nanoscience and Nanotechnology* 7 (11) (2007) 4146–4149. doi:10.1166/jnn.2007.013. [Cited on pages 96 and 101.]
- [310] S. Hamdioui, M. Taouil, N. Z. Haron, Testing Open Defects in Memristor-Based Memories, *IEEE Transactions on Computers* 64 (1) (2015) 247–259. doi:10.1109/TC.2013.206. [Cited on page 96.]
- [311] Xiangyu Dong, Cong Xu, Yuan Xie, N. P. Jouppi, NVSim: A Circuit-Level Performance, Energy, and Area Model for Emerging Nonvolatile Memory, *IEEE Transactions on Computer-Aided Design of Integrated Circuits and Systems* 31 (7) (2012) 994–1007. doi:10.1109/TCAD.2012.2185930. [Cited on page 96.]
- [312] J. Liang, H.-S. P. Wong, Cross-Point Memory Array Without Cell Selectors—Device Characteristics and Data Storage Pattern Dependencies, *IEEE Transactions on Electron Devices* 57 (10) (2010) 2531–2538. doi:10.1109/TED.2010.2062187. [Cited on page 96.]
- [313] N. J. Lee, B. H. An, a. Y. Koo, H. M. Ji, J. W. Cho, Y. J. Choi, Y. K. Kim, C. J. Kang, Resistive switching behavior in a Ni-Ag₂Se-Ni nanowire, *Applied Physics A: Materials Science and Processing* 102 (4) (2011) 897–900. doi:10.1007/s00339-011-6319-y. [Cited on page 96.]
- [314] I. Vourkas, G. C. Sirakoulis, Memristor-based combinational circuits: A design methodology for encoders/decoders, *Microelectronics Journal* 45 (1) (2014) 59–70. doi:10.1016/j.mejo.2013.10.001. [Cited on page 96.]
- [315] LTspice IV Software, Version 4.20p, <https://www.analog.com/en/design-center/design-tools-and-calculators/ltspice-simulator.html> (2014). [Cited on page 96.]
- [316] See supplementary material at <http://dx.doi.org/10.1063/1.4922148> for depiction of the memristor-based Willshaw network dynamics under defect-free, stuck-at-0 and stuck-at-1 conditions. [Cited on page 98.]
- [317] J. Buckingham, D. Willshaw, On setting unit thresholds in an incompletely connected associative net, *Network: Computation in Neural Systems* 4 (4) (1993) 441–459. doi:10.1088/0954-898X_4_4_003. [Cited on page 102.]
- [318] B. Graham, D. Willshaw, Information efficiency of the associative net at arbitrary coding rates, in: *Artificial Neural Networks—ICANN 96*, Vol. 2, Springer, Berlin, Heidelberg, 1996, pp. 35–40. doi:10.1007/3-540-61510-5_10. [Cited on page 102.]
- [319] F. Rosenblatt, *The Perceptron - A Perceiving and Recognizing Automaton*, Tech. rep., Cornell Aeronautical Laboratory, Inc (1957). [Cited on page 102.]

- [320] T. Hogg, G. Snider, Defect-tolerant Logic with Nanoscale Crossbar Circuits, *Journal of Electronic Testing* 23 (2007) 117–129. doi:10.1007/s10836-006-0547-7. [Cited on page 103.]
- [321] D. Strukov, H. Kohlstedt, Resistive switching phenomena in thin films: Materials, devices, and applications, *MRS Bulletin* 37 (2) (2012) 108–114. doi:10.1557/mrs.2012.2. [Cited on page 103.]
- [322] G. S. Rose, R. Pino, Q. Wu, A low-power memristive neuromorphic circuit utilizing a global/local training mechanism, in: *The 2011 International Joint Conference on Neural Networks, IEEE, 2011*, pp. 2080–2086. doi:10.1109/IJCNN.2011.6033483. [Cited on page 103.]
- [323] A. Thomas, Memristor-based neural networks, *Journal of Physics D: Applied Physics* 46 (9) (2013) 093001. doi:10.1088/0022-3727/46/9/093001. [Cited on page 103.]
- [324] F. Alibart, E. Zamanidoost, D. B. Strukov, Pattern classification by memristive crossbar circuits using ex situ and in situ training, *Nature Communications* 4 (1) (2013) 2072. doi:10.1038/ncomms3072. [Cited on page 103.]
- [325] C. Li, D. Belkin, Y. Li, P. Yan, M. Hu, N. Ge, H. Jiang, E. Montgomery, P. Lin, Z. Wang, W. Song, J. P. Strachan, M. Barnell, Q. Wu, R. S. Williams, J. J. Yang, Q. Xia, Efficient and self-adaptive in-situ learning in multilayer memristor neural networks, *Nature Communications* 9 (1) (2018) 2385. doi:10.1038/s41467-018-04484-2. [Cited on page 103.]
- [326] E. Zamanidoost, F. M. Bayat, D. Strukov, I. Kataeva, Manhattan rule training for memristive crossbar circuit pattern classifiers, in: *2015 IEEE 9th International Symposium on Intelligent Signal Processing (WISP) Proceedings, IEEE, 2015*, pp. 1–6. doi:10.1109/WISP.2015.7139171. [Cited on pages 104 and 105.]
- [327] M. Lichman, {UCI} Machine Learning Repository, <http://archive.ics.uci.edu/ml> (2013). [Cited on page 106.]
- [328] M. Hasenjäger, H. Ritter, Perceptron Learning Revisited: The Sonar Targets Problem, *Neural Processing Letters* 10 (1) (1999) 17–24. doi:10.1023/A:1018654611986. [Cited on page 106.]
- [329] M. Z. G. Salama, M. B. Abdelhalim, Breast Cancer Diagnosis on Three Different Datasets Using Multi-Classifiers, in: *International Journal of Computer Applications & Information Technology, IEEE, 2012*, pp. 36–43. [Cited on page 107.]
- [330] A. F. M. Agarap, On breast cancer detection, in: *Proceedings of the 2nd International Conference on Machine Learning and Soft Computing - ICMLSC '18, ACM Press, New York, New York, USA, 2018*, pp. 5–9. doi:10.1145/3184066.3184080. [Cited on page 107.]
- [331] A. L. Hodgkin, A. F. Huxley, A quantitative description of membrane current and its application to conduction and excitation in nerve, *The Journal of Physiology* 117 (4) (1952) 500–544. doi:10.1113/jphysiol.1952.sp004764. [Cited on page 108.]
- [332] A. L. Hodgkin, A. F. Huxley, A quantitative description of membrane current and its application to conduction and excitation in nerve, *Bulletin of Mathematical Biology* 52 (1-2) (1990) 25–71. doi:10.1007/BF02459568. [Cited on page 108.]
- [333] L. Chua, V. Sbitned, H. Kim, Hodgkin–Huxley axon is made of memristors, *International Journal of Bifurcation and Chaos* 22 (3) (2012) 1230011. doi:10.1142/S021812741230011X. [Cited on page 108.]

- [334] S. Gurban, G. Gergely, J. Toth, D. Varga, A. Jablonski, M. Menyhard, Experimental determination of the inelastic mean free path (IMFP) of electrons in selected oxide films applying surface excitation correction, *Surface and Interface Analysis* 38 (4) (2006) 624–627. doi:10.1002/sia.2302. [Cited on page 154.]
- [335] S. Tanuma, C. J. Powell, D. R. Penn, Calculations of electron inelastic mean free paths. III. Data for 15 inorganic compounds over the 50-2000 eV range, *Surface and Interface Analysis* 17 (13) (1991) 927–939. doi:10.1002/sia.740171305. [Cited on page 154.]

List of Publications

Several contributions were made to the scientific community, directly related to the work developed in the present thesis, including 17 oral communications, 3 poster presentations and the following publications:

1. C. Dias, L. M. Guerra, J. Ventura, P. Aguiar, Memristor-based Willshaw network: Capacity and robustness to noise in the presence of defects, *Applied Physics Letters* 106 (22) (2015) 223505. doi:10.1063/1.4922148
2. C. Dias, H. Lv, R. Picos, P. Aguiar, S. Cardoso, P. Freitas, J. Ventura, Bipolar resistive switching in Si/Ag nanostructures, *Applied Surface Science* 424 (2017) 122–126. doi:10.1016/j.apsusc.2017.01.140
3. C. Dias, L. M. Guerra, B. D. Bordalo, H. Lv, A. M. Ferraria, A. M. Botelho do Rego, S. Cardoso, P. P. Freitas, J. Ventura, Voltage-polarity dependent multi-mode resistive switching on sputtered MgO nanostructures, *Physical Chemistry Chemical Physics* 19 (17) (2017) 10898–10904. doi:10.1039/C7CP00062F
4. C. Dias, J. Ventura, P. Aguiar, Memristive-Based Neuromorphic Applications and Associative Memories, in: S. Vaidyanathan, C. Volos (Eds.), *Memristors, Memristive Devices and Systems*, Springer-Verlag, 2017, pp. 305–342. doi:10.1007/978-3-319-51724-7_13
5. L. M. Guerra, C. Dias, J. Pereira, H. Lv, S. Cardoso, P. P. Freitas, J. Ventura, Unipolar Nonvolatile Resistive Switching in Pt / MgO / Ta / Ru Structures Deposited by Magnetron Sputtering, *Journal of Nanoscience and Nanotechnology* 17 (1) (2017) 564–567. doi:10.1166/jnn.2017.12333
6. C. Dias, L. M. Guerra, P. Aguiar, J. Ventura, The concept of Metal-Insulator-Metal nanostructures as Adaptive Neural Networks, *U.Porto Journal of Engineering* 3 (1) (2017) 1–10. doi:10.24840/2183-6493.003.001.0001
7. C. Dias, D. J. Silva, P. Aguiar and J. Ventura, "Associative networks and perceptron based on memristors: fundamentals and algorithmic implementation" in *Handbook of Memristor Networks*, Springer, (2019), *in Press*.

Nevertheless, several collaborations also took place, resulting in 13 poster presentations and the following publications:

8. R. Krishna, D. M. Fernandes, V. F. Domingos, E. S. Ribeiro, J. C. Gil, C. Dias, J. Ventura, C. Freire, E. Titus, Reduction of 4-nitrophenol to 4-aminophenol using a novel Pd@Ni₃BSiO₂/RGO nanocomposite: enhanced hydrogen spillover and high catalytic performance, *RSC Advances* 5 (74) (2015) 60658–60666. doi:10.1039/C5RA05523G

9. R. Krishna, D. M. Fernandes, E. Venkataramana, C. Dias, J. Ventura, C. Freire, E. Titus, Improved Reduction of Graphene Oxide, *Materials Today: Proceedings* 2 (1) (2015) 423–430. doi:10.1016/j.matpr.2015.04.049
10. R. Krishna, C. Dias, J. Ventura, E. Titus, Synthesis of Ni(OH)₂@Ni/RGO Nanocomposite: Formulation of One Dimensional Array, *Materials Today: Proceedings* 2 (1) (2015) 407–413. doi:10.1016/j.matpr.2015.04.046
11. R. Krishna, D. M. Fernandes, C. Dias, J. Ventura, E. Venkata Ramana, C. Freire, E. Titus, Novel synthesis of Ag@Co/RGO nanocomposite and its high catalytic activity towards hydrogenation of 4-nitrophenol to 4-aminophenol, *International Journal of Hydrogen Energy* 40 (14) (2015) 4996–5005. doi:10.1016/j.ijhydene.2014.12.045
12. N. I. Polushkin, A. C. Duarte, O. Conde, N. Bundaleski, C. Dias, J. O. Ventura, J. P. Araujo, G. N. Kakazei, P. Lupo, A. O. Adeyeye, S. Cardoso, Electrical switching of magnetization in a layer of α -Fe with a naturally hydroxidized surface, *Journal of Materials Chemistry C* 4 (33) (2016) 7751–7755. doi:10.1039/C6TC00700G
13. O. Okhay, G. Gonçalves, A. Tkach, C. Dias, J. Ventura, M. F. Ribeiro da Silva, L. M. Valente Gonçalves, E. Titus, Thin film versus paper-like reduced graphene oxide: Comparative study of structural, electrical, and thermoelectrical properties, *Journal of Applied Physics* 120 (5) (2016) 051706. doi:10.1063/1.4958956
14. M. Cerquido, M. P. Proença, C. Dias, D. C. Leitão, S. Cardoso, P. P. Freitas, P. Aguiar, J. Ventura, Tailoring the cap's morphology of electrodeposited gold micro-mushrooms, *Applied Surface Science* 445 (2018) 512–518. doi:10.1016/j.apsusc.2018.03.158
15. O. Okhay, G. G. Gonçalves, C. Dias, J. Ventura, E. Vieira, L. M. Gonçalves, A. Tkach, Tuning electrical and thermoelectric properties of freestanding graphene oxide papers by carbon nanotubes and heat treatment, *Journal of Alloys and Compounds* 781 (2019) 196–200.

APPENDIX A

Runsheets

A.1 Shadow Mask

Run Sheet

Shadow Mask Single junction definition

Process Start _____

Process Finish _____

Flexible substrate/Ti(25)/Pt(1000)/Si(200)/Ag(100)/TiW(1000) (Å)

STEP 1 **Bottom deposition**

Date: __/__/__

Machine: N3000

Deposit Ti(25 Å)/Pt (1000 Å) on the substrate and check if the conductivity is good.

Assist Neut: 50% subst.rot 80° subst.pan

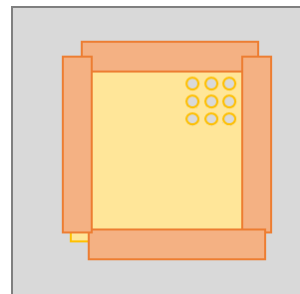
Assist Gun	Power (W)	V+ (V)	I+ (mA)	V- (V)	I- (mA)	Xe Flux (sccm)
Set Values	100	1022	24	300	-	1.8

STEP 2 Sample preparation

Date: __/__/__

Use physical shadow masks on top of Pt before depositing Si/Ag and TiW, in order to avoid chemical solutions in the process.

Put kapton tape near the holes and everywhere needed to avoid space left between the substrate and the mask.

**STEP 3 Stack Deposition**

Date: __/__/__

Machine: Alcatel

Si(200 Å)/Ag(100 Å)

Power: 20 W; Ar Flux: 20 sccm; Pressure: 1.83×10^{-3} Torr**STEP 4 Top deposition**

Date: __/__/__

Machine: N7000

1000 Å – No N₂ with 10s etching – corner covered with tape to give access to the bottomMod 3-f.19: (TiWN₂ deposition) - Power: 0.5 kW; Pressure: 3 mTorr; Flux: 50 sccm Ar + 10 sccm N₂

Read Values	0.5 kW	428 V	1.18 A	49.8 sccm	3.3 mTorr
-------------	--------	-------	--------	-----------	-----------

A.2 Single Junction

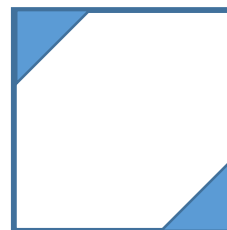
Run Sheet Single junction definition

Process Start _____

Process Finish _____

Si/SiO/Ti (250)/Pt (1500) (Å) substrates

->Substrate corners covered with tape to give access to the bottom



STEP 1 Stack Deposition

Date: __/__/__

- Si, Ag: Alcatel
- TiW: N7000
- MgO, Ta, Ru: N2000
- Al2O3, Al, Cu: N3000

STEP 2 Lithography – Top contact definition

Date: __/__/__

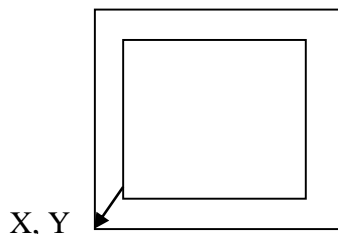
Machine: Vacuum bake/vapour prime; photoresist tracks; DWL

1) Lithography

Mask: IFIMUP_Shadow.dxf - (INVERTED)

Map: 2x2

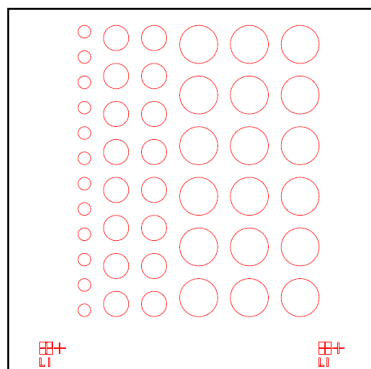
Origin of the die:
X, Y = 3000, 3000
um



Energy : _____%
Power : _____mW Focus : _____

Alignment marks: not used

Inset here the corresponding Autocad layer for this lithography step:



2) Develop : Recipe 6/2

Developer: TMA238WA

Development parameters:
Bake at 110°C for 60s
Cool for 30s
Developer for 60s

Note: Check the feature size and shape under the optical microscope; check if resist is in expected areas. Check the resist thickness using profilometer.

STEP 3 Etching – Top contact definition

Date: __/__/__

Machine: **N3600**

Total thickness to etch: __250+50__ Å (etch rate: ~1 Å/s -> time: __300 s__)

Base Pressure (Torr): 2.04×10^{-7} Torr

Batch: etch junction

Recipe etch junction stack all : etch pan 60 deg

cool_down_200s

Assist Gun: 160W 105mA +750V/-350V 12sccm Ar; Assist Neut: 30% subst.rot 60° subst.pan

Assist Gun	Power (W)	V+ (V)	I+ (mA)	V- (V)	I- (mA)	Ar Flux (sccm)
Set Values	190	735	105	350	-	11
Read Values	201	724.3	104.2	344.8	2.3	10.2

STEP 5 Resist Strip

Date: __/__/__

Machine: Chemical Workbench:

Started:_____ Stopped:_____

Total Time in Hot Micro-Strip : _____ Ultrasonic Time : _____

Optical Inspection:

Sample	Comments

A.3 Crossbar Network

Run Sheet

Memristor crossbar network

Process Start _____

Process Finish _____

Si/SiO/Ti(250)/Pt(1500)/MgO(300)/Ta(200)/Ru(50) (Å)

STEP 1 1st Lithography – Bottom contact definition

Date: __/__/__

Machine: Photoresist tracks; DWL

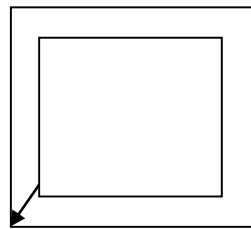
1) LithographyMask: Network_BOTTOM.dxf – **BOTTOM (INVERTED)**

Map: AMSION

Easy Axis



X, Y



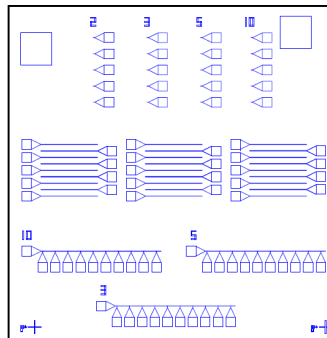
Energy : _____%

Power : _____mW

Focus : _____

Origin of the die:
 X, Y = 3000, 3000
 um

Alignment marks: not used

Inset here the corresponding Autocad layer for this lithography step:**2) Develop:** Recipe 6/2

Developer: TMA238WA

Development parameters:
Bake at 110°C for 60s
Cool for 30s
Developer for 60s

Note:

Check the feature size and shape under the optical microscope; check if resist is in expected areas.

Check the resist thickness using profilometer.

STEP 2 1st Ion Milling – Bottom contact definition

Date: __/__/__

Machine: **N3600**

Total thickness to etch: 1750+50 Å (etch rate: ~1 Å/s -> time: 1800 s)

Base Pressure (Torr): 2.04×10^{-7} Torr

Standard Etching Recipe (Junction Etch):

Recipe etch junction stack all : etch pan 45 deg (9x 200 s)
cool_down_200s

Assist Gun: 150W/ 735V/-350V, 105mA, 10sccm Ar; 30rpm 45° subst.pan

Assist Gun	Power (W)	V+ (V)	I+ (mA)	V- (V)	I- (mA)	Ar Flux (sccm)
Set Values	190	735	105	350	-	11
Read Values	202.0	724.3	104.5	344.8	2.3	10.2

STEP 3 Resist Strip

Date: __/__/__

Machine: Chemical Workbench:

Started: _____ Stopped: _____

Total Time in Hot Micro-Strip : _____ Ultrasonic Time : _____

Optical Inspection:

Sample	Comments

STEP 4 2nd Lithography – Junction/Top Definition

Date: ____/____/____

Machine: Photoresist tracks; DWL

1) LithographyMask: Network_TOP.dxf – **JUNCTION (NON-INVERTED)**

Map: AMSION

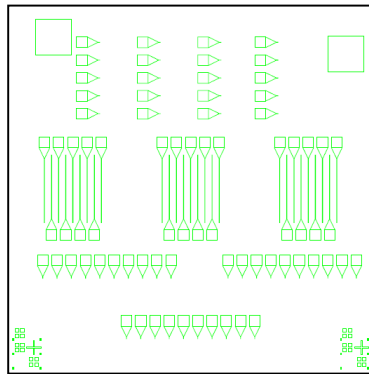
Energy : ____%

Power : ____mW

Focus : ____

Alignment marks: _____

Inset here the corresponding Autocad layer for this lithography step:

**2) Develop:** Recipe 6/2

Developer: TMA238WA

Development parameters:
Bake at 110°C for 60s
Cool for 30s
Developer for 60s

Note:

Check the feature size and shape under the optical microscope; check if resist is in expected areas.

STEP 5 Stack Deposition

Date: __/ __/ __

Machine: N2000

Target	Power (W)	I (mA)	Ar Flux (sccm)	Pressure (mTorr)	Rotation (rpm)	Sep (%)
MgO	130 (RF)	-	9	13	5	50
Ta	-	40	10	4.5	5	100
Ru	-	40	8	5	5	100

STEP 6 Resist Strip

Date: __/ __/ __

Machine: Chemical Workbench

Started: _____ Stopped: _____

Total Time in Hot Micro-Strip : _____ Ultrasonic Time : _____

Optical Inspection:

Sample	Comments

APPENDIX B

Quantitative analysis of XPS data

A useful XPS analysis is the quantification of a single element through different peaks. Since the respective photoelectrons have different kinetic energies, they are differently attenuated when crossing the solid and therefore the ratio of the integrated intensities between different peaks is related to the stratification of the sample especially if their kinetic energies are quite different. Table B.1 presents the atomic ratios that one would expect assuming the model and respective nominal thicknesses [(MgO (30) / Ta (2) / Ru (1) (nm)], compared with the experimental atomic ratios computed from the areas of the different XPS peaks and considering the sensitivity factors mentioned in the experimental section.

For magnesium photoelectrons coming from the MgO layer, the expected intensities of Mg X photoelectrons, that is Mg 2s or Mg 1s, considering atomically flat layers and neglecting any shadow effects, should be given by Eq. B.1 that accounts for the attenuation of the photoelectrons when crossing the different layers. Tantalum and ruthenium X photoelectrons (*i.e.* Ta 4d, Ta 4p_{3/2}, Ru 3d and Ru 3p) intensities are described by Eqs. B.2 and B.3.

$$I_{MgX} \propto [1 - \exp(-\frac{\ell_{MgO}}{\lambda_{Mg}X_{(MgO)}})] \times \exp(-\frac{\ell_{Ta}}{\lambda_{Mg}X_{(Ta)}}) \times (-\frac{\ell_{Ru}}{\lambda_{Mg}X_{(Ru)}}) \quad (B.1)$$

$$I_{TaX} \propto [1 - \exp(-\frac{\ell_{Ta}}{\lambda_{Ta}X_{(Ta)}})] \times \exp(-\frac{\ell_{Ru}}{\lambda_{Ta}X_{(Ru)}}) \quad (B.2)$$

$$I_{RuX} \propto [1 - \exp(-\frac{\ell_{Ru}}{\lambda_{Ru}X_{(Ru)}})] \quad (B.3)$$

Table B.1 – XPS ratios expected vs. experimental.

	Expected	Experimental
Mg 2s/Mg 1s	72.0	1.2
Ta 4d/Ta 4p _{3/2}	1.0	0.9
Ru 3d/Ru 3p	0.9	0.9

where ℓ_{MgO} , ℓ_{Ta} and ℓ_{Ru} are the nominal thicknesses of the MgO, Ta and Ru layers, respectively, and $\lambda_{Mg}X_{(MgO)}$, $\lambda_{Mg}X_{(Ta)}$, $\lambda_{Mg}X_{(Ru)}$, $\lambda_{Ta}X_{(Ta)}$, $\lambda_{Ta}X_{(Ru)}$ and $\lambda_{Ru}X_{(Ru)}$ are the Inelastic Mean Free Paths (IMFP) of Mg 2s or Mg 1s, Ta 4d or Ta 4p_{3/2}, Ru 3d or Ru 3p photoelectrons in the different materials. IMFP of photoelectrons crossing MgO, Ta and Ru were interpolated from the IMFP (calculated from TPP-2M equation or from optical data) reported in [334, 335].

Considering the nominal thicknesses ℓ_{Ta} and ℓ_{Ru} equal to 2 and 1 nm, respectively, the calculated expected ratios Ta 4d/Ta 4p_{3/2} and Ru 3d/Ru 3p are quite close to the experimental XPS ratios. However, since the couples of chosen photoelectrons have close kinetic energies (1257 eV and 1082 eV for Ta 4d and Ta 4p and 1207 eV and 1025 eV for Ru 3d and Ru 3p, respectively) they are not very sensitive to the ℓ_Y values, Y being the material of the different layers. For the Mg 2s and Mg 1s regions (kinetic energies are 1397 eV and 184 eV, respectively) a striking difference between the expected and the experimental Mg 2s/Mg 1s ratios exists. The most plausible explanation is the existence of some intermixing between Mg and the “external” layers or, alternatively, the existence of holes in those layers. Taking into consideration that some MgO diffusion through the metallic overlayers may occur, Eq. B.1 should be as follows:

$$I_{MgX} \propto [1 - \exp(-\frac{\ell_{MgO}}{\lambda_{Mg}X_{(MgO)}})] \times \exp(-\frac{\ell_{Ta}}{\lambda_{Mg}X_{(Ta)}}) \times (-\frac{\ell_{Ru}}{\lambda_{Mg}X_{(Ru)}}) + f_i [1 - \exp(-\frac{\ell_{MgO_i}}{\lambda_{Mg}X_{(MgO)}})] \times \exp(-\frac{(\ell_{Ta} + \ell_{Ru}) - \ell_{MgO_i}}{\bar{\lambda}X_{(Ta,Ru)}}) \quad (B.4)$$

Being f_i ratio between the intermixed magnesium and the layered one, ℓ_{MgO_i} the intermixing extent and $\bar{\lambda}X_{(Ta,Ru)}$ a weighted average IMFP value of magnesium X photoelectrons crossing Ta and Ru. The experimental Mg 2s/Mg 1s ratio is found for $f_i = 0.375$ and considering a maximum length of intermixing $\ell_{MgO_i} = 3$ nm.

Since the MgO layer thickness is very high compared to the Mg 1s IMFP, even when compared to the one for Mg 2s, the expected decrease of its value when the intermixing occurs has no impact on the estimated values.

Regarding the fraction of oxidized tantalum, the XPS spectrum shows that most of tantalum is Ta⁵⁺. In fact the experimental atomic ratios Ta/Ru, computed, from different XPS regions (Ta 4d or 4p_{3/2} and Ru 3d or 3p) and considering the atomic densities 0.123, 0.092 and 0.037 mol/cm³ for Ru, Ta and Ta₂O₅, respectively, shows that (72 ± 5)% of tantalum is in the Ta⁵⁺ oxidation state. The value obtained is the average of the 4 fitted values for 4 atomic ratios (Ta 4d/Ru 3d, Ta 4d/Ru 3p, Ta 4p_{3/2}/Ru 3d and Ta 4d/Ru 3p). Equation B.5 was used to estimate the fraction of oxidized tantalum, fox, neglecting the impact that the oxidation has on $\frac{\ell_{Ta}}{\lambda_{Ta}X_{(Ta)}}$. The nominal thicknesses of Ru and Ta (oxidized and not oxidized) layers, described above, were considered.

$$\frac{Ta}{Ru} = \frac{(1 - f_{ox}) \times d_{Ta} + f_{ox} \times d_{Ta_2O_5}}{d_{Ru}} \times \frac{[1 - \exp(-\frac{\ell_{Ta}}{\lambda_{Ta}X_{(Ta)}})] \times \exp(-\frac{\ell_{Ru}}{\lambda_{Ta}X_{(Ru)}})}{[1 - \exp(-\frac{\ell_{Ru}}{\lambda_{Ru}X_{(Ru)}})]} \quad (B.5)$$

APPENDIX C

Random Circuit Breaker

```

1  #RCB.py
2  ---
3
4  from ahkab import new_ac, new_op, run, devices
5  from ahkab.circuit import Circuit
6  from ahkab.plotting import plot_results # calls matplotlib for you
7  import numpy as np
8  from random import*
9
10 from PIL import Image, ImageDraw
11
12 import matplotlib.pyplot as plt
13
14 from collections import Counter
15 from collections import OrderedDict
16
17
18 #V=R*I
19 Roff=1000
20 Ron=1
21 p=0.005 ## (probability of initial defects)
22 Icomp=0.5 #A (fixed in the paper)
23 Icomp2=5. #A (for the RESET and SET process)
24 #von>>voff
25 voff=0.01
26 von=0.2
27 #it was assumed the absolute value of the voltage differential for boundary conditions,
28 #since it can "switch" in either direction
29
30 #Source voltage parameters
31 Vmax=4.
32 Vmin=0.
33 deltaV=0.1
34
35 #switching ratio (for iteration to stop)
36 ratioF=20.
37 ratioR=2.
38 ratioS=2.
39
40 #MxN network
41 M=2 #rows
42 N=3 #columns (it counts less one column by default)
43 #for more than 20x20 to work, the value dense_matrix_limit in file options.py (line 65) was
44 #changed from 400 to 2000 because otherwise there was an error when creating the sparse matrix

```

```

45  #n file dc_analysis.py (line 797)
46
47  #for drawing
48  s=50 #scaled up by 10
49
50  #if M=3 and N=2 and not boundary:
51  # -----
52  # R1          R3
53  #           R2
54  # R4          R6
55  #           R5
56  # R7          R8
57  # -----
58
59  #if M=3 and N=2 and boundary:
60  # -----
61  # R1          R3
62  #           R2          R4
63  # R5          R7
64  #           R6          R8
65  # R9          R10
66  # -----
67
68  #draw the circuit -----
69  def draw_circ(S,Rs,s,step,it,v,boundary):
70      """draws the circuit
71      S: simulation number
72      Rs: resistances matrix
73      s: scale
74      step: 'forming', 'set' or 'reset'
75      it: iteration number
76      v: voltage value
77      boundary: 0 for no boundary conditions and 1 for boundary conditions"""
78      # create a new pixel image surface (default is black bg)
79      if boundary:img = Image.new("RGB", (s*(N-1)+s+1, s*M+1), '#313131')
80      else:img = Image.new("RGB", (s*(N-1)+1, s*M+1), '#313131')
81      # set up the new image surface for drawing
82      draw = ImageDraw.Draw (img)
83
84      R_per_r=2*N-1 # resistors per row - N+(N-1)=2N-1
85      #R_last=R_per_r*M # last row resistor (except for last row)
86      #R_total=M*N+(M-1)*(N-1) +M-1 # total number of resistors in the systems - M*N+(M-1)*(N-1)
87      #N_per_r=N # nodes per row (+1 - name of the node)
88
89      #middle definition
90      #counters for rows and columns
91      Mc=1
92      Nc=1
93      index_counter=0
94      jump=1 #1 for vertical resistors and 0 for horizontal
95      for r in Rs: #define color
96          if r==Roff: col='#AFAFAF' #OFF resistance - black
97          elif r==Ron: col='#35DB24' #ON resistance - green
98

```

```

99     #vertical resistors
100     if jump:
101         if Nc<=N: draw.line(((Nc-1)*s,(Mc-1)*s, (Nc-1)*s, (Mc-1)*s+s-1), fill=col,width=15)
102         if Mc<M: jump=0
103         if Mc==M: Nc+=1 #last row
104         if index_counter+1==R_per_r*Mc: #last column
105             if not boundary: #no boundary
106                 Mc+=1
107                 Nc=1
108                 jump=1
109             else: #boundary
110                 if Mc<M: jump=0
111
112     #horizontal resistors
113     #no boundary
114     elif not boundary and index_counter+1<R_per_r*Mc: #if not the last column
115         if Mc<M: draw.line(((Nc-1)*s,(Mc-1)*s+s, (Nc-1)*s+s, (Mc-1)*s+s), fill=col,width=15)
116         Nc+=1
117         jump=1
118     #boundary
119     else: #if not the last row
120         if boundary:
121             draw.line(((Nc-1)*s,(Mc-1)*s+s, (Nc-1)*s+s, (Mc-1)*s+s), fill=col,width=15)
122             Nc+=1
123             if Nc-1==N:
124                 Nc=1
125                 Mc+=1
126             jump=1
127
128     index_counter+=1
129
130     if boundary:
131         draw.line((0,0, s*(N-1)+s, 0), fill='#0A6AFF',width=20) #top electrode definition
132         draw.line((0, M*s, (N-1)*s+s, M*s), fill='#0A6AFF',width=20) #bottom electrode definition
133     else:
134         draw.line((0,0, s*(N-1), 0), fill='#0A6AFF',width=20) #top electrode definition
135         draw.line((0, M*s, (N-1)*s, M*s), fill='#0A6AFF',width=20) #bottom electrode definition
136     img.save("S"+str(S)+"_b_"+step+str(it)+'_'+str(v)+"V.png") #save picture
137     del img, draw
138     return None
139
140 def circ_Rs(cir,rs, boundary):
141     """Defines the existing matrix of resistances
142     cir: created circuit
143     rs: matrix of previous resistances or 0 if first iteration"""
144     if rs: #existing circuit
145         Rs_history=rs
146         Rs=rs[-1]
147         R_count=1
148     for i in range(1,M+1): #row
149         for j in range(1,N+1): #column
150             if i==1: #first row
151                 cir.add_resistor('R'+str(R_count), 'n1', 'n'+str(i+j), Rs[R_count-1])
152                 R_count+=1

```

```

153         if j!=N: #horizontal - except last column
154             cir.add_resistor('R'+str(R_count), 'n'+str(i+j), 'n'+str(i+j+1), Rs[R_count-1])
155             R_count+=1
156         else: #last column of the first row
157             if boundary: #connecting resistor
158                 cir.add_resistor('R'+str(R_count), 'n'+str(i+j), 'n2', Rs[R_count-1]) #boundary
159                 R_count+=1
160     elif i==M: #last row - verticals only
161         if not M%2: cir.add_resistor('R'+str(R_count), 'n'+str(N*(M-2)+j+1), cir.gnd, Rs[R_count-1])
162         else: cir.add_resistor('R'+str(R_count), 'n'+str(N*(M-2)+j+1), cir.gnd, Rs[R_count-1])
163         R_count+=1
164     else:
165         cir.add_resistor('R'+str(R_count), 'n'+str((i-2)*N+1+j), 'n'+str((i-1)*N+1+j),
166                                     Rs[R_count-1])
167         R_count+=1
168         if j!=N: #except last column
169             cir.add_resistor('R'+str(R_count), 'n'+str((i-1)*N+1+j),
170                                     'n'+str((i-1)*N+1+j+1), Rs[R_count-1])
171             R_count+=1
172         else:
173             if boundary: #connecting resistor
174                 cir.add_resistor('R'+str(R_count), 'n'+str((i-1)*N+1+j),
175                                     'n'+str((i-1)*N+1+1), Rs[R_count-1]) #boundary
176             R_count+=1
177     else:
178         Rs_history=[]
179         R_count=1
180         Rs=[]
181         for i in range(1,M+1): #row
182             for j in range(1,N+1): #column
183                 if i==1: #first row
184                     if random()<=p:R=Ron
185                     else:R=Roff
186                     cir.add_resistor('R'+str(R_count), 'n1', 'n'+str(i+j), R)
187                     Rs+=[R]
188                     R_count+=1
189                 if j!=N: #horizontal - except last column
190                     if random()<=p:R=Ron
191                     else:R=Roff
192                     cir.add_resistor('R'+str(R_count), 'n'+str(i+j), 'n'+str(i+j+1), R)
193                     Rs+=[R]
194                     R_count+=1
195                 else:
196                     if boundary: #connecting resistor
197                         if random()<=p:R=Ron
198                         else:R=Roff
199                         cir.add_resistor('R'+str(R_count), 'n'+str(i+j), 'n2', R) #boundary
200                         Rs+=[R]
201                         R_count+=1
202             elif i==M: #last row - verticals
203                 if random()<=p:R=Ron
204                 else:R=Roff
205                 if not M%2: cir.add_resistor('R'+str(R_count), 'n'+str(N*(M-2)+j+1), cir.gnd, R)
206                 else: cir.add_resistor('R'+str(R_count), 'n'+str(N*(M-2)+j+1), cir.gnd, R)

```

```

207         Rs+= [R]
208         R_count+=1
209     else:
210         if random()<=p:R=Ron
211         else:R=Roff
212         cir.add_resistor('R'+str(R_count), 'n'+str((i-2)*N+1+j), 'n'+str((i-1)*N+1+j), R)
213         Rs+= [R]
214         R_count+=1
215         if j!=N: #except last column
216             if random()<=p:R=Ron
217             else:R=Roff
218             cir.add_resistor('R'+str(R_count), 'n'+str((i-1)*N+1+j),
219                             'n'+str((i-1)*N+1+j+1), R)
220             Rs+= [R]
221             R_count+=1
222         else:
223             if boundary: #connecting resistor
224                 if random()<=p:R=Ron
225                 else:R=Roff
226                 cir.add_resistor('R'+str(R_count), 'n'+str((i-1)*N+1+j),
227                                 'n'+str((i-1)*N+1+1), R) #boundary
228                 Rs+= [R]
229                 R_count+=1
230     return cir, Rs, Rs_history
231
232 def run_circ(cir):
233     """Defines the analysis
234     cir: circuit to evaluate"""
235     dc1 = new_op()
236     res = run(cir, dc1) # run it
237     return cir, res
238
239 def I_calc(v, res, Rs, Is, Is_top, boundary):
240     """Calculates the current flowing in the circuit
241     v: voltage applied
242     res: calculated resistances in the circuit
243     Rs: matrix of resistances
244     Is: list of currents
245     Is_top: list of top currents
246     boundary: 0 for no boundary conditions and 1 for boundary conditions"""
247     #current calculation
248     I=0
249     I_top=0
250     R_count=1
251     rs_contados=[]
252     if boundary: #boundary conditions
253         for i in range(1, M+1): #row
254             for j in range(1, N+1): #column
255                 if i==1 and R_count%2: #first row - verticals (odd resistors)
256                     I_top+=(v-res['op']['Vn'+str(i+j)])/Rs[R_count-1]
257                     rs_contados+= [R_count]
258                     R_count+=2
259                 elif i==M: #last row - verticals
260                     I+=res['op']['Vn'+str(N*(M-2)+j+1)]/Rs[R_count-1]

```

```

261         rs_contados+=R_count]
262         R_count+=1
263     else:R_count+=2
264 else: #no boundary conditions
265     for i in range(1,M+1): #row
266         for j in range(1,N+1): #column
267             if i==1 and R_count%2: #first row - verticals (odd resistors)
268                 I_top+=(v-res['op']['Vn'+str(i+j)])/Rs[R_count-1]
269                 rs_contados+=R_count]
270                 if j!=N:R_count+=2
271                 else: R_count+=1
272             elif i==M: #last row - verticals
273                 I+=res['op']['Vn'+str(N*(M-2)+j+1)]/Rs[R_count-1]
274                 rs_contados+=R_count]
275                 R_count+=1
276             else:
277                 if j==N:R_count+=1
278                 else:R_count+=2
279
280     Is+=I.tolist()[0]
281     #print 'Rini =', np.float64(0.1)/I[0][0], 'ohms' #I is zero, some v would be needed
282     Is_top+=I_top.tolist()[0]
283     print 'I_top=',I_top[0][0], 'A'
284     print 'I_bottom=',I[0][0], 'A'
285     if abs(I_top[0][0]-I[0][0])>1e-11:raw_input('error: Different top and bottom currents')
286     return I,Is,Is_top
287
288 def ratio(v, step,Is,I,I_compare):
289     """Checks the ratio criteria for each step"""
290     if step=='forming' and len(Is)>3 and abs(Is[-1])>1e-3 and (deltaV/I_compare)/(v/I)>=ratioF:
291         I=Icomp #if the ratio is high, it is ON in principle, so it can stop
292         print 'Resistance change higher than',str(ratioF), '(Forming)'
293     elif step=='reset' and v and (v-deltaV) and abs(Is[-1])>1e-3 and
294             (v/I)/(deltaV/I_compare)>=ratioR:
295         I=Icomp #if the ratio is high, it is ON in principle, so it can stop
296         print 'Resistance change higher than',str(ratioR), '(Reset)'
297     elif step=='set' and v and (v-deltaV) and abs(Is[-1])>1e-3 and
298             (deltaV/I_compare)/(v/I)>=ratioS:
299         I=Icomp #if the ratio is high, it is ON in principle, so it can stop
300         print 'Resistance change higher than',str(ratioS), '(Set)'
301     return I,I_compare
302
303 #define the circuit and do the iterations -----
304 def circ_cal(rs,Is,S,step,Vmin,Vmax,deltaV,f,it,Ising,boundary):
305     """The actual circuit solution uses a modified version of the Newton Rhapson method.
306     rs: matrix of previous resistances or 0 if first iteration
307     Is: matrix of previous currents or 0 if first iteration
308     S: Simulation number
309     step: 'forming', 'reset' or 'set'
310     Vmin: starting voltage value
311     Vmax: ending voltage value
312     deltaV: voltage increment
313     it: iteration number
314     Ising: file name for data saving

```



```

315 boundary: boundary conditions (1) or no boundary conditions (0) ""
316 # Define the circuit
317 cir = Circuit('Circuit')
318 #Voltage source
319 voltage_step = devices.pulse(v1=0, v2=1, td=500e-9, tr=1e-12, pw=1, tf=1e-12, per=2)
320 cir.add_vsource("V1", "n1", cir.gnd, 0, 1, function=voltage_step) #0 volts
321
322 cir,Rs,Rs_history=circ_Rs(cir,rs, boundary) #Rs in place
323
324 print 'Vext = 0 V\nIteration: 0'
325 #circuit calculation
326 cir,res=run_circ(cir)
327 #currents calculation
328 Is=[]
329 Is_top=[]
330 I,Is,Is_top=I_calc(0,res,Rs,Is,Is_top,boundary)
331 #iteration drawing - before starting
332 draw_circ(S,Rs,s,step,0,0, boundary)
333 #save and clean resistances
334 Rs_history+= [Rs]
335 Rs=[]
336
337 #next iterations-----
338 Rs_changed=[0]*len(Rs_history[-1]) #Rs cannot switch back to OFF
339 for v in np. arange(Vmin,Vmax+deltaV,deltaV): #the first one is 0V again
340     changed=1
341     print '-----'
342     print '\nVext = '+str(v)+'V'
343     if I>=Icomp:
344         print 'Icomp reached'
345         break
346     while changed and I<Icomp:
347         it+=1
348         print 'Iteration:',it
349         print step
350         changed=0#at least one resistance must change
351         # Define the circuit
352         cir = Circuit('\nCircuit')
353         voltage_step = devices.pulse(v1=0, v2=1, td=500e-9, tr=1e-12, pw=1, tf=1e-12, per=2)
354         cir.add_vsource("V1", "n1", cir.gnd, v, 1, function=voltage_step) #v volts
355         R_count=1
356         Rs=[]
357         #all R's for all v's
358         for i in range(1,M+1): #row
359             for j in range(1,N+1): #column
360                 if i==1: #first row
361                     if Rs_history[-1][R_count-1]==Roff and
362                         (res['op']['Vn1']-res['op']['Vn'+str(i+j)])>von:
363
364                         R=Ron
365                         print 'R',R_count,': Roff to Ron'
366                         Rs_changed[R_count-1]=1 #this R cannot change again
367                         changed=1 #do the rest of the circuit for the rest of Rs equal to obtain all Vs
368                     elif Rs_history[-1][R_count-1]==Ron and
369                         (res['op']['Vn1']-res['op']['Vn'+str(i+j)])>voff and not Rs_changed[R_count-1]:

```

```

369         R=Roff
370         print 'R',R_count,': Ron to Roff'
371         changed=1 #do the rest of the circuit for the rest of Rs equal to obtain all Vs
372     else: R=Rs_history[-1][R_count-1] #same R
373     VV=res['op']['Vn1']-res['op']['Vn'+str(i+j)] #voltage accross R
374     cir.add_resistor('R'+str(R_count), 'n1', 'n'+str(i+j), R)
375     Rs+= [R]
376     R_count+=1
377     if j!=N: #horizontal - except last column
378         if Rs_history[-1][R_count-1]==Roff and
379             (res['op']['Vn'+str(i+j)]-res['op']['Vn'+str(i+j+1)])>von:
380             R=Ron
381             print 'R',R_count,': Roff to Ron'
382             Rs_changed[R_count-1]=1
383             changed=1
384         elif Rs_history[-1][R_count-1]==Ron and
385             (res['op']['Vn'+str(i+j)]-res['op']['Vn'+str(i+j+1)])>voff
386                 and not Rs_changed[R_count-1]:
387             R=Roff
388             print 'R',R_count,': Ron to Roff'
389             changed=1
390         else: R=Rs_history[-1][R_count-1]
391             VV=res['op']['Vn'+str(i+j)]-res['op']['Vn'+str(i+j+1)]
392             cir.add_resistor('R'+str(R_count), 'n'+str(i+j), 'n'+str(i+j+1), R)
393             Rs+= [R]
394             R_count+=1
395     if j==N and boundary: #boundary
396         if Rs_history[-1][R_count-1]==Roff and
397             abs(res['op']['Vn'+str(i+j)]-res['op']['Vn2'])>von:
398             R=Ron
399             print 'R',R_count,': Roff to Ron'
400             Rs_changed[R_count-1]=1
401             changed=1
402         elif Rs_history[-1][R_count-1]==Ron and
403             abs(res['op']['Vn'+str(i+j)]-res['op']['Vn2'])>voff
404                 and not Rs_changed[R_count-1]:
405             R=Roff
406             print 'R',R_count,': Ron to Roff'
407             changed=1
408         else: R=Rs_history[-1][R_count-1]
409             cir.add_resistor('R'+str(R_count), 'n'+str(i+j), 'n2', R)
410             Rs+= [R]
411             R_count+=1
412     elif i==M: #last row
413         point=(M-1)*N+1-N+j
414         if Rs_history[-1][R_count-1]==Roff and (res['op']['Vn'+str(point)]-[[0]])>von:
415             R=Ron
416             print 'R',R_count,': Roff to Ron'
417             Rs_changed[R_count-1]=1
418             changed=1
419         elif Rs_history[-1][R_count-1]==Ron and (res['op']['Vn'+str(point)]-[[0]])>voff
420                 and not Rs_changed[R_count-1]:
421             R=Roff
422             print 'R',R_count,': Ron to Roff'

```

```

423         changed=1
424     else: R=Rs_history[-1][R_count-1]
425         VV=(res['op']['Vn'+str(point)]-[[0]])
426         cir.add_resistor('R'+str(R_count), 'n'+str(point), cir.gnd, R)
427         Rs+=[R]
428         R_count+=1
429     else:
430         if Rs_history[-1][R_count-1]==Roff and
431             (res['op']['Vn'+str((i-2)*N+1+j)]-res['op']['Vn'+str((i-1)*N+1+j)])>von:
432             R=Ron
433             print 'R',R_count,': Roff to Ron'
434             Rs_changed[R_count-1]=1
435             changed=1
436         elif Rs_history[-1][R_count-1]==Ron and
437             (res['op']['Vn'+str((i-2)*N+1+j)]-res['op']['Vn'+str((i-1)*N+1+j)])>voff
438             and not Rs_changed[R_count-1]:
439             R=Roff
440             print 'R',R_count,': Ron to Roff'
441             changed=1
442         else: R=Rs_history[-1][R_count-1]
443         cir.add_resistor('R'+str(R_count), 'n'+str((i-2)*N+1+j), 'n'+str((i-1)*N+1+j), R)
444         Rs+=[R]
445         R_count+=1
446         if j!=N: #except last column - horizontal
447             if Rs_history[-1][R_count-1]==Roff and
448                 (res['op']['Vn'+str((i-1)*N+1+j)]-res['op']['Vn'+str((i-1)*N+1+j+1)])>von:
449                 R=Ron
450                 print 'R',R_count,': Roff to Ron'
451                 Rs_changed[R_count-1]=1
452                 changed=1
453             elif Rs_history[-1][R_count-1]==Ron and
454                 (res['op']['Vn'+str((i-1)*N+1+j)]-res['op']['Vn'+str((i-1)*N+1+j+1)])>voff
455                 and not Rs_changed[R_count-1]:
456                 R=Roff
457                 print 'R',R_count,': Ron to Roff'
458                 changed=1
459             else: R=Rs_history[-1][R_count-1]
460             VV=res['op']['Vn'+str(i+j+1)]-res['op']['Vn'+str(i+j+2)]
461             cir.add_resistor('R'+str(R_count),
462                             'n'+str((i-1)*N+1+j), 'n'+str((i-1)*N+1+j+1), R)
463             Rs+=[R]
464             R_count+=1
465         if j==N and boundary: #boundary
466             if Rs_history[-1][R_count-1]==Roff and
467                 abs(res['op']['Vn'+str((i-1)*N+1+j)]-res['op']['Vn'+str((i-1)*N+1+1)])>von:
468                 R=Ron
469                 print 'R',R_count,': Roff to Ron'
470                 Rs_changed[R_count-1]=1
471                 changed=1
472             elif Rs_history[-1][R_count-1]==Ron and
473                 abs(res['op']['Vn'+str((i-1)*N+1+j)]-res['op']['Vn'+str((i-1)*N+1+1)])>voff
474                 and not Rs_changed[R_count-1]:
475                 R=Roff
476                 print 'R',R_count,': Ron to Roff'

```

```

477         changed=1
478     else: R=Rs_history[-1][R_count-1]
479     cir.add_resistor('R'+str(R_count),
480                     'n'+str((i-1)*N+1+j), 'n'+str((i-1)*N+1+1), R)
481     Rs+=R]
482     R_count+=1
483
484     cir,res=run_circ(cir)
485
486     I,Is,Is_top=I_calc(v,res,Rs,Is,Is_top,boundary)
487
488     print 'R =', '%.3f'%(np.float64(0.1)/I[0][0]), 'ohms'
489     fig=plt.figure("resistance")
490     if step=='forming':plt.plot(it,np.float64(v)/I[0][0], 'ok')
491     if step=='reset':plt.plot(it,np.float64(v)/I[0][0], 'xr')
492     if step=='set':plt.plot(it,np.float64(v)/I[0][0], '.b')
493     plt.xlabel('Iteration (#)')
494     plt.ylabel('Resistance (ohms)')
495     plt.legend(loc=2)
496     fig.savefig('S'+str(S)+'_Resistance(iteration)')
497
498     #update files
499     f.write(str(v)+'\t'+str(I[0][0])+'\t'+ '%.3f'%(np.float64(v)/I[0][0])+'\n')
500
501     if v==deltaV: I_compare=Is[-1] #first I of each step
502     if v: I,I_compare=ratio(v, step,Is,I,I_compare) #ratio criteria
503
504     #iteration drawing
505     if I<Icomp: #don't count last iteration if >Icomp
506         if changed: draw_circ(S,Rs,s,step,it,v,boundary) #do not draw if nothing happens
507     #save and clean resistances
508     Rs_history+=Rs]
509     Rs=[]
510
511     Ising.write(str(v)+'\t'+str(Rs_history[-1].count(Ron))+'\n') #Ising 2D
512
513     return v-deltaV,Rs_history,Is,it
514
515
516 def I_it(Is,S,it,step):
517     """Plots and saves the evolution of the current with the number of iterations
518     Is: currents
519     S: simulation number
520     it: iteration
521     step: 'forming', 'set' or 'reset'"""
522     fig=plt.figure("current")
523     if step=='comp':plt.plot(np.ones(it+2)*Icomp, 'k', label='Icomp')
524     else: plt.plot(range(len(Is))+np.ones(len(Is))*it,Is, '.', label=step)
525     plt.yscale('log')
526     plt.xlabel('Iteration (#)')
527     plt.ylabel('Current (A)')
528     plt.legend(loc=2)
529     fig.savefig('S'+str(S)+'_Current(iteration)')
530     return None

```

```

531
532 def R_it(Rs,S,it,step):
533     """Plots and saves the evolution of the current with the number of iterations
534     Rs: resistances
535     S: simulation number
536     it: iteration
537     step: 'forming', 'set' or 'reset'"""
538     fig=plt.figure("resistance")
539     plt.plot(range(len(rs))+np.ones(len(rs))*it,rs,'.',label=step)
540     plt.yscale('log')
541     plt.xlabel('Iteration (#)')
542     plt.ylabel('Resistance (ohms)')
543     plt.legend(loc=2)
544     fig.savefig('S'+str(S)+'_Resistance(iteration)')
545     return None
546
547 def plotBars(ss,vs_f,vs_r,vs_s):
548     """Plots and saves the bar plots of the voltages
549     ss: total number of simulations
550     vs_f: forming voltages
551     vs_r: reset voltages
552     vs_s: set voltages"""
553     #bar plotting of voltages for all simulations
554     VS_F=Counter(vs_f)
555     VS_R=Counter(vs_r)
556     VS_S=Counter(vs_s)
557     VS_F=OrderedDict(sorted(VS_F.items(), key=lambda t: t[0]))
558     VS_R=OrderedDict(sorted(VS_R.items(), key=lambda t: t[0]))
559     VS_S=OrderedDict(sorted(VS_S.items(), key=lambda t: t[0]))
560     fig=plt.figure()
561     plt.bar(VS_F.keys(),VS_F.values(),color='blue', width=0.05,label='Forming')
562     plt.bar(VS_R.keys(),VS_R.values(),color='red', width=0.05,label='Reset')
563     plt.bar(VS_S.keys(),VS_S.values(),color='black', width=0.05,label='Set')
564     plt.legend()
565     plt.xlabel('Voltage (V)')
566     plt.ylabel('# switchs')
567     fig.savefig('S='+str(ss)+'_Vs')
568
569     SAVE=open('S='+str(ss)+"bar_plot_V_forming.txt",'w')
570     SAVE.write("Voltage (V)\tRepetition\n")
571     vs=[]
572     no=[]
573     for data in VS_F.keys():
574         vs+=[data]
575     for data in VS_F.values():
576         no+=[data]
577     for ii in range(len(vs)):
578         SAVE.write(str(vs[ii])+"\t\t"+str(no[ii])+"\n")
579     SAVE.close()
580
581     SAVE=open('S='+str(ss)+"bar_plot_V_reset.txt",'w')
582     SAVE.write("Voltage (V)\tRepetition\n")
583     vs=[]
584     no=[]

```

```

585     for data in VS_R.keys():
586         vs+=[data]
587     for data in VS_R.values():
588         no+=[data]
589     for ii in range(len(vs)):
590         SAVE.write(str(vs[ii])+"\t\t"+str(no[ii])+"\n")
591     SAVE.close()
592
593     SAVE=open('S='+str(ss)+"bar_plot_V_set.txt",'w')
594     SAVE.write("Voltage (V)\tRepetition\n")
595     vs=[]
596     no=[]
597     for data in VS_S.keys():
598         vs+=[data]
599     for data in VS_S.values():
600         no+=[data]
601     for ii in range(len(vs)):
602         SAVE.write(str(vs[ii])+"\t\t"+str(no[ii])+"\n")
603     SAVE.close()
604     return None
605
606 def files(i,boundary):
607     """Saves two files with I,R(V) and the # of ON resistors for each voltage applied
608     i: iteration number
609     boundary: boundary conditions (1) or no boundary conditions (0)"""
610     f=open('S'+str(i+1)+"I(V).txt",'w')
611     f.write("#Icomp="+str(Icomp)+'A\n')
612     f.write("Voltage\tCurrent\tResistance\n")
613     f.write("(V) \t (A) \t (ohms)\n")
614     Ising=open('RON(V)_S'+str(i)+'.txt','w')
615     if boundary: Ising.write('with boundary conditions\n')
616     else: Ising.write('without boundary conditions\n')
617     Ising.write('Total # Rs = '+str(M*N+(M-1)*(N-1) + M-1)+'\n')
618     Ising.write('Voltage\tRon\n')
619     return f,Ising
620
621 def conditions():
622     c=open("conditions.txt",'w')
623     c.write('M = '+str(M)+' V\n')
624     c.write('N = '+str(N)+' V\n')
625     c.write('Roff = '+str(Roff)+' ohms\n')
626     c.write('Ron = '+str(Ron)+' ohms\n')
627     c.write('p = '+str(p)+'\n')
628     c.write('voff = '+str(voff)+' V\n')
629     c.write('von = '+str(von)+' V\n')
630     c.write('Vmax = '+str(Vmax)+' V\n')
631     c.write('Vmin = '+str(Vmin)+' V\n')
632     c.write('deltaV = '+str(deltaV)+' V\n')
633     c.write('Icomp = '+str(Icomp)+' A\n')
634     c.write('Icomp2 = '+str(Icomp2)+' A\n')
635     c.write('ratioF = '+str(ratioF)+' V\n')
636     c.write('ratioR = '+str(ratioR)+' V\n')
637     c.write('ratioS = '+str(ratioS)+' V\n')
638     c.write('s = '+str(s)+' V\n')

```

```

639     c.close()
640     return None
641
642 def RCB(simulations,cycles,boundary=1):
643     """Performs the Random Circuit Breaker model to a MxN resistor matrix
644     ss: number of simulations (forming-reset-set, each)
645     c: number of cycles (reset-set) for each simulation
646     boundary: boundary conditions (1) or no boundary conditions (0)"""
647     vs_f=[]
648     vs_r=[]
649     vs_s=[]
650     first=1
651     print '[' ,M,'x',N,'] network'
652     for i in range(simulations):
653         print '##### Simulation no.: ', i+1,'/',simulations
654         f,Ising=files(i,boundary)
655         if first: #forming+first reset
656             v,rs,Is,it=circ_cal(0,0,i+1,'forming',Vmin,Vmax,deltaV,f,0,Ising,boundary)
657             first=0
658             vs_f+=[v]
659             I_it(Is,i+1,0,'forming')
660             it_previous=it #to plot starting on the previous
661             v,rs,Is,it=circ_cal(rs,Is,i+1,'reset',Vmin,Vmax,deltaV,f,it,Ising,boundary)
662             vs_r+=[v]
663             I_it(Is,i+1,it_previous+1,'reset')
664         for med in range(cycles):
665             print '\n##### Cycle no.: ', med+1,'/',cycles, '(' ,i,')'
666             it_previous=it
667             v,rs,Is,it=circ_cal(rs,Is,i+1,'set',Vmin,Vmax,deltaV,f,it,Ising,boundary)
668             vs_s+=[v]
669             I_it(Is,i+1,it_previous,'set')
670             it_previous=it
671             v,rs,Is,it=circ_cal(rs,Is,i+1,'reset',Vmin,Vmax,deltaV,f,it,Ising,boundary)
672             vs_r+=[v]
673             I_it(Is,i+1,it_previous+1,'reset')
674             I_it(Is,i+1,it,'comp') #current compliance line plotted in the end
675             first=1
676         f.close()
677         Ising.close()
678
679     print '\n**END of iterations**'
680     print 'Switching Voltages'
681     print 'forming:', vs_f
682     print 'Resets:', vs_r
683     print 'Sets:', vs_s
684
685     plotBars(simulations,vs_f,vs_r,vs_s) #plot the voltages and save into files
686     conditions() #save simulation conditions
687     return None

```


APPENDIX D

Perceptron

To illustrate with a simple example of how a memristor-based perceptron works, a simulation example using an algorithm written in python 2.7 is given here. The needed libraries are numpy, matplotlib, pylab and csv. To see comments and the details of the algorithm please go to <https://github.com/danieljosesilva/memristivenetworks>. There are two possible ways to run the code. The first is by simply running the .py file, where the simulation conditions are stated and can be changed inside the condition if `__name__ == "__main__"`: at the end of the file. The other way is by creating objects and making operations, step by step, in a python shell, which gives a deeper understanding of the algorithm. The following tutorial will help with the last one.

Opening the python shell in the directory where the .py file is located one must use the command `from perceptron import *`. To import data from a .csv file or randomly generate data for the weight/height classification example used in the main text, a class called `Data` was created. If an input file (e.g. 'data.csv') is given, the respective `__init__` function converts the first N-1 elements of each row of length N to floating point format and creates a dictionary between the two possible last values (usually in the string format) and the integers 0 and 1, in order to perform calculations. If there is no input file, a given number (`npoints`, set to 20 by default) of pairs (weight, height) are randomly generated, using the BMI = 25 criteria for group separation. The function `folds` separates the data into the training (`training_data`) and test (`test_data`) datasets, of sizes $(1 - 1/k)$ and $1/k$ of total data size, respectively.

```
>>> from perceptron import *
>>> data = Data( filename='BMI.csv' )
Dictionary: { 'O': 0, 'N': 1}
>>> len( data.dataset )
46
>>> data.folds(5)
>>> len( data.training_data )
36
>>> len( data.test_data )
9
```

The conductance variation values are given by the class `SetReset`, whose object loads the data of the conductance variation as a function of the actual conductance from a .csv file (conductance

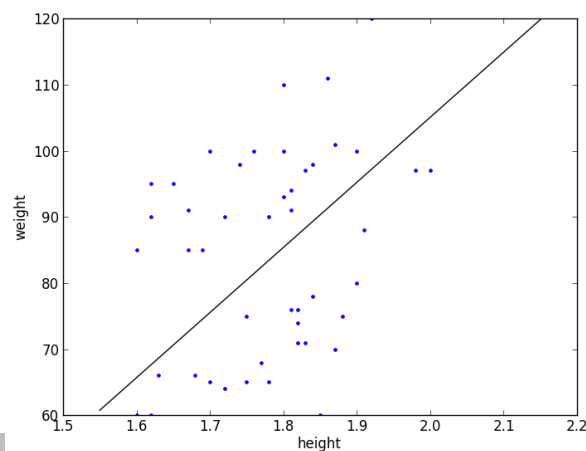
in the first column and conductance variation in the second). Function `deltaG` returns the interpolation of the conductance variation for a given conductance. The network object is created by the class `Perceptron`, initialized (`__init__`) by the number of input neurons (`NA`; 2 by default), the number of output neurons (`NB`; 1 by default), bias constant input (1 by default) and Set and Reset conductance change file names ('`set.csv`' and '`reset.csv`' by default, respectively). It creates two matrices, `A_memristors` and `B_memristors`, that represents all the pairs of weights mentioned in the last section. Empty lists to save the errors at present iteration (`errors`), errors history (`errorshist`), weights history (`Ahist` and `Bhist`) and voltage pulses (`VA` and `VB`) are also created.

```
>>> network = Perceptron(NA=2, NB=1, bias=1,
    setFileName='set.csv', resetFileName='reset.csv')
>>> network.A_memristors
array([[ 0.82141779],
       [ 0.68005111],
       [ 0.17115392])
>>> network.errors
[]
```

Four remaining methods perform the perceptron training and classify operations. The first is the `train` method that allows the training of the perceptron by weight actualization. The input is the index (`iteration`) of the pattern (inputs and expected value) to compute in the training data list. This method is called inside the second method `trainMany` that allows one to train the perceptron under a set of data and over a given number of iterations (`n_epoch`). Therefore, the set of data to train and the number of iterations are the inputs. The third is the `read` method, that gives the classification of the data in the form of 0 or 1. Once more this is used in the fourth method `readMany`, which updates the list `errors` with the number of errors for each test pattern in the list `test_data` give as input. An additional method (`eq_hyperplane`) gives the 2D equation of the hyperplane for visualization purposes.

```
>>> network.trainMany(data.training_data,
    numberIterations=25, l_rate=0.1)
epoch = 1, lrate = 0.100, error = 15
epoch = 2, lrate = 0.100, error = 16
epoch = 3, lrate = 0.100, error = 16
epoch = 4, lrate = 0.100, error = 16
epoch = 5, lrate = 0.100, error = 18
epoch = 6, lrate = 0.100, error = 10
epoch = 7, lrate = 0.100, error = 6
epoch = 8, lrate = 0.100, error = 6
epoch = 9, lrate = 0.100, error = 6
epoch = 10, lrate = 0.100, error = 6
epoch = 11, lrate = 0.100, error = 6
```

```
epoch = 12, lrate = 0.100, error = 6
epoch = 13, lrate = 0.100, error = 6
epoch = 14, lrate = 0.100, error = 6
epoch = 15, lrate = 0.100, error = 6
epoch = 16, lrate = 0.100, error = 2
epoch = 17, lrate = 0.100, error = 0
epoch = 18, lrate = 0.100, error = 0
epoch = 19, lrate = 0.100, error = 0
epoch = 20, lrate = 0.100, error = 0
epoch = 21, lrate = 0.100, error = 0
epoch = 22, lrate = 0.100, error = 0
epoch = 23, lrate = 0.100, error = 0
epoch = 24, lrate = 0.100, error = 0
epoch = 25, lrate = 0.100, error = 0
>>> network.readMany(data.test_data)
Correct tested patterns: 100.0 %
>>> network.errors
[0.0, 0.0, 0.0, 0.0, 0.0, 0.0, 0.0, 0.0, 0.0]
>>> height = [i[0][0] for i in data.dataset]
>>> weight = [i[0][1] * 100 for i in data.dataset]
>>> plt.plot(height, weight, '.')
>>> plt.plot(np.arange(1.55, 2.2, .2),
network.eq_hyperplane(np.arange(
    1.55, 2.2, .2)) * 100, '-k')
>>> plt.xlabel('height')
>>> plt.ylabel('weight')
>>> plt.show()
```



Other straightforward and common test to check if the algorithm is working can be performed using the linearly separable logic gates (AND and OR, and obviously, NAND and OR). The Boolean

functions are summarized in Table A2.1.

Table A2.1 – AND, OR, NAND and NOR logical operations.

A	B	$A \text{ AND } B$	$A \text{ OR } B$	$A \text{ NAND } B$	$A \text{ NOR } B$
0	0	0	0	1	1
0	1	0	1	1	0
1	0	0	1	1	0
1	1	1	1	0	0

The proposed algorithm successful classification of these logical operations is shown in Fig. A2.1. This shows that the memristive perceptron is able to implement logical operations, computing binary inputs to produce a single binary output.

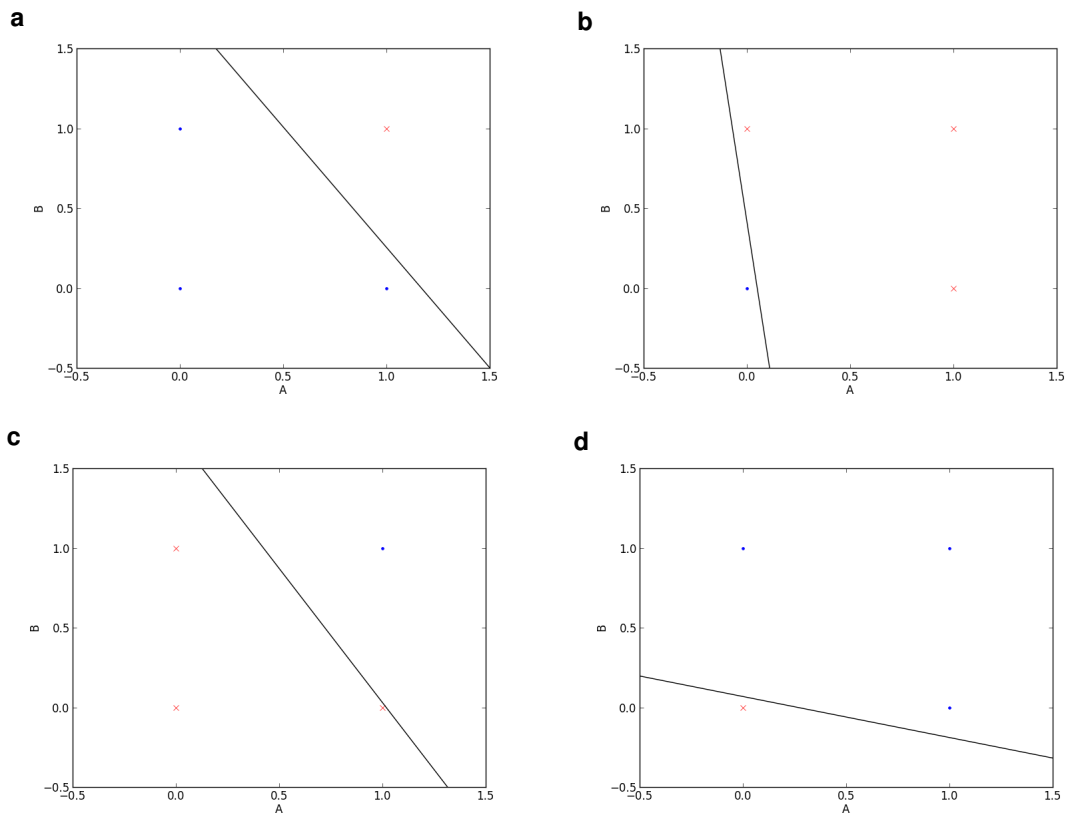


Figure A2.1 – Memristive-perceptron classification of the (a) AND, (b) OR, (c) NAND and (d) NOR logical operations. Blue dots and red crosses represent 0's and 1's, respectively.

```

1  #memristivePerceptron.py
2  ---
3
4  import numpy as np
5  import matplotlib.pyplot as plt
6  import pylab
7  from csv import reader
8
9
10 class Data:
11
12     def __init__(self, filename=None, npoints=20):
13         self.dataset = []
14         self.training_data = []
15         self.test_data = []
16         if filename:
17             self.keys = dict()
18             with open(filename, 'r') as file:
19                 csv_reader = reader(file)
20                 for row in csv_reader:
21                     if not row: continue
22                     self.dataset.append(row)
23             for i in range(len(self.dataset[0]) - 1):
24                 for row in self.dataset:
25                     row[i] = float(row[i].strip())
26             column = len(self.dataset[0]) - 1
27             class_values = [row[column] for row in self.dataset]
28             unique = set(class_values)
29             for i, value in enumerate(unique):
30                 self.keys[value] = i
31             for row in self.dataset:
32                 row[column] = self.keys[row[column]]
33             print 'Dictionary:', self.keys
34             for i in range(len(self.dataset)):
35                 self.dataset[i] = [np.array(self.dataset[i][: -1]),
36                                     np.array([float(self.dataset[i][ -1])])]
37         else:
38             BMI = 25
39             for i in range(npoints):
40                 height = np.random.uniform(1.6, 2.0)
41                 group = np.random.randint(2)
42                 if group:
43                     arg = BMI * height * height / 100 + .05
44                     weight = np.random.uniform(arg, 1.2)
45                 if not group:
46                     arg = BMI * height * height / 100 - .05
47                     weight = np.random.uniform(.4, arg)
48                 self.dataset.append([np.array([height, weight]), np.array([float(group)])])
49
50     def folds(self, kfold):
51         i = 0
52         indexes = []
53         while i < int((1. - 1./kfold) * len(self.dataset)):
54             k = np.random.randint(len(self.dataset))

```

```

55         if k not in indexes:
56             indexes.append(k)
57             self.training_data.append(self.dataset[k])
58             i += 1
59     compare_data = [self.training_data[i][j].tolist() for i in range(
60         len(self.training_data)) for j in range(len(self.training_data[i]))]
61     i = 0
62     while i < int((1./kfold) * len(self.dataset)):
63         k = np.random.randint(len(self.dataset))
64         if self.dataset[k][0].tolist() not in compare_data:
65             self.test_data.append(self.dataset[k])
66             i += 1
67
68     class SetReset:
69
70     def __init__(self, fileName, norm=1E3):
71         input = open(fileName, 'r')
72         s = input.readlines()
73         self.xDistribution = []
74         self.yDistribution = []
75         for line in s:
76             pair = line.split(',')
77             self.xDistribution.append(norm * float(pair[0]))
78             self.yDistribution.append(norm * float(pair[1]))
79         input.close()
80
81     def deltaG(self, xValue):
82         return pylab.interp(xValue, self.xDistribution, self.yDistribution)
83
84
85     class Perceptron:
86
87     def __init__(self, NA=2, NB=1, bias=1, setFileName='set.csv', resetFileName='reset.csv'):
88         self.A_memristors = np.random.rand(NA + 1, NB)
89         self.B_memristors = np.random.rand(NA + 1, NB)
90         self.Ahist = []
91         self.Bhist = []
92         self.NA = NA
93         self.NB = NB
94         self.bias = bias
95         self.errors = []
96         self.errorshist = []
97         self.set = SetReset(setFileName)
98         self.reset = SetReset(resetFileName)
99         self.VA = [[0]] * (NA + 1)
100        self.VB = [[0]] * (NA + 1)
101        self.Ahist.append(np.copy(self.A_memristors))
102        self.Bhist.append(np.copy(self.B_memristors))
103
104    def train(self, iteration, l_rate, voltSet=-1.7, voltReset=2.6):
105        inputs = np.copy(iteration)
106        inputs[0] = np.lib.pad(inputs[0], (0, 1), 'constant', constant_values=(self.bias))
107        unit_step = lambda x: 0 if x <= 0 else 1
108        result = []

```

```

109 error = np.zeros(self.NB)
110 for i in range(self.NB):
111     result.append(np.dot(inputs[0], (self.A_memristors.T[i] - self.B_memristors.T[i])))
112     error[i] = inputs[1][i] - unit_step(result[-1])
113     er = error[i]
114     self.errors.append(er)
115     for j in range(self.NA+1):
116         idealA = self.A_memristors[j][i] + l_rate * er * inputs[0][j] / 2.
117         idealB = self.B_memristors[j][i] - l_rate * er * inputs[0][j] / 2.
118         if er > 0: #increase A, decrease B
119             cc = 1
120             while self.A_memristors[j][i] < idealA and cc < 1E3:
121                 dgA = abs(self.set.deltaG(self.A_memristors[j][i]))
122                 self.A_memristors[j][i] += dgA
123                 self.VA[j].append(voltSet)
124                 cc += 1
125             cc = 1
126             while self.B_memristors[j][i] > idealB and cc < 1E3:
127                 dgB = abs(self.reset.deltaG(self.B_memristors[j][i]))
128                 self.B_memristors[j][i] -= dgB
129                 self.VB[j].append(voltReset)
130                 cc += 1
131         if er < 0: #decrease A, increase B
132             cc = 1
133             while self.A_memristors[j][i] > idealA and cc < 1E3:
134                 dgA = abs(self.reset.deltaG(self.A_memristors[j][i]))
135                 self.A_memristors[j][i] -= dgA
136                 self.VA[j].append(voltReset)
137                 cc += 1
138             cc = 1
139             while self.B_memristors[j][i] < idealB and cc < 1E3:
140                 dgB = abs(self.set.deltaG(self.B_memristors[j][i]))
141                 self.B_memristors[j][i] += dgB
142                 self.VB[j].append(voltSet)
143                 cc += 1
144             if self.A_memristors[j][i] > 1: self.A_memristors[j][i] = 1
145             if self.A_memristors[j][i] < 0: self.A_memristors[j][i] = 0
146             if self.B_memristors[j][i] > 1: self.B_memristors[j][i] = 1
147             if self.B_memristors[j][i] < 0: self.B_memristors[j][i] = 0
148     self.Ahist.append(np.copy(self.A_memristors))
149     self.Bhist.append(np.copy(self.B_memristors))
150
151 def trainMany(self, training_data, numberIterations, l_rate):
152     for i in range(numberIterations):
153         self.errors = []
154         for j in range(len(training_data)):
155             self.train(training_data[j], l_rate, voltSet=-1.7, voltReset=2.6)
156             self.errorshist.append(np.copy(self.errors))
157             print ('>epoch = %d, lrate = %.3f, error = %d' %
158                   (i+1, l_rate, sum(map(abs, self.errorshist[i]))))
159
160 def read(self, pattern):
161     pattern = np.lib.pad(pattern, (0, 1), 'constant', constant_values=(self.bias))
162     unit_step = lambda x: 0 if x <= 0 else 1

```

```

163     result = []
164     for i in range(self.NB):
165         arg = self.A_memristors.T[i] - self.B_memristors.T[i]
166         result.append(unit_step(np.dot(pattern, arg)))
167     return np.array(result)
168
169 def readMany(self, patterns):
170     self.errors = []
171     for pattern in patterns:
172         self.errors.append(sum(map(abs, (self.read(pattern[0]) - pattern[1]))))
173     arg = (len(patterns) - sum(map(abs, self.errors))) / len(patterns)
174     print 'Correct tested patterns:', arg * 100, '%'
175
176 def eq_hyperplane(self, x):
177     m = -(self.A_memristors[0] - self.B_memristors[0]) / \
178         (self.A_memristors[1] - self.B_memristors[1])
179     b = -(self.A_memristors[2] - self.B_memristors[2]) / \
180         (self.A_memristors[1] - self.B_memristors[1])
181     return m * x + b
182
183 if __name__ == "__main__":
184
185     l_rate = 0.1
186     n_epoch = 50
187     kfolds = 5  #(1-1/k) of data used for training and 1/k for test
188
189     data = Data()
190     data.folds(kfolds)  #separate data
191     print 'Training points:', len(data.training_data)
192     print 'Testing points:', len(data.test_data)
193
194     network = Perceptron()
195     network.trainMany(data.training_data, n_epoch, l_rate)  #training dataset
196     network.readMany(data.test_data)  #test dataset
197
198      #plot dG(G)
199     plt.figure('Experimental data')
200     plt.plot(network.set.xDistribution,
201              network.set.yDistribution, '-g', label='Set')
202     plt.plot(network.reset.xDistribution,
203              network.reset.yDistribution, 'x-r', label='Reset')
204     plt.xlabel('G (S)')
205     plt.ylabel('$\Delta$G (S)')
206     plt.xlim([0, 1])
207     plt.ticklabel_format(axis='y', style='sci', scilimits=(0, 0))
208     plt.legend()
209
210      #plot data
211     if len(data.dataset[0][0]) == 2:  #2 inputs - 2D representation
212         plt.figure('BMI')
213         plt.xlabel('height (m)')
214         plt.ylabel('weight (kg)')
215
216     height_normal_training=[i[0][0]

```



```

217                                     for i in data.training_data if not i[1]]
218 height_over_training=[i[0][0] for i in data.training_data if i[1]]
219 weight_normal_training=[i[0][1]*100
220                                     for i in data.training_data if not i[1]]
221 weight_over_training=[i[0][1]*100
222                                     for i in data.training_data if i[1]]
223 height_normal_test=[i[0][0] for i in data.test_data if not i[1]]
224 height_over_test=[i[0][0] for i in data.test_data if i[1]]
225 weight_normal_test=[i[0][1]*100
226                                     for i in data.test_data if not i[1]]
227 weight_over_test=[i[0][1]*100 for i in data.test_data if i[1]]
228 plt.plot(height_normal_training,weight_normal_training,
229          'ob', label='normal weight (training)')
230 plt.plot(height_over_training,weight_over_training,
231          'sr', label='overweight (training)')
232 plt.plot(height_normal_test,weight_normal_test, 'ob',
233          fillstyle='none', label='normal weight (test)')
234 plt.plot(height_over_test,weight_over_test, 'sr',
235          fillstyle='none', label='overweight (test)')
236
237 plt.xlim(min([i[0][0] for i in data.training_data]) - 0.05,
238          max([i[0][0] for i in data.training_data]) + 0.05)
239 plt.ylim(min([i[0][1] * 100 for i in data.training_data]) -
240          10, max([i[0][1] * 100 for i in data.training_data]) + 10)
241 plt.legend(loc='upper left')
242
243 plt.plot(np.arange(1.55, 2.2, .2), network.eq_hyperplane(
244          np.arange(1.55, 2.2, .2)) * 100, '-k')
245
246 #plot error sum
247 plt.figure('Error')
248 plt.xlabel('epoch')
249 plt.ylabel('error sum')
250 plt.xlim([1, n_epoch + 1])
251 plt.plot(np.arange(1, n_epoch + 1),
252          [sum(map(abs, i)) for i in network.errorshist], '-b')
253
254 #plot weights
255 if len(data.dataset[0][0]) == 2: #2 inputs
256     plt.figure('weights')
257     plt.xlabel('iteration')
258     for i in range(len(network.Ahist)):
259         for j in range(network.NA + 1):
260             plt.subplot(((network.NA + 1) * 2 + 1) * 100 + 10 + 2 * j + 1)
261             plt.plot(i,network.Ahist[i][j], '.r')
262             plt.ylabel('wA'+str(j + 1))
263             plt.ylim([0, 1])
264             plt.xticks([])
265             plt.yticks(np.arange(0, 1 + 0.25, 0.25))
266             if j == network.NA: plt.ylabel('wAb')
267             plt.subplot(((network.NA+1) * 2 + 1) * 100 + 10 + 2 * j + 2)
268             plt.plot(i,network.Bhist[i][j], '.b')
269             plt.ylabel('wB'+str(j + 1))
270             plt.ylim([0, 1])

```

```

271         plt.xticks([])
272         plt.yticks(np.arange(0, 1 + 0.25, 0.25))
273         if j == network.NA: plt.ylabel('wBb')
274     plt.subplot((len(network.Ahist[0]) * 2 + 1) * 100 + 10 +
275                (len(network.Ahist[0]) * 2 + 1))
276     plt.ylabel('error')
277     plt.xlabel('iteration')
278     plt.ylim([-1, 1])
279     plt.yticks([-1, 0, 1])
280     plt.xlim([0, n_epoch * len(data.training_data)])
281     cc = 1
282     for i in range(n_epoch):
283         for j in range(len(data.training_data)):
284             plt.bar(cc - 1, network.errorshist[i][j])
285             cc += 1
286
287     #plot pulses
288     if len(data.dataset[0][0]) == 2: #2 inputs
289         plt.figure('pulses')
290         for i in range(network.NA + 1):
291             plt.subplot((network.NA + 1) * 2 * 100 + 10 + 2 * i + 1)
292             plt.plot(np.arange(len(network.VA[i])), network.VA[i], 'r')
293             plt.ylabel('VA'+str(i + 1))
294             plt.xticks([])
295             plt.yticks([min(network.VA[i]), 0, max(network.VA[i])])
296             if j == network.NA: plt.ylabel('VAb')
297             plt.subplot(len(network.Ahist[0]) * 2 * 100 + 10 + 2 * i + 2)
298             plt.plot(np.arange(len(network.VB[i])), network.VB[i], 'b')
299             plt.ylabel('VB'+str(i + 1))
300             if not i == network.NA: plt.xticks([])
301             plt.yticks([min(network.VA[i]), 0, max(network.VA[i])])
302             if j == network.NA: plt.ylabel('VBb')
303             if i == network.NA: plt.xlabel('pulse number')
304
305 plt.show()

```